UNIVERSITY OF GENOVA

PHD PROGRAM IN SCIENCE AND TECHNOLOGY FOR ELECTRICAL ENGINEERING, MARINE ENGINEERING AND COMPLEX SYSTEMS FOR MOBILITY

Experimental investigation on propeller and blade loads during off-design conditions

by

Fabrizio Ortolani

Thesis submitted for the degree of *Doctor of Philosophy* (33° cycle)

March 2021

Prof. Michele Viviani	Supervisor
Dr. Giorgio Tani	Supervisor
Dr. Giulio Dubbioso	Supervisor
Prof. Mario Marchesoni	Head of the PhD program

CC BY NC ND

DITEN

Department of Electrical, Electronics and Telecommunication Engineering and Naval Architecture

Declaration

I hereby declare that except where specific reference is made to the work of others, the contents of this dissertation are original and have not been submitted in whole or in part for consideration for any other degree or qualification in this, or any other university. This dissertation is my own work and contains main parts of articles published during the three years of my PhD, concerning the topic of my thesis and nothing which is the outcome of work done in collaboration with others, except as specified in the "Citations", text and "Acknowledgements" has been used.

Fabrizio Ortolani
June 2021

Citations

Material from this dissertation has been published in the following form:

Ortolani F., Viviani M., Tani G., Dubbioso G.. 'Experimental Investigation of Single Blade Loads by Captive Model Tests in Pure Oblique Flow. Part II: Propeller loads and preliminary comparison with transient loads'. 2021 Ocean Engineering, 234, 15, 109149

Ortolani F, Dubbioso G, 'In-plane and single blade loads measurement setups for propeller performance assessment during free running and captive model tests' – 2020 Ocean Engineering 217, 107928

Ortolani F., Viviani M., Tani G., Dubbioso G., 'Experimental investigation of single blade loads by captive model tests in pure oblique flow'. 2020 - Ocean Engineering. DOI: 10.1016/j.oceaneng.2019.106789

Ortolani F., Dubbioso G., 'Experimental investigation of blade and propeller loads: Steady turning motion'. 2019. Applied Ocean Research 91. DOI: 10.1016/j.apor.2019.101874

Ortolani F., Dubbioso G., 'Experimental investigation of single blade and propeller loads by free running model test. Straight ahead sailing' 2019. Applied Ocean Research 87. DOI: 10.1016/j.apor.2019.03.005

Acknowledgements

I would like to express my sincere gratitude towards my supervisor Prof. Michele Viviani. He always provided me the guidance and support when required and his experience has often been the cherry on top of this research achievements. I also thank Dr. Giorgio Tani for his contribution, that have indeed enriched my investigation. I would like to thank Prof. Pablo Carrica for the thoughtful and comprehensive comments and recommendations which contributed, from multiple perspectives, to enrich the content of this dissertation. I also thank Prof. Antonio Scamardella for the time devoted to the review and his appreciation of my research activity. The research reported in the present thesis is part of my working activity at CNR-INM. This allowed me to have a valuable support in the development of the setups and have the priceless possibility to use the facilities to perform the experimental activities. Therefore, I want to thank CNR-INM for the opportunity to perform my PhD in such a prestigious environment, supporting the investigation within RESMARE and EDA FLOWIS projects. More specifically, I hereby express my gratitude to Dr. Fabio Di Felice and Dr. Salvatore Mauro, for giving me the opportunity to perform the experimental campaigns and Dr. Ivan Santic for his valuable support during the tests. I sincerely thank Roberto Zagaglia and Fabio Carta for their creative input through mechanical drawings and also, Massimiliano Sellini and Alberto Sabelli for their help in electronic issues. Thanks to all the facilities' staff, which played a crucial role in setup and testing. Thank you to Luca Mauro and Elena Paifelman for being always present, patiently supporting my hard time sharing laughter and coffees. I would like to thank my parents, my brothers, my whole family and my wife who have always believed in me and endured my mood swings and my daughters who have been my best distraction. Giulio Dubbioso, I kept you for the last. In 2011 I met a new colleague, now I know that I've found one of my best friends. You have been my mentor in the last years and this research is the fruit of our common, enthusiastic passion for research and your ability to trigger my inclination for tough challenges. I really want to thank you for all your encouragement, the squabbles, the scoldings and the whole days spent trying to transfer your knowledge to my 'curdled brain', compensated by trying to teach you how to use a screwdriver, in short, all the good time that made us like the Beavis and Butthead iconic pair!

Abstract

The present thesis wants to take a step forward towards the understanding and quantification of the complex hydrodynamic mechanisms which characterize the propeller performance during real operative scenarios: a novel set–up, based on the measure of three forces and moments exerted by the single blade of the propulsor, has been developed, installed and successfully tested on a twin screw scaled model at the CNR-INM maneuvering basin and towing tank. At first, the new setup is presented, reporting the results of the extensive experimental activity performed on the selected test case, dedicated to quantify, for the first time by means of free-running model test, the entity of the single blade forces and integrated propeller loads in different operating conditions. Although free running model tests still represent the primary approach for a reliable performance assessment, they require facilities and devices that are not commonly affordable; alternatively, rectilinear towing tank can be used for manoeuvring investigations by static or dynamic tests and can be a valid alternative to investigate propeller performance in off-design. Considering this, another experimental campaign has been performed at CNR-INM towing tank. In the experiments, the drift angle and the advance speed of the model were varied systematically, to focus on the relation between propeller operating conditions and loads. Moreover, the averaged and periodic blade and propeller loads are compared, in terms of the equivalent drift angle, to the measurements obtained by free running model tests, in order to demonstrate the feasibility of simulating turning circle stabilized phase with pure oblique flow tests, providing a preliminary quantification of the off-design loads developed by the propeller. The research ends with the comparison of single blade loads that arise during transient motions of the turning manoeuvres at weak and tight rudder angles, performed at the same reference speed of the captive model test. This section allows to analyse the possibilities and limitations of the characterization of propeller performance under time varying inflow by means of quasi-steady towing conditions. The availability of cycle–resolved blade loads further highlighted their fluctuating nature with respect to the averaged ones and opens new paths for the investigation of hydrodynamic phenomena that characterize the performance of the propeller and blade(propeller)/wake interaction in behind hull, both during design and off-design conditions.

Table of contents

List of figures

List of tables

Nomenclature

Acronyms / Abbreviations

α Incidence angle of flow with respect to the blade foil

δ Rudder angle

ω Propeller angular speed

Θ Geometric pitch of generic blade section

θ Reference blade angular position

CG Blade center of gravity

CP Blade center of hydrodynamic forces

D Propeller diameter

Fn Froude number

P Blade pitch

Q_x^C, Q_y^C, Q_z^C Moments due to centrifugal force (in transducer 'T' frame)

Q_x^H, Q_y^H, Q_z^H Moments due to hydrodynamic forces (in transducer 'T' frame)

T_x^C, T_y^C, T_z^C centrifugal force (in transducer 'T' frame)

T_x^H, T_y^H, T_z^H hydrodynamic forces components (in transducer 'T' frame)

u Axial component of the speed relative to the propeller

V Flow speed relative to the propeller

v_t Tangential component of the speed relative to the propeller

W Propeller weight

W_{blade} Blade weight

x^B, y^B, z^B blade coordinate system (rotating)

x^H, y^H, z^H propeller hub coordinate system (fixed)

x^T, y^T, z^T Six axes transducer coordinate system (rotating)

x_{CG}, y_{CG}, z_{CG} coordinates of blade center of gravity

x_{CP}, y_{CP}, z_{CP} coordinates of hydrodynamic center of pressure

Chapter 1

Introduction

1.1 Why study off-design conditions?

In the last decade, an increasing interest on propeller performance in off–design conditions has been evident among the industries, classification societies and research institutions: the main reason lies in the demand of fulfilling some aspects like safety, low emissions and continuity of operation for the new ships, that are not completely assessed during the early design phases. In fact, in realistic operational conditions, the propulsion system of a ship experiences functioning regimes that can be completely different from the optimal one at the design point, as a consequence of environmental disturbances (wind, waves) and ship handling (maneuvering, change of speed). In these conditions, the flow around the hull, and hence, the inflow to the propeller are modified with consequent alteration of developed loads and degradation of propulsion efficiency, causing an increase of required power to the prime mover. The wake field generated by the upstream hull causes the marine propeller to operate in a spatially non–homogeneous and unsteady inflow field (Breslin and Andersen (1994)) and, consequently, the blades develop a complete system of unsteady, fluctuating loads. In fact, in off-design conditions, flow separation from the hull and appendages due to vertical and lateral motions produce non–negligible tangential velocity components and more severe gradients of the velocity field. Hence, the blade sections, designed to operate at their maximum efficiency at the target point in calm water and rectilinear motion, might experience completely different hydrodynamic conditions that alter the mean and fluctuating components of the blade loads. The quantification and prediction of these load components are of utmost importance to improve the design procedures, to guarantee the operational life of the propulsion system and the continuity of operation at sea (thus reducing the risk of damage and maintenance costs) as well as to develop novel solutions to reduce undesired effects associated to propeller functioning (i.e., pressure pulses, noise). The propeller mean loads are critical for the structural strength of the shafting system as well as the dynamic response of the vessel; for example, in maneuvering conditions, thrust and torque experience increases up to 100% with respect to the value experienced in the approach phase (Coraddu et al. (2013)) and relevant in–plane forces and moments are also developed (Dubbioso et al. (2017); Ortolani et al. (2015a)). Those loads are the main cause of scoring and wiping stern tube bearing, as shown in Figure 1.1.

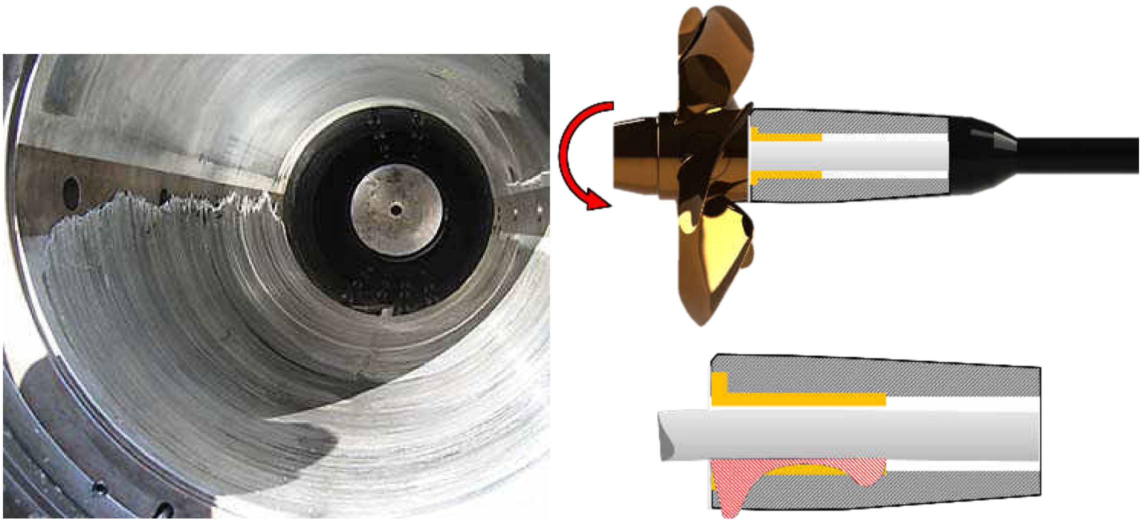

Figure 1.1 Shaft bearing failure (with courtesy of DNV) and graphic explanation

Moreover, the fluctuations of blade (and, hence, propeller) loads, that can be extremely critical if compared to the average overloading, are associated to vibrations transmitted to the hull via the shafting support, fatigue loads of the shafting and propeller system, pressure pulses to the hull and radiated noise.

In this respect, modern design techniques are being improved to also consider realistic and typical off–design conditions experienced by the ship and its propulsion system, in order to increase the operational life of the ship and the safety at sea, as well as its overall efficiency. In particular, in the framework of the NATO STO Task Group AVT-204 ("Assess the Ability to Optimize Hull Forms of Sea Vehicles for the Best Performance in a Sea Environment"), a non–standard design approach was pursued considering the operation in waves: the optimal propeller shape was designed by using a set of different wake profiles caused by motion in waves for the optimization of the shape of the propeller blades instead of considering only the wake in calm water (Grigoropoulos et al. (2017)). This approach is supported by the fact that the nominal wake of the ship is altered as a consequence of the motion in waves; in particular, velocity gradients experienced by the propeller blades can be more critical, because the phasing, the extent and the dynamics of the cavitation volume might be affected worsening the propeller efficiency and giving rise to undesired effects (Taskar and Steen (2016); Taskar et al. (2017)). Similar situations occur in maneuvering conditions: recent free running tests (Ortolani et al. (2015a)) on a twin screw scaled model showed abrupt overloading of thrust and torque, up to 100% in excess of the value in rectilinear motion and non–negligible forces and moments acting in the plane of the propeller. A further outcome of these activities, confirmed by *CFD* simulations (Dubbioso et al. (2017); Muscari et al. (2017)), was the fact that maneuvers at small drift angle could be as critical as tighter ones. In these situations, the combination of low propeller loading and detachment of coherent structures convected through the propeller disk causes very complex propeller/wake interactions that yield strong peaks for the in–plane loads. In turn, the onset of these phenomena amplifies side effects such as propeller–hull induced vibratory loads, pressure pulses and noise emission that, during transient motions, can be further exacerbated.

Maneuvering and motion in waves are also important to consider in the case of orientable propulsion unit (i.e. POD). These devices, replacing the action of the rudder to control and maneuver the ship, might operate in severe oblique flow conditions. Consequently the blades might develop large fluctuating loads and in–plane forces and moments, that can be further amplified by dynamic effects during transients (Amini and Steen (2011)) and ventilation effects due to wave–induced motions (Berchiche et al. (2018)).

1.2 State of the art of single blade loads characterization

Numerical techniques typically utilized in propeller design are based on potential based solvers like Vortex Lattice or Boundary Elements Methods (VLM and BEM). These tools are extensively validated for propeller operating in typical design conditions in rectilinear motion, otherwise their reliability in off–design conditions might be worsened due to the higher angle of attack experienced by the blade sections and their inability to describe accurately flow separation. Although viscous solvers overcome these drawbacks some way and the computation of the flow of a rotating propeller past a ship is nowadays affordable (Carrica et al. (2012); Castro et al. (2011); Dubbioso et al. (2013, 2014); Mofidi and Carrica (2014); Muscari et al. (2011); Sun et al. (2018); Yao (2015)), this kind of computations requires a huge amount of computational resources and, therefore, is a prohibitive approach to a routine application during the design; in case of maneuvering or seakeeping simulations, the computational effort further increases, since hundreds of propeller cycles have to be resolved to cover the characteristic period of the motion. Moreover, the limited studies proposed in literature did not provide a validation of the calculated blade/propeller forces.

On these basis, the complementary aid of experimental activities and the development of non-standard set-up play a fundamental role to the understanding and quantification of the propeller loads operating in realistic and off-design conditions. Last but not least, accurate experimental data are necessary for the validation of numerical/theoretical propeller models.

The traditional as well as standardized approach for analyzing propeller performance in isolated and behind hull condition in ship model testing relies on the measurements of only propeller thrust and torque. The realization of a set–up to monitor the complete system of loads developed by the blade or propeller both in the isolated and behind hull configurations is very challenging. In fact, in standard applications, the positioning of the measuring devices offers a large versatility and is not constrained to be in the close proximity of the propeller (for example, the thrust/torque transducer is usually installed along the propeller shaft in a dry environment in self–propelled models). Conversely, the measurements of the in–plane propeller loads and the single blade loads require the transducer/sensing device to be placed inside the propeller or very close to it, and it always operates in a wet (and/or depressurized) environment. This constraint remarkably complicates the set–up (i.e., ad–hoc design of the propeller hub, transfer of the signal from a rotating to a fixed frame via the shafting) and increases the cost of the experiment.

In literature, developments and applications on the subject are poorly documented, both for isolated and behind hull configurations; these non–standard set–up were adopted to investigate specific aspects associated to traditional or novel propulsor devices operating in design and off–design conditions, i.e. structural loads of controllable pitch propellers, azimuth propulsors and propeller ice–interactions.

The first attempt to measure single blade loads, for a propeller in isolated condition, was tasked to understand the unsteady nature of propeller loads and propeller–hull induced pressure and to provide useful data to validate numerical codes, based on blade element and potential based theory (Boswell et al. (1981); Breslin and Andersen (1994)). In these experiments, the wake field was reproduced by means of screens, in order to obtain excitation of blade loads at integer multiples of the blade passing frequency (BPF). The single blade was constrained to a custom transducer, designed to measure two components at a time, so the complete system of blade loads was derived by multiple measurements for the same operative conditions, changing the transducer orientation. In Jessup (1990), the same set–up was used to characterize the unsteady thrust and torque of the research propellers $P4119$ and 4119. Moreover, in Jessup et al. (2009), the effect of cavitation on alternating blade loads for the controllable pitch propeller $P4990$ were assessed by setting the propeller at incidence in the 24–inch DTRC (David Taylor Research Center) Cavitation Tunnel. This study, showed that extensive cavitation could cause 35% load fluctuation with respect to the mean value.

The complete characterization of propeller loads was carried out in last decades to investigate the performance of azimuthal propulsors (thruster and POD – propulsor orientable device), with particular emphasis on the effects of oblique flow, motion in waves and ventilation phenomena. In this framework, Koushan (2006) and Amini and Steen (2012) developed an hub mounted blade and propeller transducer to deeply investigate these problems and obtain high quality experimental data for the validation of viscous flow solvers (Berchiche et al. (2018); Krasilinov et al. (2009)).

Finally, single blade loads measurements were investigated in the field of ice–propeller interaction; this is a very complex process due to high propeller blade tip velocities, complexity of the flow in the propeller disk and the randomness in the shape and the way an ice piece interacts with a propeller.

In Wang et al. (2006) a model of POD propulsor equipped with commercial transducer for the measurement of single blade, propeller and complete unit loads is presented; Hagesteijn et al. (2012) developed a 6–component in–house transducer for single blade load measurements that was also successfully tested for propeller in isolated condition to monitor blade spindle torque (Funeno et al. (2013)).

The first attempt to measure single blade loads for a propeller operating in behind–hull condition dates back to Blaurock (1975). The single blade loads of a propeller mounted behind a single screw merchant ship model were measured by a custom cantilever beam transducer constrained to the blade root and the hub; the device allowed for the direct measure of two blade root moments at different points of the beam, from which the blade thrust and side force were obtained, assuming a linear distribution of the moments. The experiments were carried out for the ship model in straight ahead and static drift angle, and the effect of the number of blades was also investigated. The non standard set–up developed in Boswell et al. (1981) for the analysis of unsteady blade and propeller loads in isolated conditions was used to investigate the blade loads of controllable pitch propeller operating in behind hull in Boswell et al. (1976); Jessup and Boswell (1982); Jessup et al. (1977) simulating different sailing conditions in calm water, waves and crash back/ahead. In this case, the set–up was further complicated by the fact that the propeller and the measuring device was included in a dummy hull used to case the set–up. The study allowed for the first time to characterize blade loads in behind hull conditions. Due to the presence of the dummy body, the motions of the model were always prescribed and the motion of the dummy models were carefully studied in order to always guarantee the same position of the propeller with respect to the shafts. This set–up was affected by the non–simultaneous measure of the loads, since only two quantities per time were allowed by the transducer. Savio et al. (2013) carried out free running experiments of a free running model equipped with an azimuthal propulsor in maneuvering and in waves; the study was focused on ventilation events and only these effects on blade thrust were documented. In Queutey et al. (2014) a ship model fitted with POD system was tested in waves in the depressurized wave tank of *MARIN* with the aim to investigate the combined effect of ventilation and cavitation on the propulsive efficiency; the POD was equipped with the 6–component load transducer for measuring the single blade load developed in Hagesteijn et al. (2012), although only single blade thrust was discussed and adopted to validate the numerical simulations performed with a *ISIS* CFD code. Propeller hub loads were measured in Atsavapranee et al. (2010), focusing on the steady turning phase for the $DTMB5617$ model by means of the constrained circular motion test. To this purpose, a 6–component transducer was fitted in the propeller hub. The study highlighted the asymmetric trend of the loads developed by the propeller in the leeward and the windward side of the maneuver, with particular emphasis on thrust and the side force, that play a relevant role to the dynamic response of the vessel.

1.3 How do results could impact real navigation?

Accounting for off-design conditions both at an analysis level or in the design loop is a very challenging issue, because these conditions are associated to very complex flow phenomena (massive flow separation, ventilation and cavitation) that demand the use of advanced numerical or experimental techniques to complement the capability of established approaches in traditional design (Gaggero et al. (2019)).

Although advanced CFD techniques have reached high level of maturity and reliabilty to solve extremely complex phenomena, their validation to correctly predict single blade and propeller loads in these conditions has not been yet completed according to the authors' knowledge. On the other hand, free running model testing is yet probably the most reliable approach to investigate these problems, in particular those related to transient motions. However, these kind of tests are usually performed during the latest stages of the design and are not practically included in the design loop and, moreover, the required facilities are not commonly affordable to researchers and engineers in contrast to indoor towing tanks. As a matter of fact, these approaches are too expensive and impractical to adopt in earlier design stages, where massive evaluation of geometric configurations are considered and, at least, can be used for analysis of a limited set or the final geometry. On the contrary, a broad set of off–design conditions (maneuvering and safety maneuvers) can be analyzed by captive model testing in traditional towing tanks. Additionally, these kind of tests are more suited to systematic investigations for developing parametric description of the physical phenomena.

In this context, as introduced in the previous paragraph, in order to inspect the feasibility of captive model tests to reproduce the behavior of the propeller in off–design, the single blade loads measured during the steady turning motion of free running model have been compared to oblique towing tests for a twin screw model. Specifically, the tests consisted in systematic analysis of a broad set of drift angles (up to 30°) and speed drops comparable to those experienced in the stabilized phase of the turn. The analysis, described in detail in Chap. 6, showed that the comparison of blade and propeller loads in terms of equivalent drift angle and nearest speed drop was very satisfactory and the discrepancies were mainly ascribed to the distribution of the drift angle along the hull that could have determined differences in the evolution of the flow.

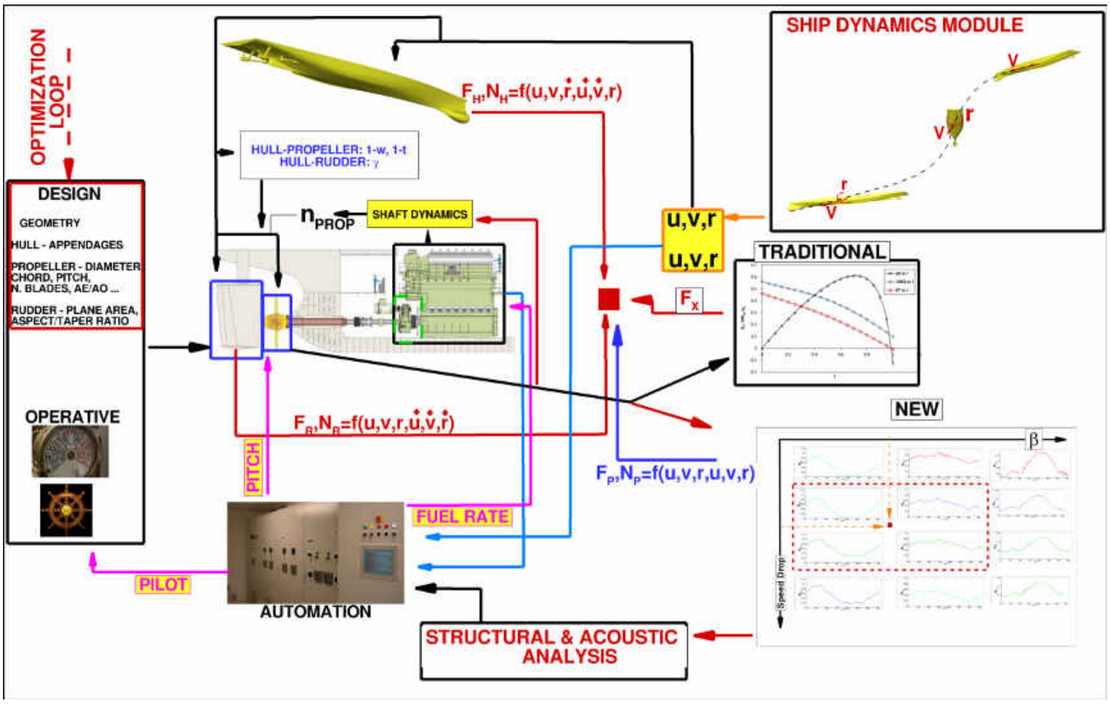

Figure 1.2 Example of a comprehensive model flow chart

In relation to ship design, the use of captive model tests has practical implication for a remarkable enhancement of comprehensive models. These are semi–empirical tools used to describe, in a multidisciplinary fashion, the behavior of a marine vehicle in realistic operative conditions and off–design. Since physical phenomena are modeled by physical based laws enriched by parametric experimental data, these solvers allow real time results and therefore, they are an attractive solution to complement existing tools in the optimization loop. The use of these tools spread to the analysis of the interaction of prime mover with propulsion system during maneuvers (Coraddu et al. (2013)), motion in waves (Saettone et al. (2020)) up to the design of alternative control laws of the control system in off–design (Altosole and Martelli (2017); Vrijdag et al. (2010)). Figure 1.2 sketches a typical flow chart for these tools, in this case specified for ship maneuvering for the sake of clarity. In brief, once the geometries and the operative conditions are given in input, the solver evaluates the dynamic response of the ship integrating the rigid body motion equation. The forcing terms are represented by the hydrodynamic loads, acting on the main elements of the ship, i.e. hull, rudder and propeller described by parametric laws function of ship's speed and acceleration. Moreover, the propeller operative condition (revolution, pitch) depends on the dynamic behavior of the prime mover and the action of the control law. In fact, observing the sketch depicted in figure 1.2, the standard modeling of the propeller relies on the use on the open water characteristics of the propeller to yield the thrust and torque for the solution of the motion and engine dynamic equations. These information guide the operation of the propulsion control unit to automatically modify the operative input (fuel rate, propeller pitch or rudder angle) or interact in real–time with the pilot/helmsman and, alternatively, are crucial for the optimization of its gains coefficients during its design. On the other hand, an alternative modeling strategy consists of the implementation of cycle–resolved single blade loads in terms of kinematic condition of the model (drift angle and speed drop) and geometric characteristics of the blade (i.e., pitch to diameter ratio, not considered in this study). As showed in the figure, at each time step of the simulation, the single blade loads can be obtained from interpolation of the cycles about the operating condition. The resolution of the complete set of loads developed by the blade allows to describe accurately the propeller contribution to the dynamic response of the ship and, in particular, analyze critical design aspects associated to vibration and emitted noise that can be noticeably altered during realistic operative conditions (Dubbioso et al. (2020); Ortolani and Dubbioso (2020)).

Chapter 2

Blade loads measurement

2.1 A previous experience: propeller in-plane loads

2.1.1 Bi-axial force transducer development

The assessment of propeller loads is of paramount importance both to understand the effects on the dynamic response of the vessel and to evaluate how they affect the reliability of mechanical structures and the comfort on-board during navigation. From this point of view, the availability of highly accurate data, both experimental or numerical, about propeller performance is pivotal for the enhancement of traditional investigation and simulation tools and the development of innovative ones. In general, the measurements of the propeller induced radial force is very challenging for the standard experimental set–up adopted in model tests: the main reason is the fact that the device should be located as close as possible to the position of the aftermost bearing of the propeller, in order to detect the actual deflection of the propeller shaft. The layout of conventionally shafted propulsion system on a relatively small test model, coupled with limited useful space inside the shaft bossing or stern tube, constrains the transducer to be submerged in water. Moreover, the use of a free running, self propelled model sailing in an outdoor environment represents a further complication for the execution of the experimental tests with respect to investigations carried out in indoor facilities (either with "captive" or free running models). In this paragraph, the solution developed by the author for the assessment of propeller in-plane loads is presented as introductory background to the following blade loads discussion. The measurements of the bearing radial force were achieved by an in-house developed, pass-through hole biaxial transducer, positioned between the propeller and the tail of the bossing of the astern V-brackets. The transducer was made completely waterproof and the data-transmission was accomplished via two cables properly attached on the wet surface of the brackets and the hull, in order to avoid any marked discontinuity of the geometry of the brackets that could modify the propeller inflow; this solution was forced by the manufacturing constraints of the shafting and shall be improved in the future. In figure 2.1 the actual shaft arrangement with the addition of the transducer is shown.

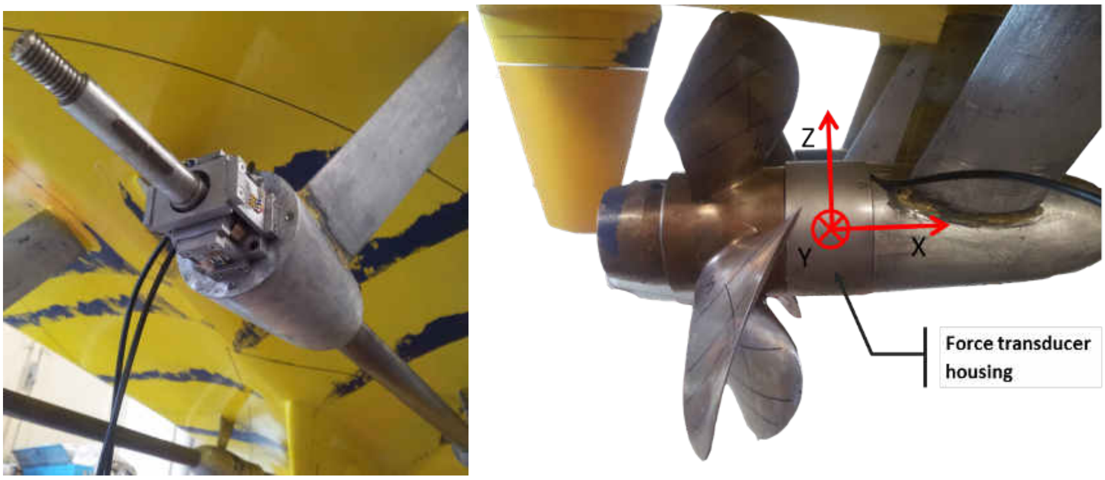

Figure 2.1 Layout of the shaft with the bi–axial transducer

The operating principle of the transducer is based on the conversion of the deflection of sensitive beams, caused by forces acting on the shaft, into a voltage signal using strain gauges sensors. The transducer is composed of independent structures, designed in order to obtain a fully decoupled measure of orthogonal components of the radial force and to eliminate the effects due to bending moments. The pass-through hole feature has the great advantage of having the transducer working both as a frame and as measuring device, allowing to perform measurements in a real operative condition. Moreover, the transducer, it being fixed with respect to the rotating shaft, provides the direct measurements of the radial load with the model's fixed frame; therefore, it does not require any temporal synchronization with the angular position of the shaft, as it is needed in case of rotating transducer (Amini and Steen (2011)): this aspect plays in favor of simplicity and robustness for execution of free running model tests in an outdoor environment as well as in the post-processing of the data. Moreover, because of the peculiar structural layout of the transducer, scalability to smaller models than the one adopted in this application, while still preserving sensitivity, is straightforward.

2.1.2 EFD and CFD results

The investigation on propeller in–plane loads has been carried out by means of both experimental and numerical approach. The former provided a massive data collection and a first assessment of loads magnitude and evolution with respect the different tested operational conditions (Ortolani et al. (2015a) and Ortolani et al. (2015b)) as well as a valuable data–set for the numerical code validation, the second has yielded a thorough insight into the phenomena and the detailed explanation of the cause–effect of complex propeller/wake interactions (Dubbioso et al. (2017) and Muscari et al. (2017)). In particular, the experimental tests were carried out by means of free running model tests. This procedure offers the possibility to analyse the realistic dynamic qualities of a ship under the action of the rudder. These tests are yet considered the most reliable mean to predict the maneuvering qualities of the ship in contrast to other experimental based (captive model tests and related system based simulations) or numerical methods (CFD), obviously neglecting scale effects. In particular, free running provides unique insight in the transient response. Usually, these tests are considered for standardized manoeuvres defined by international rules and regulations. The execution of those tests can help to anticipate and correct possible problems in the design phase, or, in the worst case, to analyse the reasons of issues encountered during the sea trials. The numerical studies relied on hybrid approach consisting of the use of a viscous solver based on the solution of the unsteady Reynolds Averaged Navier Stokes equations ($uRANSE$) for the computation of the nominal wake and a semi-empirical propeller solver based on the Blade Element Momentum Theory ($BEMT$) for the analysis of the propeller loads. The numerical simulations inspected both the steady turning phase of the turning circles maneuvres from mild to tight maneuvers (Dubbioso et al. (2017)) and the complete maneuver with transient and pull–out (Muscari et al. (2017)). In these simulations, the motion of the model was always prescribed on the basis of the outcomes of the free running model tests and the rudders were removed.

CNR-INM Outdoor/Manoeuvring basin allows to test large free-running, self-propelled unmanned models, simulating realistic operative conditions while monitoring and acquiring the main physical quantities related to ship motion and loads developed along the shaft line. The selected test case was a scaled model of a twin screw ship (C2520). In table 2.1, principal geometric characteristics of the model and the propeller are reported in terms of ratio of ship length (L), beam (B), draft (T) and block coefficient (C_B). The interest for this particular propulsive configuration lies in its well-known troublesome and critical operation during maneuvering, related to the different behaviours of the two propellers.

MODEL DATA	
L/B	7.5
B/T	3.25
C_B	0.5
Number of blades (Z)	5
Pitch ratio (P/D)	1.35
Expanded area ratio	0.79
Hub ratio	0.250

Table 2.1 Geometric characteristics of the ship and propeller model

The experimental assessment covered a wide range of operative conditions and the complete test matrix is summarized in Table 2.2. The analysis was carried out both in a phenomenological style on reference manoeuvres and systematically analysing the data in terms of rudder angles and speeds.

FREE RUNNING TESTS		
Test	Speed	Rudder angle
self-propulsion	$0.05 < Fn < 0.45$	$\delta = 0°$
turning circle (with pull-out)	Fn = 0.26, 0.32	$\delta = \pm 15$, $\delta = \pm 25$, $\delta = \pm 35$
turning circle (with pull-out)	Fn = 0.35	$\delta = \pm 35$
zig–zag	Fn=0.26, 0.32, 0.35	$\delta = 10 - 10, 20 - 20, 35 - 35$

Table 2.2 Free running test matrix

The new setup, beside confirming the loads unbalances of the forces and torque between the two propellers during the manoeuvre, as reported in figures 2.2 where loads developed during turning circle, for different Fn and rudder values, are summarized in unified graphs (positive and negative rudder angles correspond respectively to internal and external propellers), shed light over another peculiar phenomenon: the transients phases are remarkably critical for the internal shaft, because of very complicated propeller-wake interactions.

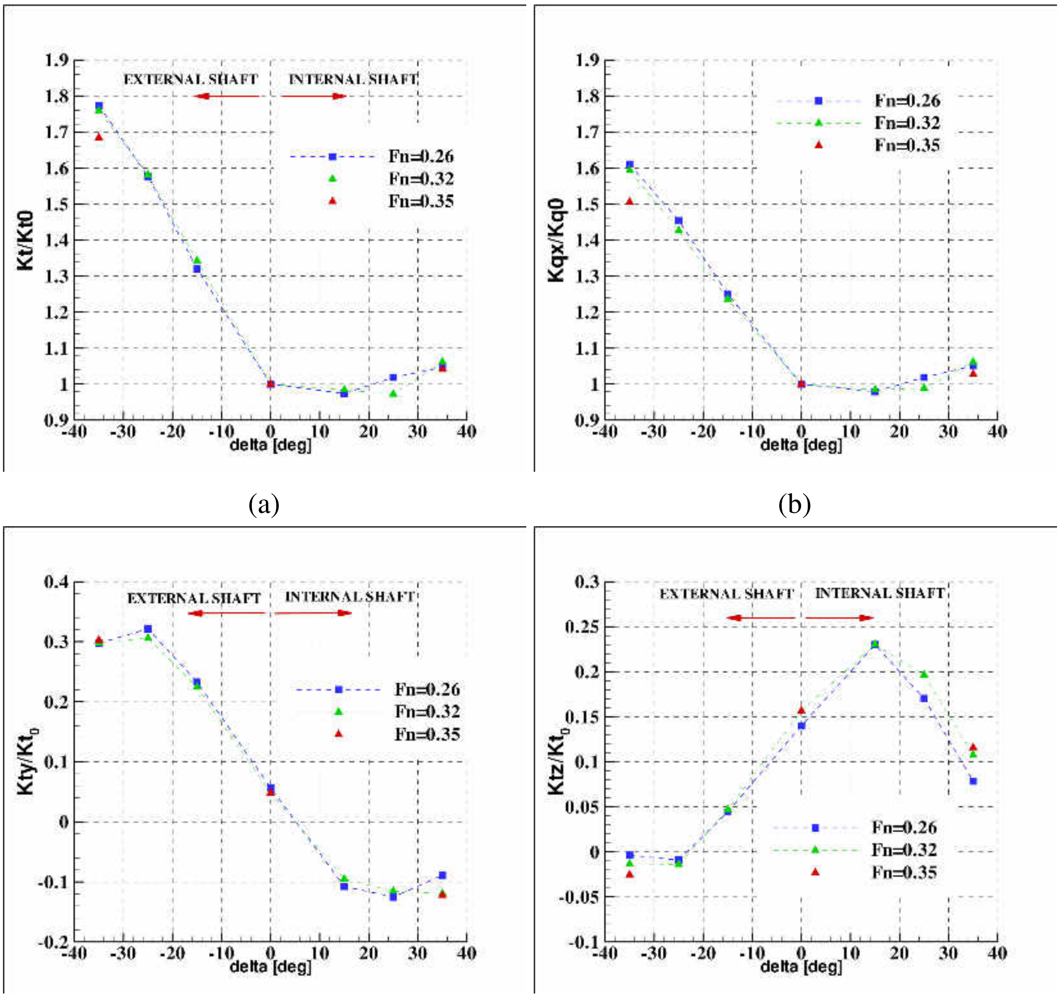

(a) (b) (c) (d)

Figure 2.2 Propeller loads during turning circle: (**a**) thrust, (**b**) torque, (**c**) side force, (**d**) vertical force.

These result in strong peaks that occur immediately after the rudder actuation (see Figure 2.4) at relatively small drift angles. In fact, in this circumstance, the evolution of the upstream hull wake modifies the propeller inflow over a limited area of the disk, giving onset to an asymmetric distribution that yields development of stronger in-plane forces. These considerations have been backed up by the complementary *CFD* results and wake analysis by the BEMT solver (Dubbioso et al. (2017) and Muscari et al. (2017)).

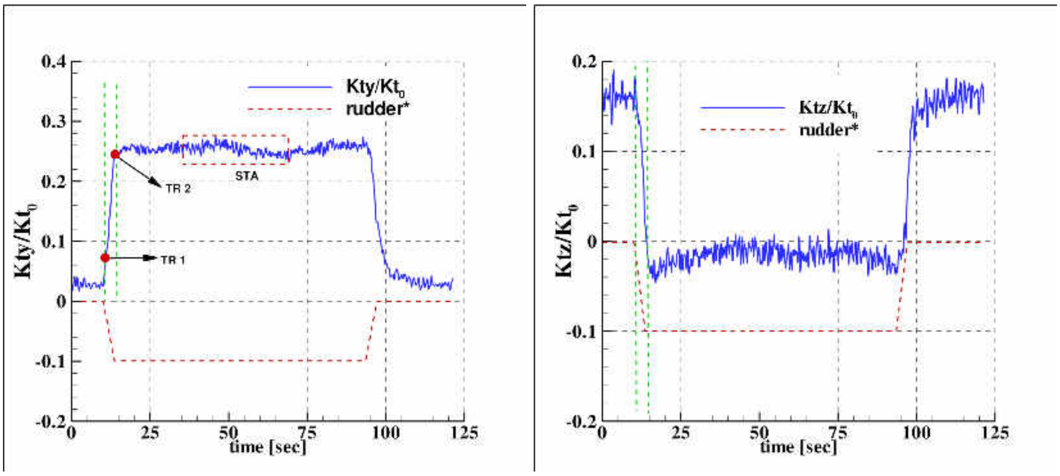

Figure 2.3 External propeller ($\delta = 35°$ Port) radial load components (Kty on the left and Ktz on the right)

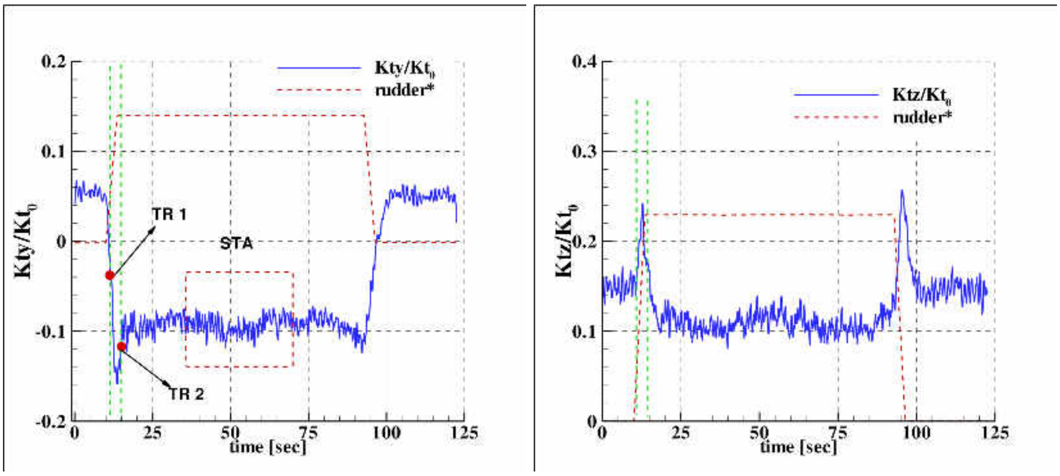

Figure 2.4 Internal propeller ($\delta = 35°$ STBD) radial load components (Kty on the left and Ktz on the right)

Figure 2.5 highlights that during a maneuver, strong and persistent vortices detach from the hull body and its appendages; these structures are deflected towards the lee side and, consequently, while windward side experiences a condition similar to a pure oblique flow, the inflow on the leeward propeller shows a perturbed and articulated topology and consequently loads are characterized by more complex interactions.

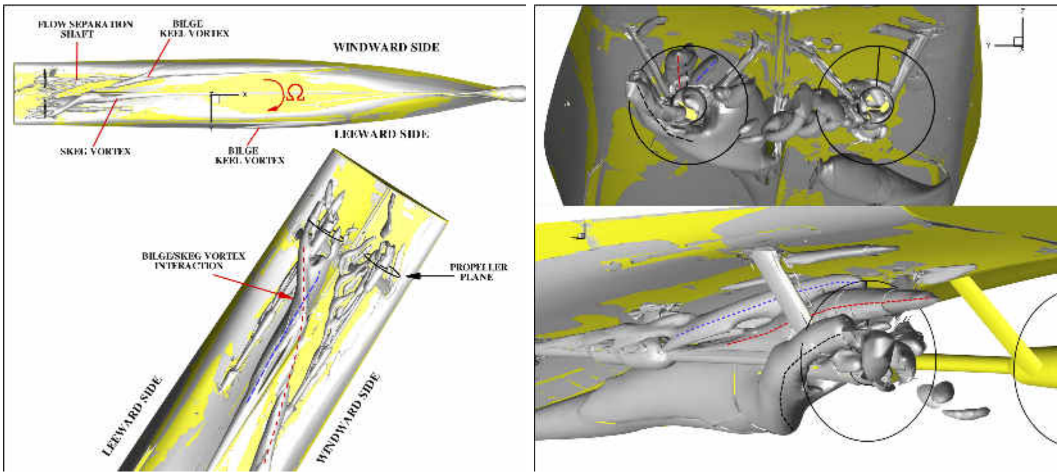

Figure 2.5 Vortex structures developed during maneuver

One of the outcomes of this research activity is that the use of this novel transducer, improved the actual state of the art methodologies of free running and captive model test setup. It increases the potential capability to investigate very complicated hydrodynamic phenomena related to propeller hydrodynamics, operating in design and off-design conditions whose identification, otherwise, would not be as much immediate by the sole measurements of thrust and torque. Moreover, it provided valuable data for numerical simulation validation, confirming the concept that those two ways of analysis are not mutually exclusive but their combination produces the best results.

2.2 Blade loads measuring system

The results described above motivated the research to move a step further to the development of a new set-up, tasked to the measure of single blade loads for a propeller in behind-hull condition, that is the main topic of the present thesis. The setup has been installed on a twin screw ship scaled model (about 6 metres), described in more detail in section 3.1, and several experimental activities have been performed in order to evaluate the propeller performance both in design and off-design conditions. The system provides an innovative view of the propulsor's hydrodynamics, with greater degree of detail of wake interactions. Moreover, by a very effective and simple method based on the analysis the single blade loads during the period of revolution described in Chapter 4 (Dubbioso et al. (2017)), it is possible to explain the onset of the in-plane global propeller loads and moments.

2.2.1 New propeller and shaft line design

The assessment of single blade loads required the development of a new experimental setup. The lack of similar approaches in literature led to the complete redesign of the propeller and the shaft line and a long phase of research on the best solutions: the first step was the search for off-the-shelf transducers that could provide the desired measure. In particular the attention was directed on waterproof multi-component transducers which could provide both forces and moments and a complete set of loads (three forces and corresponding moments) was desirable. One of the main constrains of this search was the diameter of the hub, in which to place the transducer, that was about 50mm. Moreover, the propeller has five blades, so for the mechanical design, the space needed for the transducer should not have undermined the robustness of the propeller. From previous experimental activities performed on the same model (self-propulsion and seakeeping), an estimate of expected loads has been made, in order to fix the operative range of the transducer with a safe linearity and overload margins. The limitations came from the moments because, in most examined devices, despite the range of forces were compatible with the experiment, the effect of the arm of the expected hydrodynamic force, considered at 0.7D, made the resulting moment to exceed the limits of most of the devices.

Figure 2.6 Selected transducer

Physical Specifications	
Weight	0.0634 kg
Diameter	25 mm
Height	21.6 mm

Table 2.3 Main features

The choice fell on the commercial transducer shown in Figure 2.6. The device is an IP68 six-component sensor, which provides the full set of forces and moments acting on its sensitive plate and its dimensions allow it to fit into the hub. The calibrated ranges and measurements uncertainties, provided by the manufacturer of the transducer, are reported in Table 2.4.

LOAD	CALIB. RANGE	UNCERTAINTY
T_X	± 250 [N]	1.25%
T_Y	± 250 [N]	1.25%
T_Z	± 1000 [N]	1.25%
Q_X	± 6 [Nm]	2.00%
Q_Y	± 6 [Nm]	2.00%
Q_Z	± 3.4 [Nm]	1.50%

Table 2.4 Transducer calibration values

The transducer is produced in two configurations: with axial or radial cable: this last has proven to be the best solution since the cable could exit from the fore part of the propeller without bending problems. The transducer definition was followed by the design of the propeller. Several solution were considered: in this case the selected criteria were the robustness of the final design but most of all, the manufacturing process. The mandatory aim was to obtain an accurate reproduction of the model, with few parts to be assembled and the smallest possible amount of machine working changes, in order to limit, as much as possible, errors propagation to the final object.

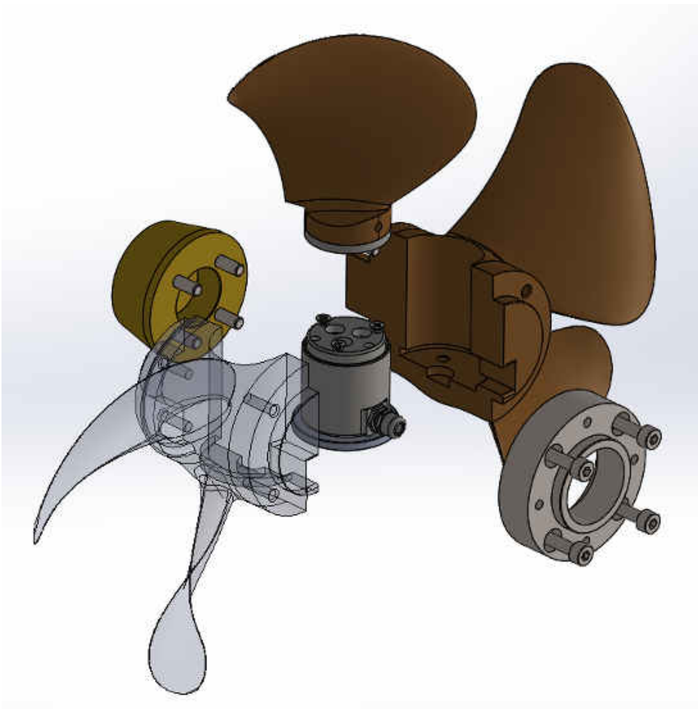

Figure 2.7 Exploded view of the instrumented propeller

For this reason, the propeller has been designed in two parts which can be assembled together to house the transducer. Each part carries two blades, the fifth one is independent and rigidly connected to the measuring plate of the transducer. In Figure2.7 an exploded view of the propeller is shown. The new propeller is quite different from the usual ones used in standard tests; in fact, the absence of passing through hole for the shaft and the need to get the transducer's cable to the acquisition system on-board the model, has resulted in the development of a new shaft-line. The main issue was to design the new setup, without radically modifying the existent one. Moreover, all the modifications should have been reversible; for example, the bushing of the shaft needed to remain of the same diameter (12mm). The adopted solution has been an hollow shaft, with a passing through hole large just enough to let the cable pass. Two commercial sizes, with internal diameters 9mm and 5mm, have been found and both have been tested. The different internal diameter and in particular a larger one, means a significant reduction in thickness (1.5mm and 3.5mm respectively), which affects shaft rigidity: using the thinnest shaft, large whirling vibrations arose with a consequent critical degradation of the measured loads. For this reason, the data presented are only the ones related to the thicker shaft. The new shaft houses the output cable of the transducer and allows to bring the signals inside the model. Here, a high quality, low noise and low resistance slip ring provides the transmission between the rotating shaft and the fixed acquisition system. In Figure 2.8 the assembly of the new shaft line is shown.

Figure 2.8 Exploded view of the new shaft line

After the preparation of final executive drawings, the propeller has been manufactured and mounted. Figure 2.9 shows the propeller completely disassembled and the final result.

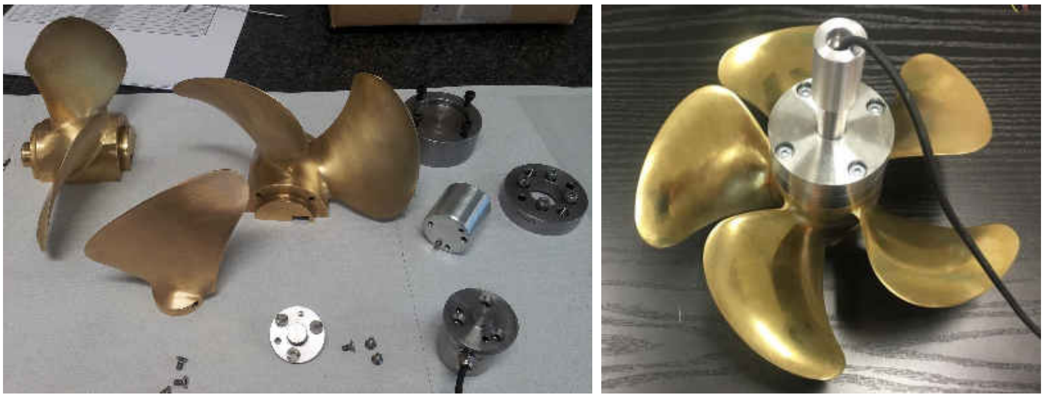

Figure 2.9 The novel instrumented propeller

2.2.2 Bench tests

A schematic view of the complete setup with the actual shaft arrangement and the addition of the instrumented propeller is shown in figure 2.10.

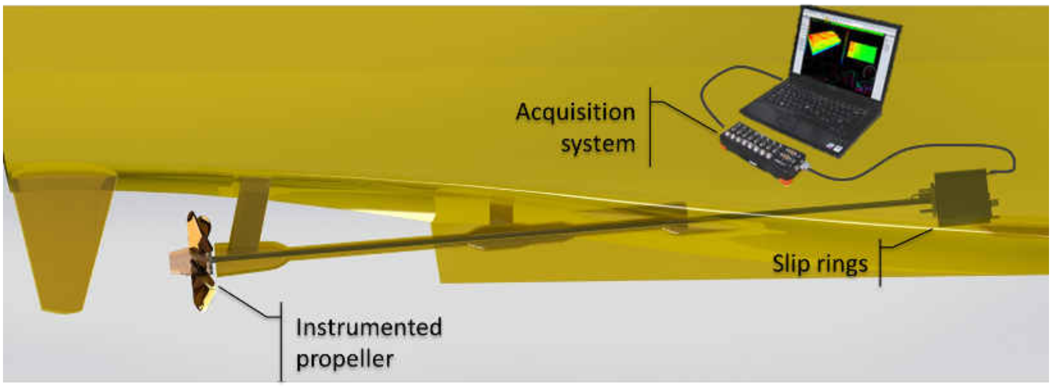

Figure 2.10 Schematic view of the measuring system

The transducer is accompanied by a calibration certificate and a compensation matrix. The matrix take into account the cross-talk or between components through its weightings: signals coming from the sensor are multiplied with the coefficient-matrix and summed up, resulting in fully compensated force and moment values along X, Y and Z direction. To preliminary asses the reliability of the whole measuring system and to validate its static and dynamic behavior within the operative propeller revolutions considered in the experiments, a test bench which simulates the final shaft-line installation has been built (see figure 2.11). It reproduces the same structural configuration of the shafting system (propeller, shaft, bearings, slip ring and electric motor) installed in the fully appended model. In particular, the same number of bearings at the same distance from the propeller are positioned.

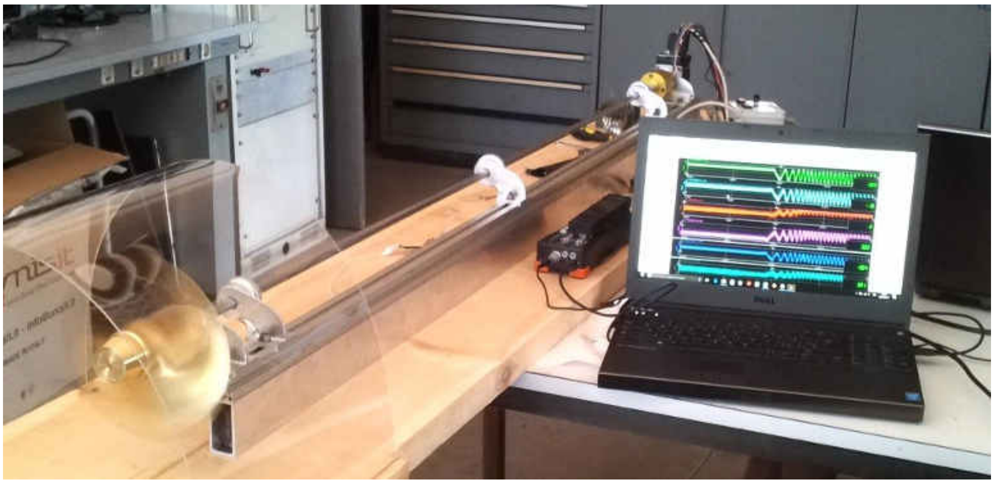

Figure 2.11 Setup of test bench

This preliminary activity allowed to assess the reliability of the components of the setup, such as the absence of vibrations and whirling of the hollow shaft. Another important aspect to be investigated was the effect of the slip ring on the electric signals coming from the transducer. The first test has been the comparison between the theoretical blade weight value (178g i.e. 1.75N) and the values provided by the transducer. The values of Fz_{exp} and Fy_{exp}, considered as the two components of the weight force of the blade during the revolution, have been collected while the propeller was rotating at very low rpm (0.25 Hz). (See Fig.2.12)

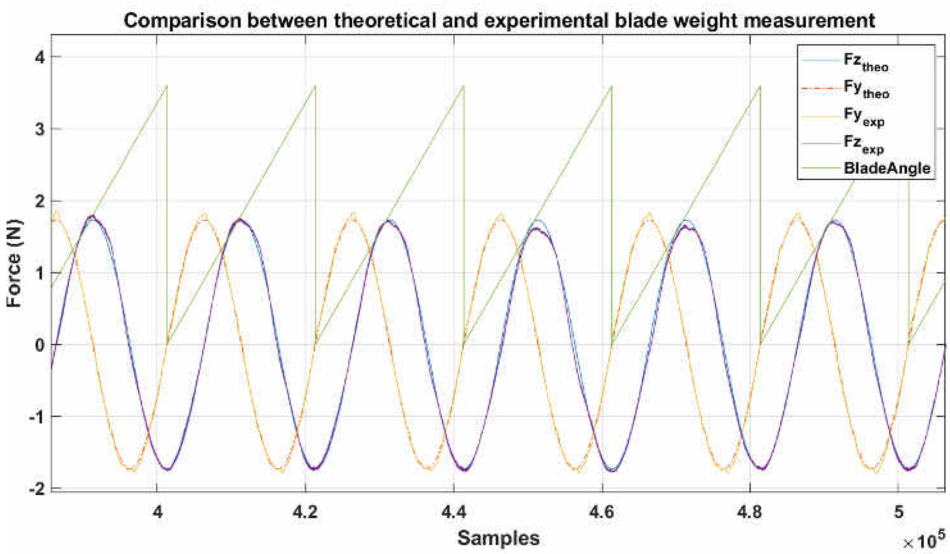

Figure 2.12 Comparison between theoretical and experimental values of F_z and F_y

The plot includes also the recorded blade angle θ (properly scaled by a factor 100 to fit the plot), with 0° value corresponding to the blade in vertical position pointing upward and the orientation being concordant with the sense of rotation. Since the transducer coordinates frame has 'x' axis pointing forward, 'z' axis pointing upward and 'y' axis that follows the right hand rule, the F_z component has its minimum at $\theta = 0°$, the weight force pointing downward, while F_y component is equal to 0. As expected, when the propeller rotates, the two forces have a sinusoidal trend with a phase angle of 90°. A good agreement between the experimental and theoretical values was confirmed.

Moreover the influence of rotation, during dynamic measurements was assessed: the centrifugal force calculated using the formula $F_{cent} = W_{blade} \cdot \omega^2 \cdot R_{cg}$ (where ω is the angular speed, W_{blade} is the blade weight and R_{cg} the radial coordinate of the center of gravity of the blade, provided by CAD) has been compared with the radial force (Fz^H), provided by the transducer during tests in air. The results are reported in figure 2.13 and evidence the congruence between the two quantities.

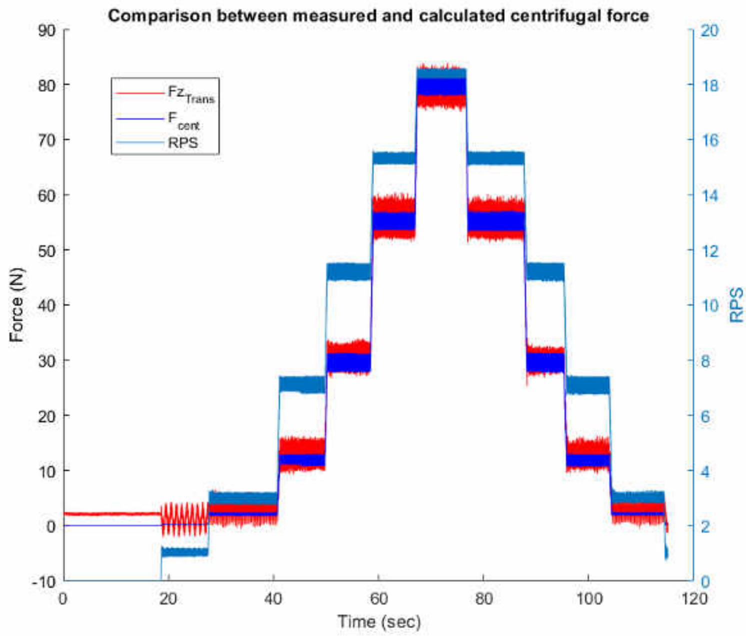

Figure 2.13 Comparison between theoretical and experimental values of centrifugal force

Chapter 3

Experimental activities

3.1 Test case

Off-design operations for ships with twin screw configuration are more critical with respect to single screw ships, because of the different inflow conditions for the two propellers. In fact, in twin screw propulsive configurations, the hull is characterized by a larger cutoff and, during maneuvering, the "shadow" effect of hull is weaker; for this reason, the external propeller experiences an inflow inclined by an equivalent angle given by the kinematic of the model (during tight maneuver this angle might be of the order of 30°). On the contrary, the internal propeller has the higher probability to be impinged by coherent structures detached from the fore portion of the hull or appendages that are convected toward the leeward side. Moreover, the quantification of the asymmetric behavior of the propellers is of utmost importance in case of cross-connect configurations, because the reduction gear can experience very large fatigue loads. In particular, in Coraddu et al. (2013) the analysis was entirely focused to monitor the overloading and unbalancing phenomena of propeller thrust and torque during maneuvering conditions for a modern twin screw ship. The same experimental set-up and the model was also considered for the campaign dedicated to the quantification of the in-plane loads developed by the propeller during steady and unsteady maneuvers, described in Par. 2.1 (Ortolani et al. (2015a,b)). For these reasons, a similar ship was the subject of the investigation of the present thesis. The selected test case is a scaled model (about 6 meters) of a fast twin screw/twin rudder unit (C2430); the principal geometric characteristics of the model and the propeller (E1617) are reported in table 3.1.

MODEL DATA	
L/B	7.5
B/T	3.25
C_B	0.5
Number of blades (Z)	5
Pitch ratio (P/D)	1.35
Expanded area ratio	0.79
Hub ratio	0.250

Table 3.1 Geometric characteristics of the ship and propeller model

The ship and propeller model are visualized in figure 3.1. The model is equipped with two couples of stabilizer fins, bilge keels, horn rudders and the typical configuration of propulsive shaft supported with brackets; the stern is V–shaped and the skeg is not very pronounced as in modern pram stern. In the standard propulsive configuration, the CPP propeller is five bladed and rotates counterclockwise (inward rotating from top).

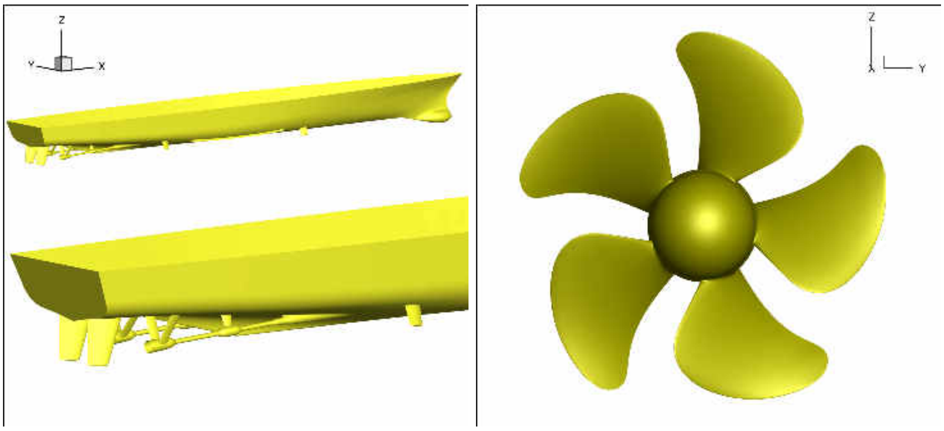

Figure 3.1 Hull and propeller models

3.2 Operative conditions

The design of the propeller yet remarkably consists on the maximization of its performance (hydrodynamic efficiency, cavitation, noise) with respect to straight advance and calm water. Any other navigation condition (maneuvering, emergency stop, presence of waves) can be considered as off-design. In order to evaluate the ship hydrodynamic performance, a series of standard manoeuvres can be performed, both in real and in scaled model tests: zigzag maneuver, crash stop and turning circle, with or without pull-out, are the most common trials used to assess ship behaviour and capabilities. The turning circle manoeuvre aims at the evaluation of the turning ability of a ship, under the action of its main directional control devices (i.e. rudders, POD etc). The rudder angle has to be the maximum permissible at the test speed and tests are performed both to port and starboard: results are the mean value of the two conditions.

Figure 3.2 Turning circle main quantities

With reference to Figure 3.2, the main properties obtained by this test are the advance, the transfer and the tactical diameter. During a turning circle manoeuvre, three different hydrodynamic conditions may be discerned corresponding to the three main sailing situation: a visual explanation of these phases is depicted in Figure 3.3.

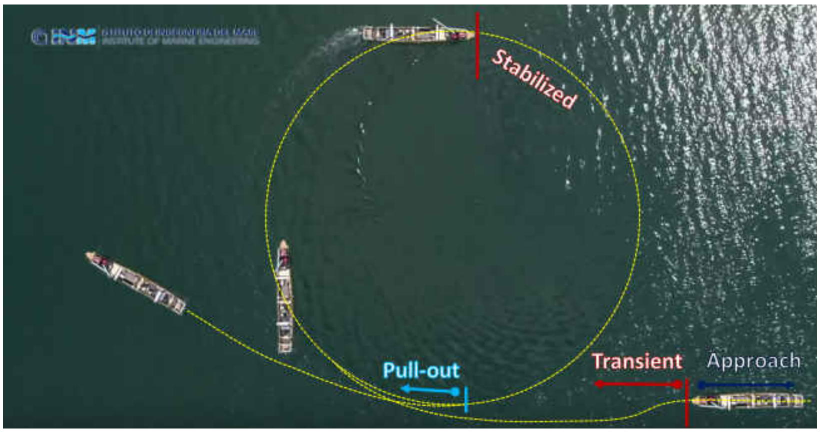

Figure 3.3 Turning circle phases

The approach phase corresponds to the straight ahead navigation, when the rudder is at neutral position; this can be identified as the design condition, with the propeller working in a well defined wake. Just after the rudder actuation, the transient phase starts. This phase is characterized by a rapid evolution of hydrodynamic forces acting on the hull and a subsequent complex evolution of the inflow to the propeller. When all the forces reach the equilibrium and the wake is fully developed, the stabilized phase starts. At the end of the turning circle, the pull-out phase begins when the rudder is moved back to its neutral position and after a certain number of ship lengths, the ship returns to straight sailing.

3.3 Free running model test

The experimental activity was performed at the CNR-INM outdoor manoeuvring basin located at the Nemi Lake. Being a large, natural and low anthropic disturbance environment, with long windless periods and calm water, is an ideal facility to perform any kind of manoeuvring test regardless the model size and speed.

(a) Scaled model during free running tests

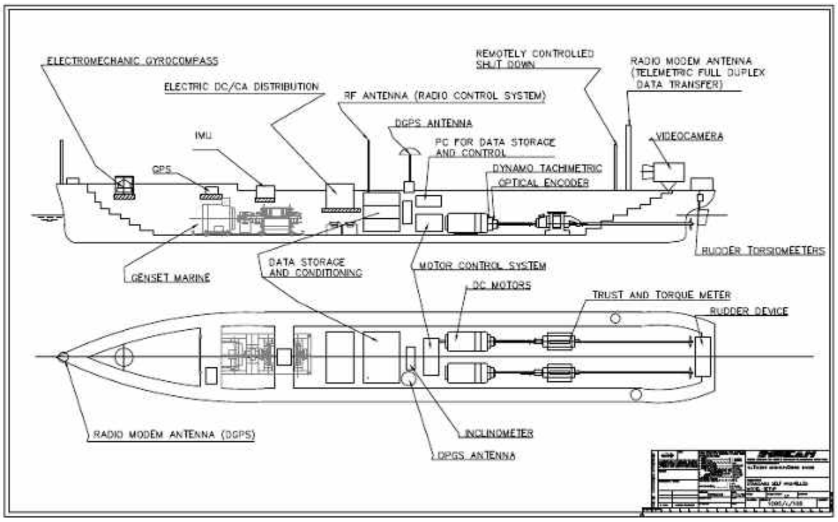

(b) Schematic view of standard free running setup

Figure 3.4 Free running setup and real model

The ship selected for the present analysis is described in Par. 3.1: the scaled model, shown in figure 3.4a, was prepared in order to carry out free running model tests according to the layout of the set–up and the measurements devices sketched in figure 3.4b. In particular:

- each propeller shaft is driven by a dedicated electric brush–less motor and is equipped by a dynamometer for the measurements of propeller thrust and torque;
- DGPS, dynamo–tachometers and real time data transmission devices necessary to carry out the experimental activity;
- IMU inertial platform device for the reconstruction of the $6DoF$ motion of the model;
- a diesel electric generator for providing the whole energy demand of the on–board instruments

The experimental campaign was focused on the propeller performance during off-design conditions, with particular focus on the single blade loads. Standard (turning circle and zig–zag) and safety maneuvers (crash stop/ahead) have been executed in order to follow well-defined and standard procedures which could ensure repeatability, well-known conditions and also compliance with other investigation approaches (i.e. CFD). For this novel setup, the starboard shaft line of the model has been equipped with the custom instrumented propeller described in Par. 2.2.1, to measure the complete system of loads (3 forces and 3 moments) acting on a single blade.

A set of typical operative speeds of the model V_m, corresponding to Froude number ($F_N = \frac{V_m}{\sqrt{gL}}$) 0.26, 0.34 and 0.4 and different rudder angles δ were considered; moreover, two different propeller configurations, namely inward and outward rotation obtained by switching the propellers, were tested. The complete test matrix of the experimental campaign is summarized in Table 3.2. At least five runs were repeated for each test condition. According to the repetition of tests, forty runs are considered for the two lowest speeds (F_N=0.26 and 0.34) and thirty runs for the highest one; in fact, at this speed the power generator installed on the model was not able to provide the required power at the tightest maneuver ($\delta = 35°$). The selected interval of the approach phase includes more than two hundred propeller revolutions, therefore the analysis is based on eight thousand cycles for each speed. All tests were carried out at constant propeller rate of revolution and in a calm environment, in order to avoid external disturbances.

TEST	F_N	δ	Test Reps
TURNING CIRCLE	0.26,0.34 0.40	±7.5°, ±15°, ±25°, ±35° ±7.5°, ±15°, ±25°	5
ZIG–ZAG	0.26,0.34, 0.40	±10°/∓10°, ±20°/∓20° ±35°/∓35°,±35°/∓60°	5
CRASH–BACK/AHEAD	0.08, 0.10,0.12,0.14,0.16	0°	5

Table 3.2 Test matrix of the experimental campaign

With reference to figure 3.3, in this thesis the comparison between loads developed during the approach, transient and stabilized phases of free running model test and the simulated, quasi-steady conditions, reproduced in captive tests at CNR-INM towing basin is discussed.

3.4 Captive model tests: straight navigation and pure drift

Tests have been carried out in the CNR-INM towing tank facility. The towing tank features a 475 m long, 13.5 m wide and 6.5 m deep basin. Four electric main motors (92 kW) and two secondary motors (45kW) can drive the tank carriage up to 15 m/s with an accuracy of 1 mm/s and speed fluctuations within 3%. These experiments were carried out with the same model adopted in the previous campaign, obviously without all the equipment used for self-propulsion, control and on-board power, with the fully appended model with rudders removed. The carriage has been equipped with a planar motion mechanism (PMM): this device allows to impose to the model a prescribed trajectory, combining sway and yaw motions, if the purpose is the investigation of dynamic forces during complex manoeuvres. Actually, during the presented tests, PMM has been only used to easily change and measure the drift angle within the desired range with more accuracy. In fact, by using this device it has been possible to set the drift angle β_{eff} between the model axis and the direction of motion of the carriage with an accuracy of $0.1°$. A picture of the model during tests and a scheme of the towing tank set-up is shown in Figure 3.5. According to Fig. 3.5b positive and negative drift angles match respectively a port and a starboard side turn. Based on this approach, and since all of the measurements were related to the starboard propeller, the propeller inflow and loads at positive β_{eff} are representative of the propeller at the windward (external) side during a maneuver, whereas negative β_{eff} corresponds to the propeller on the leeward (internal) side. Figure 3.5a shows the model during testing at drift angle.

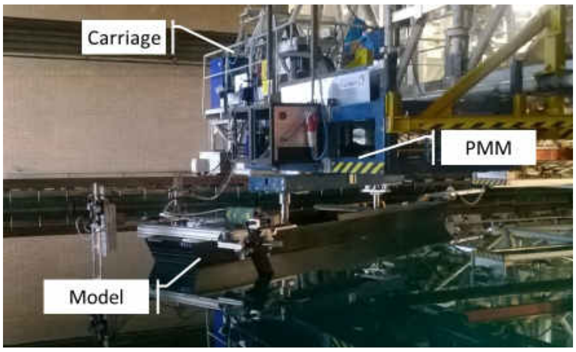

(a) Model under pure drift test

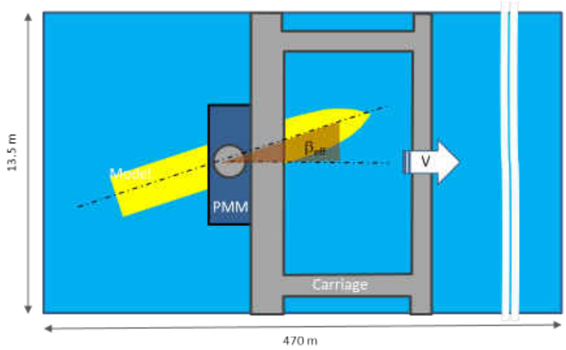

(b) Equivalent β setup

Figure 3.5 Captive model test to simulate manoeuvres

Experiments were carried out in straight ahead (i.e. $\beta_{eff} = 0°$) and steady drift motions with the aim to simulate weak and tight maneuvering conditions obtained during free running maneuvering tests. For steady drift conditions, the drift angles $\beta_{eff} = \pm 7.5°$, $\beta_{eff} = \pm 15°$, $\beta_{eff} = \pm 20°$ and $\beta_{eff} = \pm 30°$ were analyzed, with roll motion constrained to the neutral position. The nominal advance speed corresponds to $F_N = 0.26$ and Reynolds number $R_e = 1.053e7$, propeller angular speed is set at the model self–propulsion point in straight ahead motion ($\beta_{eff} = 0°$) and, in order to mimic the propeller functioning during free running model tests, *RPS* are kept constant during the towing. The nominal advance coefficient of the propeller J at $\beta_{eff} = 0°$, evaluated with the speed of the model, is 1.05. Reduction ratios 0.9, 0.8 and 0.7 have been set during tests in steady drift, to take account of the speed loss of the turning maneuver. The complete test matrix of the experimental campaign is summarized in table 3.3; at least five runs were repeated for each test condition.

β_{eff}	V/V_0
$0°, \pm 7.5°, \pm 15°, \pm 20°, \pm 30°$	1.0, 0.9, 0.8, 0.7

Table 3.3 Test matrix of oblique towing tests

Chapter 4

Data analysis

4.1 Blade and propeller loads construction

Loads measurements, specifically forces (T_{xyz}) and moments (Q_{xyz}), are performed by the transducer housed inside the hub; the device has its own reference frame ("T"superscript), centered on the top surface, at the contact with the blade root.

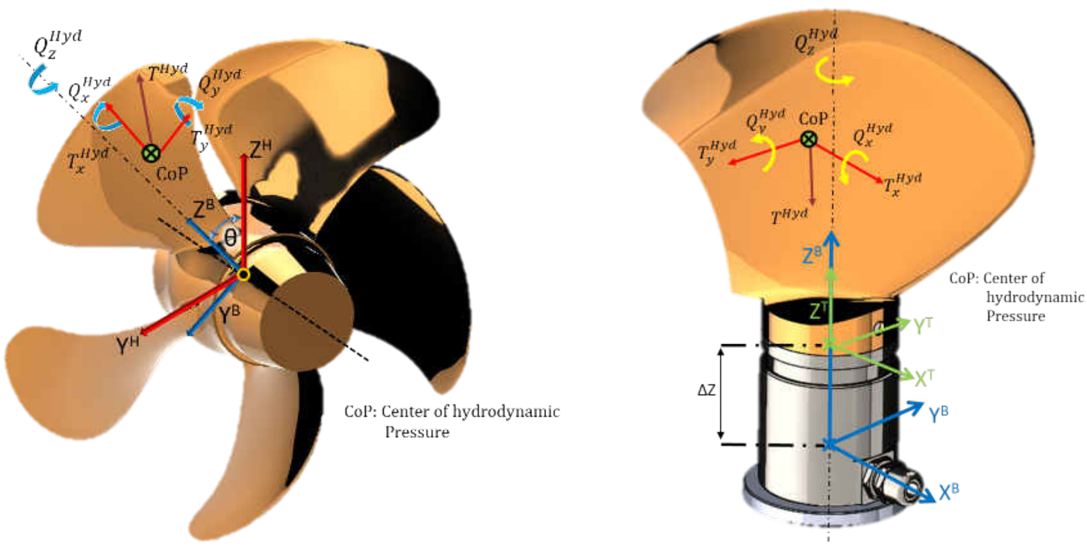

Figure 4.1 Transducer, blade and hub reference frames scheme (left); detailed view of transducer and blade frames (right)

With reference to figure 4.1, two additional frames have been adopted in order to have data consistent with the conventional frame centered along the shaft, at the mid-plane of the propeller: the first one, called "blade frame "("B"superscript), rotating with the blade, is defined with x pointing forward, z radially outward and coincident with the z of the transducer and y determined by right-hand rule; the second one, fixed with the model, is defined with x pointing forward, z radially upward and and y to the left, called “hub frame”(“H”superscript). Starting from transducer (“T”) frame, data have been evaluated in the rotating (“B”) and fixed (“H”) frames applying the following expressions:

$$T_x^B = T_x^T = T_x^H; \quad T_y^B = T_y^T; \quad T_z^B = T_z^T; \tag{4.1}$$

$$Q_x^B = Q_x^T - T_y^T \Delta Z; \quad Q_y^B = Q_y^T + T_x^T \Delta Z; \quad Q_z^B = Q_z^T; \tag{4.2}$$

$$\begin{bmatrix} T_y^H(\theta) \\ T_z^H(\theta) \end{bmatrix} = \begin{bmatrix} cos(\theta) & sin(\theta) \\ -sin(\theta) & cos(\theta) \end{bmatrix} \begin{bmatrix} T_y^B(\theta) \\ T_z^B(\theta) \end{bmatrix}; \tag{4.3}$$

$$\begin{bmatrix} Q_y^H(\theta) \\ Q_z^H(\theta) \end{bmatrix} = \begin{bmatrix} cos(\theta) & sin(\theta) \\ -sin(\theta) & cos(\theta) \end{bmatrix} \begin{bmatrix} Q_y^B(\theta) \\ Q_z^B(\theta) \end{bmatrix} \tag{4.4}$$

where θ is the angular position of the blade with respect to z^H. The measured loads result from the contribution of inertial loads and hydrodynamic loads. The analysis was carried out both on total loads and hydrodynamic loads, properly derived from the total one subtracting the inertial contribution. For the aim of the thesis, only the hydrodynamic loads will be considered. Inertial load include both centrifugal force (T_{cent}) and gravity (T_g^T); their effect has been calculated considering the weight of all mechanical parts that stand on the transducer. If the total mass is W_{blade}, the gravity contribution is:

$$\begin{bmatrix} T_{g_x}^T(\theta) \\ T_{g_y}^T(\theta) \\ T_{g_z}^T(\theta) \end{bmatrix} = \begin{bmatrix} 0 & 0 & 0 \\ 0 & cos(\theta) & -sin(\theta) \\ 0 & sin(\theta) & cos(\theta) \end{bmatrix} \begin{bmatrix} 0 \\ 0 \\ -W_{blade}g \end{bmatrix} \tag{4.5}$$

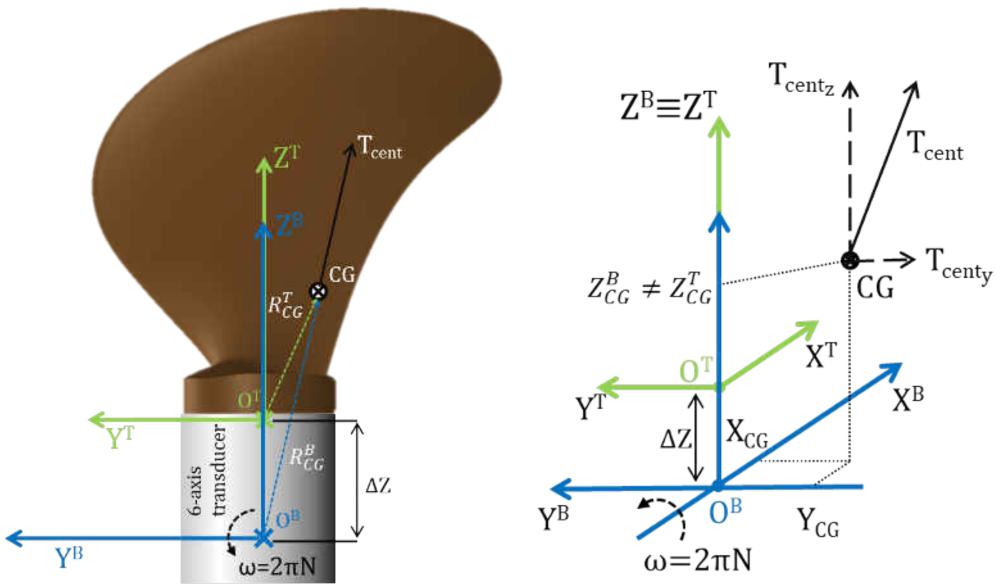

Figure 4.2 Transducer and blade reference frames (left); Centrifugal force vectors scheme (right)

As depicted in figure 4.2, the centrifugal force that contributes to the measure of the loads on the transducer is applied to the center of gravity (CG) of the blade. Once its magnitude has been calculated using equation 4.6, being ω the rotational speed ($\omega = 2\pi N$, N is the propeller RPS) and y^B_{CG} and z^B_{CG} the coordinates of the center of gravity in the blade reference frame, the moments at the transducer due to the components T_{cent_y} and T_{cent_z} have been obtained by equation 4.7 as follows:

$$T_{cent_x} = 0; \quad T_{cent_y} = W_{blade} \cdot \omega^2 \cdot y^B_{CG}; \quad T_{cent_z} = W_{blade} \cdot \omega^2 \cdot z^B_{CG}; \tag{4.6}$$

$$Q^T_{cent} = R^T_{CG} \times T_{cent} \tag{4.7}$$

so hydrodynamic force T_{hydro} has been evaluated from measured one (T_{meas}) as

$$T_{hydro} = T_{meas} - T_{cent} - T_W. \tag{4.8}$$

Collected data are sampled at 5KHz, but, since in case of free running tests at different Fn, the rotational speed of the propeller changes as the speed changes, loads and other correlated data are re-sampled according to 360 steps, corresponding to a complete revolution of the propeller with one degree of resolution, in order to perform a consistent analysis, at the same blade angle, for all phases of the maneuver (steady and transient), at different RPS.

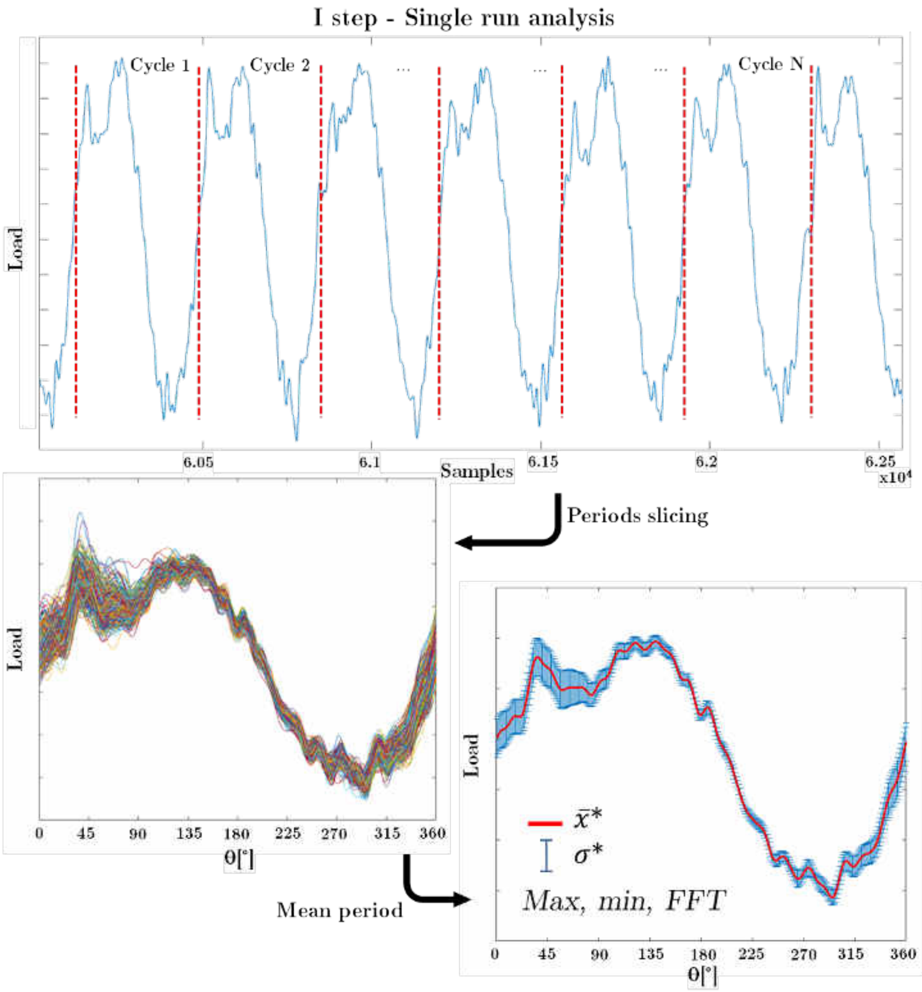

Figure 4.3 Analysis phases. I phase: evaluation of load's mean period for a single run

The measurements were analyzed by a simple statistical analysis at two different steps (figures 4.3 and 4.4).

In the first step, each run was sliced considering every period of revolution of the blade and a basic statistic analysis (arithmetic mean and r.m.s, $\bar{x_1}^*$ and $\sigma_1{}^*$) was performed at every blade position θ to obtain the representative trend for the blade loads during the cycle, their mean values and harmonic content, evaluated by a standard FFT decomposition. The statistic analysis was performed considering more than 200 cycles per run. In the second step, the statistical analysis was performed to obtain the representative trend of the blade loads, grouping all the set of maneuvers corresponding to the same conditions, for each different Froude number. In this case, the statistical description was provided in terms of arithmetic and weighted mean ($\bar{x_1}$ and $\bar{x_2}$) and standard deviation (σ_1 and σ_2).

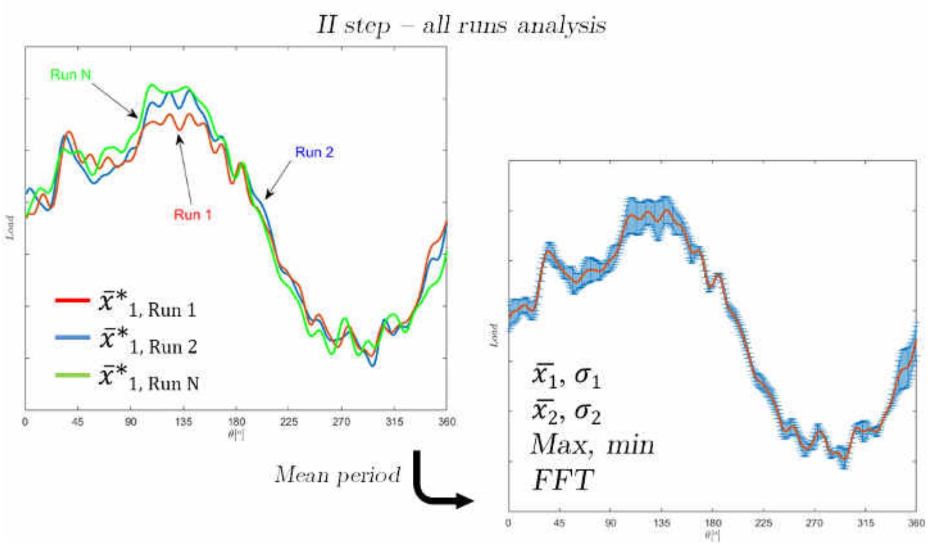

Figure 4.4 Analysis phases. II phase: evaluation of aggregate mean period

This approach is justified by the different nature of evidences that is possible to carry out. In fact, the arithmetic mean and σ highlight the discrepancies between each single run that is carried out at different RPS or model speed mainly due to disturbances of the outdoor environment. Conversely, the weighted statistics provides a valuable assessment of the goodness of measurements and reliability of the measuring system. For the sake of completeness, the weighted mean $\bar{x}_2$ and standard deviation σ_2 are evaluated from the arithmetic mean and standard deviation $\bar{x^*}_{1t}$ and $\sigma^*{}_{1t}$ relative to each single test t, calculated at the first step of the analysis for the generic variable (at every blade position θ), as:

$$\bar{x}_2 = \frac{\sum_{t=1}^{N_t} \frac{\bar{x}^*_{1t}}{\sigma^{*2}_{1t}}}{\sum_{t=1}^{N_t} \frac{1}{\sigma^{*2}_{1t}}} \tag{4.9}$$

$$\sigma_2 = \frac{1}{\sqrt{\sum_{t=1}^{N_t} \frac{1}{\sigma^{*2}_{1t}}}} \tag{4.10}$$

where N_t is the total number of runs. For the sake of clarity, the superscript "*" is adopted to distinguish between the arithmetic mean calculated in the first step for a single run from the one of the second step. Note that in the right panel of figure 4.4 only the weighted mean and standard deviations are visualized for improving its readability. The two–step analysis was further performed on the mean values of blade loads (calculated over the period), amplitudes and phases obtained by standard FFT decomposition.

The global propeller loads have been obtained from the single blade measurements by a suitable procedure able to take account of the temporal variations of the inflow (for example during transient or induced by motions caused by external disturbances).

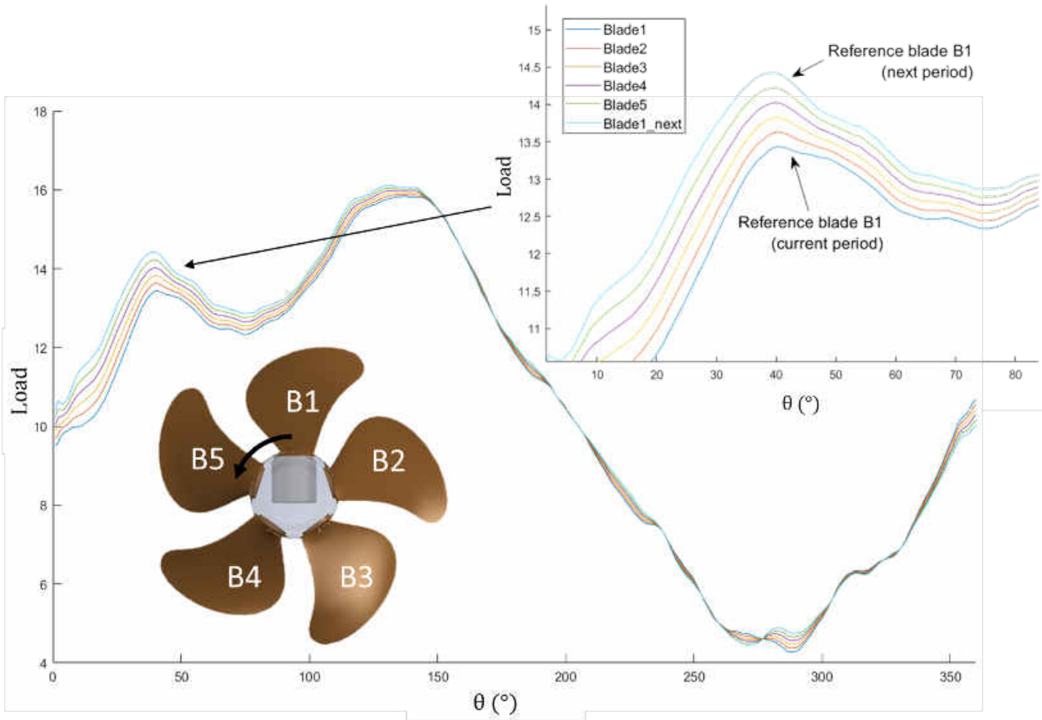

Figure 4.5 Blades load signal reconstruction

In fact, data have not been just repeated and shifted given by $\phi_b = \frac{360}{Z} \cdot b$, where Z is the number of blades and b is the blade index, but a more realistic evaluation has been performed in order to take into account the wake evolution, and consequently, the variations of the loads, and the reciprocal position of each blade during the period. As depicted in figure 4.5, the estimation of blade loads for the non–instrumented blades was calculated by a weighted interpolation between blade loads of two consecutive cycles at each blade position angle. Following this approach, the generic load component (force or moment) L for the blade b at specified angle θ has been calculated as expressed in equation 4.11:

$$L_b(\theta) = L_{1,1cyc}(\theta) + \left[L_{1,2cyc}(\theta) - L_{1,1cyc}(\theta)\right] \frac{b-1}{Z} \tag{4.11}$$

where $L_{1,1cyc}$ and $L_{1,2cyc}$ are the signals of the two adjacent cycles for the reference blade ($b = 1$). Once loads are calculated for each blade, values are shifted (by the quantity ϕ_b) according to the reciprocal positions and summed, namely:

$$L^{TOT}(\theta) = \sum_{b=1}^{Z} L_b(\theta - \phi_b) = \sum_{b=1}^{Z} L_b\left(\theta - \frac{360}{Z}\cdot b\right) \tag{4.12}$$

Apart from thrust and torque, always measured in ship model testing, in–plane loads can be accurately assessed with this novel measurement technique; moreover, the origin of these loads can be accurately inspected by the single blade loads converted in the H–frame of reference. In fact, the in–plane loads are ascribed to imbalances of the blade loads during its motion in the four quadrant of the propeller disk (Dubbioso et al. (2017)). For example, referring to the schematic description reported in figure 4.6, the average side force developed by one blade K_{Ty}^{H} arises from the different distribution in the upper (1^{st} and 4^{th} quadrants) and the lower (2^{st} and 3^{th} quadrants) halves of the disk.

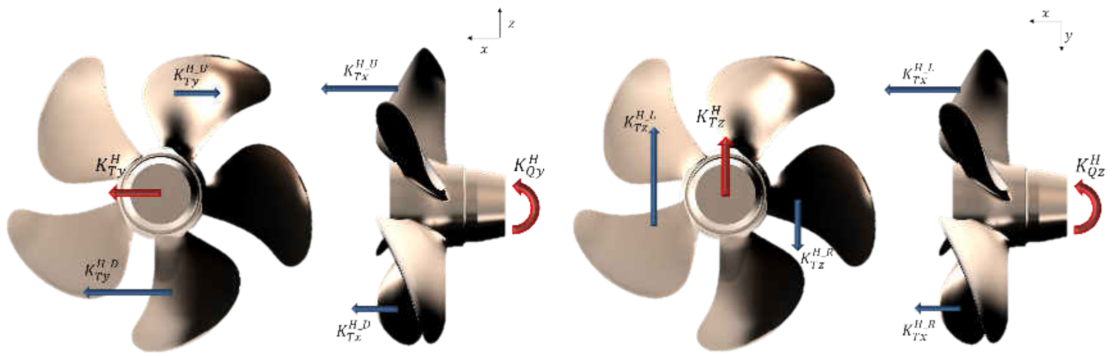

(a) side force and pitch moment (b) vertical force and yaw moment

Figure 4.6 Load imbalances leading to the generation of in–plane loads

Referring to the contribution from the generic blade (in the H-frame):

$$K_{Ty}^{H} = \left|K_{Ty}^{H-U}\right| - \left|K_{Ty}^{H-D}\right| = \left|\left[\int_{0}^{\pi/2} K_{Ty}^{H}(\theta)\,d\theta + \int_{3\pi/2}^{2\pi} K_{Ty}^{H}(\theta)\,d\theta\right]\right| - \left|\left[\int_{\pi/2}^{3\pi/2} K_{Ty}^{H}(\theta)\,d\theta\right]\right| \tag{4.13}$$

where U and D refer to the upper and lower half of the disk. According to this simple representation, it is easy to conclude that the vertical force arises from discrepancies of K_{Tz}^{H} in the left and right halves of the disk (L and R) and in–plane moments arises from imbalance of K_{Tx} in the upper/lower and left/right halves of the disk for K_{Qy}^{H} and K_{Qz}^{H}, respectively.

In the following results paragraphs, the loads are presented in the usual non–dimensional form, i.e., the forces and moments are made non–dimensional by factors $\rho N^2 D^4$ and $\rho N^2 D^5$, respectively, where N is the propeller rate of revolution, D is the diameter and ρ is water density:

$$K_{Tx,y,z} = \frac{T_{x,y,z}}{\rho N^2 D^4}; \quad K_{Qx,y,z} = \frac{Q_{x,y,z}}{\rho N^2 D^5} \tag{4.14}$$

The amplitudes of the harmonics analysis are presented in terms of ratio with respect to the mean value. The period of revolution of the propeller is divided in four sectors, the first one defined for $0° < \theta < 90°$, and so on, where θ is the blade angle and is positive oriented with the sense of rotation and $\theta = 0°$ considered for the blade at the top–right position.

4.2 Representative wake field

The determination, at least qualitative, of the relation between the inlet velocity of the propeller given by the wake evolution past the hull and the blade loads is propaedeutic to understand the variation of propeller performance during the operative conditions under study. The characteristics of the nominal wake for the rectilinear motion and pure oblique towing at $\beta_{eff} = 15°$ and $30°$, that are representative of weak and tight maneuvers, are briefly summarised in figure 4.7, obtained by preliminary *CFD* computations with a coarse grid, which are part of a parallel on-going detailed numerical validation (Calcagni et al. (2021)). The nominal wake is expressed in terms of colour maps of axial u, made non–dimensional with respect to the speed of the model in the approach phase, and vector field of the tangential velocity. Given the nominal wake, the evolution of the loads during a revolution can be inferred synthesizing the blade hydrodynamics with the 2D hydrofoil approach described in Par. 4.3. In the representation in drift, the starboard propeller is on the leeward side and the cross flow is directed from left to right. The results are presented for the instrumented propeller, i.e. the starboard one; depending on its relative position during the maneuver, it is referred to *internal* and *external* when located in the leeward and windward side of the hull, respectively. In the presentation of the data, the internal and external propeller is ascribed to maneuvers at positive and negative rudder angles, respectively. Figure 4.7 highlights the asymmetric evolution of the wake that determines the different behavior of the propeller: on the windward side, the inflow progressively evolves to a pure oblique flow and the deficit of the axial velocity is mainly confined in the 1^{st} quadrant, whereas, the *internal* propeller is strongly affected by the wake of the hull and appendages swept toward the leeward side. In particular, the flow around this propeller is characterized by vortical structures that interact with the wake of hull and downstream appendages to yield complex hydrodynamic blade–wake interactions.

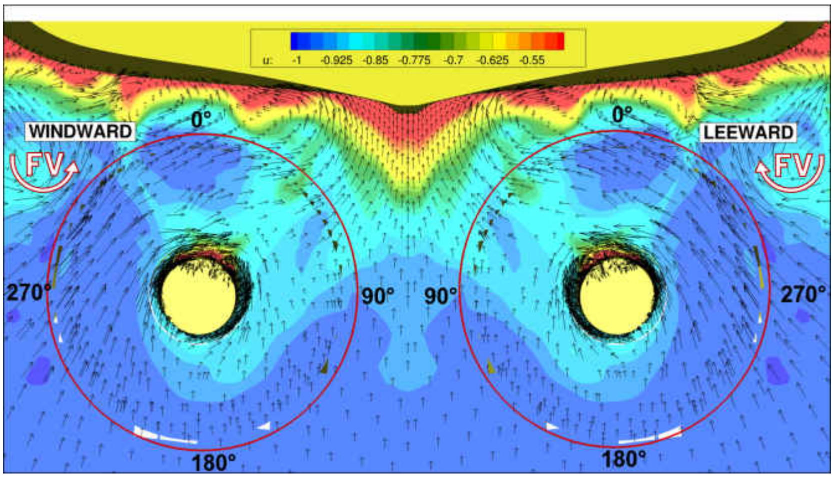

(a) $\beta_{eff} = 0°$

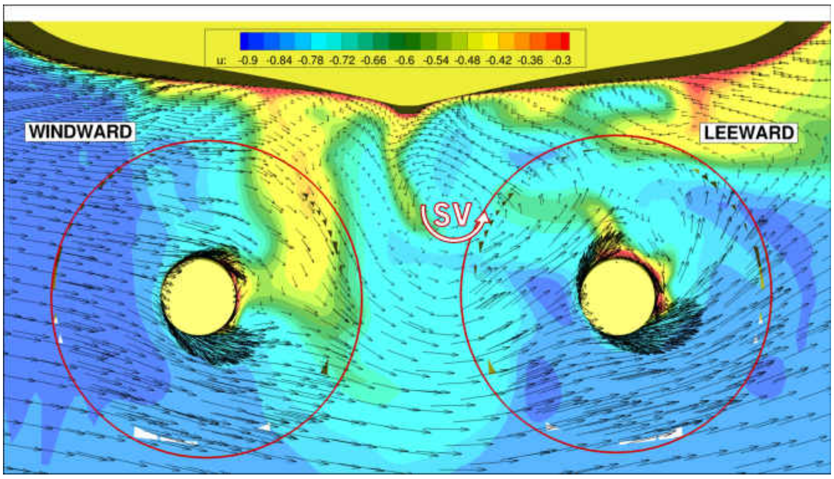

(b) $\beta_{eff} = 15°$

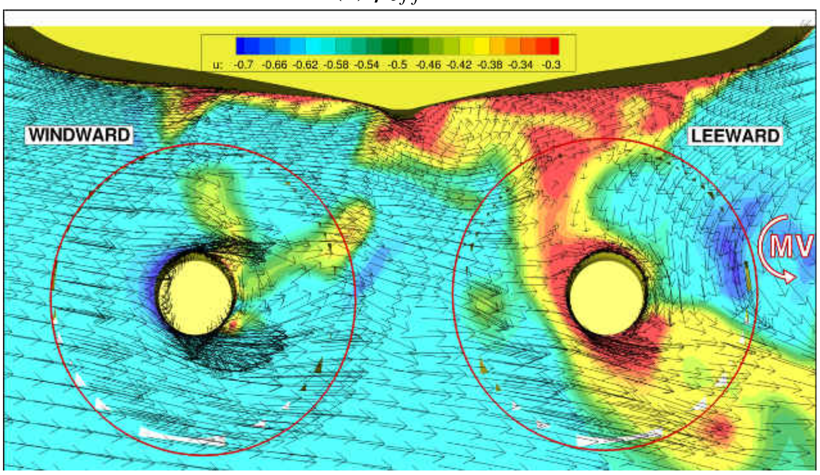

(c) $\beta_{eff} = 30°$

Figure 4.7 Nominal wake by CFD computations

Albeit the phenomenological aspects are detailed in the following sections, it is propaedeutic to identify these structures, namely:

- stabilizer fin vortex (*FV*), whose signature is clearly visible on the left (right) of the windward (leeward) propeller for the model in straight ahead, see figure 4.7a.
- skeg vortex (*SV*), evidenced by the swirling flow for the drift condition at $\beta_{eff} = 15^\circ$ in figure 4.7b.
- large mixed vortex (*MV*), that is evident on the right of the leeward propeller at the highest drift angle, see figure 4.7c. This structure comes from the interaction of skeg, bilge keel (not evidenced in these plots) and other structures detached from the appendages (for example, the shaft)

In general, these structures and the features of the wake differently evolve for the three different test conditions considered in this study.

4.3 Force components on single blade

In order to support the link between the measurements and their cause by a straightforward and immediate approach, the origin of the forces and moments developed by the blade are explained assuming the equivalence of the blade with a 2D foil, see Figure 4.8.

The generic section, located at span wise station r and characterized by the geometric pitch Θ, is impinged by the flow at a resultant speed V and incidence α, as a results of the combination of the axial (u) and tangential velocity (v_t) components. By applying 2-dimensional airfoil theory, the loads are directly proportional to the incidence angle α of the propeller sections, that results from the combination of the axial velocity u_a and the tangential velocity v_t relative to the blade foil. Introducing the velocity components of the flow u, v and w at the generic section, the propeller angular speed $\omega = 2\pi N$, where N are *RPS*, and the geometric pitch angle of the section Θ, the total tangential velocity v_{tan}, the relative inflow angle ϕ and the incidence angle can be easily determined:

$$
\begin{array}{ll}
\text{Axial velocity:} & u_a = u \\
\text{Tang. velocity (wake):} & v_t = v \cdot cos\theta + w \cdot sin\theta \\
\text{Tang. velocity (total):} & v_{tan} = \omega \cdot r + v_t \\
\text{Inflow angle:} & \phi = tan^{-1}\left(\frac{u_a}{v_{tan}}\right) \\
\text{Incidence:} & \alpha = \Theta - \phi
\end{array}
\tag{4.15}
$$

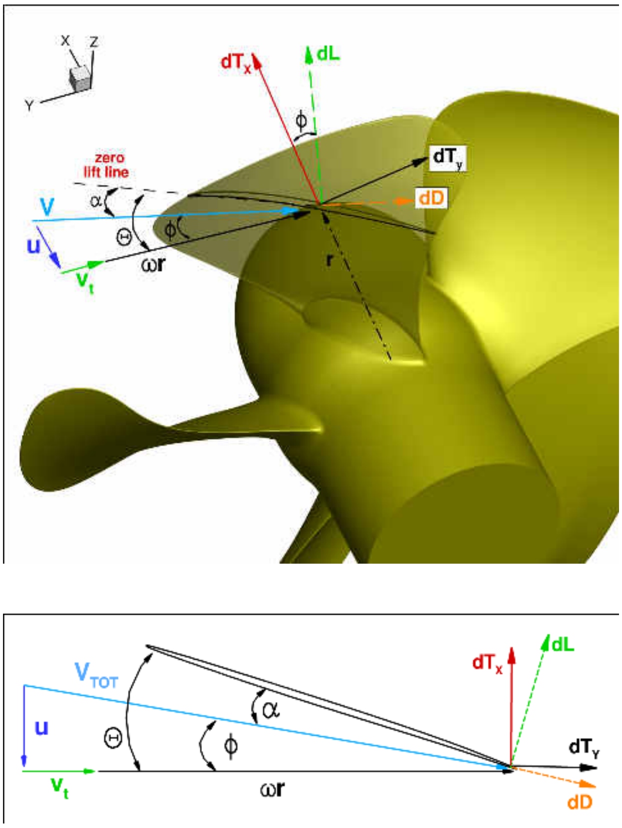

Figure 4.8 Blade element description

Introducing the section hydrodynamic lift and drag coefficients C_L and C_D and the distance sectional centre of pressure of the loads from the spindle axis d_{CP} of generic section position r along the blade span, the total axial blade forces ($T^H_{(x,y,z)}$) and moments ($Q^H_{(x,y,z)}$), developed by the blades, result from the cumulative contribution of the loads generated by the different blade sections from the hub r_h to the tip r_t. Without loss of generality, equations 4.16 define blade thrust and spindle torque Q_Z.

$$
\begin{aligned}
&\text{Elemental thrust:} && dT_X = dL \cdot cos\phi - dD \cdot sin\phi \\
&\text{Elemental side force:} && dT_Y = -dL \cdot sin\phi - dD \cdot cos\phi \\
&\text{Sectional lift:} && dL \sim V_{TOT}^2 \frac{\partial C_L}{\partial \alpha} \alpha \\
&\text{Sectional drag:} && dD \sim V_{TOT}^2 C_D \left(\alpha, \alpha^2\right) \\
&\text{Blade thrust:} && T_X = \int_{r_h}^{r_t} dT_X \cdot dr \\
&\text{Blade spindle torque:} && Q_Z = \int_{r_h}^{r_t} (dT_X \cdot d_{CP} \cdot cos\Theta + dT_Y \cdot d_{CP} \cdot sin\Theta) \cdot dr
\end{aligned}
\tag{4.16}
$$

As a general assumption

$$Load \propto \alpha = \Theta - tan^{-1}(\frac{u}{2\pi Nr + v_t}) \tag{4.17}$$

In behind-hull, the wake of ship (u and v_t) is not uniform and the angle of attack of the blade changes during the single period of revolution, generating fluctuating loads (see equation 4.17). Moreover, the wake of the ship in realistic conditions can be completely modified with respect to the wake considered during the design (calm water), due to wave induced motions or manoeuvres and, consequently, the loads can markedly change from the ones considered during the design phase. The novel system presented in this thesis allows to asses, with high detail, those loads in all the standard hydrodynamic model tests (self-propulsion, free running or seakeeping) without introducing any hydrodynamic disturbance.

Chapter 5

Free running results

The results of the analysis of turning circle manoeuvres performed during free running model tests are reported. Three speeds, corresponding to Fn 0.26, 0.34 and 0.40, and five rudder angles ($0°, \pm 7.5°, \pm 15°, \pm 25°$ and $\pm 35°$) have been investigated, which cover a wide range of off-design operative conditions. The single blade loads are presented and discussed in terms of their cyclic evolution, mean values and harmonic content, by a standard Fourier Decomposition, referring to both the blade (rotating) and hub (fixed) frames of reference. The focus on the blade loads converted in the fixed frame of reference is useful to describe the propeller loads, with particular emphasis on the in–plane loads and their fluctuating character.

5.1 Blade loads

5.1.1 Straight ahead navigation

The periodic trend of the single blade loads, with arithmetic (black) and weighted (green) error bands, obtained in the frame rotating with the blade (B-frame) are reported in figure 5.1, for the three different speeds. The forces and moments are presented in terms of ratio with respect to the mean value of T_x^B and Q_x^B experienced during the approach phase at $F_N = 0.26$, respectively, in order to appreciate the effects of speed and the difference between the two error bands. Mean values of the loads, with corresponding errors, are summarized in usual non–dimensional form in tables A.1–A.3 (see Appendix A). In general, the trend of the loads are very similar for all speeds, as it is confirmed by the similar non–dimensional values reported in the tables.

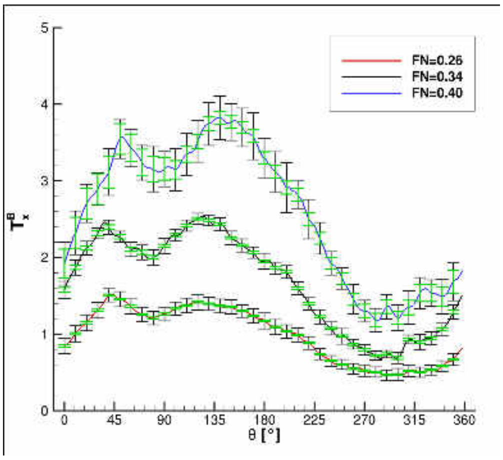

(a) Thrust

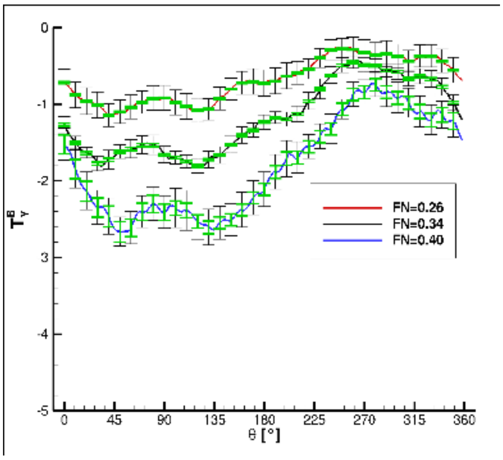

(b) Side force

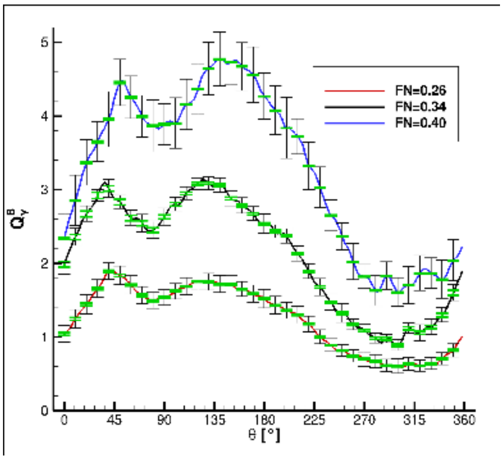

(c) Bending moment

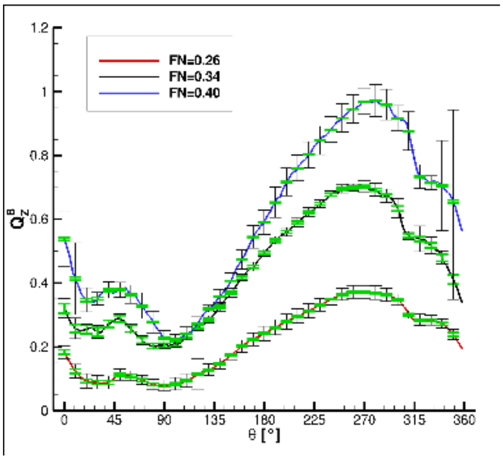

(d) Spindle torque

Figure 5.1 Single blade loads (blade frame) and errors represented in terms of σ_1 (black) and σ_2 (green)

This fact confirms that the inflow to the propeller is almost the same for the three speeds; minor differences can be ascribed to modifications of the hull wake, associated to change of attitude of the model in the vertical plane, as well as stern flow due to wet–dry transom stern at the higher speeds. In general, the arithmetic error bands of the time histories increases with speeds and, at the highest F_N is of the order of 1N for blade thrust and side force and 0.08Nm and 0.01Nm for pitch moment and spindle torque. The marked difference between the arithmetic and weighted error is caused by the fact that the former indicator can be affected by non exactly equal condition of the test due to environmental disturbances. The weighted error further stresses the high quality and repeatability of the measurements. Similar considerations justify the discrepancy between σ_1 and σ_2 relative to the mean values.

The same conclusion is corroborated by the slight discrepancy relative to the weighted and arithmetic means, the standard r.m.s. being almost equal for the complete set of runs.

The trend of these loads are discussed considering their relation with the nominal wake at four representative blade angles, specifically at $\theta = 0°, 60°, 130°$ and $300°$, see figure 5.2.

The nominal wake, obtained by CFD simulations, is described in terms of the axial (contour lines) and tangential velocity fields (arrows). Briefly, the defects of the axial velocity u results behind the shaft brackets and in the upper half of the disk due to the wake of the hull, while in the lower half the flow is rather undisturbed; the tangential velocity is mainly upwards oriented due to the cut–off of the stern and slightly inwards oriented. These characteristics are similar for twin screw ships and qualitatively similar features were also observed in Jessup et al. (1977).

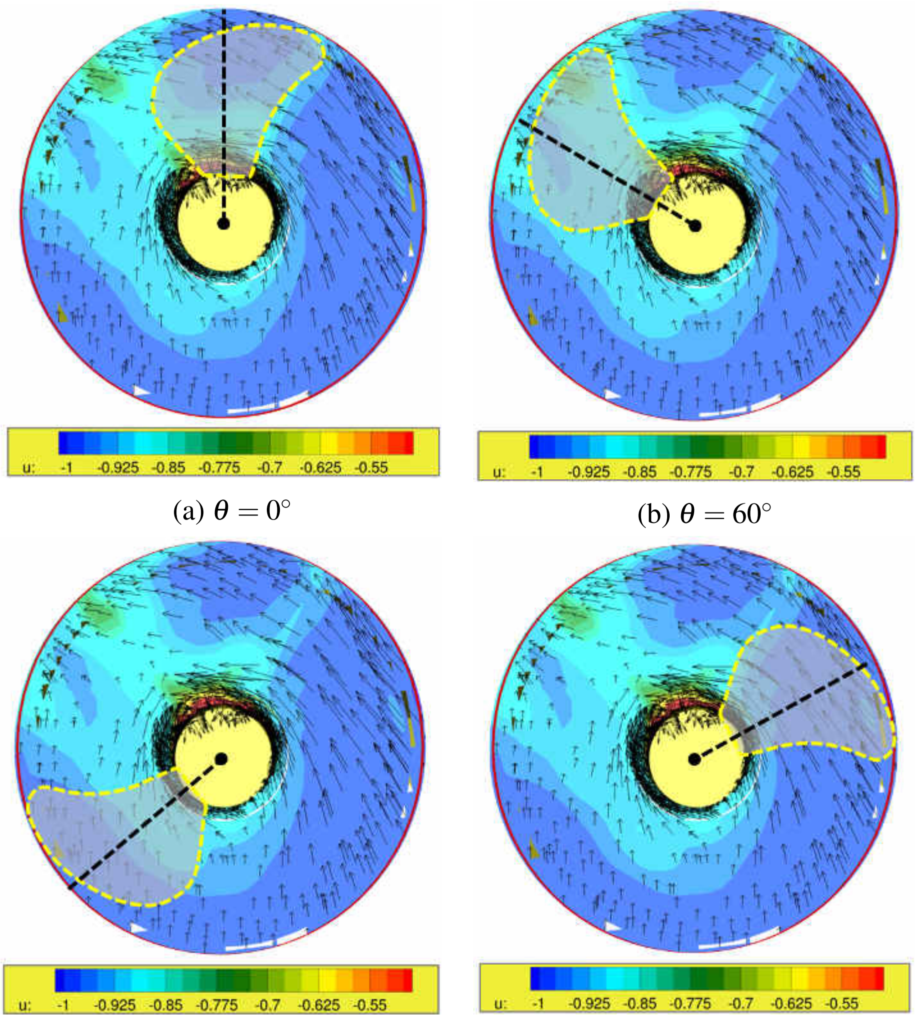

(a) $\theta = 0°$ (b) $\theta = 60°$

(c) $\theta = 130°$ (d) $\theta = 300°$

Figure 5.2 Inflow (calculated by CFD) encountered by the blade

In general, the blade thrust (and pitch moment) and side force (and torque, not reported for the sake of brevity) fluctuate, because the blade encounter the non–homogeneous flow perturbed by the hull and stern appendages. The load is higher during the first half of the cycle, because the blade rotates in a region perturbed by the wake of the hull and appendages. Moreover, in this sector the loads experience a double peaked evolution. Then the loads decreases almost monotonically to a minimum in correspondence of $\theta = 300^{\circ}$ and, then, further rise.

The variable operating condition of the blade can be alternatively inspected in the open water characteristics chart, see figure 5.3. The thrust and torque curves have been obtained from the ratio of propeller characteristics and the number of blades for the proof of concept, disregarding the contribution of the hub. The overlap of the measured single blade loads on the open water characteristics identifies the range of an equivalent advance coefficient of the blade. As previously discussed, the advance coefficient is inversely proportional to the angle of attack of the blade sections that, on its turn, depends on both axial and tangential component of the inflow. In the figure, the mean value of blade thrust is identified by the asterisk. Although the mean value is close to the point of maximum efficiency, the blade experiences up to $\pm 14\%$ of deviation from this design condition during a complete revolution.

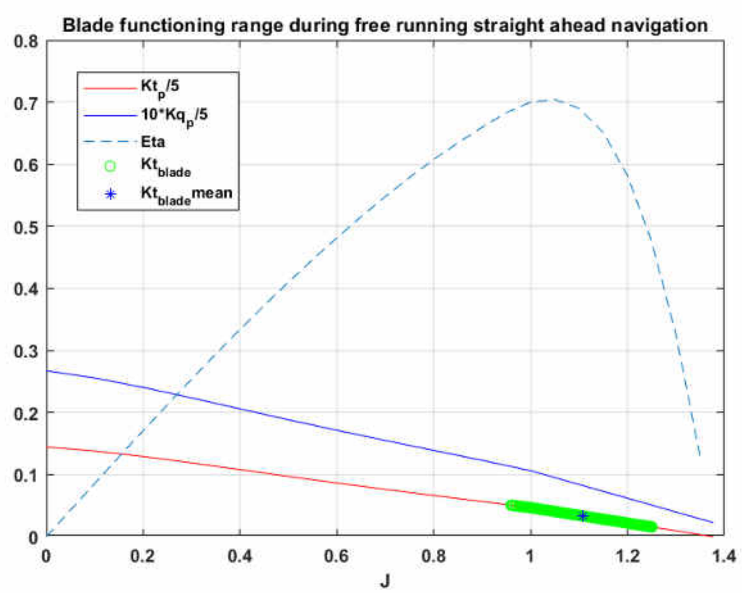

Figure 5.3 Propeller open water curves and blade operational points during straight navigation

Following the blade during the revolution, the loads increase because the blade gradually overloads moving from $\theta = 0^{\circ}$ (see figure 5.2a) to $\theta = 60^{\circ}$ (see figure 5.2b). In fact, at

$\theta = 0^\circ$, the blade passes in–between the brackets and the flow is almost unperturbed (note that the tangential is concordant to blade rotation and further contribute to reduce the angle of attack). After, the inflow to the blade is gradually affected by the perturbation of the inner brackets, causing the load to achieve a maximum in correspondence of $\theta = 60^\circ$; the overloading of the blade can be ascribed to the large defect of the axial speed, because the tangential speed is moderate due to the blockage of the hull and oriented almost radially to the blade, see figure 5.2b. After a slight decrease, the loads experience a second peak with magnitude similar to the previous one at $\theta = 130^\circ$, see figure 5.2c. In this case, the peak is caused by the increase of the in–plane component of the flow that is oppositely oriented to blade rotation, while u increases to the undisturbed value in the lower half of the disk. The increase of load caused by the tangential flow during the down–stroke motion of the propeller was documented in Jessup et al. (1977) for a V–shaped stern twin screw ship. It is worth to note that, the blade position θ of the peak at 60° does not perfectly match with that of the brackets due to the skewed shape of blade; in fact the skew allows the different blade sections to encounter the flow disturbance in a staggered way with respect to a perfectly straight blade in order to mitigate the load fluctuation. Moreover, the phase shift between the peaks of thrust and tangential force (and analogously, bending and spindle moments) might be partially imparted to this effect. During the rotation in the lowest half of the disk the blade is unloaded, because the axial flow is close to the nominal advance velocity. The loads achieves a minimum about $\theta = 300^\circ$, the tangential flow being concurrent to the blade rotation and, therefore, acting to reduce the local incidence of the blade foils, see figure 5.2d. Finally, in the 4^{th} quadrant the loads increase as a consequence of the defect of u associate to the wake of the external astern bracket.

A dedicated discussion is deserved for Q_z^B (figure 5.1d). This moment is representative of the torque of the hydro–loads about the axis of the blade and results positive during the whole cycle; the trend is opposite with respect to the other loads, because it is governed by the evolution of the center of pressure on a skewed blade and its direct relation with blade loading is not immediate. First of all, the positive sign of Q_z^B indicates that this couple acts to reduce the geometric pitch of the blade, or, alternatively, the resultant centre of pressure of the loads oscillates always past the vertical axis of the blade. It can be inferred that during the cycle the centre of pressure moves from larger to smaller radial positions when the blade loading increases and vice versa. Due to the skew, the centre of pressure starts behind the spindle axis (to yield a positive couple) and gradually moves forward to cross over it (to reduce and yield a negative spindle arm).

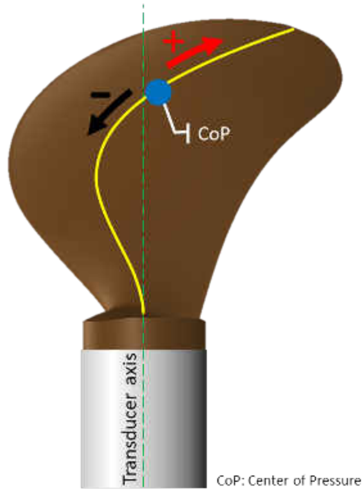

Figure 5.4 Schematic view of how the shift of the center of pressure along the blade causes the variation of spindle torque

With reference to figure 5.4, observing the shape of the blade and the blade set–up, the reduction of the moment during the first half cycle can be explained with the fact that the centre of pressure shifts towards middle sections, thus leading a lower arm (black arrow). On the contrary, at lower loading, the centre of pressure moves to outer radii (the blade is geometrically back–skewed) and the arm (and moment) increases (red arrow). An alternative perspective on the nature of the loads and pressure distribution on the blade is proposed in figure 5.5 in terms of the radial coordinate of the estimated point of application of thrust and lateral force, defined by:

$$R_{Tx} = \frac{Q_Y^B}{T_X^B} \quad R_{Ty} = \frac{Q_X^B}{T_Y^B} \tag{5.1}$$

In the figure, R_{Tx} and R_{Ty} are reported in terms of ratio with respect to the propeller radius. The trend is very similar for all the speeds investigated and further corroborates the previous explanation about the evolution of the spindle torque. In fact, in the 1^{st} and 2^{nd} quadrants, both radii are smaller than in the last interval, confirming that the centre of pressure moves towards inner sections during overloading and vice versa. Moreover, it is interesting to observe that the phase angle θ of the side force radius increases with F_N and resembles the same trend of the minima and maxima of blade T_Y^B and Q_Z^B, respectively.

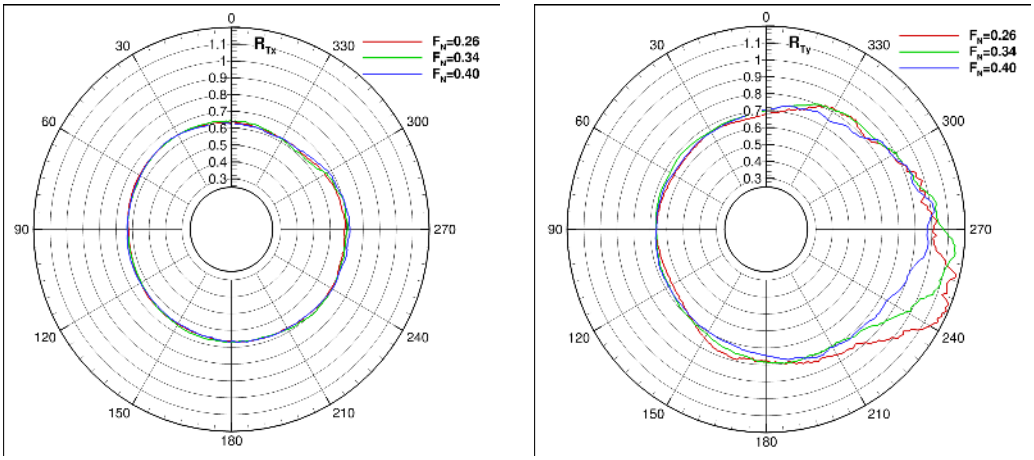

(a) blade thrust radius (b) blade side force radius

Figure 5.5 Variation of blade thrust and side force radius

The results of the standard Fourier Analysis of the blade loads, summarized in figure 5.6 and tables B.1–B.9, allows to explain, in more detail, the origin and features of the propeller induced vibratory loads on the shaft and hull structures. In the figures the amplitudes are reported in terms of ratio with respect to the mean value and in the tables (up to the 5^{th} BPF) in the usual non–dimensional form. The spectra reported in the figures is typical for a propeller operating in non–cavitating regime, characterized by a fast decay of the harmonics in the low frequency range (Breslin and Andersen (1994)), as it was also concluded by the experiments presented in Jessup et al. (1977). In the present case, the characteristics of the signal can be synthesized with the first ten harmonics. In the figures, the spectra is developed up to the 30^{th} BPF, in order to stress the reliability of the experimental set–up, and also verify that resonance of the system never appeared as broadband humps in the higher frequency range. The contribution of the 1^{st} BPF is dominant with respect to its multiples; in fact, the amplitude is suddenly cut by almost 80% for all the loads with the exception of the spindle torque, for which multiples are reduced by about 90%. The fluctuation of the blade loads is significant, corresponding to about 50% of the mean values for blade thrust and lateral force, 40% for the torque and 60% for the spindle torque. It is worth mentioning that the 1^{st} BPF of the spindle torque is about 10% of the mean value of blade torque (see values in the tables). In general, the effect of speed is negligible and the slight differences can be ascribed to minimal change of the wake associated to the actual test condition. In general, the r.m.s. of the harmonics for of the loads is about 10% for σ_1 and 2% for σ_2, confirming the validity and repeatability of the measurements.

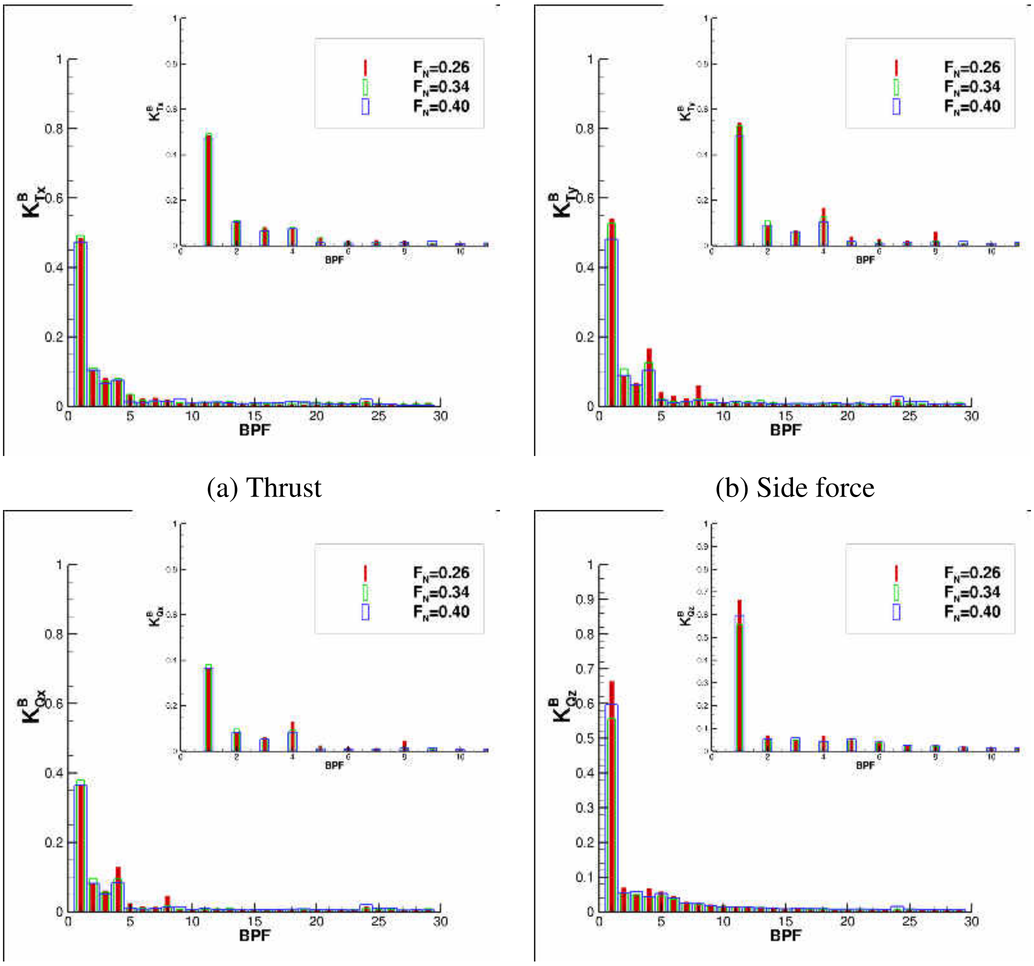

(a) Thrust (b) Side force

(c) Torque (d) Spindle moment

Figure 5.6 Harmonic content (amplitudes) of the single blade hydrodynamic loads (blade frame)

5.1.2 Steady turning

The maneuvering response of the model during the steady turn is described in terms of usual parameters, namely turning diameter (FD), speed drop (i.e. the reduction of the absolute speed), rotational velocity, roll angle and drift, see table 5.1. The data are made non–dimensional by L_{PP} (length between perpendicular) and U_0 (approach speed). As expected, the increase of rudder angle leads to smaller turning diameter, higher yaw rate ($\dot{\psi}$) and higher values of the roll (ϕ) of the ship (the contribution of the centrifugal force and lift on the hull increases with respect to the opposite moment provided by the rudders (Lewis (1998))). Moreover, the speed drop is reduced, because the relative angle of drift β of the model increases with the severity of the maneuver.

	F_N=0.26					F_N=0.34					F_N=0.40				
δ	FD	U/U_0	$\dot{\psi}$[°/s]	ϕ[°]	β[°]	FD	U/U_0	$\dot{\psi}$[°/s]	ϕ[°]	β[°]	FD	U/U_0	$\dot{\psi}$[°/s]	ϕ[°]	β[°]
±35°	3.35	0.70	7.9	1.7	14.4	3.51	0.71	10.4	3.4	14.9	-	-	-	-	-
±25°	4.42	0.80	6.8	1.7	11.2	4.63	0.82	8.9	3.3	11.6	5.2	0.86	9.9	4.1	12.2
±15°	7.22	0.89	4.7	1.6	8.4	7.44	0.92	6.3	2.8	8.1	8.1	0.96	7.1	3.5	9.9
±7.5°	13.94	0.95	2.6	1	4.5	14.37	0.98	3.4	1.7	4.4	17.72	0.98	3.8	2.2	4.4

Table 5.1 Maneuvering characteristics of the model

The development of the nominal wake during maneuvers has been introduced in Par. 4.2 and will be further referred to during the discussion of the single blade loads.

The time history of the single blade loads in the rotating frame, with arithmetic and weighted error bands, are reported in appendix A.2.3 for the different rudder angles and speeds. Blade thrust, side force and spindle moment are only reported, because bending moment and torque show the same trend of thrust and side force, respectively. The loads are visualized in the real dimensional scale to appreciate the effects of speed and the two error bands. It can be evidenced that both the mean and fluctuating components of the loads are different for the leeward and windward propeller. The amplitude of the error bands is small and of the same order observed for the straight ahead case and, furthermore, it is not sensitive to rudder angle. The errors for the lowest and intermediate speed are comparable, whereas at the highest one it is larger, although it always remains within satisfactory limits. In general, σ_1 is higher with respect to σ_2 because it is affected by the test conditions (see also the discussion in Par. 4.1). The weighted mean values of the single blade loads are summarized in figure 5.7 and listed in tables A.4–A.6. In the tables, only the weighted mean value of the loads is reported for savings in space. As expected, the leeward ($\delta > 0°$) and windward ($\delta < 0°$) propeller experience an asymmetric behavior. The effect of F_N is negligible and this fact confirms that, qualitatively, the inflow to the propellers is almost similar for the three speeds and minor differences can be ascribed to modifications of the hull wake, associated to change of attitude of the model. Specifically, on the external propeller the loads linearly increase with rudder angle; on the internal propeller the trend is linear only for the intermediate F_N, since the loads for $0° < \delta < 7.5°$ experience a local maxima. The blade on the windward side results markedly overloaded with respect to the leeward side, the percentage increase with respect to the straight ahead condition ($\delta = 0°$) being of the order of 100% at the maximum rudder angle for thrust, side force and bending moment; the overloading on the leeward side is more than halved (K_{Tx} and K_{Qy} show 45% increase and K_{Ty} shows 30% increase). The spindle torque K_{Qz} is weakened, see figure 5.7d: on the leeward side, it is close to zero at the maximum rudder angle, whereas on the external propeller its orientation is inverted. In other words, the centre of pressure of the resultant loads tends to move towards the leading edge and, taking account for the skewed shape of the propeller, to the inner sections of the blade. It has to be stressed that the almost neutral loading on the leeward propeller is not desirable condition, because any kind of disturbance could give rise to small amplitude vibrations that can lead to fretting wear (Dubbioso and Ortolani (2020)) and, ultimately, fatigue damages.

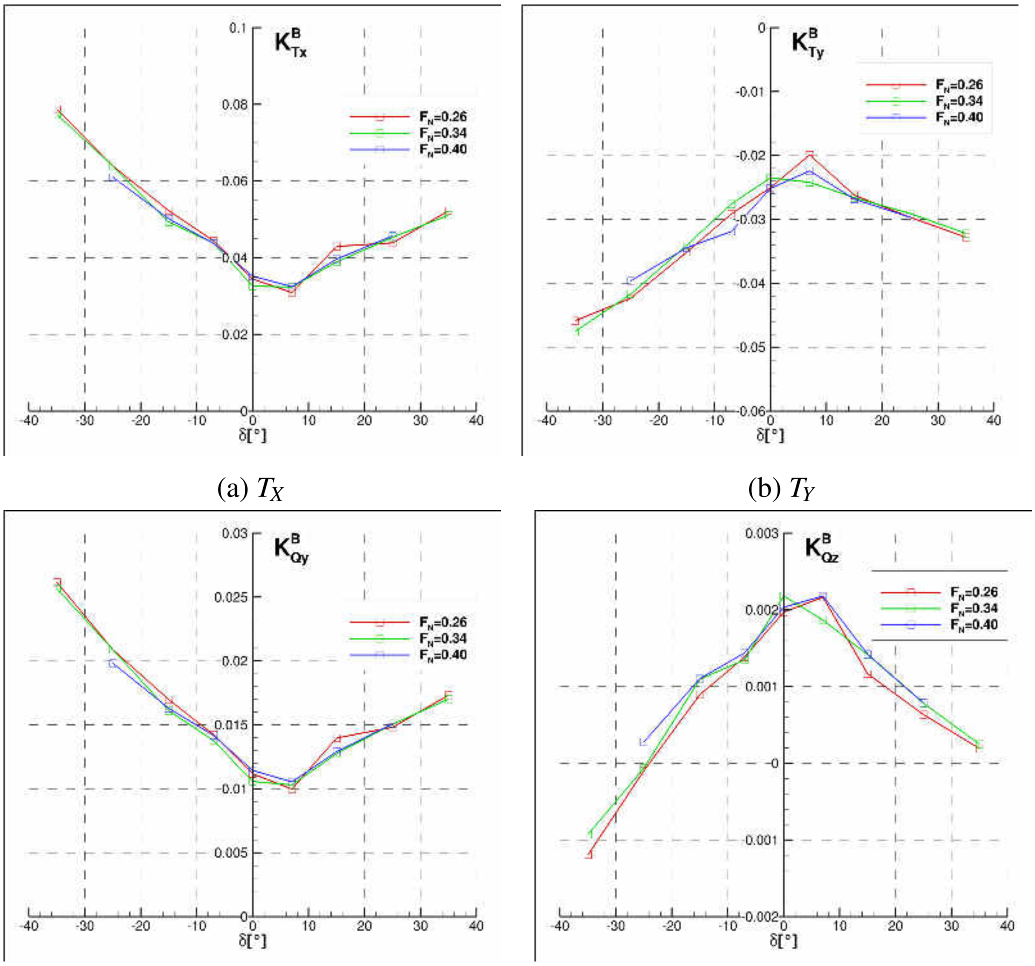

(a) T_X (b) T_Y

(c) Q_Y (d) Q_Z

Figure 5.7 Mean single blade loads (rotating frame)

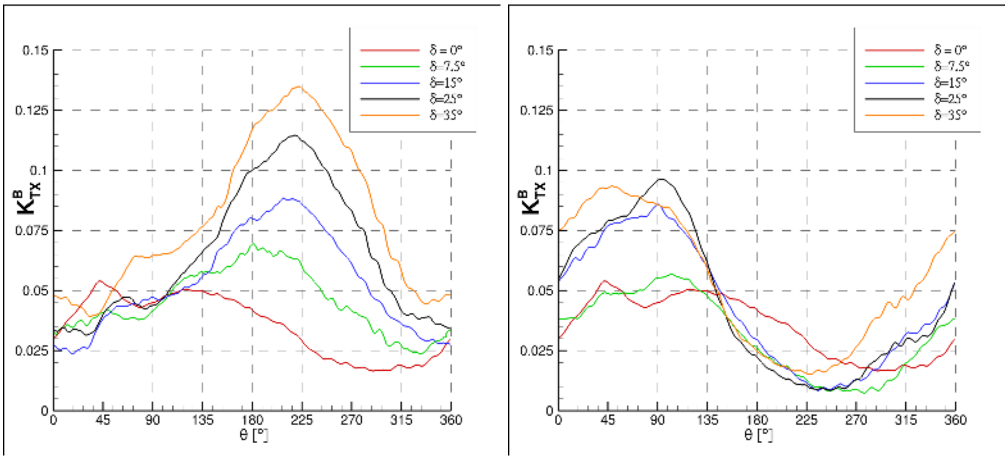

(a) K^B_{TX}

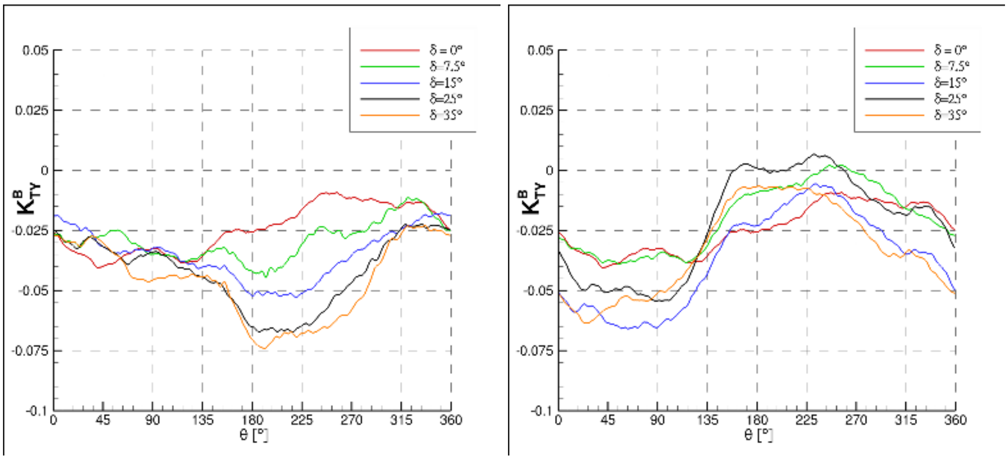

(b) K^B_{TY}

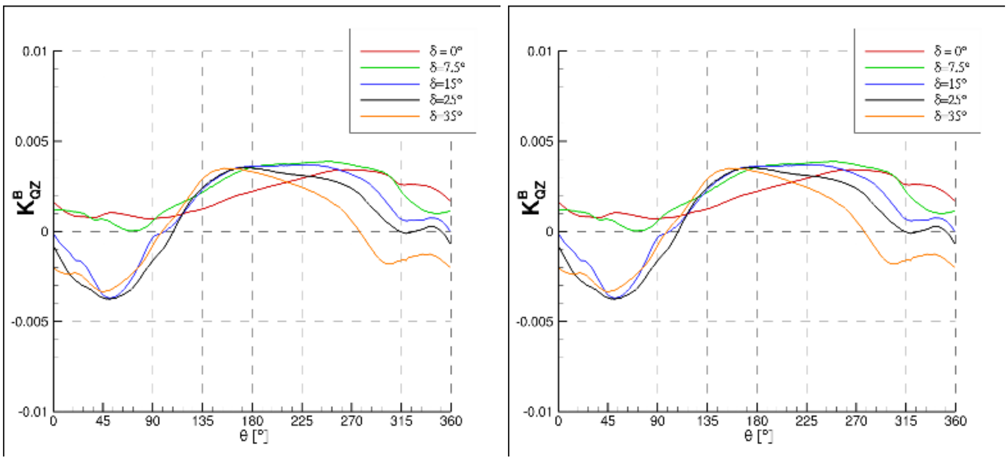

(c) K^B_{QZ}

Figure 5.8 Periodic single blade loads (rotating frame). Internal propeller (right); external propeller (left). $F_N = 0.26$

The periodic variation of the single blade loads, visualized in figure 5.8, are related to the representative nominal wake in figure 4.7. In the figures, the blade loads measured for the lowest speed are considered, because a similarity of the wakes can be inferred from the results in figure 5.7. Given the inflow and the rotational regime of the propeller, the trend of the loads is qualitatively discussed referring to the analogy of the blade with a 2D foil introduced in 4.3. The fluctuations of the blade thrust and side force are qualitatively consistent with each others according to equation 4.17; for this reason, the following discussion is developed referring to K_{Tx}. In straight ahead motion, as discussed in the previous paragraph, K_{Tx} is characterized by two peaks in the 1^{st} and 2^{nd} quadrants, associated to reduction of axial velocity past the inner bracket, $\theta = 45°$, and to the upwards oriented tangential velocity at $\theta = 120°$ (opposite to blade rotation, thus causing the increase of incidence), respectively. The load diminishes up to $\theta = 300°$ because the nominal wake is not perturbed (and the tangential flow is concordant to blade rotation) and then rises again due to the increase of the velocity defect past the outer bracket and blockage of the hull (figure 4.7a). During maneuvering, as a consequence of the different distribution of the wake, the loads evolve differently during a complete revolution for the leeward and windward side. The loads differ with respect to the straight ahead case for all maneuvers. On the leeward side, K_{Tx}^{B} (figure 5.8a on the left) is markedly sensitive to rudder angle for $0° < \theta < 135°$. In fact, in the sector $0° < \theta < 135°$, the wake of the hull experiences a remarkable variation with rudder angle (compare figures 4.7a, 4.7b and 4.7c). At $\delta = 7.5°$, the double peak shape disappears and the thrust achieves a maximum value (of the same magnitude of the peaks at $\delta = 0°$) at $\theta = 100°$, that can be associated to the deflection of the wake of the hull towards the disk. In fact, the representation in figure 4.7b suggests that the upwards oriented tangential velocity is suddenly deflected at $\theta = 90°$ as soon as the maneuver starts. At $\delta = 15°$ the thrust abruptly increases and keeps the same magnitude for the higher rudder angles (25° and 35°); the trend at $\delta = 15°$ and 25° shows peaks at the same blade position, $\theta = 90°$, that are 50% higher with respect to the maximum observed at $\delta = 0°$ and $\delta = 7.5°$. At $\delta = 15°$, the blade overloading can be ascribed to its interaction with the *SV* vortex detached from the skeg of the hull, that causes a local increase of the upwards tangential velocity, as shown by the recirculation region at $\theta = 60°$ in figure 4.7b. The persistence of a similar flow phenomenology, although weakened, can be supposed in case of the maneuver at $\delta = 25°$, given the similar evolution of the loads. Obviously, at $\delta = 25°$, the greater speed reduction of the model causes the increase of the thrust. At $\delta = 35°$, the signal is more flat in correspondence of the peak (shifted at $\theta = 45°$), probably because its nature is related to defect of axial velocity rather than a local interaction of the blade with vortical structures (see figure 4.7c), although the propeller is being immersed in a region were the flow is massively separated (figure 2.5 for a similar hull and propulsive configuration). In the sector $160^\circ < \theta < 250^\circ$, K^B_{Tx} progressively diminishes. This can be ascribed to the fact that the tangential velocity, concurrent with propeller rotation, counteracts the blade overloading caused by the reduction of the axial velocity associated to speed drop and flow separation. In fact, as described in the sequence of figures 4.7b–4.7c, the tangential velocity is progressively deflected horizontally and, therefore, v_t acts to reduce the circumferential velocity relative to the local blade sections. However, the effect provided by v_t is weakened with the severity of the maneuver, because the velocity defect progressively extends to larger portion of the disk due to the development of larger vortical structures and flow separation from the hull and appendages (MV). Note, for example, that at $\delta = 35^\circ$ the percentage increase of the load is due to the presence of MV which gives rise to a v_t opposite to propeller rotation (figure 4.7c). The increase of velocity defect in the upper half of the disk (additional disturbance of brackets and hull) also explains the rise of the load in the last interval of the cycle.

On the windward side, the evolution of K^B_{Tx} is similar for all the rudder angles. Due to the deflection of the wake, the load is smaller ($0^\circ < \theta < 60^\circ$) or similar ($60^\circ < \theta < 90^\circ$) with respect to the straight ahead motion for all maneuvers up to $\delta = 25^\circ$, probably due to the positive interference of axial and tangential velocity. In fact, the region of higher axial velocity in–between the brackets is deflected and spreads to the lee side; moreover, the cross flow induced by the motion is oriented to reduce the relative tangential velocity of the blade, and, consequently, the hydrodynamic incidence and the load (equation 4.17). In case of the tighter maneuver ($\delta = 35^\circ$), the thrust suddenly increases for $45^\circ < \theta < 90^\circ$: this can be ascribed to flow separation from the shaft, that causes further reduction of u, see figure 4.7c. In the rest of the cycle, K^B_{Tx} is similar for all maneuvers, because the wake evolves like a pure oblique flow on the windward side. The trend is strictly associated to the effect of the tangential velocity, because u is almost homogeneously distributed as confirmed by the figures. In the lowest half of the disk, namely up to $\theta = 225^\circ$, the tangential velocity acts to increase the circumferential velocity of the foil, whereas its effect is opposite up to end of the cycle. It is worth to notice that the maximum peaks of K^B_{Tx} (K^B_{Ty}) during the tighter maneuver are 150% (100%) and 70% (50%) higher with respect to the maximum value experienced in rectilinear motion and about 70% (50%) on the windward and leeward side, respectively.

The spindle torque, K^B_{Qz} generated by the blade is visualized in figure 5.8c. The trend of the moment is determined by the shift of the point of application of the resultant force along the chord and, hence, its functional relation with loading (i.e. incidence) is not immediate. The variation of this load is sensitive to spanwise movement of the centre of pressure and the rate of back–skew of the blade, as discussed in Par. 5.1.1. In particular, it was observed that the spindle torque increased in regions inwhich the blade loading was lower and viceversa; alternatively, with the increase of blade loading, the centre of pressure would shift toward the inner radial stations. This conclusion seems to be confirmed also in case of maneuvering conditions. In fact, it can be observed that K_{Qz}^{B} decreases during blade overloading and viceversa for both the leeward and windward propeller. For example considering the maneuver at $\delta = 35°$ on the leeward side (panel on the left), K_{Qz}^{B} is negative in the 1^{st} quadrant (the blade thrust is higher and the centre of pressure is shifted inwards at smaller radii with respect to the straight ahead motion). Then, after achieving a minimum in correspondence of the thrust peak, the moment is reduced up to change sign (positive) in correspondence of the motion of the blade in the lowest half of the disk ($90° < \theta < 220°$) and the centre of pressure gradually moves outwards. Finally, the blade load again increases and K_{Qz}^{B} decreases, the centre of pressure gradually moves to the inner stations and ahead of the radial axis. The blade experiences a considerable and alternate fluctuation of the load: on the leeward side, it is almost doubled with respect to the straight ahead case for all maneuvers (with the exception of the turn at $\delta = 7.5°$) whereas, on the windward side, the fluctuation increases with rudder angle. As already introduced in section 5.1.1, additional information about the blade operational conditions can be obtained by the superposition of the periodic blade thrust measured during the turning maneuvers at different rudder angles on the open water characteristic, see Figure 5.9. Plots refer to the external and internal propeller on the left and right respectively and the mean K_{Tx} of the complete period of revolution is marked with an asterisk.

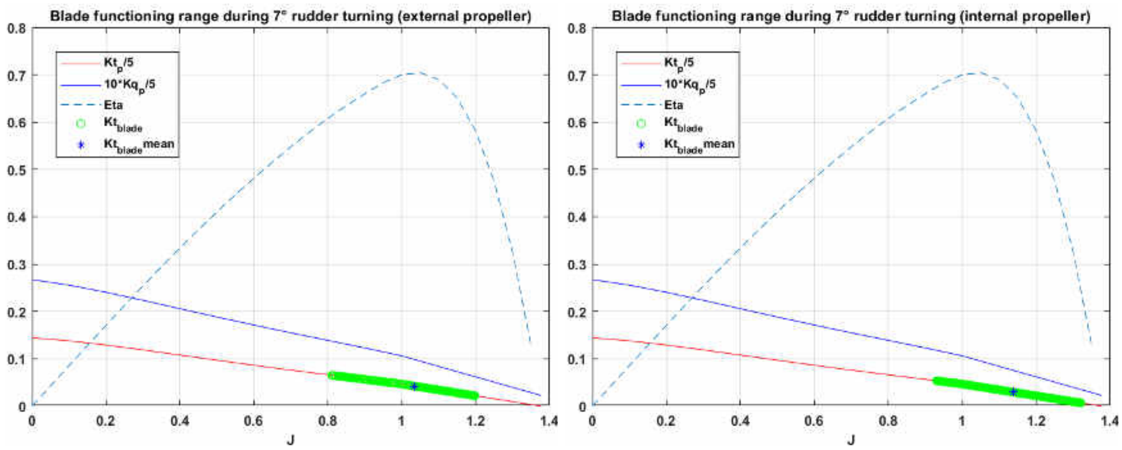

(a) Rudder angle $\delta = 7°$

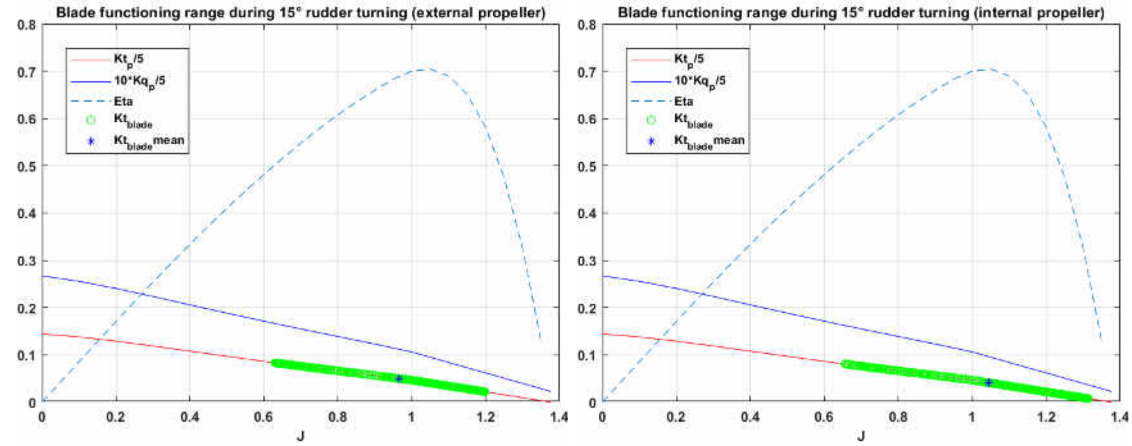

(b) Rudder angle $\delta = 15°$

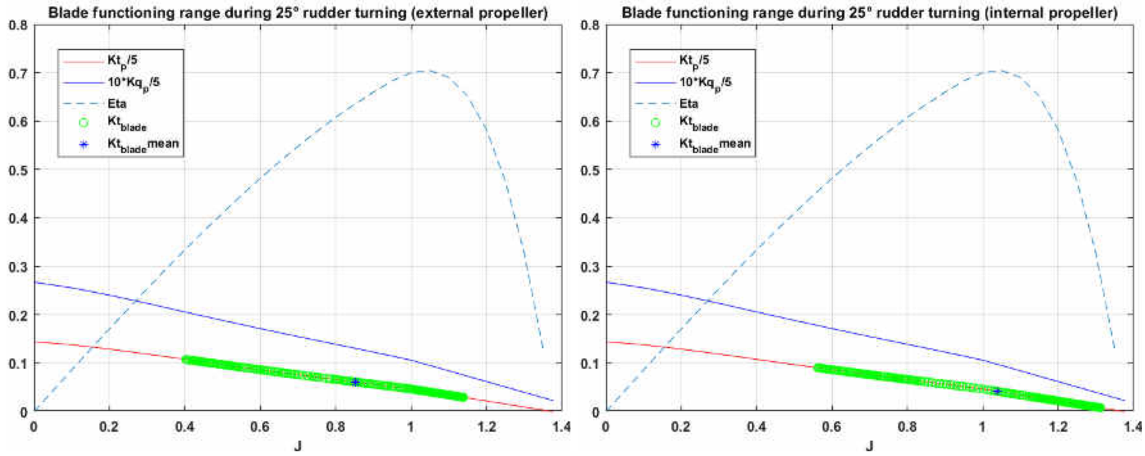

(c) Rudder angle $\delta = 25°$

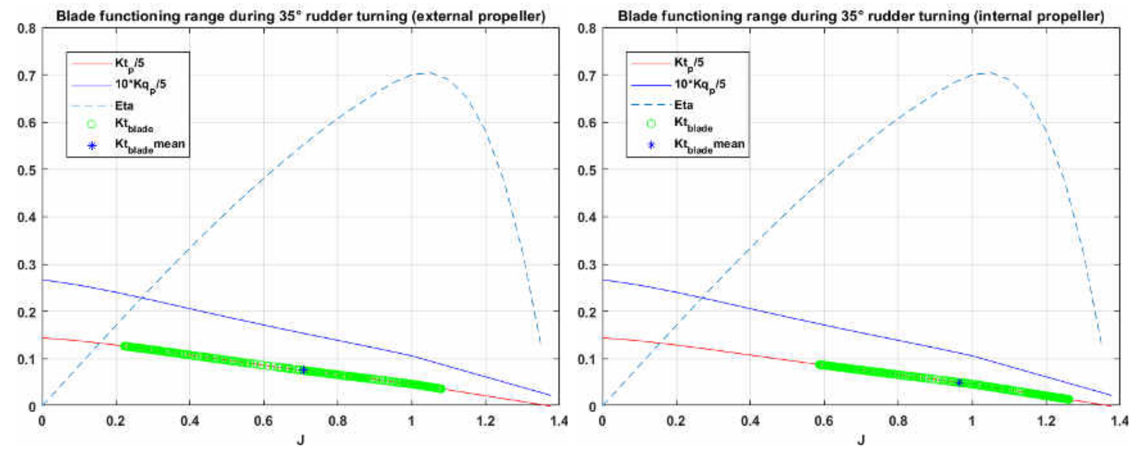

(d) Rudder angle $\delta = 35°$

Figure 5.9 Blade K_{Tx} on top of propeller OW curves (divided by 5)

During the maneuver, the fluctuation of K_{Tx} is larger than straight ahead navigation and the asymmetric behaviour of the two propellers, related to the evolution of the wake past the hull, is clearly evidenced. The range of the equivalent advance coefficient of the external propeller grows with the severity of the maneuver and its mean value point is reduced by almost 35%. On the internal propeller, starting from 15°, the range of J is comparable for all manoeuvres and the associated mean value is always close to $J = 1$, with a maximum reduction at 35° of 13%.

A complementary insight on the effects of ship maneuvering on the fluctuating character of the blade loads is provided with the Fourier harmonic decomposition. The spectra of the blade thrust, side force and spindle moment are reported in Appendix B.2.2 for the three speeds investigated; the frequency range is represented in terms of multiples of the blade passing frequency (BPF). The absence of relevant humps up to the 30^{th} BPF stresses that the measurements are not affected by resonance phenomena of the mechanical system, according to previous studies (Jessup et al. (1977)). In general, the spectrum of the loads is qualitatively similar for all speeds: it is characterized by tonal harmonics in the low frequency range, that is consistent with the non cavitating regime of the propeller at model scale. The harmonic associated to the 1^{st} BPF is the dominant one and the decay to the higher component is fast and depends on the rudder angle; moreover, consistently with the character of the signal, the trend of the harmonics is markedly affected by the propeller position relative to the manoeuvre. These characteristics are supported referring to figure 5.10, that synthesize the variation of the 1^{st} and 2^{nd} BPF harmonics with rudder angle for the speeds investigated; tables B.13–B.15 list the harmonic associated to the 1^{st} and 2^{nd} BPF. On the windward side, the decay of the 2^{nd} harmonic is almost constant and it is smaller than the straight ahead motion. On the leeward side, the decay is non linear, namely it increases at $\delta = 7.5°$ and diminishes to similar ratio of the windward side. The amplitude at the 1^{st} BPF is weakly influenced by speed; on the contrary, differences are more evident for the propeller on the leeward side for the component associated to the 2^{nd} BPF, in particular at F_N=0.40. It is worth of noticing that the fluctuating component of the loads on the leeward side is comparable, or greater (in case of the side force), with respect to the windward side, as a consequence of the interaction of the blade with a vortex dominated wake. This aspect can be further highlighted by the higher ratio of the 1^{st} BPF component with respect to the mean value of the blade thrust and side force (compare values in tables A.4–A.6 and B.13–B.15): on the windward side, the harmonic corresponds to about 50% of the loads and in all cases is similar to the straight ahead case; on the opposite side, the harmonic is globally higher than 70% and exceeds 90% and 100% the mean value in case of the thrust and side force, respectively.

Finally, the percentage error of the harmonics of the loads is about 10% for σ_1 and 2% for σ_2, confirming the validity and repeatability of the measurements.

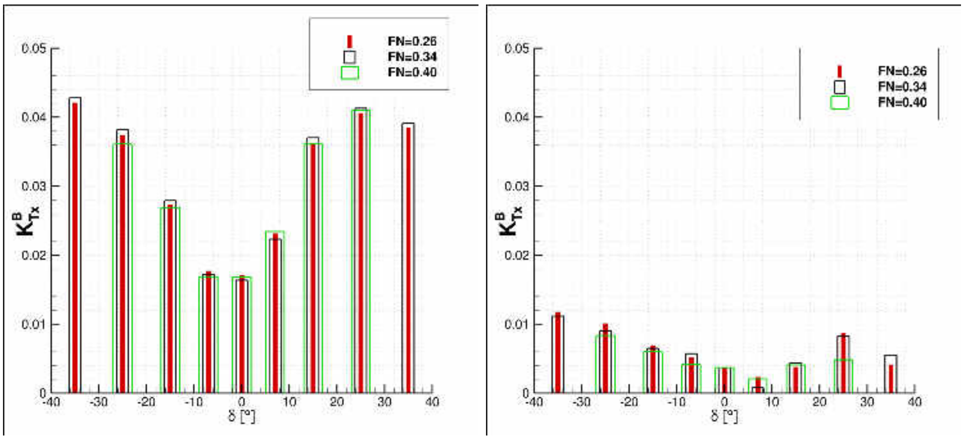

(a) K^B_{Tx}

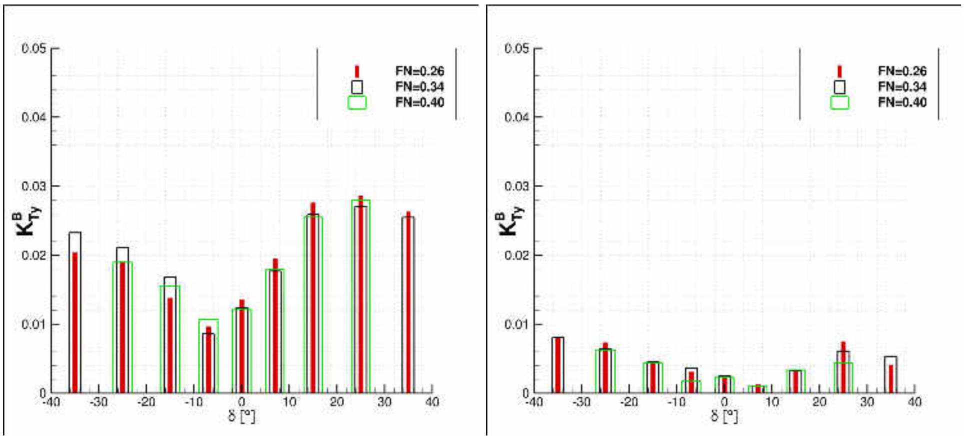

(b) K^B_{Ty}

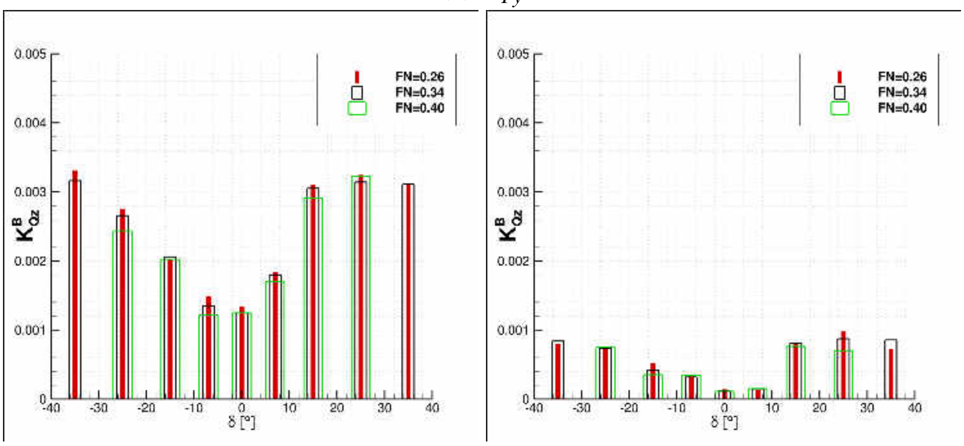

(c) K^B_{Qz}

Figure 5.10 Harmonic analysis (rotating frame); 1^{st} BPF (left) and 2^{nd} BPF (right)

5.2 Propeller loads

5.2.1 Straight ahead navigation

The propeller loads are computed from the measured single blade loads converted in the hub frame of reference by means of the procedure described in section 4.1. Thrust and torque measured by means of the shaft dynamometer are compared to the same variables obtained by single load measurements in figure 5.11, in order to demonstrate the validity of equation 4.12 and the reliability of blade measurements. Mean values are summarized in table 5.2. In general the average error in the range of investigated speeds is lower than 5% for both thrust and torque.

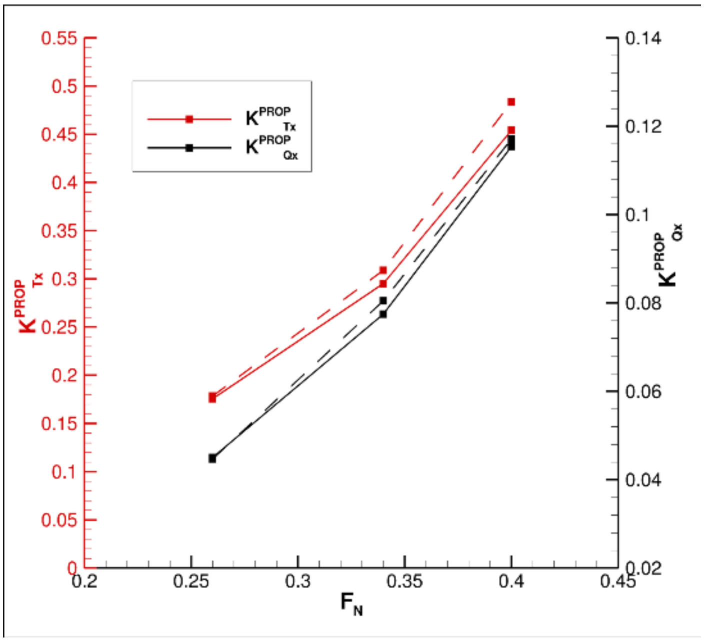

Figure 5.11 Comparison of propeller thrust and torque measured by shaft dynamometer (dashed) and reconstructed from blade transducer (solid)

The average values of in–plane loads exerted by the single blade in the H–frame are listed in table 5.3 and their variation during a complete propeller revolution is visualized in figure 5.12. In the smaller frame, the bars represent the resultant of the load computed in the different sectors of the disk. It is evident that the signals show evident imbalance in the various quadrants of the disk and the trend of the loads is similar for the range of speed investigated, consistently with previous analysis in the B-frame.

LOAD	F_N		
	0.26	0.34	0.40
K_{Tx}^{PROP}	1.77E-01	1.67E-01	1.80E-01
K_{Ty}^{PROP}	-6.20E-03	1.46E-03	5.98E-03
K_{Tz}^{PROP}	3.61E-02	3.39E-02	2.82E-02
K_{Qx}^{PROP}	4.54E-02	4.38E-02	4.56E-02
K_{Qy}^{PROP}	-7.97E-03	-7.09E-03	-1.06E-02
K_{Qz}^{PROP}	-1.30E-02	-1.26E-02	-1.08E-02

Table 5.2 Propeller loads

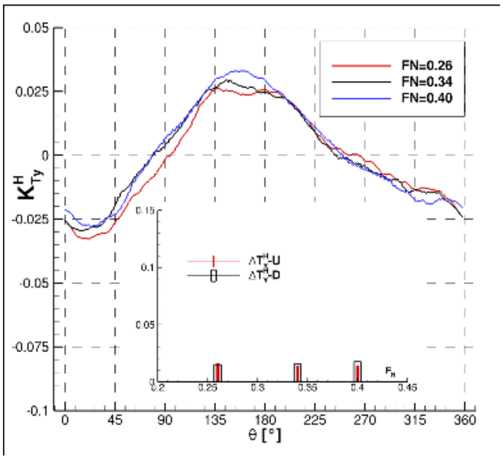

(a) Side force

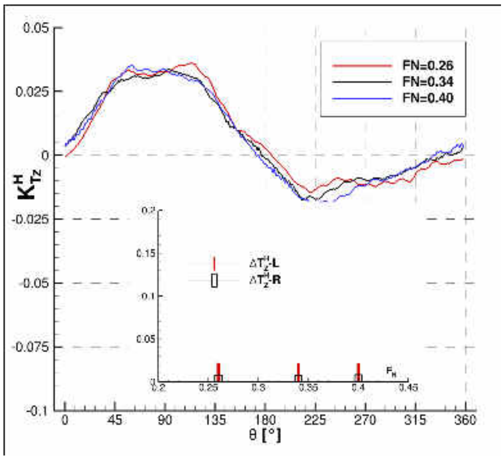

(b) Vertical force

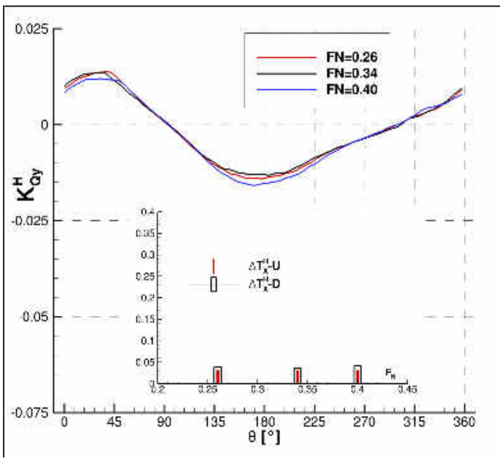

(c) Pitch moment

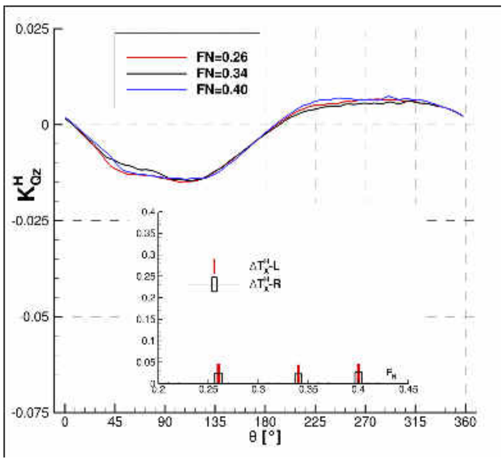

(d) Yaw moment

Figure 5.12 Single blade loads converted in the hub frame

LOAD	F_N					
	0.26		0.34		0.40	
	$\bar{x}_1$	$\bar{x}_2$	$\bar{x}_1$	$\bar{x}_2$	$\bar{x}_1$	$\bar{x}_2$
K^H_{Ty}	-1.23E-03	1.23E-03	2.93E-04	2.82E-04	1.19E-03	1.06E-03
K^H_{Tz}	7.20E-03	7.22E-03	6.80E-03	6.87E-03	5.66E-03	6.28E-03
K^H_{Qy}	-1.59E-03	-1.60E-03	-1.42E-03	-1.42E-03	-2.12E-03	-2.12E-03
K^H_{Qz}	-2.58E-03	-2.60E-03	-2.54E-03	-2.54E-03	-2.15E-03	-2.17E-03

Table 5.3 In–plane loads for the single blade (hub frame)

In particular, the propeller develops a non–negligible vertical force K_{Tz}^{PROP} (that amounts to about 20% of the thrust) and a smaller side force K_{Ty}^{PROP}. The magnitude of the vertical and lateral force are comparable to that monitored for a similar model (Ortolani et al. (2015a)), supporting also the qualitative similarity of its nominal wake for discussing the blade loads in the previous section. The side force is speed dependent, its orientation being outwards at the smallest F_N and inwards for the other cases (K_{Ty}^{H-U} gradually overcomes the K_{Ty}^{H-D}, see figure 5.12a). This sensitivity can be explained with differences of the wake, also caused by wet–dry transition of the transom; however, its magnitude is negligible with respect to other loads. The difference between the upper and lower halves is minimal, consistent with the small value of the resultant load. On the contrary, the distribution of the vertical force is markedly asymmetric between the left and right halves of the disk, the magnitude of K_{Tz}^{H-L} being more than doubled with respect to K_{Tz}^{H-R}, see figure 5.12b. In this case, the leading difference is associated to the relevant, upwards oriented, tangential velocity that acts to increase the incidence of the blade on the left and vice versa (the velocity is concordant with blade motion) on the opposite half (see figure 5.2).

Both the in–plane moments are non–negligible, K_{Qy}^{PROP} and K_{Qz}^{PROP} being of the order of 15% and 25% of K_{Qx}^{PROP}, see table 5.2. The pitch moment is negative, i.e., it acts to lower the propeller, the blades being more loaded in the lower half of the disk, see figure 5.12c. For the same reason, the yaw moment is negative, namely it acts to turn the propeller inward, the blade being more loaded in the inner half due to the disturbance of the hull and the higher tangential velocity with respect to the sections (in particular in the 2^{nd} quadrant). In this case, the difference of magnitude of the resultant values of K_{Tx}^{H-L} and K_{Tx}^{H-R} is considerably greater compared with $K_{Tx}^{H-U,D}$, consistently with the total values reported in table 5.2.

The results of the harmonic analysis of the blade loads in the H-frame is synthesized in figure 5.13 and in tables B.10–B.12 that report the harmonics associated to the leading five multiples of the BPF. Thrust and torque are not visualized in the figure and tables, because they are coincident for the two frames. In this case, the amplitudes are reported in terms of ratio with respect to the mean value of K_{Tx}^{H} and K_{Qx}^{H} generated by the blade.

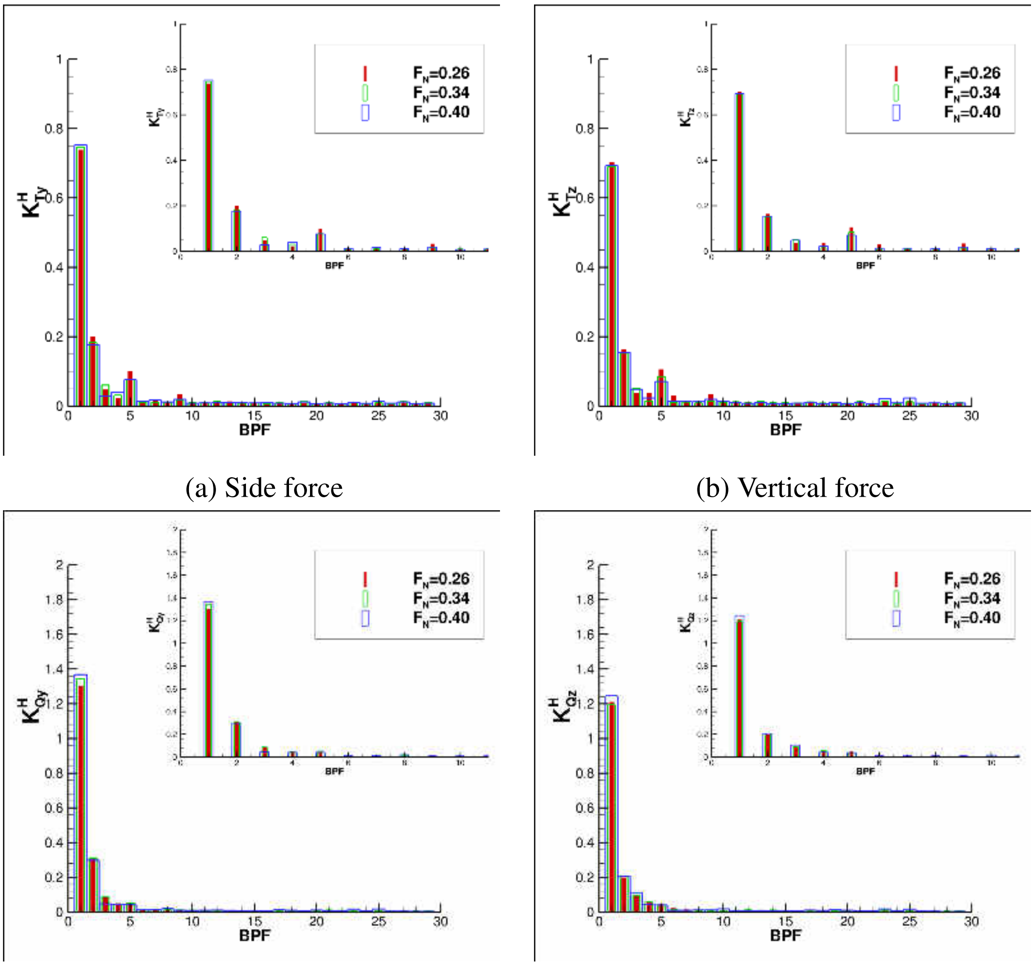

(a) Side force

(b) Vertical force

(c) Pitch moment

(d) Yaw moment

Figure 5.13 Harmonic content (amplitudes) of the single blade hydrodynamic loads (hub frame)

The analysis in the H–frame is fundamental in order to better emphasize the origin of the vibratory actions transmitted by the propeller to bearings and shaft. The qualitative characteristics of the spectra are analogous to those highlighted in the rotating frame. The largest contribution has to be ascribed to the 1^{st} BPF, and the amplitude amounts to about 70% the value of thrust and 50% higher with respect to the fundamental harmonic of thrust. Furthermore, this contribution for the in–plane moments corresponds to about 120% of the blade torque, thus doubling the torque leading harmonic.

The effect of all blades to obtain the total vibratory actions of the propeller is shown in figure 5.14 for the case at $F_N = 0.26$; the analysis for the other speeds is similar and is not reported for the sake of brevity. Amplitudes are reported in non–dimensional form.

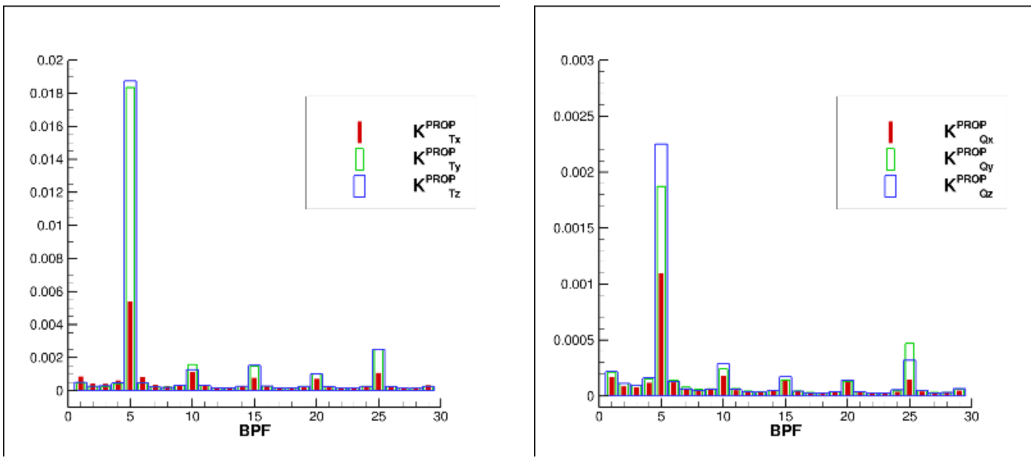

(a) forces (b) moments

Figure 5.14 Harmonic content (amplitudes) of propeller loads, $F_N = 0.26$

Obviously, in this case the fundamental harmonic is related to the 5^{th} BPF (the number of blades is 5). It is interesting to observe that the amplitude of the in–plane forces is 300% higher than thrust for the 1^{st} BPF and always higher for its multiples. Alternatively, the leading harmonics corresponds to 3% and 10% for the thrust and in–plane forces, and 2% and 5% for the torque and in–plane moments, respectively (compare the values in the figures and mean values in table 5.2).

Finally, the eccentricity of propeller thrust e is evaluated in the plane of the disk by:

$$e_y^H = \frac{Q_z^{PROP}}{T_x^{PROP}}; \quad e_z^H = \frac{Q_y^{PROP}}{T_x^{PROP}}; \quad r_e = \sqrt{e_y^{H2} + e_z^{H2}}; \quad \theta_e = tan^{-1}\frac{e_z}{e_y} \tag{5.2}$$

The variation of the eccentricity during a cycle is represented in figure 5.15 and its mean location is reported in table 5.4 in terms of polar coordinates r_e and θ_e. Consistently with the character of the in–plane moments, the thrust acts in the 2^{nd} quadrant and the point of application is lower than the radius of the propeller hub. The fluctuation during a complete propeller revolution is well circumscribed in a limited portion; effects of speed are negligible on the position and its fluctuation, although a slight reduction of the phase can be observed at $F_N = 0.40$.

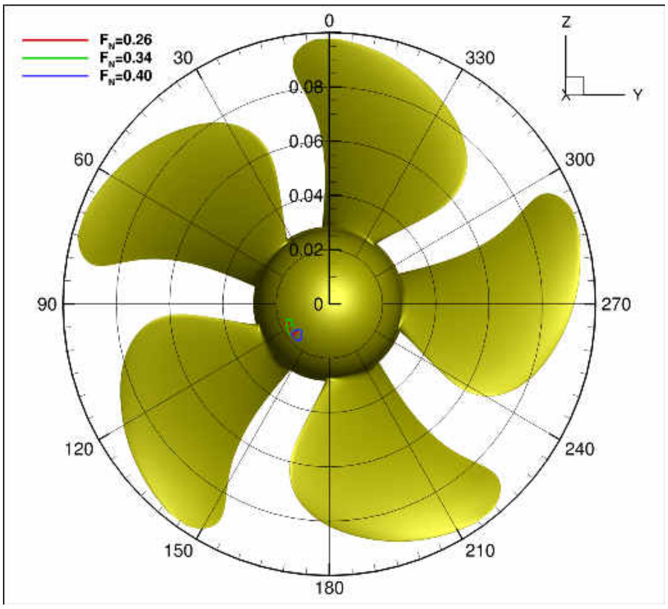

Figure 5.15 Variation of the eccentricity of thrust during a cycle

F_N	r_e	θ_e [deg]
0.26	0.17	121
0.34	0.176	118
0.40	0.168	133

Table 5.4 Thrust eccentricity

5.2.2 Steady turning

The trend of the propeller loads during the stabilized phase of the turning is discussed on the basis of considerations made in Section 5.1.2, about single blade loads and their relation to wake field. Propeller loads are asymmetric for windward and leeward propeller, consistently with the single blade measurements (and with the asymmetric evolution of the hull wake). The forces and moments are represented in figure 5.16 in terms of ratio with the thrust and torque in rectilinear motion, respectively, in order to stress the effects of maneuvering. These ratio loads are equivalent to the single blade loads and therefore, in the following description, the explanation of the trend of the resultant propeller loads is carried out referring to the single blade loads converted in the H–frame. The maneuver causes thrust and torque to increase: on the windward side, K^H_{Tx} increases more that 120% and K^H_{Qx} is higher than 70%, whereas, on the leeward side these values are approximately halved (60% and 35% for thrust and torque, respectively), see figures 5.16a and 5.16b.

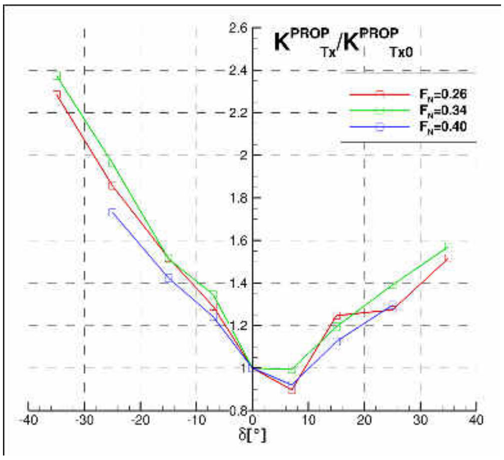

(a) K_{Tx}

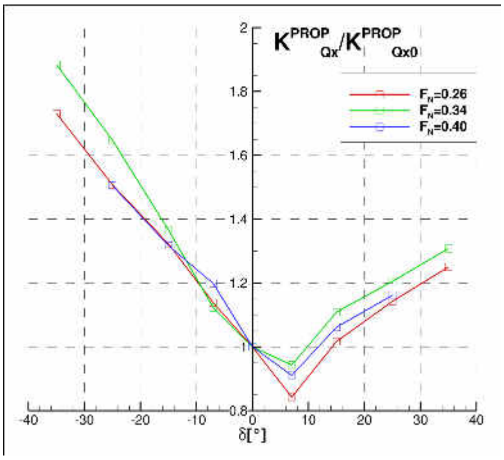

(b) K_{Qx}

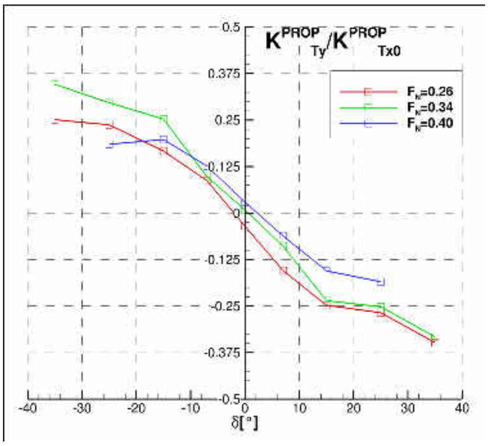

(c) K_{Ty}^{H}

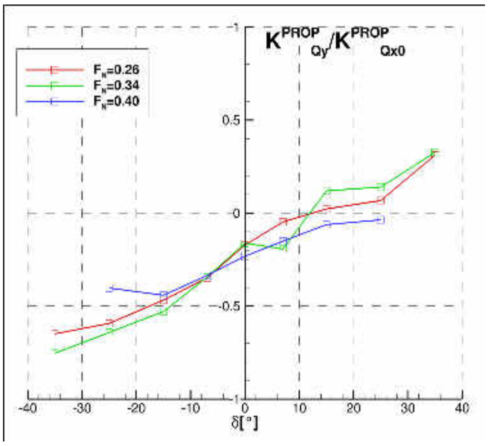

(d) K_{Qy}^{H}

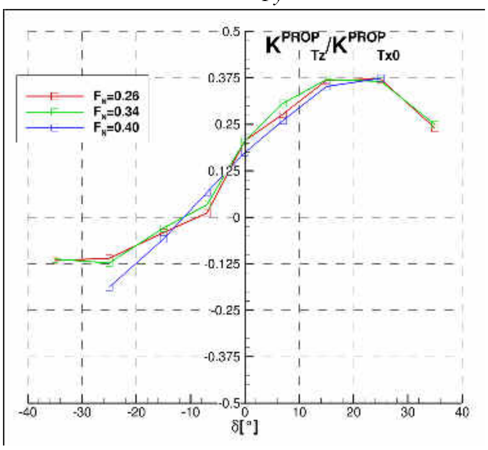

(e) K_{Tz}^{H}

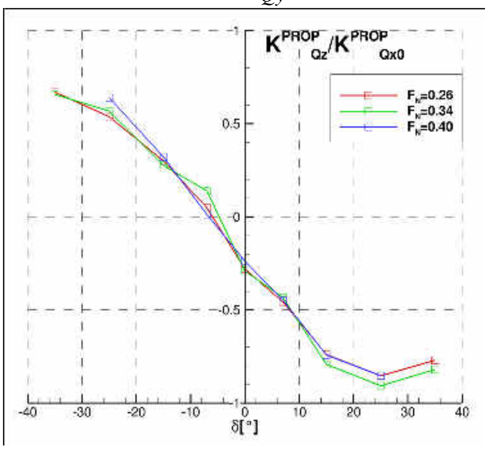

(f) K_{Qz}^{H}

Figure 5.16 Mean single blade loads (hub frame)

More interestingly, considerable in–plane forces and moments are developed by the propellers on both the lee and windward side. With respect to the straight ahead condition, the variation of these components is higher than 200% for the tightest maneuver and the magnitude corresponds to a significant fraction of the thrust and torque generated in straight ahead motion. In detail, the side force K_{Ty}^{H} experiences very similar values and almost linear trend with rudder angle for the windward and leeward propellers; for the tightest maneuver, its magnitude corresponds to about 40% of K_{Tx0}^{H}. In case of both propellers, the side force provides a stabilizing effect to the model, i.e. it creates a couple that counteracts the turning motion.

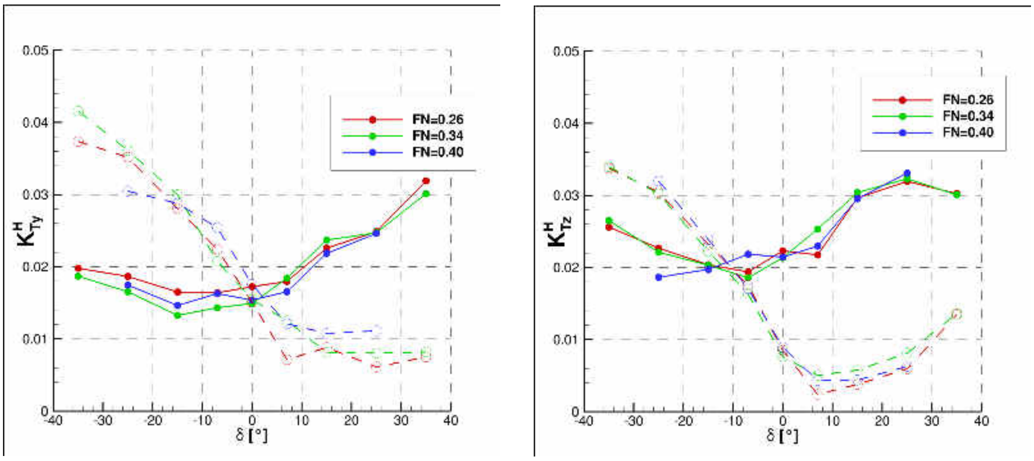

(a) K_{Ty}^{H}; upper half (solid), lower half (dashed) (b) K_{Tz}^{H}; left half (solid), right half (dashed)

Figure 5.17 Integral contribution of single blade in–plane forces on halves of the disk

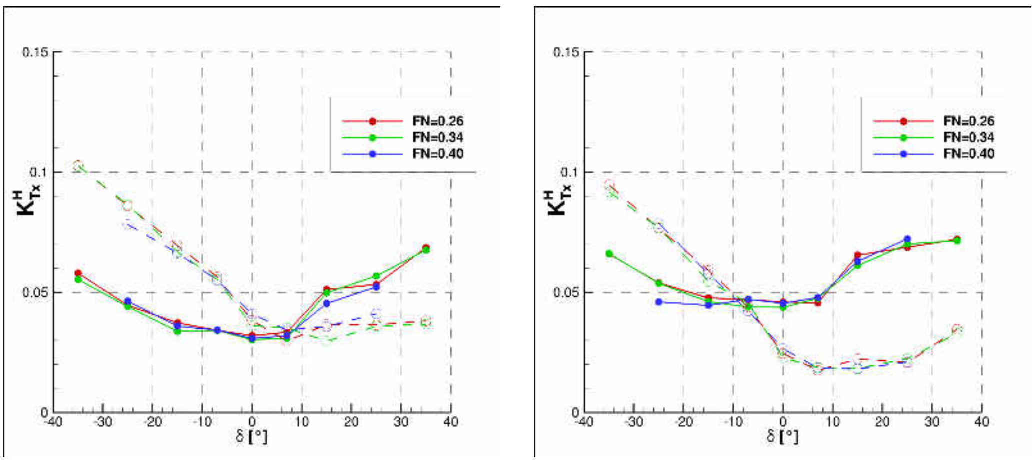

(a) K_{Tx}^{H}; upper half (solid), lower half (dashed) (b) K_{Tx}^{H}; left half (solid), right half (dashed)

Figure 5.18 Integral contribution of blade thrust loads on halves of the disk

The generation and evolution of the side force can be figured out in terms of evolution of the separate contributions in the lower and upper half of the disk, see figure 5.17a. In particular, on the windward side, K_{Ty}^{H} is generated in the lower half of the disk, where both the tangential velocity relative to the blade (induced by the motion) and the reduction of the axial speed (due to the model speed drop) act to increase the loads; on the contrary, in the upper half of the disk the side force is almost constant, because the axial and tangential components incoming to the blade sections cancel out.

On the leeward side, hydrodynamic conditions on both halves of the disk contribute to the generation and increase of the side force. In fact, K_{Ty}^{H-D} diminishes at $\delta = 7.5°$ (the unloading effect provided by the circumferential velocity is dominant with respect the opposite contribution associated to the velocity defect) and then stabilizes about a constant value for the other rudder angles. On the contrary, K_{Ty}^{H-U} grows owing to the stronger blade–wake interactions. On the same basis, it is straightforward to motivate the imbalance of the blade thrust about the y_H axis, that gives onset to the pitching moment K_{Qy}^{H}. According to the load distribution, K_{Qy}^{H} acts to push down and lift the propeller on the windward and leeward side, respectively. It is worth of noticing the close similarity of the trend of K_{Tx}^{H-U} and K_{Tx}^{H-L} with their correspondent components of the side force, see figures 5.17a and 5.18. The trend of K_{Tz}^{H} is completely different for the two propellers. In straight ahead condition, K_{Tz}^{H} is upwards oriented: in fact, see figure 5.17b, K_{Tz}^{H-L} is stronger than K_{Tz}^{H-R} as a consequence of the slower axial velocity and tangential flow relative to the blade that act to increase the blade loading during the descending motion of the blade. During maneuvering condition, on the windward side the vertical force immediately drops for $\delta = 7.5°$ and then stabilizes to negative values with magnitude slightly lower than the straight ahead case (12.5% of K_{Tx0}^{H}). This evolution can be ascribed to the effects of the oblique flow, that cause the blade to experience a stronger tangential flow during the second half of the cycle. On the contrary, the variation of K_{Tz}^{H-L} is weaker, because the tangential flow cancels out the effects of the reduction of the axial speed, associated to the deflection of the wake to the lee side (see figures 4.7b and 4.7c). On the leeward side, the trend of K_{Tz} is non–linear: for $7.5° < \delta < 15°$, it increases to a value that is almost doubled with respect to straight ahead motion and for $\delta > 25°$ it is abruptly reduced to a similar value obtained for the weakest maneuver. This trend has to be ascribed to blade–wake interactions (stronger at lower rudder angles due to coherence of *SV* flow structure passing through the disk). This is confirmed by the K_{Tz}^{H-L}, that is similar to the total counterpart, see figure 5.17b. On the other hand, K_{Tz}^{H-R} drops with respect to the straight ahead case and remains almost constant up to $\delta = 25°$, that can be associated to the unloading of the blade for $180° < \theta < 270°$ due to the cross flow induced by the motion. At $\delta > 25°$, K_{Tz}^{H-R} rises, because the effect of the speed drop (that acts to increase the load) adds up to the loading effect of the circumferential velocity due to MV, so the vertical force drops.

The close relationship of the pitch moment with the side force is also experienced by the yaw moment K_{Qz}^{H}. The trend of this couple, alongside the contribution of K_{Tx}^{H-L} and K_{Tx}^{H-R}, resembles K_{Tz}^{H}, K_{Tz}^{H-L} and K_{Tz}^{H-R}, see figures 5.16f and 5.18b. According to the load distribution, K_{Qz}^{H} acts to bend the propeller outward and inward, with respect to the symmetry plane of the hull, for the windward and leeward side respectively.

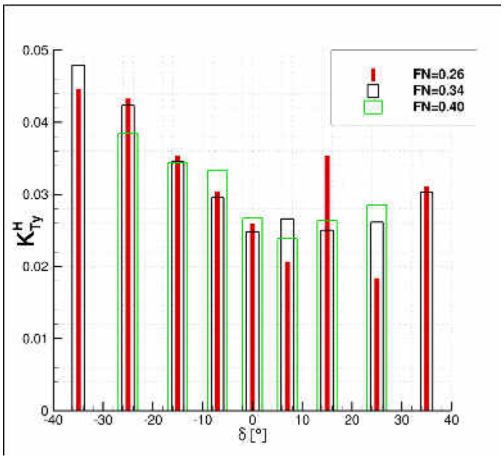

(a) K_{Ty}^{H}

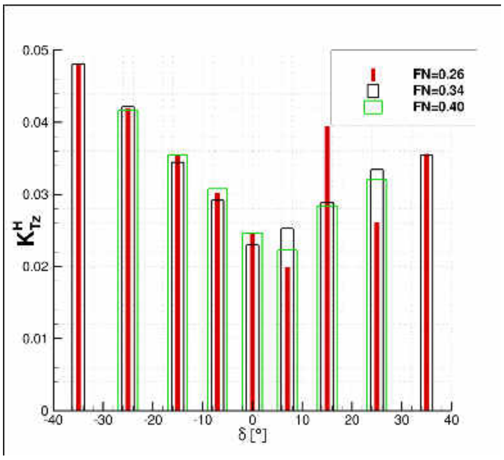

(b) K_{Tz}^{H}

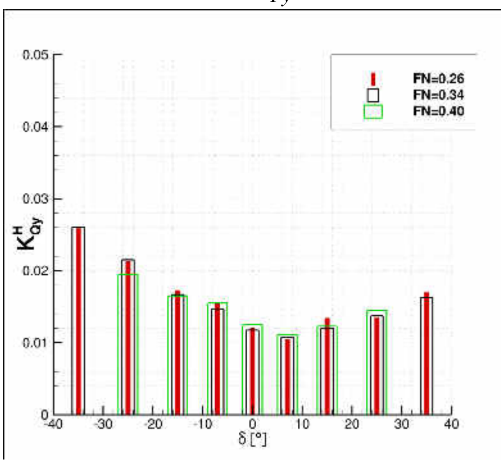

(c) K_{Qy}^{H}

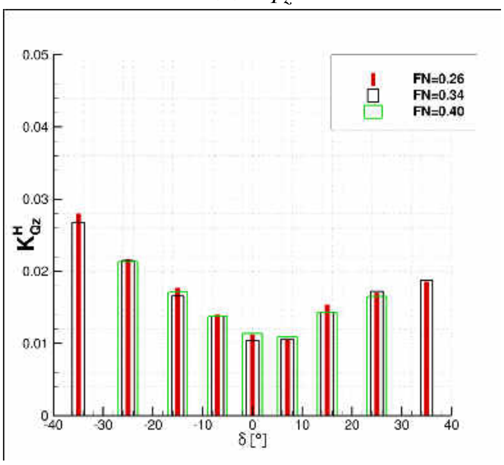

(d) K_{Qz}^{H}

Figure 5.19 Harmonic analysis (hub frame): 1^{st} BPF of single blade in–plane loads

The 1^{st} BPF of the single blade in–plane forces and moments is represented in figure 5.19. This trend is similar for all the loads and different with respect to the one observed in the rotating frame; in fact, the $1^{st}BPF$ increases almost linearly both for the leeward and windward propeller, and with a higher slope for the latter case. On the windward side, the amplitude of the forces and moments increases by about 90% and 120% with respect to the straight ahead condition, respectively. On the leeward side, the increase of the fluctuation of K^H_{Ty} and K^H_{Qy} is smaller with respect to K^H_{Tz} and K^H_{Qz} (20% and 40% for the forces, 30% and 60% for the moments, respectively).

The propeller loads, derived from the single blade ones converted in the hub frame, have the same trends of figure 5.16 when represented as ratios between manoeuvre and straight ahead motion values, for this reason they are not reported. The calculated values in the usual non–dimensional form are summarized in tables A.7–A.9.

Figure 5.20 shows the total component of the radial force and moment; it is interesting to observe that the trend on the internal propeller is non–linear and resembles the trend of the vertical force and yaw moment. The internal propeller experiences a higher K^P_{Tr} that achieves a peak value of about 40% the thrust developed in straight ahead motion; on the contrary, the asymmetry of absolute value is less evident in case of K^P_{Qr}. In this case, it is remarkable the fact that the maximum values is comparable to the torque developed in straight ahead motion and that during turns its value is almost triplicated with respect to the reference sailing condition.

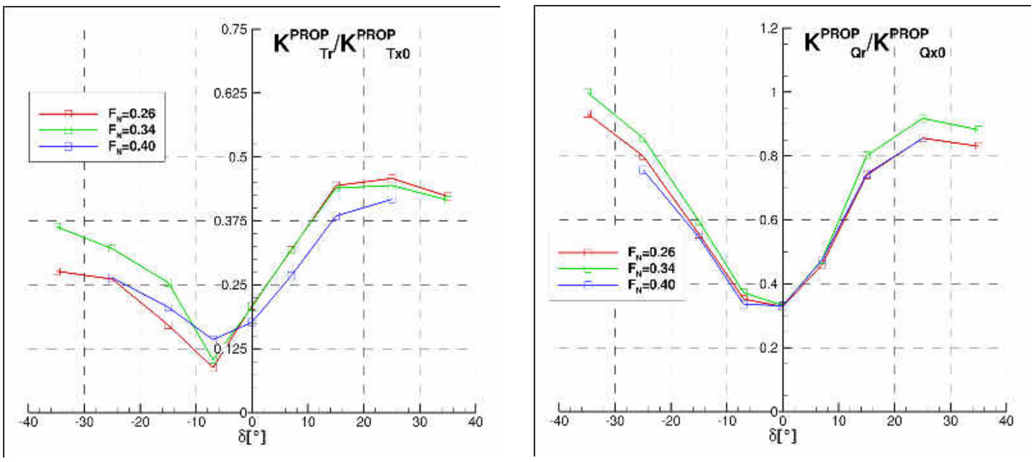

(a) Radial force K^{PROP}_{Tr} (b) Radial moment K^{PROP}_{Qr}

Figure 5.20 Total components of the bearing radial loads

An alternative description of the different behavior of the windward and leeward propellers is provided by the evolution of the thrust eccentricity in figures 5.21, relative to $F_N = 0.26$, and in A.5–A.6, relative to $F_N = 0.34$ and $F_N = 0.40$. Given the measure of the in–plane moments K^{PROP}_{Qy} and K^{PROP}_{Qz}, the eccentricity can be determined by Eq. 5.2.

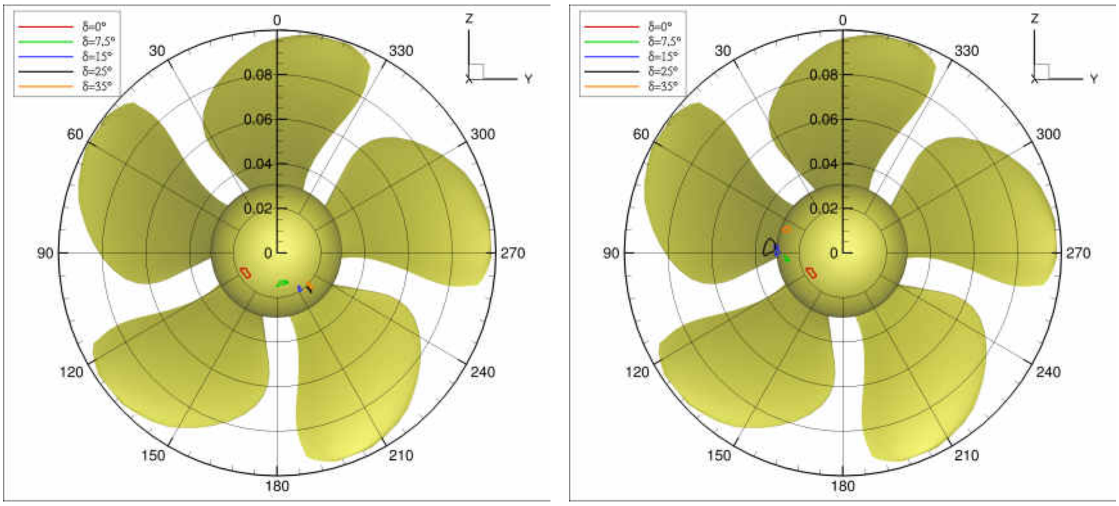

(a) external propeller (b) internal propeller

Figure 5.21 Eccentricity of propeller thrust; $F_N = 0.26$

Consistently with the similar trend of the loads with speed, the variation of the eccentricity is similar for the three F_N. In particular, on the leeward propeller, it shifts to larger radii and upwards, because the overloading of the propeller happens in the 1^{st} quadrant. The eccentricity radius changes in a non–linear fashion, it being reduced for $\delta = 35°$. On the windward side, the eccentricity moves in the lower half of the disk maintaining the same vertical distance from the y_H axis, consistently with the fact that the overloading is experienced in the 3^{rd} quadrant.

Chapter 6

Captive tests results

In this chapter, the systematic investigation of the behavior of the propeller in off–design conditions, by means of pure drift test in the $CNR-INM$ towing tank, is reported. In the experiments, drift angle was changed up to 30°and towing speeds was reduced up to 70% of the reference speed correspondent to Froude number $F_N = 0.26$. These values were set in order to obtain nominal kinematic conditions representative of the free running model tests at the same reference speed. This kind of investigation is not a standard in ship model testing and, according to the author's knowledge, few similar experiment was attempted in the past, but never providing the present completeness and detail of data. As already done for free running tests, the analysis is centred on the single blade loads and the reconstructed in-plane loads, whit a particular focus on the cause–effect relation with respect to the nominal wake features strengthened by preliminary CFD simulation (see Paragraph 4.2). The loads obtained in towing tests are further compared to the free running results for the most similar kinematic conditions in terms of both mean and cyclic load. This assessment is useful to prove the reliability of pure oblique test to accurately reproduce off–design behavior of the propellers in order to identify possible critical conditions, at least for similar twin screw configurations, with respect to free running self propelled model tests. This is the most realistic approach to simulate accurately ship operating conditions, although this kind of test requires specific indoor (oceanic tank) or outdoor (lakes with low disturbances) facilities that are not commonly affordable. On the other hand, the data obtained with this experiment are attractive for numerical validation, given the absence of undesired environmental disturbance that inevitably affect the free running experiment in an outdoor basin.

6.1 Comparison between free running and captive tests approaches

The comparison of the loads in pure drift towing with the stabilized phase of the turning circle obtained during free running test should be ideally compared at equal inflow conditions at the propellers. The terms that identify the operating condition of the propeller are the advance coefficient J (or the speed drop, since propeller rate of revolution is set equal to the free running tests) and the nominal drift angle in correspondence to the propeller plane. In case of a free running maneuver, the drift angle β_P in correspondence to the propeller plane must account for the contribution of the yaw speed of the model ($\dot{\psi}$), see figure 6.1:

$$\beta_P = tan^{-1}\frac{v_H + \dot{\psi}\cdot x_P}{u_H} \tag{6.1}$$

where u_H and v_H are the longitudinal and lateral components of the speed of the hull, and x_P is the longitudinal position of the propeller with respect to pivot point.

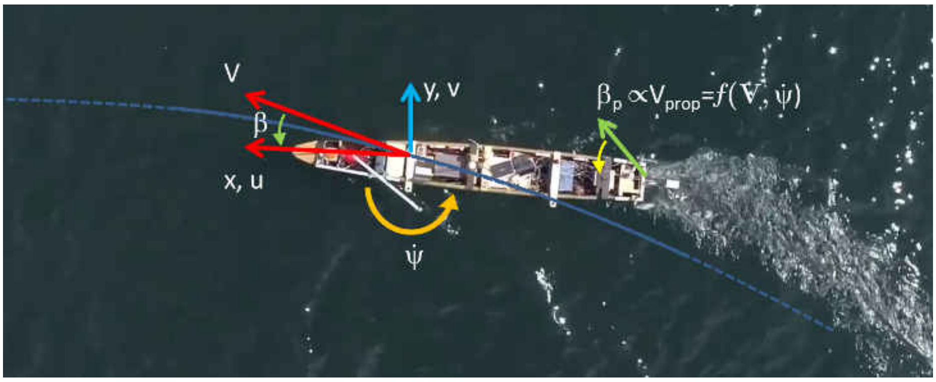

Figure 6.1 Propeller drift angle during turns

The reduction of speed adopted in the captive model tests is in the range monitored for this model in the stabilized phase of the turn from moderate to high rudder angles.

The equivalence of the drift angle in correspondence to the two maneuvers satisfies the geometric kinematic condition at the propeller but obviously does not guarantee the identical inflow. In fact the pure oblique towing implies a constant drift angle along the hull, differently from the free running where the motion is also due to yaw (see Figure 6.2) and, hence, discrepancies can be expected for the wake evolving past the hull. In fact, see Figure 6.2a, the coupled sway–yaw motion during the free running maneuver causes the longitudinal sections of the hull to experience a linear variation of the drift angle and the drift angle to switch from negative to positive values. On the other hand, during oblique towing (Figure

6.2b) the longitudinal distribution of the drift angle is constant. The higher experienced speed along the whole hull can anticipate the development of separation effects or the occurrence and characteristics of vortex structures detaching from appendages, causing hydrodynamic interactions to be stronger during downstream convection, as well as a different location with respect to the propeller disk. Obviously, a further source of discrepancies of the inflow to the propeller, and hence loads, is caused by the absence of roll motion and rudders during the towing tests.

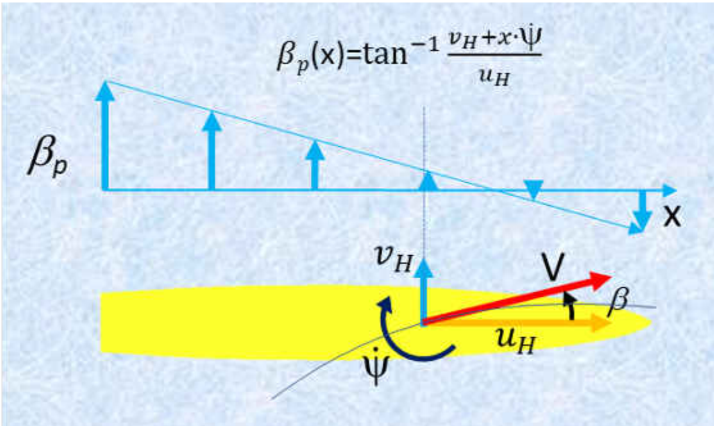

(a) Drift angle distributions in free running tests

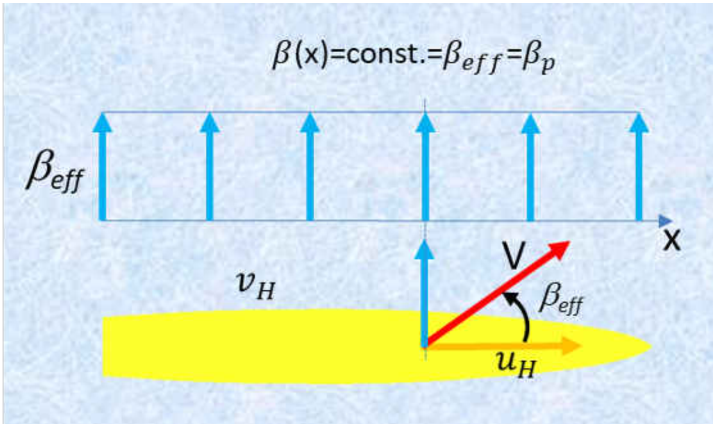

(b) Drift angle distributions in captive tests

Figure 6.2 Definition of the equivalent drift angle

6.2 Single blade loads: the effect of drift angle

The mean single blade loads and the percentage error are summarized in tables A.10–A.12. The error of the measures is in general less than 10% and is comparable to the free running results. In case of the spindle torque, the percentage error is very high given the very small magnitude of the mean.

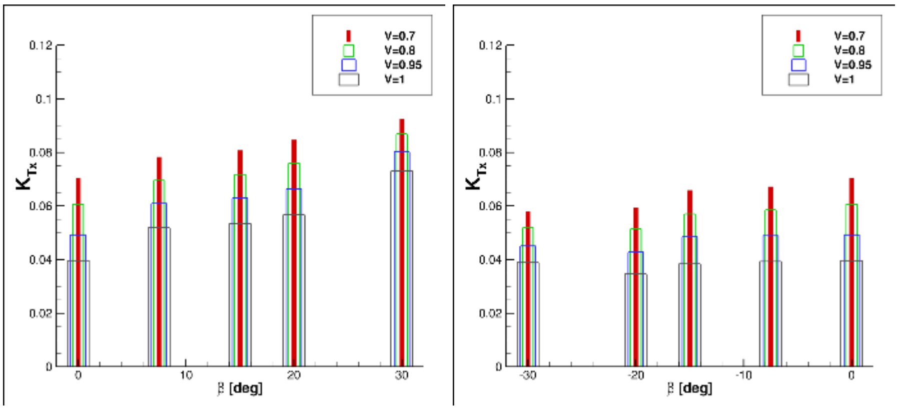

(a) K_{Tx}

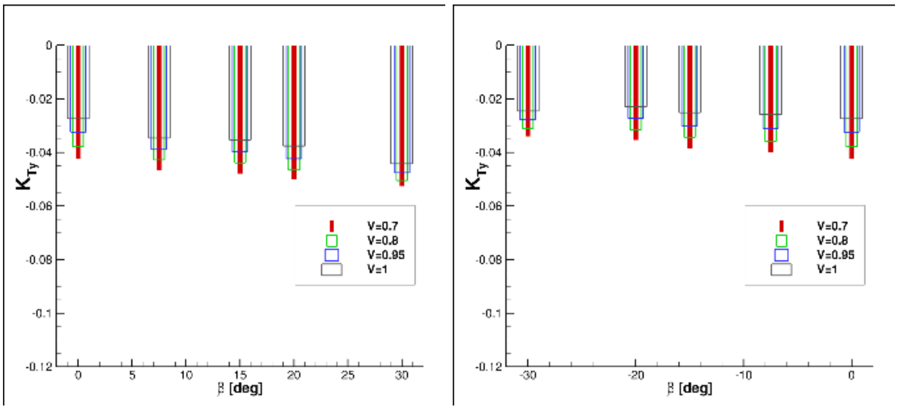

(b) K_{Ty}

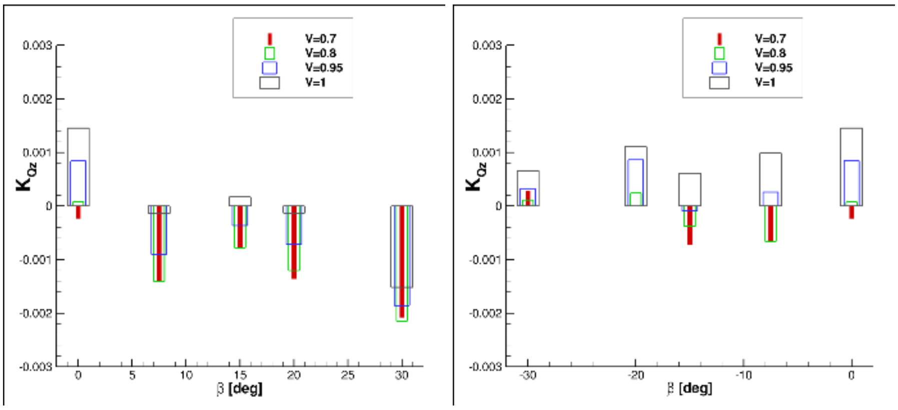

(c) K_{Qz}

Figure 6.3 Mean single blade loads. Left: external propeller; right: internal propeller

The present analysis is focused on the tests performed at the nominal towing speed $F_N = 0.26$ (i.e., $V = 1$) for both the mean and cyclic blade loads showed in figure 6.3 (grey bars) and figure 6.4. Qualitatively, the trends of blade thrust and side force are similar, given their direct proportionality with the angle of incidence, see Eq. 4.17; therefore, considerations for thrust apply to both components. In general, $\overline{K_{Tx}}$ ($\overline{K_{Ty}}$) on the windward side increases monotonically up to 90% (70%) at $\beta = 30°$ with respect to the nominal value in rectilinear motion. This behavior is attributable to the fact that the inflow to the propeller is similar to a pure oblique flow and, hence, its incidence is approximately equal to the drift of the hull. Details are provided studying the load variation during the period reported on the left of figure 6.4a and its relation with the wake sketched in figure 4.7. In straight ahead motion, K_{Tx} substantially trace the trend of free running tests, being characterized by two peaks in the 1^{st} and 2^{nd} quadrants (see red colored line) and a minimum around 300°, so the same considerations can be made. In drift motion, on the windward side, the signal is qualitatively similar for all drift angles; the blade develops the higher load in the lower half of the disk, because the cross flow is opposite to blade rotation. In the upper half of the disk, the cross flow plays the opposite effect and the blade loading reduces. However, in the 1^{st} quadrant a smaller fluctuation (approximately at $\theta = 80°$) is visible, that is caused by the axial velocity defect caused by flow separation past the shaft, see figure 4.7b. It is interesting to observe that the magnitude of the peaks at $\theta = 200°$ are more than doubled with respect to the average one for β higher than 15° and almost triplicated with respect to the mean value in straight ahead sailing. With reference to figure 6.3a(b), on the leeward side the trend of K_{Tx} (K_{Ty}) is almost constant, with the exception of a weak drop at $\beta = 20°$. As a matter of fact, this is due to the fact that during the cycle load increase and decrease are balanced each other. A better insight is provided by the periodic signals reported on the right of figure 6.4. In drift motion, the thrust varies with a similar trend for drift angle up to $\beta = 20°$. In particular, the signal is characterized by a single peak in the 1^{st} quadrant that gradually increases up to 30% of the maximum value in straight ahead. This is caused by the interaction of the blade with coherent structures (i.e. SV) detached from the appendages and bilges that increase the tangential velocity relative to the blade. Then, the load abruptly drops approximately in the 2^{nd} quadrant, because the cross flow induced by the drift motion is concordant with the blade rotation and the tangential velocity relative to the foil, the incidence angle and loads are reduced consequently. During the upstroke motion of the blade, the load starts again to increase as a consequence of the reduction of the axial speed caused by flow separation past the shaft, bracket and deflected wake of the hull. At the highest drift angle, the flow is massively separated, see figure 4.7c. In the 1^{st} quadrant the increase of the load is associated to both velocity defect past the bracket and hull and the cross flow. In the second half of the period, the almost constant trend of the load in the 3^{rd} quadrant is related to the concurrent contribution of axial and tangential speed. On one side, the axial velocity is reduced by the wake of the hull and in particular, the flow separated from the shaft, on the other side, the cross flow induces a tangential flow that is concordant to blade rotation and acts to reduce the load. Finally, in the 4^{th} the load again increases as a consequence of the combined effect of tangential velocity (downwards oriented) induced by the big vortical structure shed past the hull (i.e MV) and the axial velocity defect.

The spindle torque, in the case of a skewed blade, as discussed in Par. 5.1.1, demands a dedicated analysis because it is strictly related to the span–wise variation of the hydrodynamic centre and propeller loading. At $V = 1$, in terms of averaged values (figure 6.3c), on the leeward propeller this couple is always positive, i.e.: it acts to reduce the pitch of the blade, gradually diminishing by half its value at $\beta = 30°$, except for a small increase at $\beta = 20°$. On the windward side, its behavior is completely different: $\overline{K_{Qz}}$ is very small (neutral) for intermediate angle and then drops abruptly to a negative value having the same magnitude of $\beta = 0°$. These different trends are better explained by means of the periodic evolution reported in figure 6.4c. In general, it can be observed that the overall trend of K_{Qz} follows the behaviour of K_{Tx} and K_{Ty}, but the sign is markedly dependent on blade loading. The spindle torque values are positive for light loads, as in case of $\beta = 0°$, while they change sign and reach the highest absolute values under heavy conditions. For example, referring to the evolution of blade thrust on the windward side (left panel in figure 6.4a) for non zero drift angle, the blade loading (both K_{Tx} and K_{Ty} in absolute value) increases during the descending motion of the blade (i.e. in the 1^{st} half of the period) and diminishes after $\beta = 220°$ as a consequence of the concordant orientation of the cross flow with blade rotation. Evidently, the evolution of the spindle torque is concordant with this evolution in terms of development and plot similarity: K_{Qz}, starting from positive values, diminishes to negative during the most critical conditions. The trends reported in figure 6.4c are influenced by this behaviour in terms of unbalances between higher and lighter load occurrences, which determine the mean value during the entire period of revolution. The smaller variation of the couple on the lee side is explained with the fact that gains in the upper half of the disk (caused by wake–blade interaction mechanisms) are canceled during the blade passage in the lower half of the disk. On the contrary, on the windward side the blade loading is completely imbalanced, the increase of load in the lower half of the disk due to cross flow being higher with respect to the upper half where axial and tangential velocity provide opposite contribution.

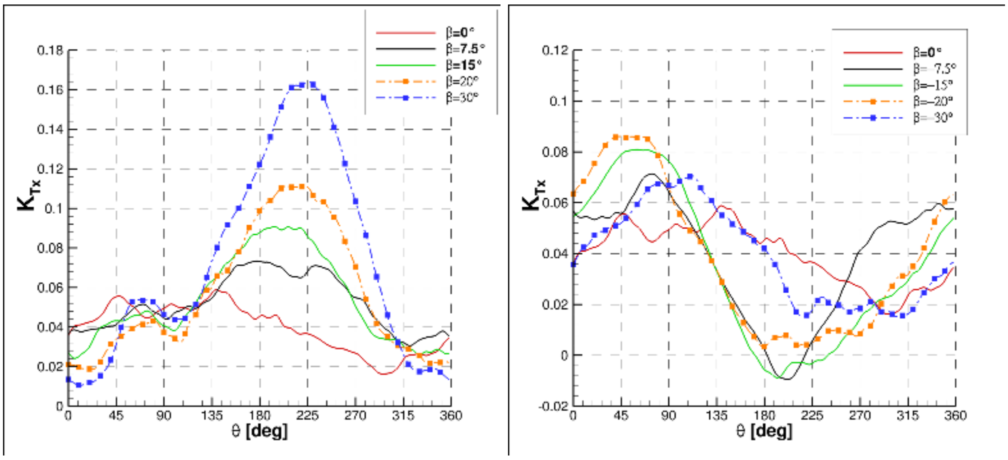

(a) K_{Tx}

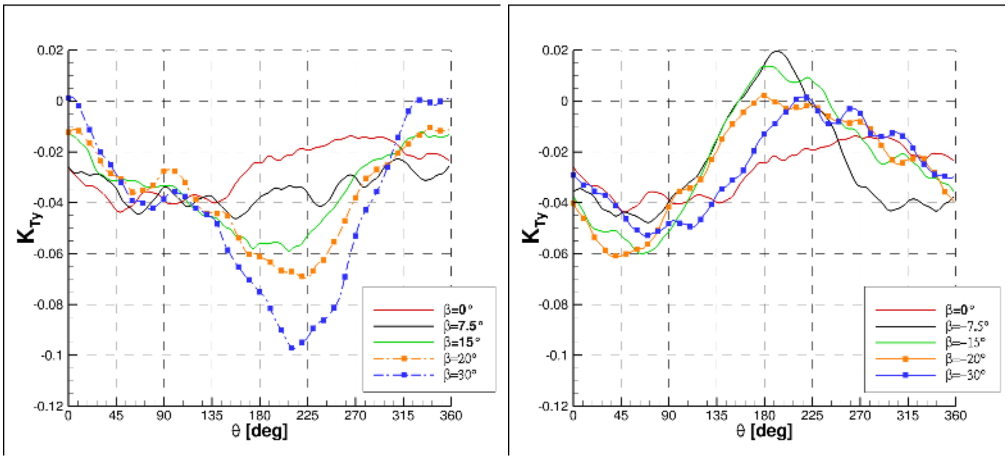

(b) K_{Ty}

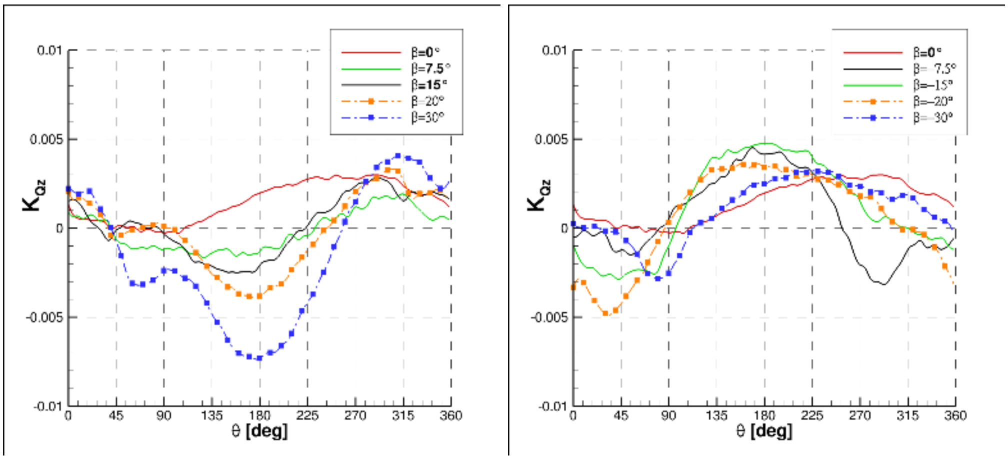

(c) K_{Qz}

Figure 6.4 Single blade loads at $V = 1.00$. Left: external propeller; right: internal propeller

6.3 Single blade loads: the effect of propeller loading

The effect of propeller loading is shown in figure 6.3 at lower towing speeds that are representative of speed drop recorded during free running turning circle maneuvers performed at different rudder angles. The reduction of the towing speed causes $\overline{K_{Tx}}$ and $\overline{K_{Ty}}$ to increase, principally because the reduction of the axial speed to the propeller causes the incidence angle to raise. In general, the maximum increase of the load is progressively reduced with the increase of the drift angle.

The thrust and side force (and related moments) on the windward side always increase with the drift angle at fixed speed. Conversely, on the leeward side, the forces diminish with β differently from the previously discussed case at $V = 1.0$. These aspects can be related to the progressive alteration of the incoming flow (nominal wake) by the self–induced velocity field, that is stronger with the increase of propeller loading. In more details, this mechanism is driven by the memory effect associated to the temporal variation of the circulation shed in the wake of the propeller. This leads to a temporal delay on the establishment of the effective angle of attack and, hence, the loads, that is stronger the more spatially variable is the incoming flow. As a result of these effects, the fluctuations of the load can be weakened (Blaurock (1975); Misztal (1933)) as in the present case for the internal propeller, whose inflow is affected by stronger velocity gradients due to the wake detached from the hull.

The increase of propeller loading in general causes the reduction of the mean value of the spindle torque at fixed drift angle. The total variation of $\overline{K_{Qz}}$ drops with β both on the leeward and windward side, although the trend at intermediate propeller loading is not well defined as observed for the forces, probably because of the strict relation with the geometric characteristics of the blade. The reduction of the spindle torque is consistent with the explanation of the periodic variation of this couple during the cycle, i.e. the hydrodynamic centre moves towards inner blade radii with the increase of angle of attack and, hence, blade loading. The periodic variation of the loads reported for the thrust and spindle moment in figures 6.5 and 6.6 provide further insight on the aspects observed for the mean values. In particular, it can be easily evidenced that the global fluctuation of the load is weakened with speed reduction.

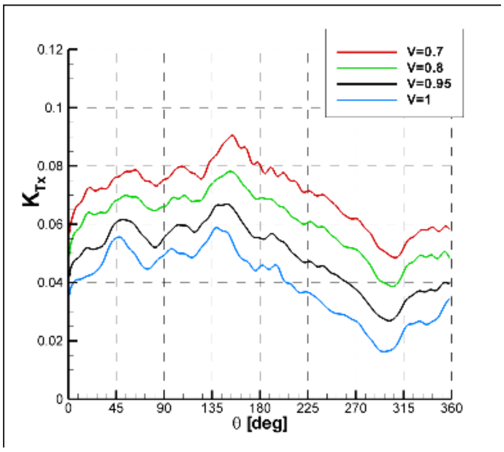

(a) $\beta = 0^{\circ}$

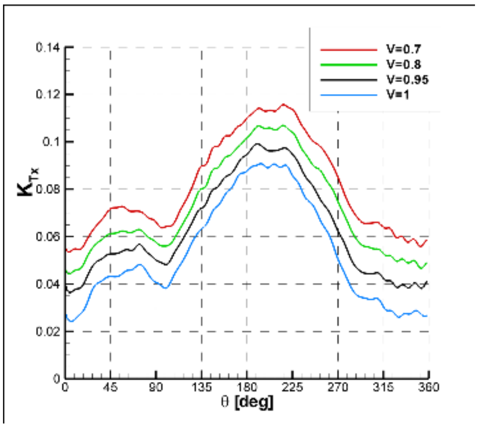

(b) $\beta = 15^{\circ}$

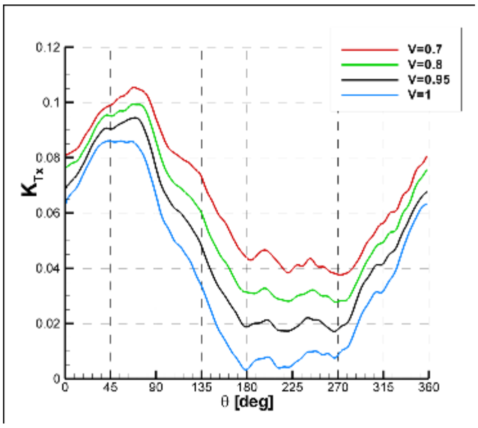

(c) $\beta = -15^{\circ}$

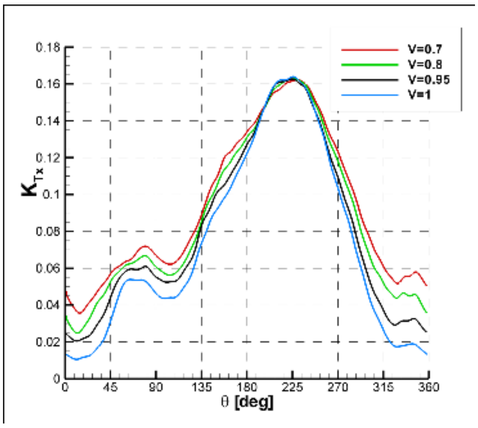

(d) $\beta = 30^{\circ}$

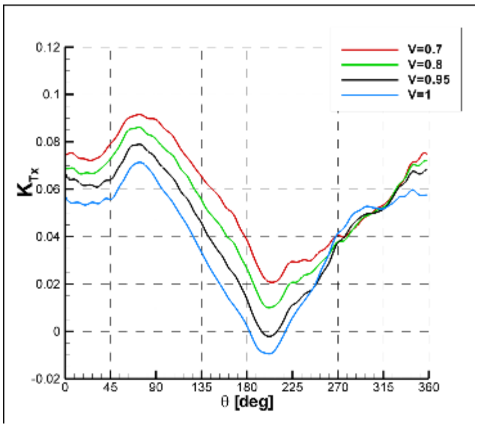

(e) $\beta = -30^{\circ}$

Figure 6.5 Single blade thrust. Left: external propeller; right: internal propeller

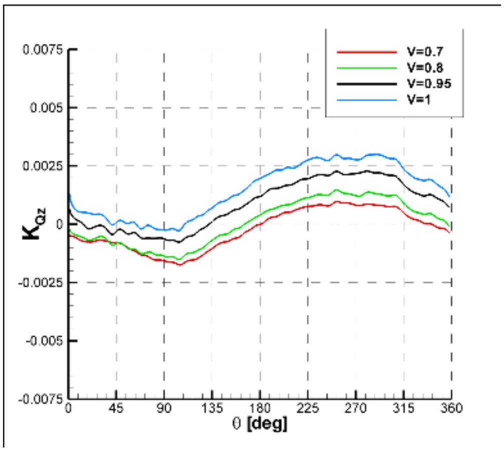

(a) $\beta = 0°$

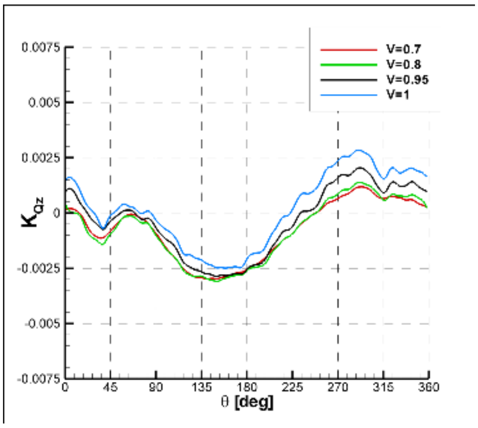

(b) $\beta = 15°$

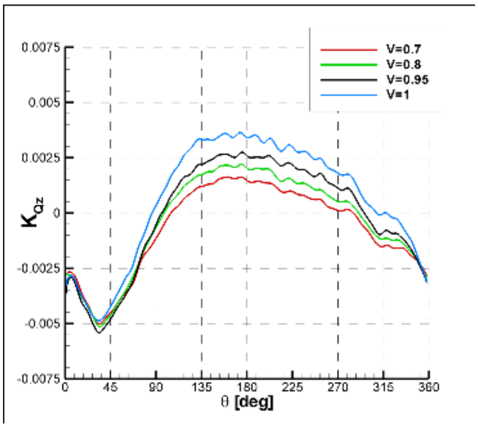

(c) $\beta = -15°$

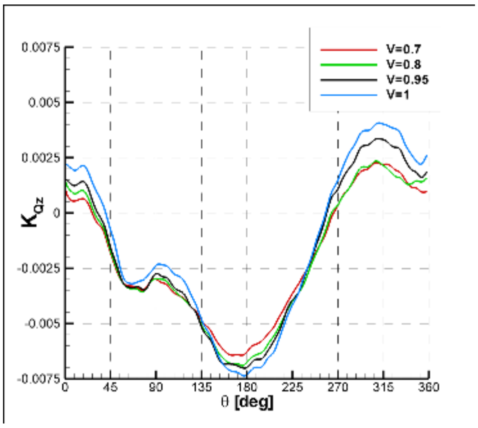

(d) $\beta = 30°$

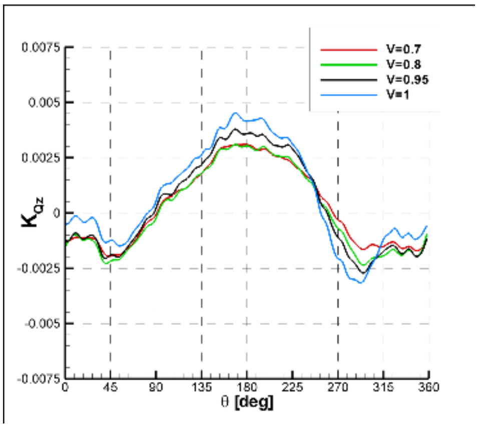

(e) $\beta = -30°$

Figure 6.6 Single blade spindle moment. Left: external propeller; right: internal propeller

The percentage variation (increase in case of K_{Tx} and decrease in case of K_{Qz}) of the loads is smaller in correspondence to higher blade loads. This fact can be clearly observed for blade thrust at $\beta = 0°$, $\beta = -15°$ (leeward side) and at $\beta = 30°$ (windward side) in figures 6.5c and 6.5d, respectively. Specifically, at $\beta = 0°$ (figure 6.5a), the peak at $\theta = 50°$ associated to the velocity defect past the shaft is gradually weakened and disappears at $V = 0.7$. On the internal side at $\beta = -15°$ (figure 6.5c), the load is gradually weakened in correspondence to the peak in the first quadrant caused by the interaction of the blade with the vortex. Conversely, on the external propeller K_{Tx} collapses during the passage in the lower half of the disk (figure 6.5d). This aspect can be also caused by localized flow separations due to the excessive increase of incidence angle, as it seems to be confirmed by trend of spindle torque shown in figure 6.6d: in fact, the evolution of the negative peak at $\theta = 180°$ matches with the outward shift of the hydrodynamic centre instead of an inward shift as expected by previous analysis in section 6.2). Finally, at $\beta = -30°$, during the second half of the cycle, the growth rate of K_{Tx} diminishes with speed drop. In this region, see figure 4.7c on the leeward side, the blade is impinged by a tangential flow that acts to increase the incidence angle. It is plausible that the reduction of the towing speed causes the premature separation of past the hull or appendages (the Reynolds number is lower) and thus the vortical structure would be convected farther from the propeller with the consequent reduction of the downward tangential flow. This trend inversion is also confirmed by spindle torque in the 4^{th} quadrant, see figure 6.6e, its variation being consistent with the outward shift of the hydrodynamic centre that happens with the unloading of the blade. At this drift angle, the trend of the loads on both windward and leeward side can be affected by the the free surface, because it can modify the evolution of the wake past the hull at stern at the different speeds.

6.3.1 Comparison with free running model tests

The comparison with free running model tests is shown in figures 6.7–6.12 for the averaged and cyclic loads. The propeller revolution are set equal to the self-propulsion condition at the nominal Froude number 0.26 obtained during the free running experiments and are kept constant for all the drift conditions. In case of the mean loads, the comparison is performed in terms of the equivalent drift angle β_{eff}. On the other hand, the comparison of the periodic loads is performed considering, for towing tests, the loads obtained at speed drops closer to the free running test in order to have a global overview on the two key parameters of this systematic analysis. In table 6.1, the equivalent drift angle and speed drop correspondent to the turning circles obtained at different rudder angles are summarized. The values of the speed drop for the free running tests are reported as labels in the figures 6.7, 6.9 and 6.11 to synthesize exhaustively the comparison of the two different kind of tests.

δ	U/U_0	$\beta_{eff}[°]$
$\pm 35°$	0.70	28.40
$\pm 25°$	0.80	22.77
$\pm 15°$	0.89	15.90
$\pm 7.5°$	0.95	8.40

Table 6.1 Kinematic parameters of free running manoeuvre at $F_N = 0.26$

The comparison of the mean value of blade thrust and side force are shown in figure 6.7 and torque and bending moment are represented in figure 6.9. The loads are presented in terms of ratio with respect to the mean value in straight ahead motion.

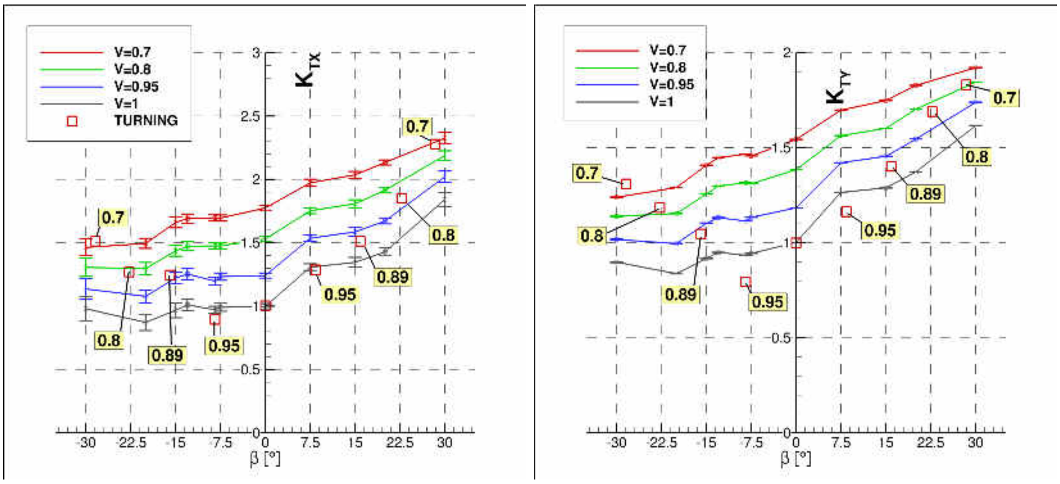

Figure 6.7 Comparisons of blade forces. Free running vs oblique towing

The correspondence of the free running results with oblique towing is very satisfactory both on the windward and on the leeward side for both forces and moments. In fact, at increasing (equivalent) drift angle, free running loads matches well with oblique towing ($O.T.$) results at diminishing speed (higher propeller loading). This trend reproduces correctly the physics, since during a turning circle manoeuvre the increase of rudder angle (here conceptually replaced by the equivalent drift angle) corresponds to a stronger reduction of the absolute velocity to the propeller. The agreement between free running and oblique towing is worse on the internal propeller in case of $\overline{K_{Ty}}$ and $\overline{K_{Qx}}$ at $\beta_{eff} = 7.5°$. Moreover, the torque seems to be overestimated by towing tests for the intermediate equivalent drift angle $\beta_{eff} = \pm 15°$ and $\pm 22.5°$. The comparison of the periodic loads is provided for blade thrust and torque in figures 6.8 and 6.10.

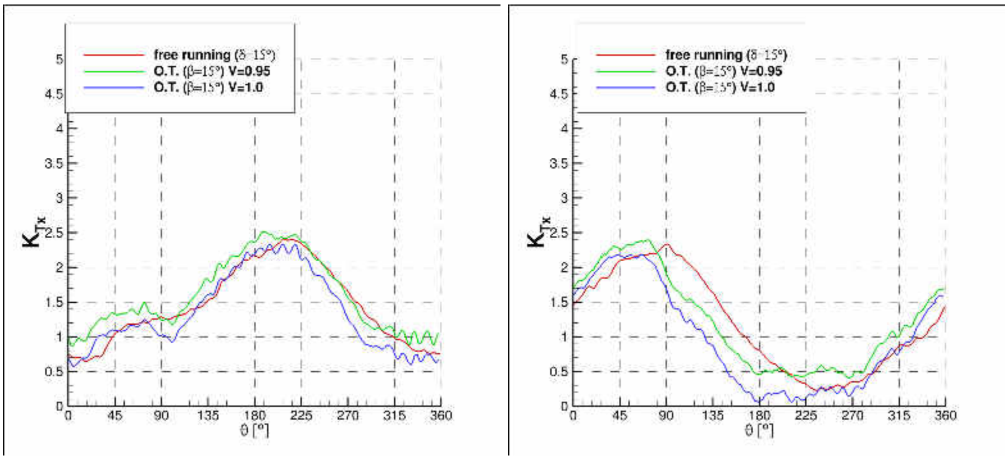

(a) Blade thrust comparison at $\beta = 15°$.

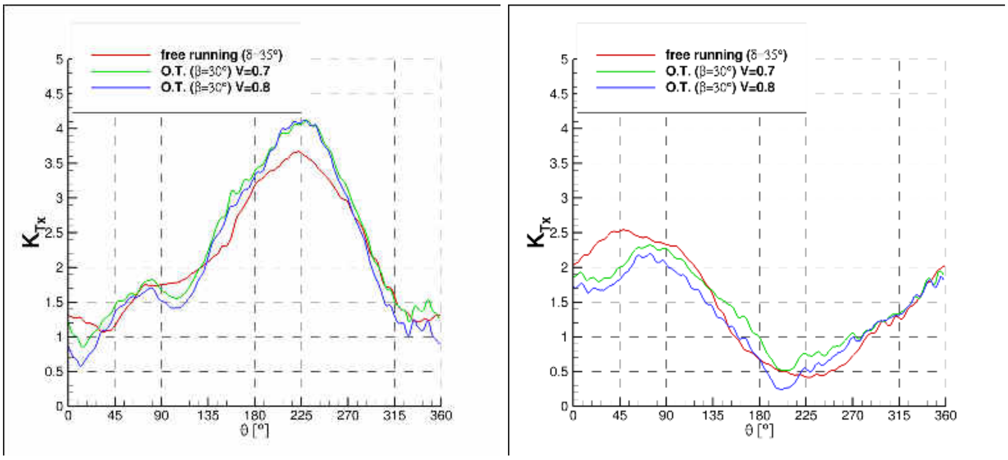

(b) Blade thrust comparison at $\beta = 30°$.

Figure 6.8 Comparisons of periodic blade loads. External (left) and internal (right) propeller.

Specifically, in case of K_{Tx} the agreement of the loads is satisfactory, although discrepancies are evident on both propellers. The fluctuation and the magnitude of the peak matches well. On the leeward side, the comparison is worse in case of the lower drift angle, because the loads are affected by the passage of vortical structures close or through the propeller disk. In fact, in the first half of the cycle the thrust is phase shifted, then the matching improves in the last interval of the cycle, $250° < \theta < 360°$. In the 3^{rd} quadrant, the thrust has a clear minima and is not constant as in case of the oblique towing. At higher drift (right panel in figure 6.8b) the error of the phase position of the peak and its magnitude is limited in the 1^{st} quadrant. Moreover, in case of the free running tests, in the lower half of the disk the variation of K_{Tx} is smoother with respect to the oblique towing. Finally, it has to be noticed that, in case of the oblique towing the maximum value is experienced at $\beta = 15°$, whereas the peak slightly increases for tightest maneuver in case of the free running. On the windward side, the agreement is better than the leeward side. The signals are correctly phased and the most evident error is experienced for the peak value at the maximum drift angle, that is overestimated by towing tests. Moreover, the fluctuation in the 1^{st} quadrant, ascribed to the interaction of the blade with the wake past the shaft, is smoother in case of the free running.

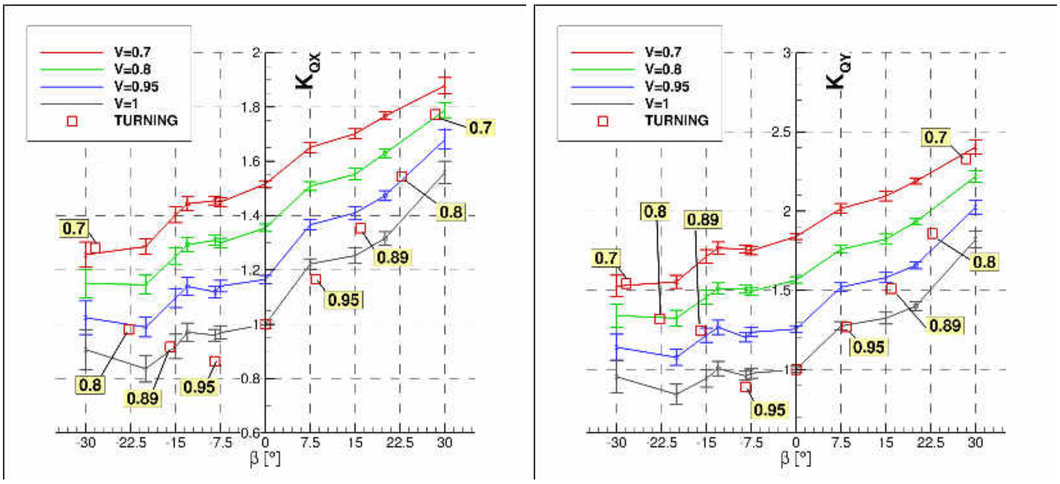

Figure 6.9 Comparisons of blade moments. Free running vs oblique towing

The comparison of the blade torque K_{Qx} is shown in figure 6.10. On the right panel the comparison is proposed for lower drift angle on the leeward side, in order to highlight the source of the discrepancy observed for the mean loads.

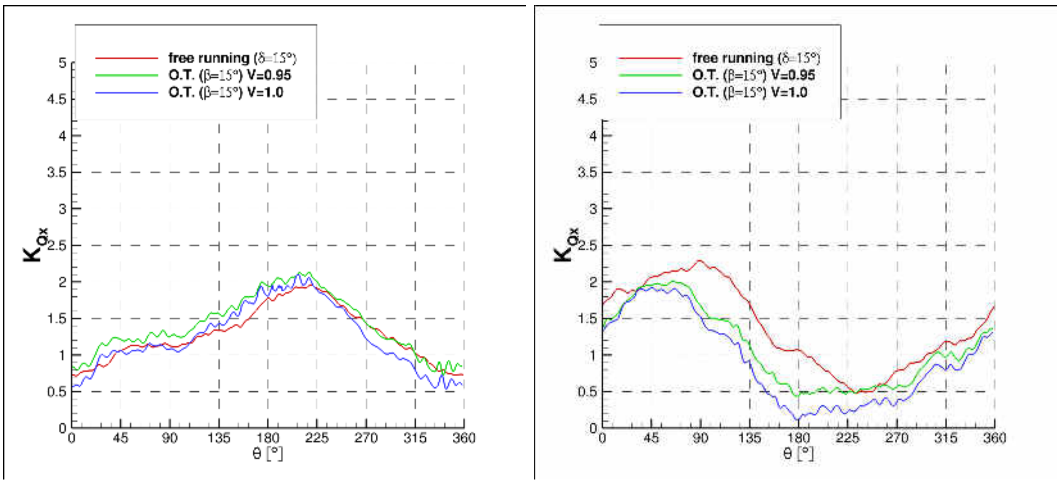

Figure 6.10 Comparisons of periodic blade torque K_{Qx} with $\beta = 15°$, for external (left) and internal (right) propeller

Qualitatively, the trend of the signals is similar to blade thrust, the agreement being satisfactory only in the last quarter of the cycle. In this case the blade loads (and distribution) are strongly affected by magnitude and phase of the inflow velocity gradients, and hence, alteration caused by the different attitude (roll) and wake evolution. On the external side (left panel), the accordance is very satisfactory, since the inflow, essentially a pure oblique flow with the exception of limited portions of the disk affected by the wake past the shaft or hull, is better reproduced by towing in drift. Finally, the comparison of the spindle torque is provided in figures 6.11 in terms of mean value and in figure 6.12 for the cyclic load. For this load, the comparison is worse than the previous ones, probably due to its higher sensitivity to differences of the inflow. In terms of mean values (figure 6.11), the trend of the free running is qualitatively captured by the towing tests associated to the equivalent drift and speed drop (propeller loading). Although in case of the internal propeller the values of the oblique towing show a quite irregular spread, the trend of free running falls within the corresponding conditions. Conversely, the external propeller is always overestimated.

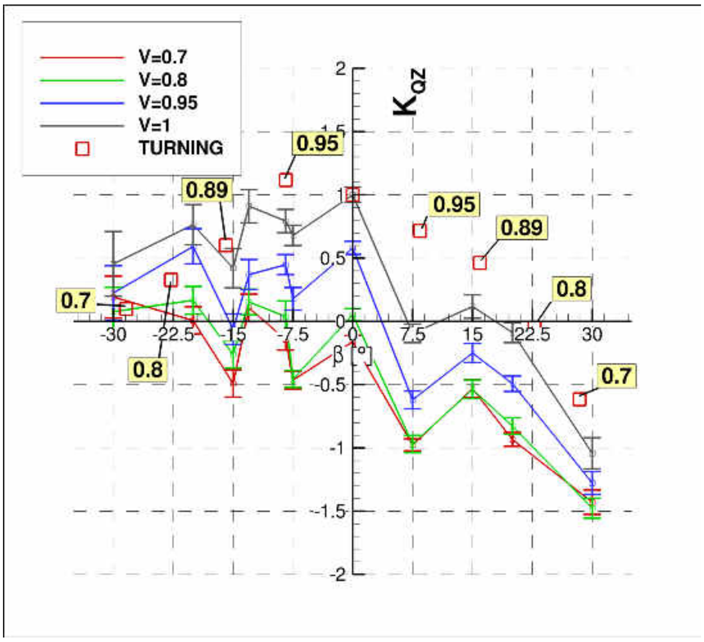

Figure 6.11 Comparisons of periodic blade torque

This aspect can be partially explained by the evolution of loads through a rotation (figure 6.12): the trends, the local maxima and phase of the two signals are well captured for both leeward and windward propellers. However, while for the internal side the over and underestimations are almost balanced over the period during mild and tight manoeuvres, on the external propeller local discrepancies amplify with the severity of the turning. In particular, the fluctuation of the loads is markedly overestimated by the towing tests, in particular in the intervals of the period where the blade overloads due to strong wake interactions (namely, 1^{st}

quadrant for the internal propeller and first half cycle for the external one). Here, the effects of the different straightening of the flow associated to the two different kinematic conditions are amplified.

On the external side, the differences of the effective drift angle of the appendages can yield local alterations of the wake incoming to the propeller blade in this sector. This is evidenced by the onset of higher harmonic content in the time history of blade thrust in figure 6.8. A more detailed inspection on this phenomenon could certainly be achieved with the aid of numerical simulations.

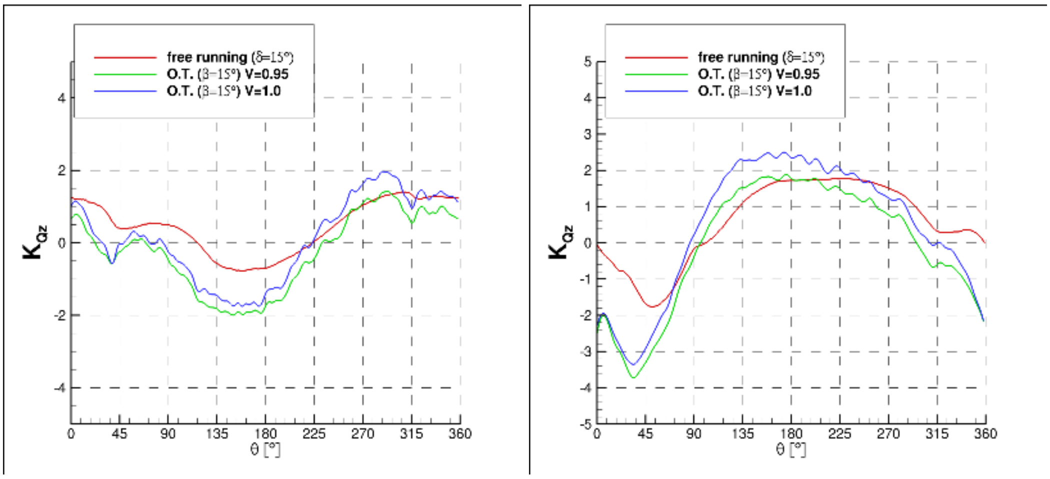

(a) Spindle torque comparison at $\beta = 15°$. Left: external propeller; right: internal propeller

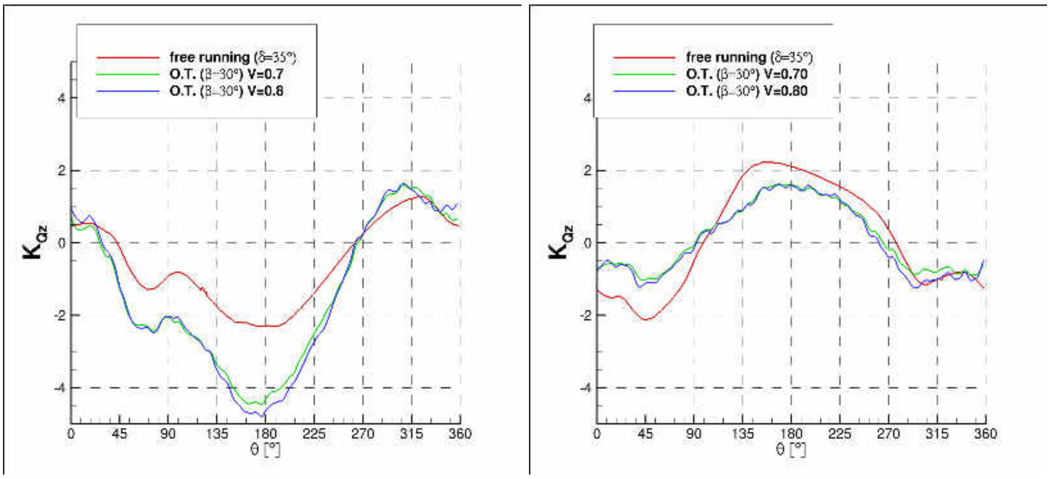

(b) Spindle torque comparison at $\beta = 30°$. Left: external propeller; right: internal propeller

Figure 6.12 Comparisons of periodic blade spindle torque

In general, the representation of the loads in terms of ratio highlights that the fluctuation of the loads and the maximum peak during the cycle can be of the order of 150% and 400% of the mean value in straight ahead condition, respectively.

6.4 Captive model test results: propeller loads

6.4.1 Hub/propeller loads during oblique towing

Dimensionless propeller loads are presented in terms of ratio with respect to the total thrust at $V = 1.0$, which corresponds to Fn=0.26, in straight ahead condition and equivalent drift angle β_{eff}, in order to have a consistent comparison with the free running results. According to the reference system defined in figure 4.1, the lateral and vertical components of the radial force are positive when directed to port-side and upwards.

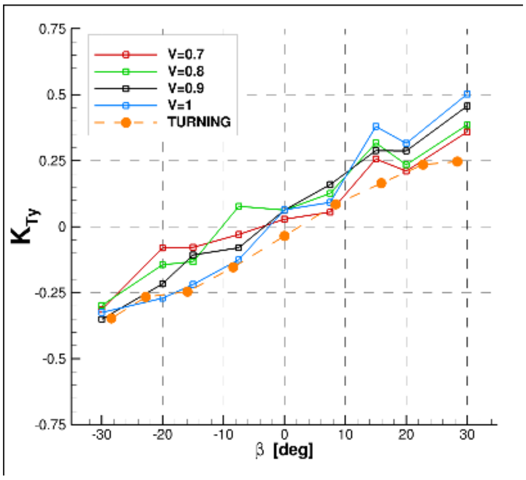

(a) K_{TY}

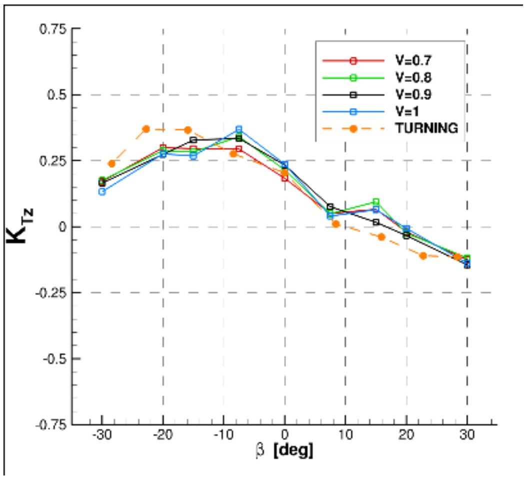

(b) K_{TZ}

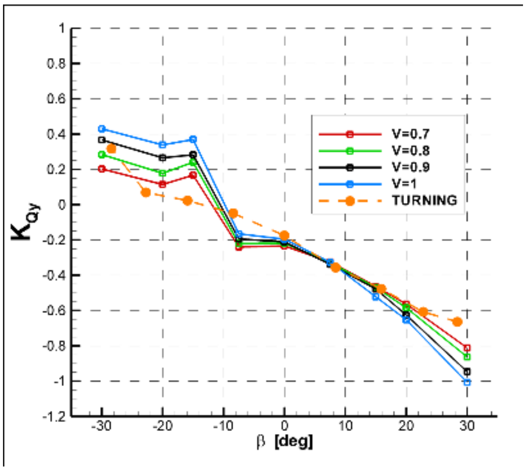

(c) K_{QY}

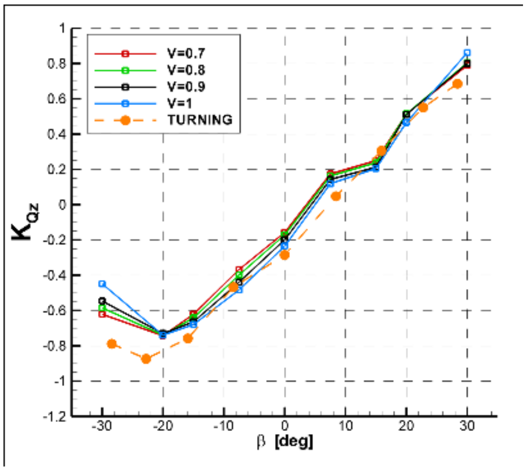

(d) K_{QZ}

Figure 6.13 In plane forces and moments

Figure 6.13 shows the in–plane loads exerted by the propeller during oblique towing and free running tests, for internal and external propeller (negative and positive β values, respectively), while the split contributions from the different halves are showed in figure 6.15. A clearer comparison is proposed in figures 6.14 and 6.16, where only the *OT* data that correspond to the closer value of speed drop of free running tests are selected. The loads are described for the starboard propeller and, therefore, the inflow field for the windward propeller should be mirrored when referring to the external side.

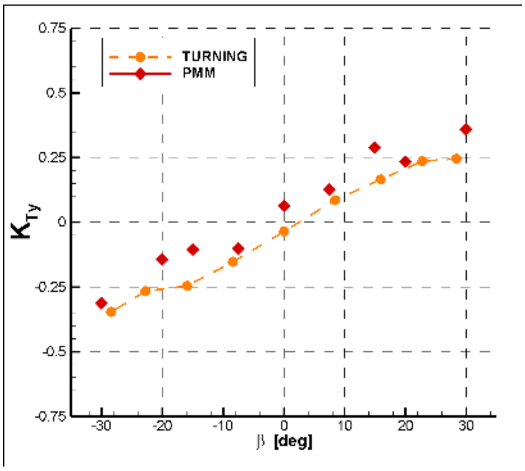

(a) K_{TY}

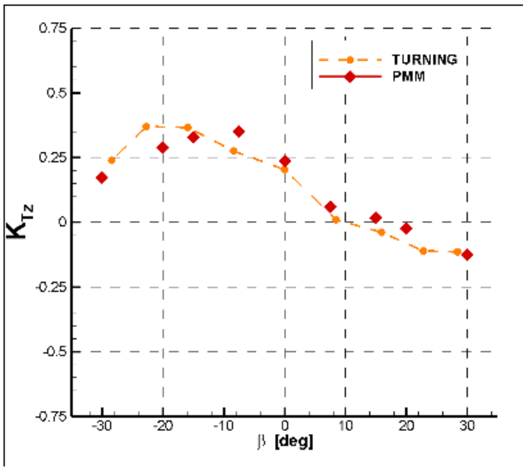

(b) K_{TZ}

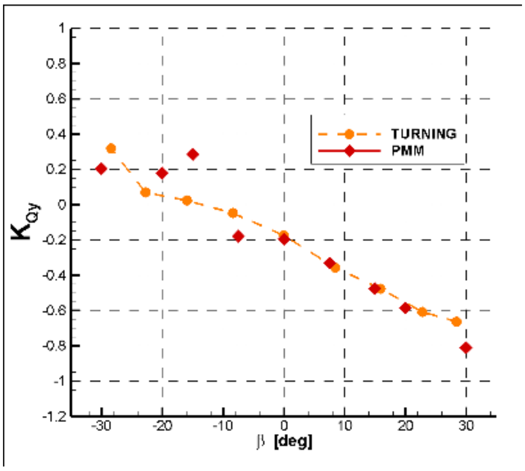

(c) K_{QY}

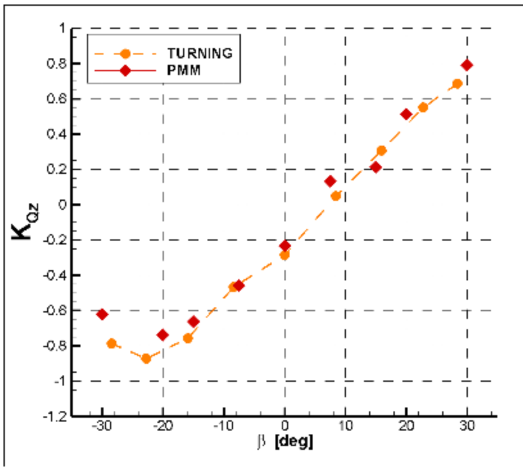

(d) K_{QZ}

Figure 6.14 Comparison between free running and captive test measured in plane forces and moments

In general, the outcome of the oblique towing tests highlights that K_{Ty} and K_{Qy} are more sensitive to propeller loading (i.e., towing speed) with respect to vertical force and pitch moment. In case of K_{Ty}, the force reduces in proportion to the decrease of towing speed at all drift angles, except for the smallest angles on both internal and external propellers and the trend with drift angle is not similar for all speeds. On the contrary, the variation of the loads with drift angle is markedly similar for the other components. In case of the pitch moment K_{Qy}, the effect of speed drop increases with the increase of β, while, in case of vertical force K_{Tz} and yaw moment K_{Qz} the data collapse about the same value. In case of the vertical force the speed drop seems to be important at intermediate drift angle $10-20^{\circ}$ on both propellers. The trend of the steady turning, and in particular the asymmetric behavior is well captured for all the components, although discrepancies evidently exist in relation to the speed drop.

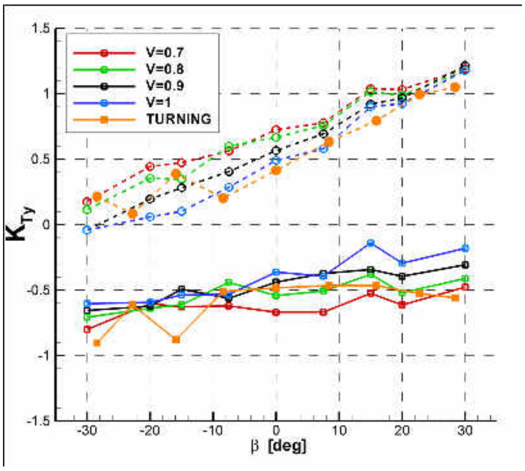

(a) K_{TY}

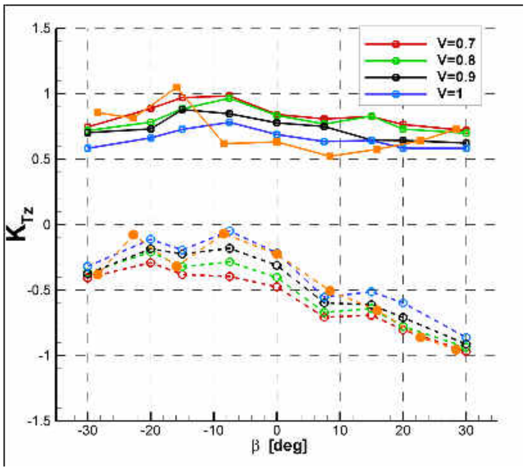

(b) K_{TZ}

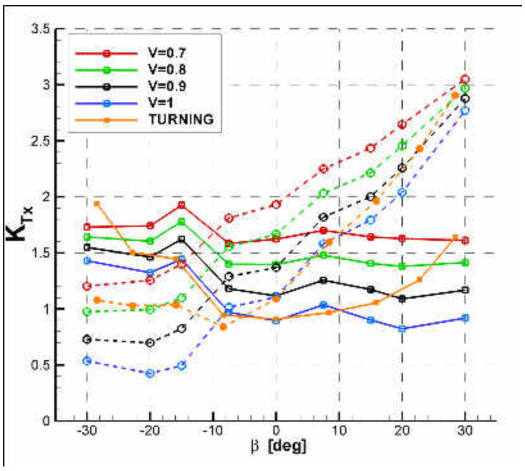

(c) K_{QY}

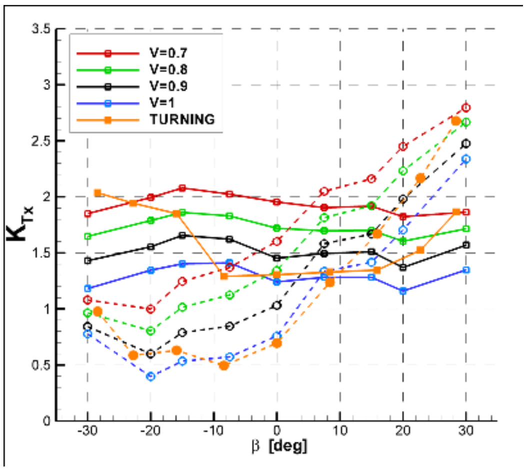

(d) K_{QZ}

Figure 6.15 Distribution of loads. Solid and dashed lines refer to upper/left and lower/right half of the disk respectively.

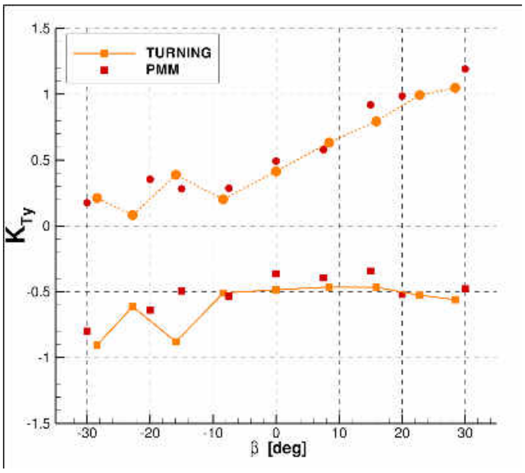

(a) K_{TY}

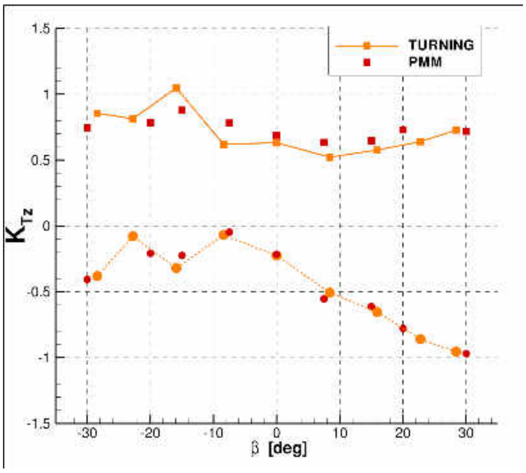

(b) K_{TZ}

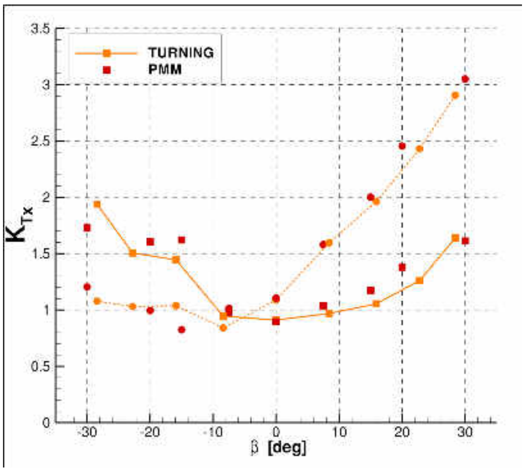

(c) K_{QY}

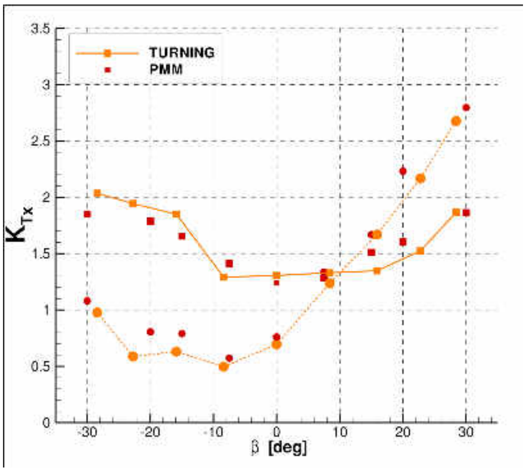

(d) K_{QZ}

Figure 6.16 Comparison between free running and captive test measured distribution of loads. Solid and dashed lines refer to upper/left and lower/right half of the disk respectively.

In greater detail, the side force K_{Ty} experiences an almost linear trend with rudder angle for the windward and leeward propellers, see figure 6.13a. In both situations, the side force provides a stabilizing effect to the model, i.e. it creates a couple that counteracts the turning motion. On the windward side, K_{Ty} is generated in the lower half of the disk: in facts, in this sector the load (dashed lines) increases while it is almost constant in the opposite sector for each velocity, see figure 6.15a. This different behavior is consequent to the concurrent effect between the tangential and axial velocity to build up the hydrodynamic load. In the lower half, the cross flow acts to increase the tangential velocity relative to the foil and, consequently, the incidence angle. This effect is opposite in the upper half. The trend revealed by *OT* highlights that the load in the lower half increases at an higher rate the more the propeller loading is reduced (the load collapse at the maximum drift angle). Probably, at higher loading, foil efficiency could be reduced due to onset of stall or other mechanisms associated to the operation of the blades in unsteady regimes. In case of ST, K_{Ty} is always lower than the oblique towing, as a consequence of the underload and overload of the lateral force in the lower and upper half of the disk, respectively.

On the leeward side, K_{Ty} establishes to a lower value with respect to external propeller due to interaction with the wake of the hull. In particular, the side force is almost constant with β in the upper half of the disk and the effect of speed drop is minimal. This is due to the fact that in the upper half of the disk the increase of the speed drop is counterbalanced by the cross flow. Conversely, in the lower half the load diminishes, because the cross flow causes the blade section to be impinged with a lower tangential velocity. The magnitude of the side force developed during ST (orange colored line) experiences a local increment on both halves about the $\beta_{EFF} \sim 15^\circ$. This behavior is driven by the SV: with reference to figure 4.7b, it provides a sort of blockage effect on the flow coming from the wind side and interacts locally with the blade. In case of the free running, the vortex could be weaker and located farther with respect to the leeward propeller in contrast to the one represented in the figure, because the skeg is impinged at smaller drift angle. As a consequence, the cross flow could reach the 2^{nd} quadrant at higher upwards deflection, amplifying the tangential flow relative to the blade sections in this sector, with consequent increase of the load.

These hydrodynamic phenomena also explain the imbalance of K_{Tx} that gives rise to the pitch moment. On the external propeller, K_{Qy} is negative, i.e. it acts to bend the propeller shaft on the top pushing downward the propeller, since the blades are overloaded in the lower half of the disk, see figure 6.15c. In case of OT the thrust resembles the side force, namely it grows monotonically in the lower half with drift angle at a rate that is faster the higher the advance velocity. This causes the curves trend to collapse at $\beta = 30^\circ$. On the contrary, on the upper half, K_{Tx} is almost constant and the effect of propeller loading is uniform at all β.

Oblique towing overestimates the free running results, in particular at the higher drift angles, see also figure 6.14c, because the thrust at same speed drop (V=0.7) is stronger in the lower half of the disk, see figure 6.15c. It can be inferred that in this sector, the wake shed from appendages is less deflected to the lee side due linear drift distribution and this can yield local increase of the load. However, the trend of K_{Qy} is very well captured by OT, on the windward side, when considering values at same speed drop. On the internal side, where K_{Qy} lifts the propeller, given the higher hydrodynamic load exerted in the upper half, the trend of OT is very different from the free running: in fact, K_{Qy} at the smallest β is close to the value in straight ahead (and it is yet negative), then abruptly rises at $\beta = 15^\circ$

and keeps an almost constant value. This is associated to the fact that the thrust in the lower half of the disk drops at a considerably higher rate with respect to the upper half. On the contrary, the pitch moment increases smoothly for the steady turning tests, except for the tightest maneuver. This behavior can be associated to the fact that the thrust increases only in the upper half, while it keeps almost constant in the lower half.

The vertical force K_{Tz} shows a completely different trend between the external and internal propeller, see figure 6.13b. In straight ahead motion, the vertical force is upwards oriented (and correspondent to about 20% of the thrust), because in the left half of the disk both the reduction of the axial component of the inflow and the upwards tangential component act to increase the blade loading. Vice versa, on the opposite half, the flow is almost clean and, being oriented in the same sense of blade motion, lessens the tangential component relative to the sections (see figure 4.8) and, on its turn, the load. On the windward propeller, K_{Tz} drops with an almost linear trend with the increase of β. This is consequent to the fact that the magnitude of the force on the right side (negative) monotonically increases, because the blade experiences a relevant cross flow that strengthens the load in the 3^{rd} quadrant. This contribution is only partially canceled in the 4^{th} quadrant, due to the opposite action of the tangential flow. It is interesting to observe that for $7.5° < \beta < 15°$, these contributions are equally balanced (the load is almost constant), probably because in the 4^{th} quadrant the blade encounters the velocity defect associated to the wake of the outer bracket. However, at larger drift angle the load further increases due to the establishment of the pure oblique flow. On the left half of the disk, the vertical force is constant due to different mechanisms that depend on the drift angle: in facts, at smaller β, the action of the *SV* structure induces a tangential flow that, being oriented in the same sense of the blade motion, weakens the increment of incidence angle of the section caused by the wake of the bracket. At the higher drifts (i.e., see figure 4.7c), the unloading due to the cross flow in the 1^{st} quadrant balances the load increase in the lower sector.

The comparison with the separate contributions developed during *ST* highlights that the source of the discrepancy arises in the 1^{st} and 2^{nd} quadrant with the exception of $\beta = 30°$: this is due to the non–consistent evolution of the flow along the model that could give rise to a stronger velocity defect as well as a different contribution from *SV* (and, consequently, higher loads). On the opposite half the vertical force is captured very accurately also in terms of the speed drop. These considerations hold to explain the features of the yaw moment K_{Qz}, see figure 6.13d. In particular, the split contribution of K_{Tx} and the difference with *ST* resembles the one discussed for the vertical force, see figure 6.15d. Briefly, the yaw moment in straight ahead is negative, and acts to bend the shaft outward. Then, it gradually changes to turn inward the propeller due to load increase in the 3^{rd} and 4^{th} quadrants.

On the leeward side, K_{Tz} exhibits a non–linear trend, see figure 6.13b: specifically, it further increases at $\beta = 7.5°$ to a value that is almost 30% and then keeps this value before definitely drop at the maximum drift. This behavior resembles the free running model tests, although the peak achieved earlier than ST, as better showed in figure 6.14b. The nature of this non–linear behavior can be ascribed to the fact that at the smaller drift angles (say, $0° < \theta < 7.5°$) the left/right imbalance increases due to the opposite trend of the force developed by the blade. Specifically, on the left half of the disk (1^{st} and 2^{nd} quadrants) the vertical force increases, because the velocity induced by the onset of *SV* causes the tangential flow relative to blade section to increase and, therefore, develop higher load. On the opposite half, it abruptly drops due to the cross flow in the 3^{rd} quadrant: this event can be inferred from figures 4.7a and 4.7b observing that in the 4^{th} the unloading effect of the in–plane velocity is similar to the straight ahead (upwards oriented to reduce the incidence of the blade sections). At higher β, the imbalance is gradually mitigated: on the left half K_{Tz} drops, because *SV* is transported to the lee side and the blade/vortex interaction mechanism ends. Simultaneously, its blockage effect dies and the cross flow reduces the incidence angle of the blades, in particular in the 2^{nd} quadrant. This mechanism is further strengthened moving to larger drift angles, see figure 4.7c: in fact, MV deflects the wake shed past the shaft and the low pressure region thus formed deviates downward the cross–flow to further reduce the component tangential to blade sections. On the right half, the vertical force, downward oriented, gradually increases due to the reduction of axial velocity in the wake past the shaft and increase of the tangential component induced by MV. More specifically, it is worth noticing the non–linear trend in the range $7.5° < \beta < 20°$: this behavior, is associated to the transition, and simultaneous evolution, of SV. For example, at $\beta = 15°$, the magnitude of K_{Tz} increases because the separation past the shaft causes the outward deflection of the tangential flow and the increase of velocity defect in the 4^{th} quadrant. Then, at $\beta = 20°$, it can be inferred that the *SV* increased in size (the skeg is impinged at higher incidence) and centred with the propeller disk to induce a tangential flow that is concordant to blade rotation and thus it acts to reduce the force of the blades. It is worth noticing that this complex behavior on the right half of disk is experienced during ST. On the contrary, the accordance is poorer on the left half of disk, for discrepancies of wake evolution from ahead of the propeller. However, as a matter of fact, the trend of ST is well captured when referring to similar speed drop, see figure 6.14b. The trend of the split contribution of K_{Tx} resembles that of the vertical force for OT and ST. It is interesting to note that the non linear behavior, experienced in both tests, is experienced at the larger drift angles. K_{Qz} is always negative, i.e. it acts to bend the propeller shaft outward to the lee side.

6.5 Comparison between transient phases and pure drift data

The analysis of the periodic blade loads during unsteady ship dynamics is considered for transient phases of a turning circle. In this preliminary study, the analysis is focused on three different conditions: the transient phase (TRA) at $\delta = 15°$ and $35°$ and the pull–out (PO) at $\delta = 35°$ at the same reference (approach) speed $F_N = 0.26$ of the oblique towing in order to carry out a consistent comparison of the data. The analysis is centred on the TRA at $\delta = 35°$, because it experiences transient states that can be compared to the steady phases for turning circles at all rudder angles tested ($\delta = 7.5° \div 35°$). On the other hand, the additional transients are included to study the effects of the different kinematic response and initial condition on the loads.

The key features of the transient maneuvers are showed in figure 6.17: in particular, figure 6.17a highlights the segment of the trajectory obtained at $\delta = 35°$, in correspondence to which the propeller experiences the same equivalent drift angles (identified by square symbols) of the steady turning phases obtained at different rudder angles. It is interesting to note that this interval covers a longitudinal movement by about two ship lengths (about sixty propeller revolution). Figure 6.17b shows the dynamic response of the model after the activation of the rudder in terms of yaw rate, speed drop and effective drift angle. In the pictures, time has been replaced by propeller cycles. At $\delta = 15°$, the transient is obviously slower due to the lower control loads and the consequent slower dynamic response of the model.

In order to relate the nominal propeller functioning regime with the dynamic response of the model, the variation of the speed drop with the effective drift angle β_{EFF} is visualized in Figure 6.18. The speed drop is the most meaningful parameter, since it can be immediately associated to the nominal propeller advance coefficient J (J = V_{abs}/ND, where N and D are propeller rate of revolution and diameter), and hence, propeller loading. The dynamic response of the model is not reversible during PO: in particular the recovery of the speed is markedly slower during the re–establishment of the straight ahead motion. On the contrary, the TRA at $\delta = 15°$ resembles the same trend of tighter maneuver.

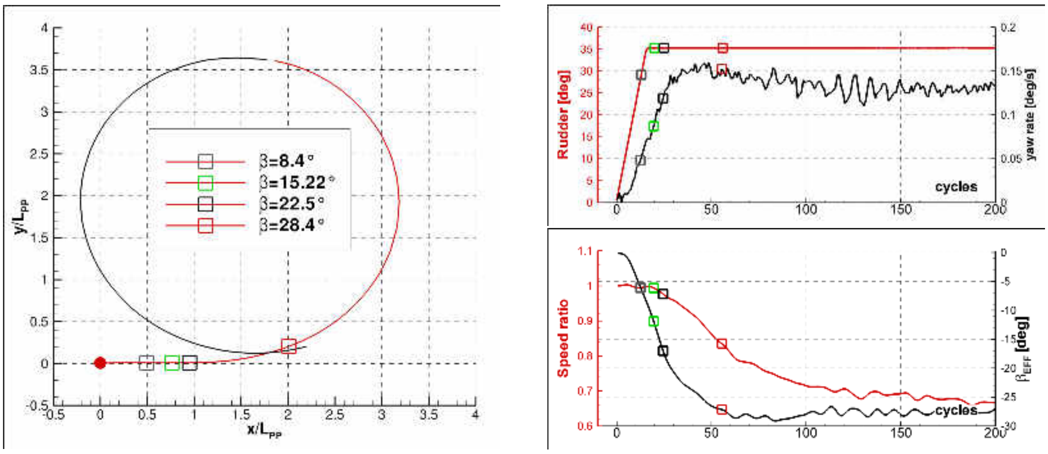

(a) trajectory (b) effective drift and speed drop

Figure 6.17 Dynamic response of the model during the transient maneuver

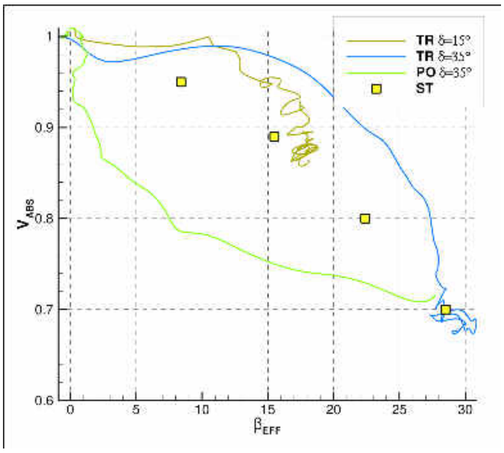

Figure 6.18 Speed drop vs effective drift angle

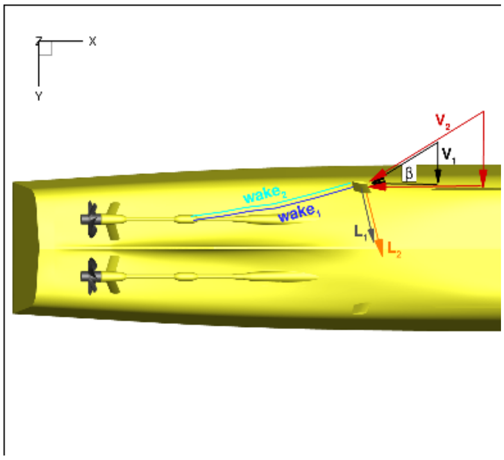

Figure 6.19 Effect of speed drop on wake development

Cycle	β_{EFF}	Speed drop - transient	Speed drop - steady
13	8.4°	0.99	0.95
20	15.22°	0.97	0.89
25	22.5°	0.96	0.8
56	27.8°	0.8	0.7

Table 6.2 Correspondence of equivalent kinematic parameters for transient and steady free running maneuvers

Before presenting the following analysis, it is important to remark the fundamental implications of the transient motion on the evolution of the wake. These aspects need to be highlighted in order to understand the nature of the discrepancy of the transient loads with respect to the quasi steady conditions (*ST* and *OT*), since the use of the wake fields in figure 4.7 is anyway considered for this purpose. In particular, given the similarity of a maneuvering hull with a low aspect ratio wing at incidence, during a transient motion, the wake past the hull is altered with respect to a steady condition by the so called circulatory and non–circulatory effects. These are associated to the temporal variation of the lateral force that causes the time varying circulation of wake structures detached from it and added–mass effects, respectively. Moreover, the size and intensity of the vortical structure is different as a consequence of the discrepancy of the absolute velocity associated to speed drop, see figure 6.19. In fact, the intensity of the vortex is proportional to the lift, that on its turn is proportional to the product of incidence angle (i.e. drift) and squared absolute speed. Therefore, vortices detached during transient, characterized by lower speed drop, are stronger (and larger) than correspondent ones generated during the quasi steady cases. In the following analysis, only this effect and added mass are considered to infer the discrepancies of the periodic blade loads, given the unknown of the time scale of memory effect of circulation.

6.5.1 Mean loads and maximum fluctuation

The averaged mean values of single blade thrust, bending and spindle moment for the transients maneuvers are showed in figure 6.20. The evolution of the loads is described in terms of equivalent drift angle instead of time, for the sake of improving the readability of the comparison with oblique towing and the steady turning phase values. Figures on the right side refer to the internal propeller.

In general, in case of both propellers, K_{Tx} and K_{Qy} during the TRA phase at both rudder angles well overlap with each other and the steady turning values (black circle), see figures 6.20a and 6.20b. The transient loads are slightly higher than the steady phase during the early stages, i.e. at $\beta_{EFF} \sim 8.4°$. This fact can be associated to the sway–yaw response of the model, that can contribute to the different establishment of the wake and, moreover, on the speed drop. In fact, figure 6.18 highlights that after the activation of the rudder the model experiences a sudden deceleration that causes higher propeller loading. During the PO, the thrust and bending moment are markedly higher with respect to TRA and steady turning phases at the same β_{EFF}. This behavior has to be ascribed to the fact that the velocity slowly grows after the activation of the rudder (it remains below 0.8 up to $\beta_{EFF} = 10°$) and, consequently, the propeller operates at a lower equivalent advance coefficient. This behavior is consistent with the fact that K_{Tx} and K_{Qy} are in–between the loads of the oblique towing tests at $V_{abs} = 0.7$ and 0.8 up to $\beta_{EFF} = 10°$ for both internal and external propeller. The evolution of the loads is different for the two propellers: on the internal side, they gradually increase up to $\beta_{EFF} = 10°$, and then drop. In particular, the loads show a faster increase for $10° < \beta_{EFF} < 20°$ (well reproduced by the $O.T.$ tests) that can be associated to the change of morphology of the wake from fully separated to the reformation of smaller and coherent structures that pass through the propeller disk. On the other hand, on the external side the loads monotonically decrease, with a faster rate for $\beta_{EFF} < 10°$. The closer inspection of the trends also reveals the wake–propeller interaction phenomenon about $\beta_{EFF} = 15°$ by the slight increment of the load.

The mean values of the spindle torque during the TRA is in accordance with the steady turning values, see figure 6.20c. In this case, the values during the PO are lower with respect to the TRA at $\delta = 35°$ as a consequence of the fact that the hydrodynamic centre of blade load moves towards inner sections and, given skewed shape of the blade, it moves toward the leading edge (i.e. the spindle axis) to yield a smaller value of the moment arm. Both transient and steady state values are underestimated by OT, although the trend with increasing β_{EFF} and speed drop is captured. As discussed at the beginning of the section, the discrepancies can be associated to localized alteration of the wake due to the speed distribution along the hull and constrained attitude of the model during the oblique towing. In this sense, small variations of loading distribution can have a noticeable effect on the spindle moment.

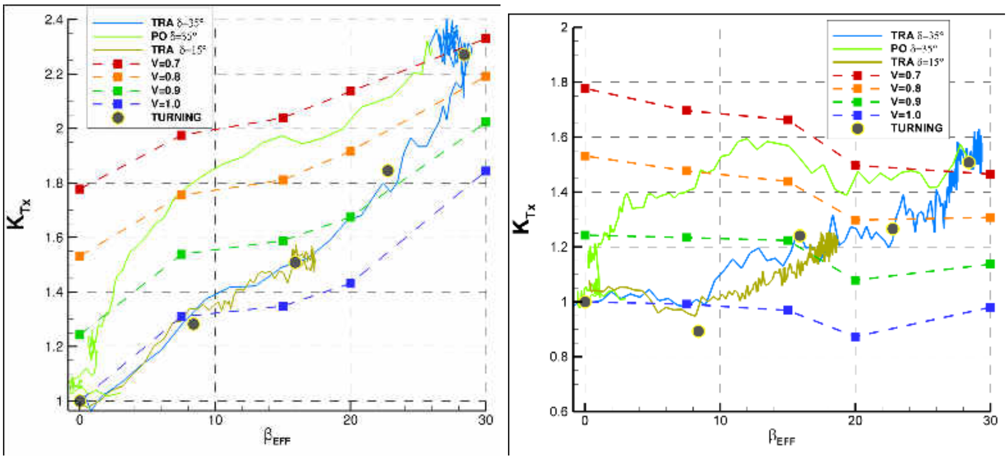

(a) K_{TX}

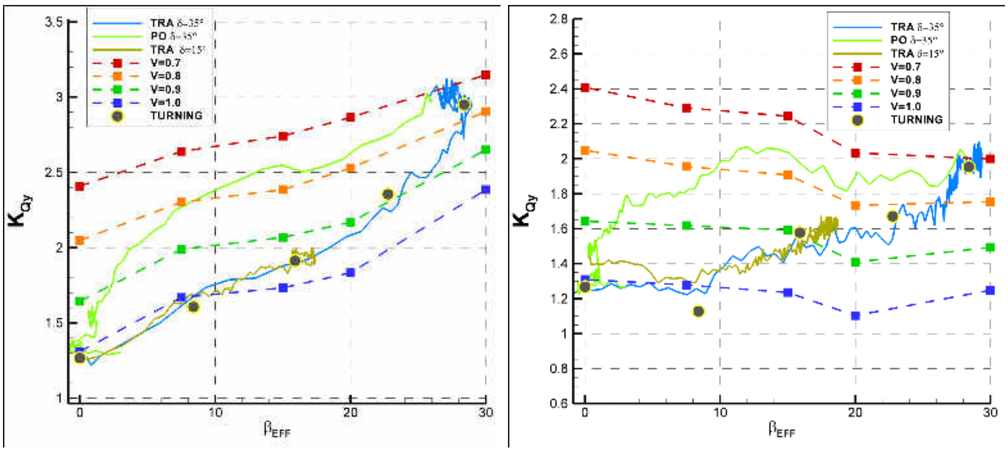

(b) K_{QY}

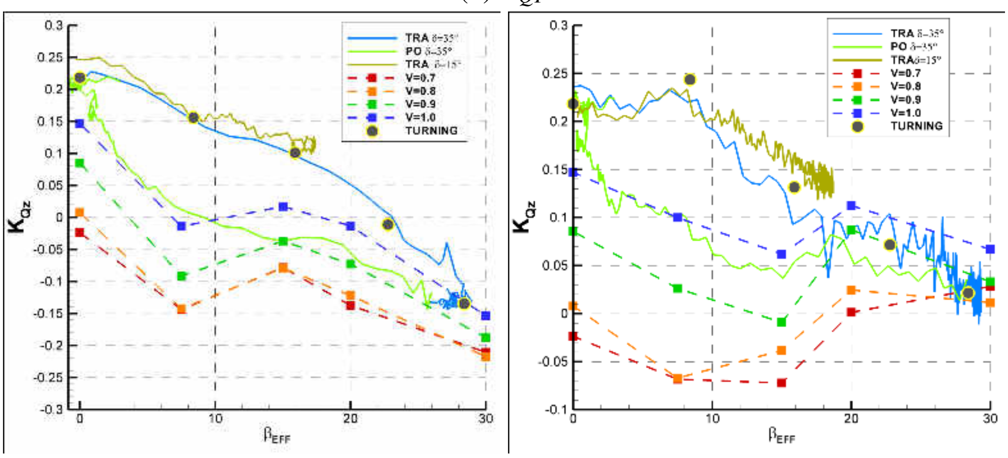

(c) K_{QZ}

Figure 6.20 Comparison between transient and steady maneuvers by oblique towing and turning maneuver. Averaged single blade loads of internal (right) and external (left) propeller

In order to better highlight the effect of the transient motions, the maximum fluctuation of the loads Δ_L (where L is the generic load), during a blade revolution is inspected. As expected, the behavior of the internal and external propeller is markedly asymmetric.

Considering the transient maneuvers, Δ_L is stronger during the TRA phase with respect to the pull out at $\delta = 35°$, because the propeller operates at lower loading and, consequently, it is more sensitive to spatial gradients and temporal fluctuations of the inflow, see figure 6.21. In contrast to the mean values, Δ_L experienced during the TRA is affected by the severity of the maneuver (i.e., rudder angle) and the most critical conditions are experienced by the internal propeller. Although the maximum value of Δ_L is similar for the two propellers, on the leeward side it grows at a faster rate than the external propeller at lower β_{EFF}, as a consequence of the interaction with the wake. By an alternative perspective, the internal propeller would experience stronger fluctuation during weaker maneuvers: this is corroborated by the TRA at $\delta = 15°$, the maximum fluctuation on the leeward propeller being 25% higher than the windward one. In more details, on the internal side, the evolution of the signal is qualitatively similar at both rudder angles. Immediately after the activation of the rudder, Δ_L smoothly grows for smaller drift angles, probably because the planar velocities are slow and the modification of the wake are not relevant. After, the signal abruptly increases for a relatively short interval of the drift angle (about 8°) and then flattens out prior to achieve the stabilized value. It is worth noticing that the slope of the signal at $\delta = 15°$ weakens before that of the tighter maneuver, because the transient is close to its end and accelerations are going to die out. During the PO, the evolution of the absolute fluctuation is smoother, given higher (equivalent) advance coefficient of the propeller. On the external side, the evolution of the fluctuation during TRA is smoother with respect to the internal side. In particular, the grow rate is almost linear and then stabilizes. At the smaller rudder angle, the fluctuation stabilizes at almost the same drift angle observed for the internal propeller ($\beta_{EFF} = 10°$). Conversely, at $\delta = 35°$, the fluctuation monotonically grows up to $\beta_{EFF} \sim 24°$ and the plateau is markedly shorter. During the PO, Δ_L initially drops at an higher rate with respect to TRA up to $\beta_{EFF} \sim 15°$ and then slowly converges to the straight ahead value.

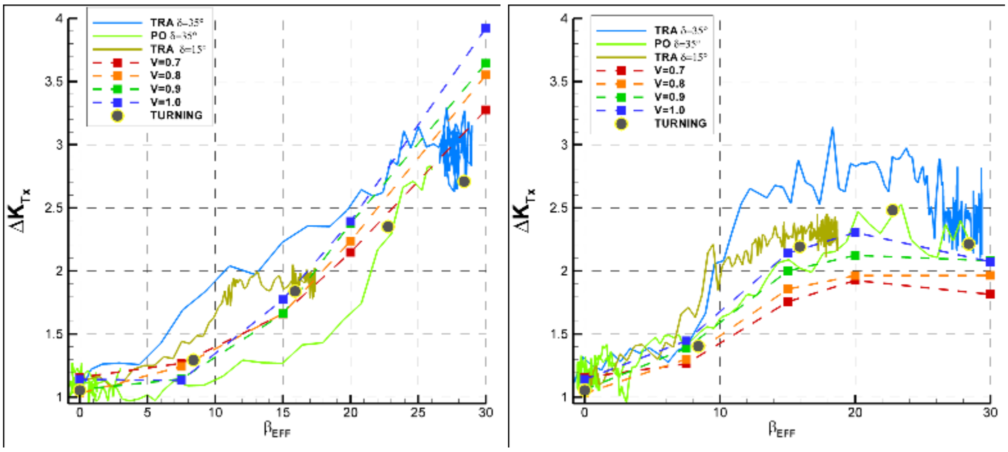

(a) K_{TX}

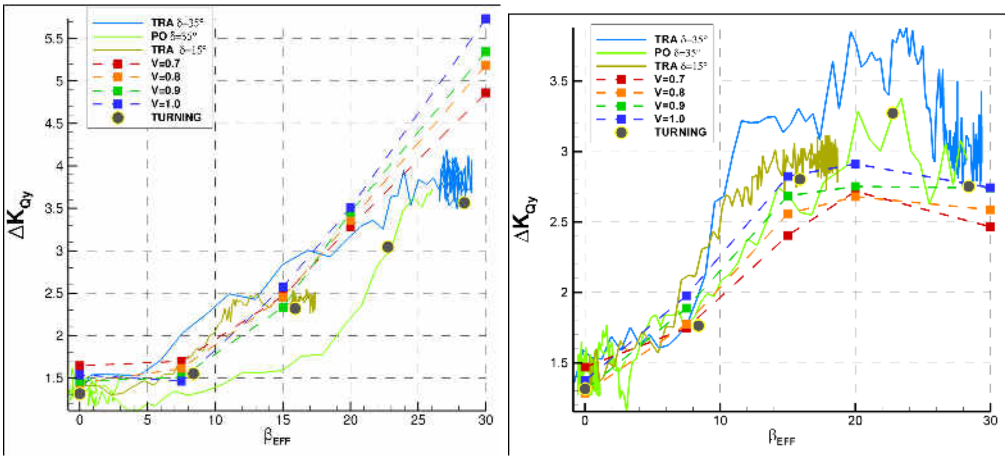

(b) K_{QY}

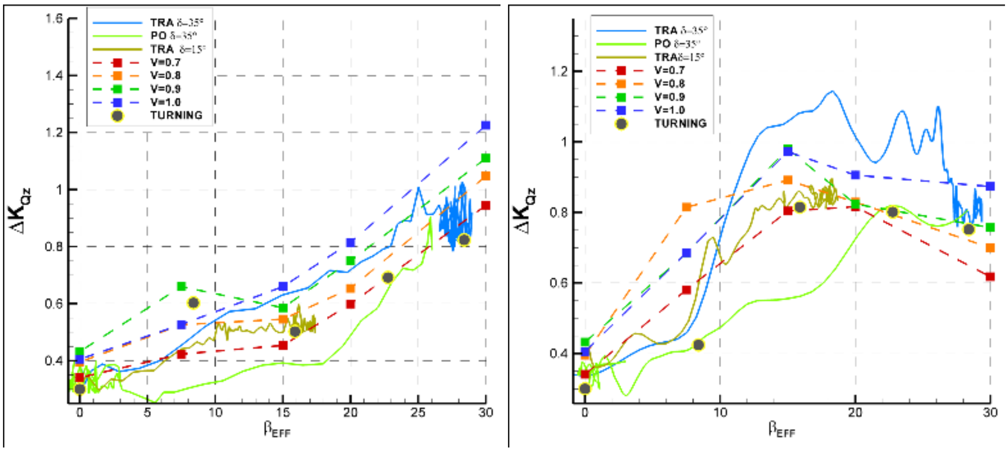

(c) K_{QZ}

Figure 6.21 Comparison between transient and steady maneuvers by oblique towing and turning maneuver. Maximum fluctuation of single blade loads of external (left) and internal (right) propeller

6.5.2 Periodic loads

The evolution of the periodic single blade thrust and spindle torque during the transient maneuvers are reported in figures 6.22–6.26 and are compared with steady turning and oblique towing loads to further explain the discrepancies discussed in the previous paragraphs. To support the cause and effect link between the loads and the inflow, the wake patterns showed in figure 4.7 are considered in relation to 2D hydrofoil theory of Par. 4.3.

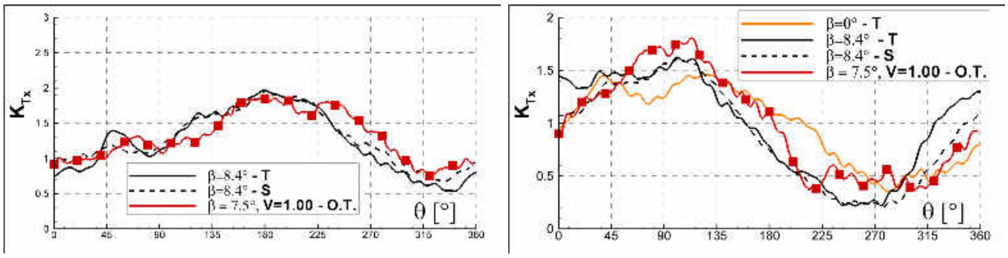

(a) $\beta_{EFF} = 8.4°$

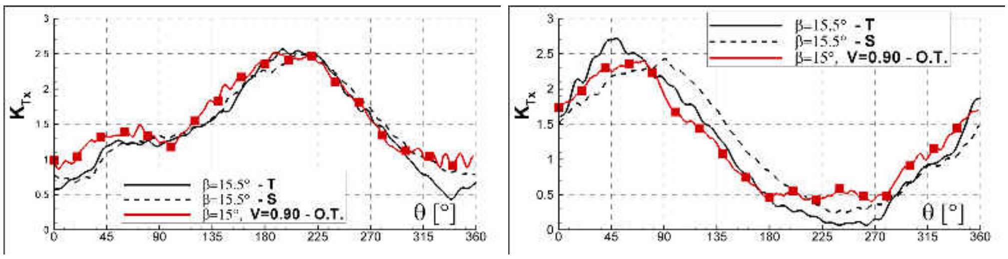

(b) $\beta_{EFF} = 15.2°$

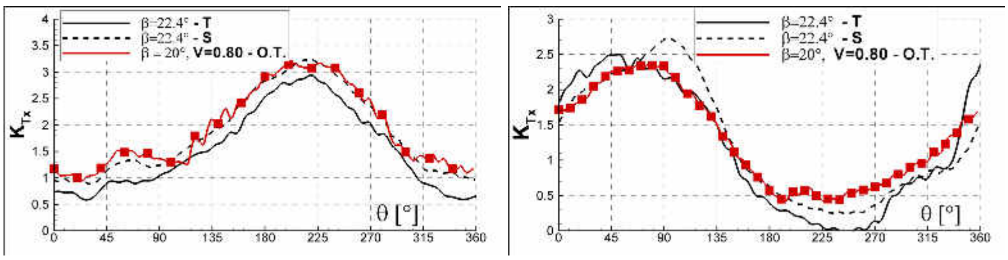

(c) $\beta_{EFF} = 22.4°$

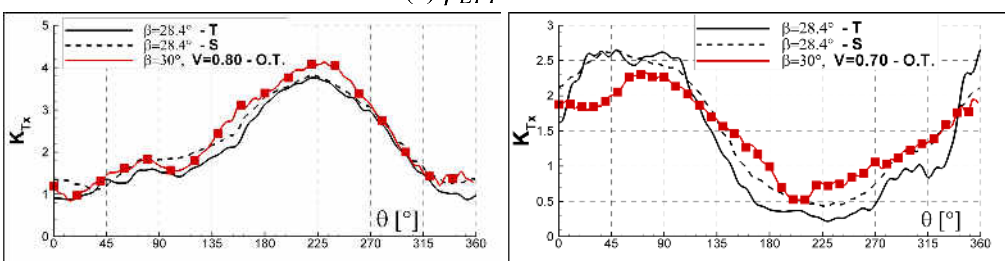

(d) $\beta_{EFF} = 28.4°$

Figure 6.22 Single blade thrust. Left: external propeller; right: internal propeller

On the internal propeller, K_{Tx} generated during TRA at $\beta_{EFF} = 8.4°$ increases in the upper half of the disk and drops in the lower half of the disk with respect to rectilinear condition (orange colored line), see figure 6.22a on the right. In more detail, in straight ahead the signal features two peaks at $\theta \sim 45$ and $120°$, caused by the perturbation of the bracket and velocity gradients of the hull wake (axial velocity defect and upwards component) respectively. From the early stage of the transient, only the peak about $\theta = 100°$ is visible. In fact, the lateral flow induced by the motion deflects the boundary layer of the hull to the leeward side, causing the increase of the incidence of the blades during the passage in the 1^{st} quadrant. In the lower half, $90° < \theta < 270°$, the cross flow acts to reduce the load, it being oriented in the same sense of blade rotation. Although the trend agrees with ST and OT, the most evident discrepancies are experienced in the upper half of the disk as a consequence of the perturbation from SV, already mentioned in section 6.4.1 (see figure 4.7b), and added mass effect. In fact, with respect to ST (dashed line), the velocity defect past the inner bracket is stronger, because the equivalent sections of the foil are thicker due to added mass. On the other hand, SV and velocity defect are stronger for the reported condition of OT, because it is generated at higher absolute speed and incidence angle, constant along the appendages. As a result, in the upper half of the disk the blade would be affected by a stronger tangential flow that increases the hydrodynamic incidence of the blades.

These effects are amplified at $\beta_{EFF} = 15.5°$ (figure 6.22b), because the acceleration of the model is yet higher and the differences in absolute speed (with respect to ST) increased. In fact, the peak of K_{Tx} experienced during TRA at $\theta = 45°$, associated to the interaction of the blade with SV, is 10% stronger with respect to the oblique towing and steady turning, see figure 4.7b. Since the speed drop is markedly smaller than the ST and OT, this structure is stronger and, hence, its disturbance. Moreover, the growth rate of the load is faster, also because the lighter loading condition causes the blade to be more sensitive to velocity gradients. On the contrary, K_{Tx} in the lower half of the disk is smaller, since the cross flow, oriented to reduce the flow incidence of the blade sections, is higher. In the 4^{th} quadrant, K_{Tx} experiences a faster grow rate with respect to ST probably because the blade encounters a stronger velocity defect past the shaft and outer brackets ($\theta = 340°$) due to both added mass effect and faster cross–flow. In the sector $180° < \theta < 360°$, during OT, the thrust is higher, probably because the inflow is characterized by a more complex wake with strong reduction of axial velocity originated by the constant value of β_{EFF}. At $\beta_{EFF} = 22.4°$ (figure 6.22c), the evolution of the loads is driven by the complex flow field that results from the interplay between SV and the wake of appendages. This interaction gives rise to MV, that is the counterclockwise rotating swirling flow that is lee–positioned with respect to the propeller at the maximum drift angle, see figure 4.7c. At this drift angle, MV is in–between position reported in the figures, plausibly almost centred with the propeller disk and globally induces a velocity field that is concordant with the rotation of the blades. A plausible situation of the vortex field affecting the leeward propeller is visualized in figure 6.23 (Muscari et al. (2017)) and it is considered in the following discussion. During TRA, the cross–flow and MV are stronger with respect to ST due to the higher absolute speed (lower speed drop). As a consequence of the stronger interaction with MV, the wake shed from the brackets is disrupted and the velocity defect is amplified. Moreover, it is reduced with respect to $\beta = 15.5°$ because the overloading effect of the cross flow is counteracted by the contribution of MV. Therefore, K_{Tx} is greater than ST for a portion of the 1^{st} quadrant ($0° < \theta < 60°$), although the propeller loading is nominally lighter. During ST, in this sector, blade thrust grows at a larger rate that culminates to the peak at $\theta = 90°$: this fact can be associated to the interaction of the blade with the wake shed past the external shaft. As it can be clearly evidenced from figure 6.23, during steady motion (panel on the right) the vortex system detached from the windward shaft, made of intertwined longitudinal and transverse structures features, seems larger with respect to the one developed during TRA. Moreover, in this case the longitudinal structures can be engulfed by the stronger MV. During the blade passage in the 2^{nd} and 3^{rd} quadrants K_{Tx} is lower than ST, because the tangential flow relative to the blade sections is reduced by the stronger cross–flow, further enhanced by the induced velocity of MV. Moreover, in the 4^{th} quadrant, it is interesting to observe that, the interaction of the blade with the wake of the shaft and brackets during TRA is strengthened with respect to ST, as proved by the abrupt increase of the load in the two sectors $280° < \theta < 320°$ and $320° < \theta < 360°$. During OT, K_{Tx} exhibits the same trend of the peak for the transient maneuver (see sequence of left panels in figures 6.22b and 6.22c). However, it seems smoother, because the wake generated by the constant distribution of β_{EFF} along hull and appendages could break further the coherency to give onset to swirling flow characterized by larger spatial scales. As discussed for the previous case, this can also cause a stronger velocity defect that causes the blade to operate at lower equivalent advance coefficient and, hence, develop higher thrust in the remaining sector of the cycle.

At $\beta = 28.4°$ (figure 6.22d), during ST, the peak of K_{Tx} reduces and shifts to lower phase angle ($\theta \sim 50°$). This reduction is probably ascribed to the effect of MV, see figure 4.7c: the induced velocity, downward oriented, acts to weaken the tangential flow from the wind side and counteracts the leeward convection of the wake of the inner bracket. It is interesting to observe that the trend is quantitatively analogous during TRA, although in that case the signal is characterized by two peaks at $\theta = 45°$ and $90°$. The first peak is more definite probably because the velocity defect past the inner bracket is thinner. In fact, as a consequence of the lower speed drop, both the magnitude (and the perturbation) of MV and cross flow are stronger than ST. On one side, the cross flow pushes the wake past the bracket to the leeward side while, on the other, MV blocks it. Analogously, the second fluctuation about $\theta = 90°$ can be associated to a stronger velocity defect induced by the wake past the external shaft. In this case, the shaft structures are not entrapped and disrupted by MV, since it is farther from the disk. The signature of shaft structures can be grasped in figure 4.7c. In the 4^{th} quadrant, the velocity induced by MV is oppositely oriented with respect to the blade motion and, therefore, acts to increase the load. Moreover, MV is stronger during transient, given the lower speed drop. This is confirmed by the fact that K_{Tx} is smaller during TRA with respect to ST and rises abruptly after the interaction with the wake past the shaft. In case of the oblique towing, MV could be formed by the merging of stronger structures, given globally higher incidence along the hull. In turns, its effect perturbs the whole inflow distribution over the disk more critically, causing K_{Tx} to be higher in the lower half of the period. In the remaining interval of the cycle, the trend of the loads is similar to the previous case (figure 6.22c), given the almost similar perturbation induced by this coherent structure.

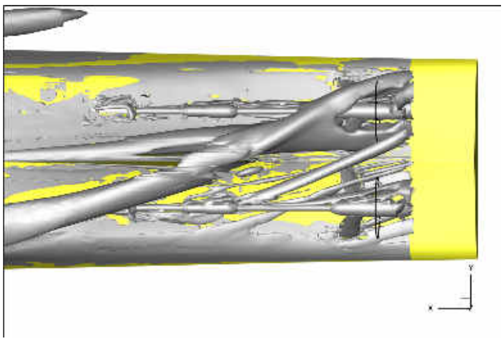

(a) transient

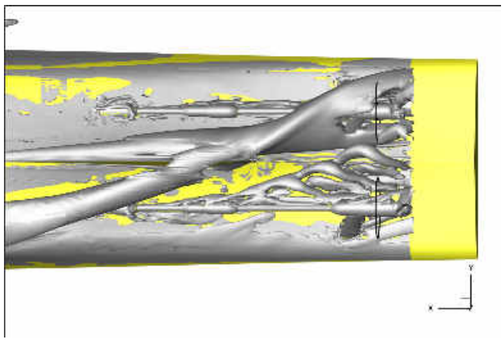

(b) steady

Figure 6.23 Comparison between vortical structures morphology during transient and steady phase

On the external side the cross flow is essentially dominated by the cross flow induced by the motion, as demonstrated by the sinusoidal trend of the signal with no evidence of phase shifts for the cases considered. The blade experiences the maximum value in the lower half of the cycle where the cross flow is opposed to blade rotation and the flow impinges the blades with an higher angle of attack. However, the interaction between the blade and wake structures can be evidenced, in particular at smaller drift angles, and differences between the evolution of the loads can be more directly ascribed to mismatch of speed drop and wake formation past the hull and appendages.

In more details, at $\beta_{EFF} = 8.4°$, K_{Tx} developed during TRA and ST are very similar to each other, see figure 6.22a on the left panel. In the 1^{st} quadrant, the load gradually increases, because the component of the cross–flow tangential to the section of the blades (that acts to mitigate the incidence angle) reduces and, at the same time, the blade is going to interact with the wake of the inner bracket, clearly visible in figure 4.7b. Since the blade loading is lighter during TRA, the thrust is smaller and, when the blade interacts with the wake of the bracket, at about $\theta = 45°$, it experiences a more severe oscillation with respect to ST. On the other hand, albeit the different speed drop, the thrust of TRA is almost coincident with ST in the lower half of the disk, $90° < \theta < 270°$. Since the accelerations are dominant in the early stages of the transient, it can be inferred that the flow is deflected and more accelerated by the added mass carried by the shaft. Therefore, the blade foils are impinged by a stronger tangential flow that, being opposite to blade rotation, further increases the load. In the 4^{th} quadrant K_{Tx} decreases, because both the axial and tangential components of the wake act to reduce the load. The discrepancy between the blade thrust developed during TRA and ST can be motivated, in addition to the propeller loading, with the different interaction with FV vortex. From the wake field showed in figure 4.7a, it can be inferred that this vortex at smaller drift angle is yet coherent and, being counterclockwise, induces a tangential flow oriented with blade rotation that reduces the blade load. This effect is magnified during the transient and oblique towing. In the former case, FV is stronger with respect to ST as a consequence of the higher absolute velocity of the model. On the other hand, during OT, FV, being detached with higher incidence due to the constant drift distribution, is convected more inward to trigger stronger interaction with the wall and wake of the brackets. Finally, it can be observed that in the sector $90° < \theta < 130°$, K_{Tx} developed during OT is lower than the steady turning, due to localized differences of the wake caused by the constant distribution of drift angle. At $\beta_{EFF} = 15.5°$, the TRA and ST differ in the last half of the 4^{th} quadrant, due to disparity of propeller loading. In the remaining interval of the period, the two loads almost coincide. As in the previous case, K_{Tx} generated during OT is strongest in the upper half of the disk due to increment of velocity defect associated to the constant distribution of the drift angle. At $\beta_{EFF} = 22.4°$ the remarkable discrepancy between TRA and ST is caused by propeller loading, the difference of speed being higher than 20%, see figure 6.18. Finally, at $\beta_{EFF} = 28.4°$, the TRA is lower than ST phase in the whole period due to the higher advance speed (and lighter propeller loading) except close to the peak, because of the added mass effect of the shaft that acts to increase the tangential flow relative to the blade sections.

On the other hand, during OT K_{Tx} is always higher with respect to free running, because the differences on the evolution of the wake field are further triggered by the different drift distribution.

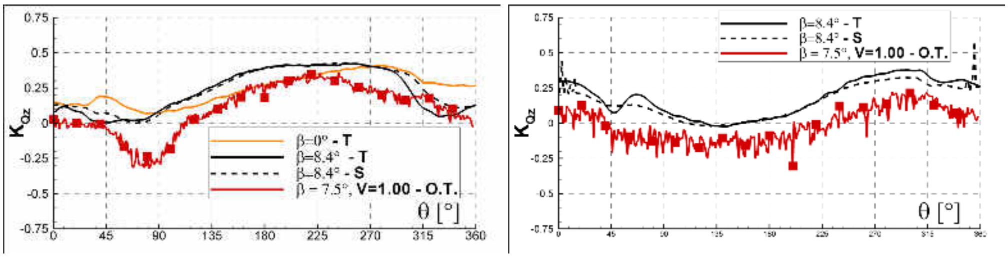

(a) $\beta_{EFF} = 8.4°$

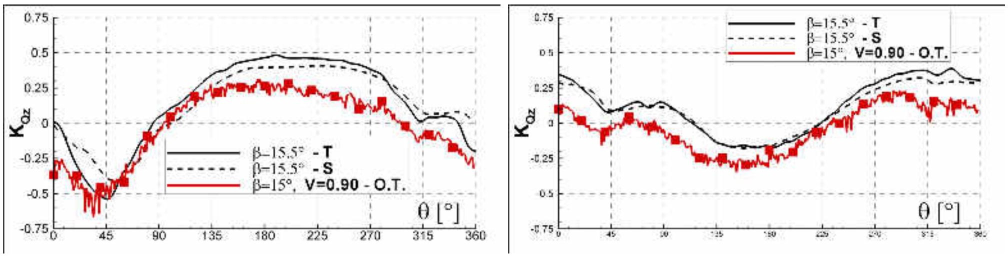

(b) $\beta_{EFF} = 15.2°$

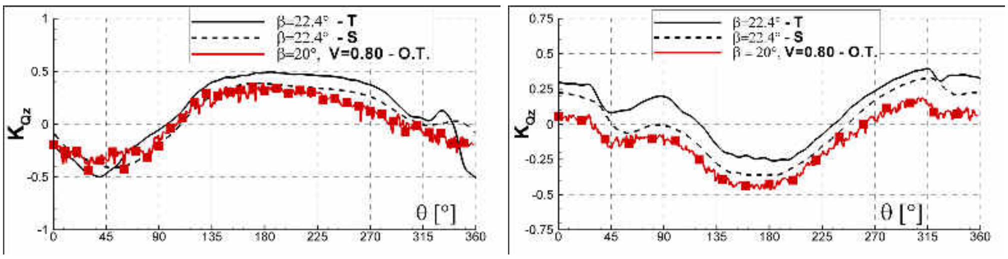

(c) $\beta_{EFF} = 22.4°$

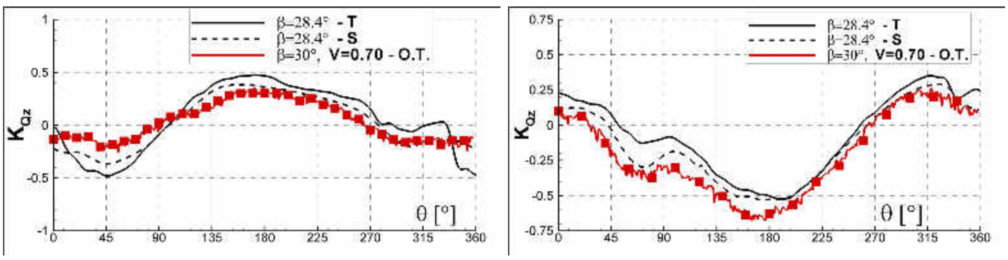

(d) $\beta_{EFF} = 28.4°$

Figure 6.24 Single blade spindle torque. Left: internal propeller; right: external propeller

The behavior of the spindle torque is reported in figure 6.24. In general, the trend of K_{Qz} is consistent with propeller loading and its variation, according to the simplified model already introduced for a skewed blade. In fact, K_{qz} decreases in contrast to the growth of propeller loading, that is, the hydrodynamic centre tends to move to the inward sections and to the leading edge (see the sign convention in figure 4.1). In this case, the TRA seems in very good agreement with the ST in contrast to the oblique towing tests. In general, the TRA and ST deviates for the external propeller at $\beta_{EFF} = 22.4°$ (figure 6.24c) because the highest difference in speed drop (i.e., propeller loading). The poorer quantitative accordance between OT and the free running results stresses that this load can be very sensitive to alterations of the wake field associated to the constant drift distribution. The evolution of the single blade thrust and spindle torque evolution during the PO phase of the turning circle at $\delta = 35°$ are showed in figures 6.25 and 6.26, respectively. In the plots, the cycle experienced during the TRA is also included to better highlight the discrepancies and, at the same time, to better highlight the differences of the cause–and–effect analysis. The oblique tests are not discussed, since these can be deduced on the basis of the following considerations. In general, the matching of the PO with steady condition is less satisfactory than the TRA, because the relative difference of propeller loading (and speed drop) is further amplified (see figure 6.18). In facts, the loads developed during PO and ST at varying β_{EFF} diverge over the cycle by an amount that is comparable to the discrepancy between the correspondent speed drop showed in figure 6.18. However, on the internal propeller, the consequences of speed drop combines with stronger propeller/wake interaction. This is evident, for example, at $\beta_{EFF} = 22.4°$: although the propeller is highly loaded during the pull–out, in the 1^{st} quadrant the trend of K_{Tx} matches with ST according to the role played by SV.

Specifically, SV impinges the disk in the 1^{st} quadrant (on the basis of the behavior of the in–plane loads discussed in section 6.4.1) and, at the same time, it is weaker and smaller with respect to ST as a consequence of the lower absolute speed. Hence, it induces a slower tangential velocity and, consequently, lower increment of angle of attack (and load) with respect to steady turning. Moreover, the weaker blockage of SV during PO provokes, in combination with the added mass of the shaft, the upwards deflection of the cross flow about $\theta = 90°$ to be weaker with consequent reduction of the developed thrust. These effects drive also the behavior of the blade loads at $\beta_{EFF} = 15.5°$, see figure 6.26b on the left panel. In the 1^{st} quadrant, the peaks of K_{Tx} during TRA and PO are oppositely phase–shifted with respect to the steady turning phase. In case of PO, SV is weaker and smaller as well as its blockage effect. Thus, the cross flow evolves in between the vortex and the shaft more upwards inclined, causing the blade to be impinged by a faster tangential flow at greater θ with respect to the analogous situation during TRA. This phenomenon seems consistent with the phase shift of the fluctuation of K_{Tx} the 4^{th} quadrant during TRA and PO, see figure 6.25b, that can be ascribed to the interaction of the blade with the wake shed past the shaft. In fact, as a consequence of the different inclination the cross flow impacts the propeller shaft, the sector with minimal tangential velocity and velocity defect visible in the 4^{th} quadrant in figure 4.7b would be crossed over by the blade at different azimuth. Finally, at $\beta_{EFF} = 8.4°$, the trend of the loads is markedly similar, although the deviation of the mean value is caused by the different loading state of the propeller during *ST* and *TRA*. The trend is different in the 4^{th} quadrant, probably because in this sector the blade is less sensitive to unsteady interaction with the wake shed by the shaft and starboard bracket.

On the external propeller, the same qualitative considerations provided for the *TRA* hold. The similarity of the trend of the signal and their phase alignment stress the dominant effect of speed drop, while differences ascribed to wake evolution matter locally. This is proved by the fact that the deviation of *PO* is almost constant during all the cycle and it resembles the same trend of the percentage discrepancy of the speed drop reported in figure 6.18.

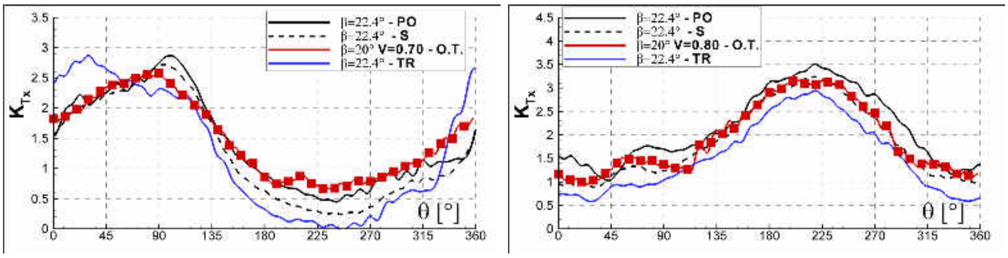

(a) $\beta_{EFF} = 22.4°$

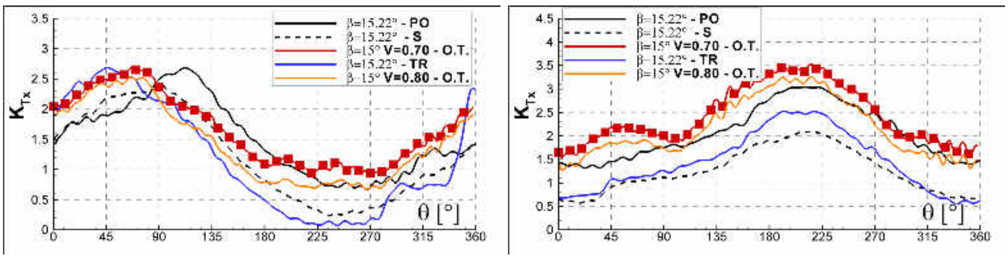

(b) $\beta_{EFF} = 15.5°$

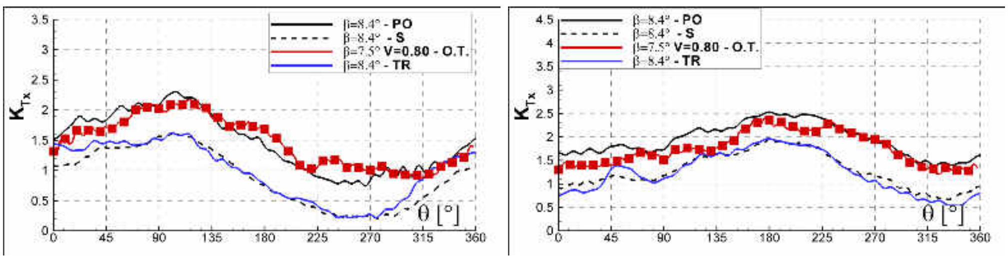

(c) $\beta_{EFF} = 8.4°$

Figure 6.25 Single blade Thrust during *PO*, $\delta = 35°$

The results of the spindle torque in *PO* is reported in figure 6.26 for the sake of completeness, essentially confirm the same behavior observed for the TRA phase, in particular the sensitivity of this load to the loading state of the blade.

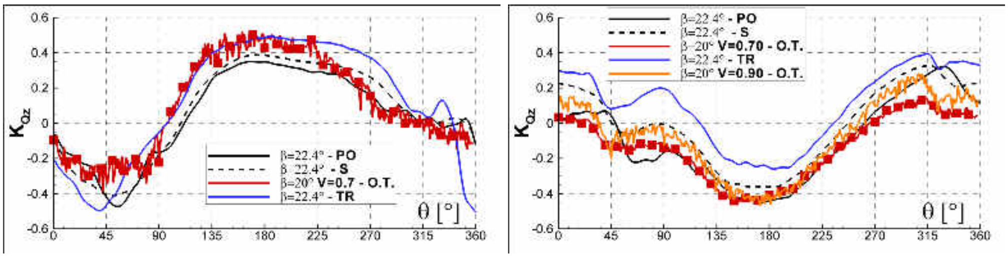

(a) $\beta_{EFF} = 22.4°$

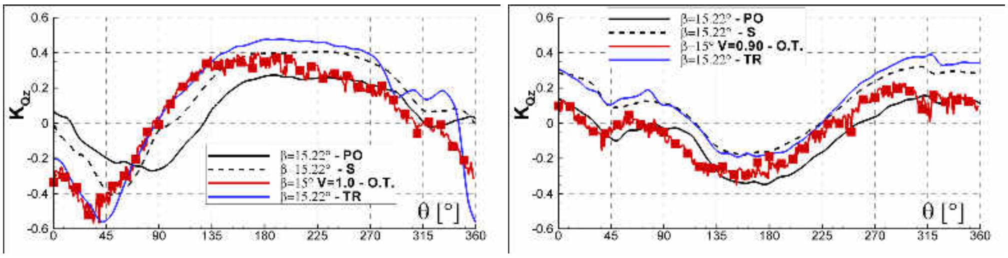

(b) $\beta_{EFF} = 15.5°$

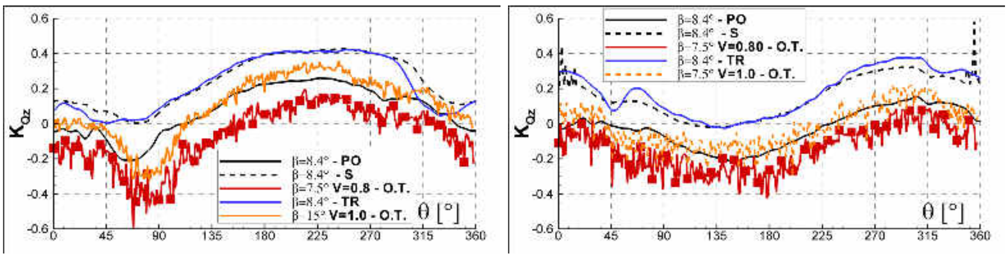

(c) $\beta_{EFF} = 8.4°$

Figure 6.26 Single blade Spindle Torque during *PO*, $\delta = 35°$

Finally, the impact of the severity of the maneuver on the evolution of the blade loads is analyzed by the comparison of transient phases correspondent to the turning maneuvers at $\delta = 15°$ (TRA_{15}) and 35° (TRA_{35}), see figures 6.27 and 6.28. The general inspection of the behavior of K_{Tx} emphasizes that the most evident discrepancy between the two transients is experienced by the internal propeller due to interactions with the wake, see figure 6.27a on the right.

In particular, during TRA_{15} at $\beta_{EFF} = 8.4°$, K_{Tx} experiences a peak that is stronger with respect to the tightest maneuver by almost 20%. This is probably consequent to the fact that *SV* is more coherent, due to the lower speed drop (high speed) of the model at same equivalent drift. As a consequence, the tangential velocity induced in the 1^{st} quadrant is stronger and amplifies the hydrodynamic incidence of the blades. At the same time, in the 4^{th} quadrant the blade develops lower thrust, probably because the upward distortion of the incoming cross–flow due to added mass of the propeller shaft is weaker due to smaller lateral acceleration. At the highest drift angle, $\beta_{EFF} = 15.5°$, K_{Tx} generated during TRA_{15} matches with the ST, because the motion is establishing the steady phase of the turn. Similarly, in case of the external propeller, as a consequence of the weaker phenomena related to blade–wake interactions with respect to the internal propeller, the signals are in better agreement with each other and converge to the steady state at the highest drift angle. The trend of the spindle torque is consistent with the loading state of the blade, see figure 6.28. As stressed for the other manuevering conditions, K_{Qz} developed during OT captures the trend of the free running maneuvers, although it is shifted in mean value due to the higher sensitivity to alteration of the wake as well as the constrained motion in the transverse plane.

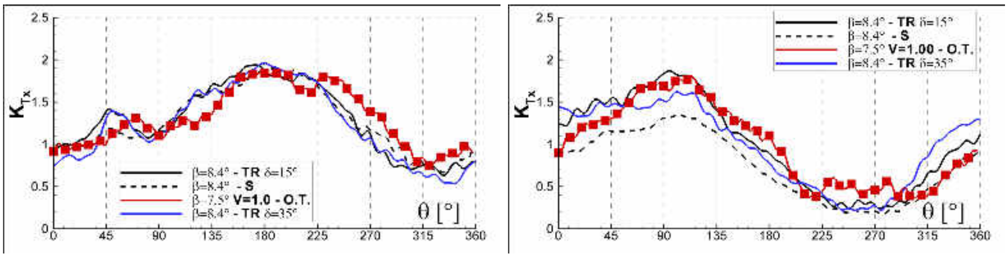

(a) $\beta_{EFF} = 8.4°$

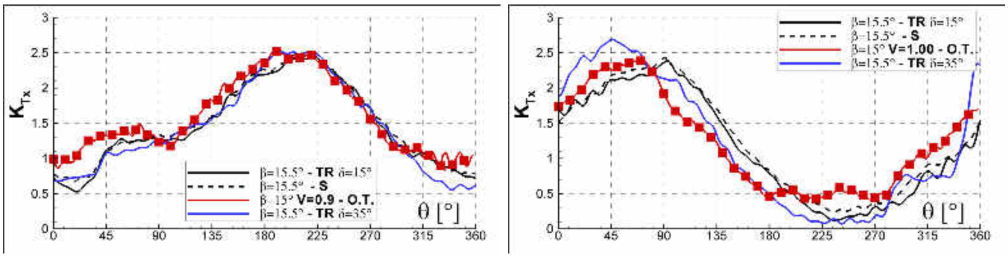

(b) $\beta_{EFF} = 15.5°$

Figure 6.27 Single blade Thrust during TRA, $\delta = 15°$

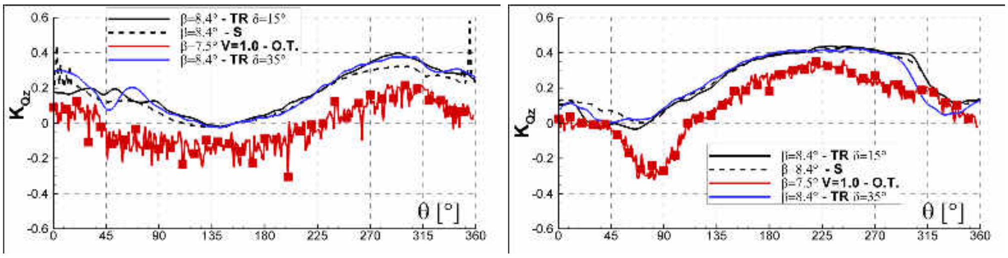

(a) $\beta_{EFF} = 8.4°$

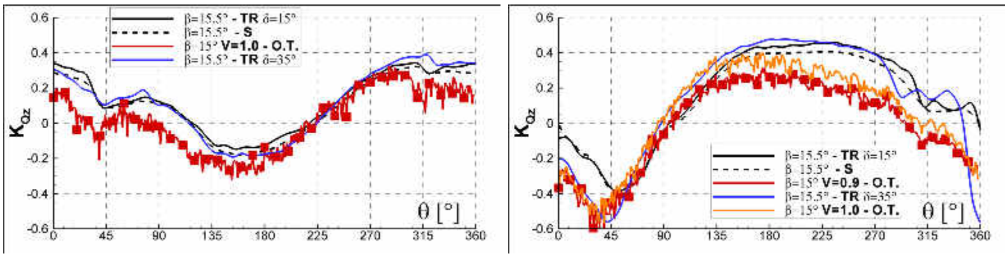

(b) $\beta_{EFF} = 15.5°$

Figure 6.28 Single blade Spindle Torque during TRA, $\delta = 15°$

6.5.3 Harmonic analysis

The harmonic analysis of K_{Tx} developed during ST, TRA and OT is reported in figure 6.29 for the conditions at $\beta_{EFF} = 15°$.

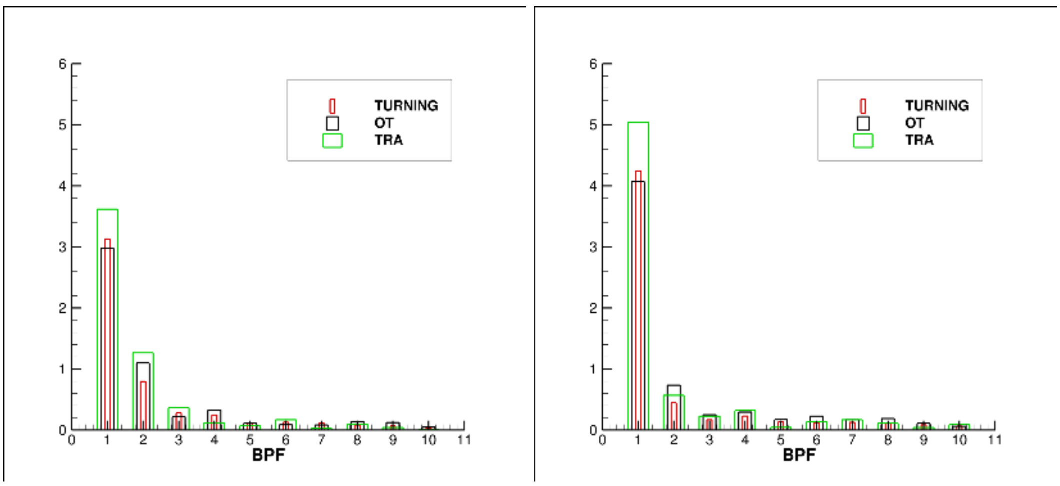

Figure 6.29 Harmonic content of K_{Tx}. Left: external propeller; right: internal propeller

The harmonic content of the signal is dominated by tonal components (multiples of the blade passing frequency - BPF) in the low frequency interval of the spectrum, consistently with the fact that the cavitation phenomena were absent and the evolution of the time histories discussed in the previous section. The harmonics drop abruptly and the signals are dominated by the 1^{st} and 2^{nd} BPF. For this reason, the detailed evolution of the amplitude of the harmonics of single blade thrust and spindle torque is showed only for the 1^{st} and 2^{nd} BPF are showed in figures 6.30 and 6.31, respectively.

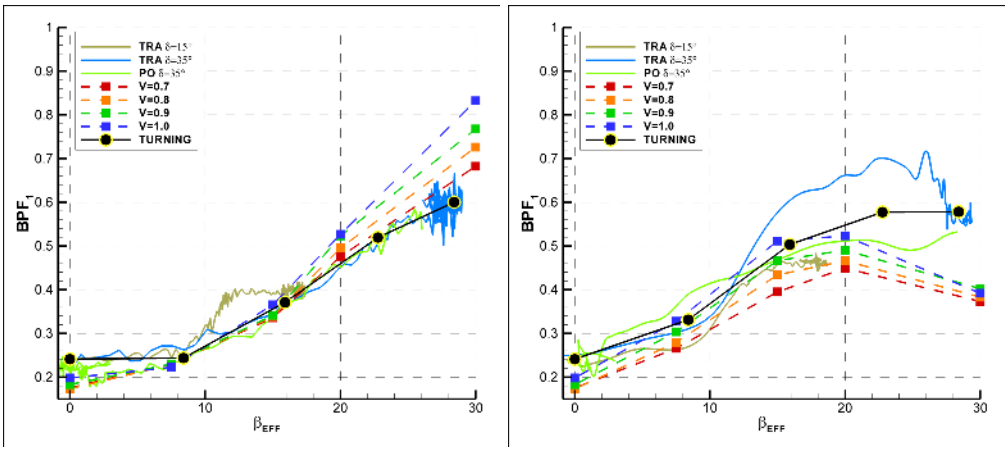

(a) K_{TX}

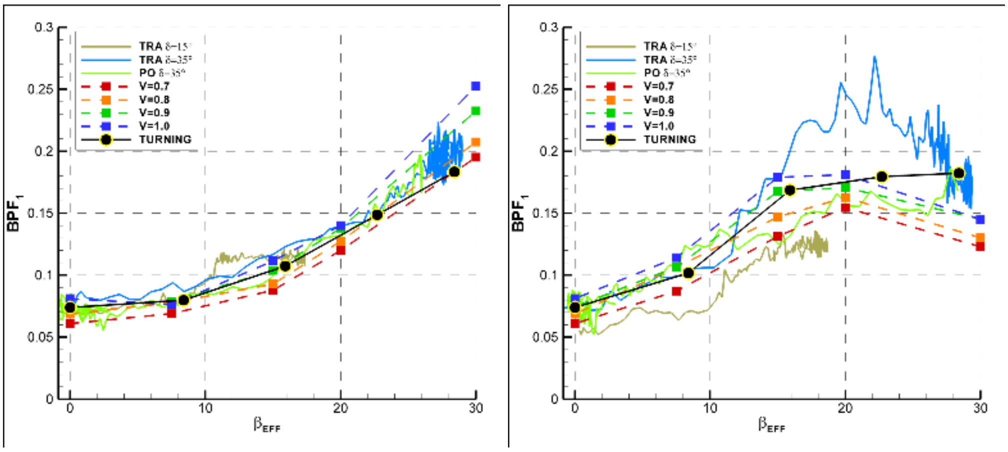

(b) K_{QZ}

Figure 6.30 Comparison between transient and steady maneuvers by oblique towing and turning maneuver. Harmonic analysis - 1^{nd} BPF. External (left) and internal (right) propeller

It is evident that the blade loads are dominated by the 1^{st} BPF, given the similar trends of Δ_L and the harmonics and in figure 6.21 and 6.30. This is also corroborated by their relative magnitude: from the transient and steady state values, the 1^{st} BPF is almost four and three times larger than the 2^{nd} BPF on the external and internal propeller, respectively.

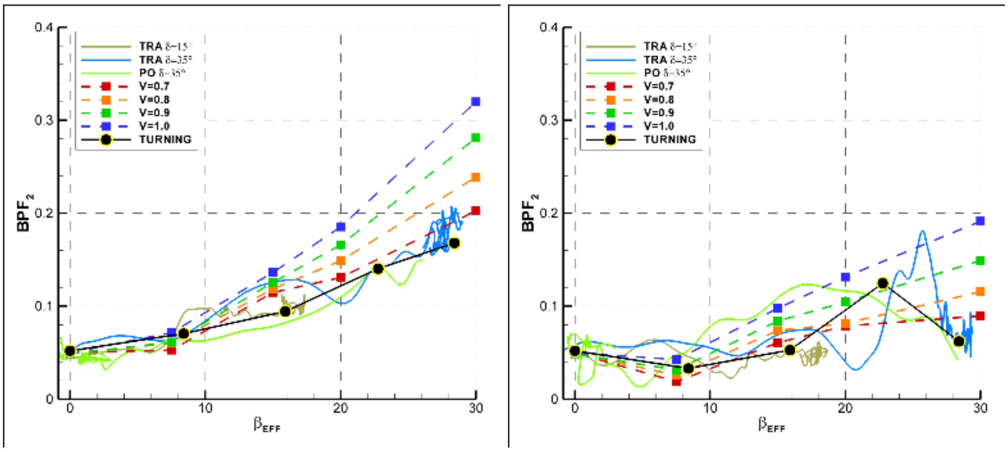

(a) K_{TX}

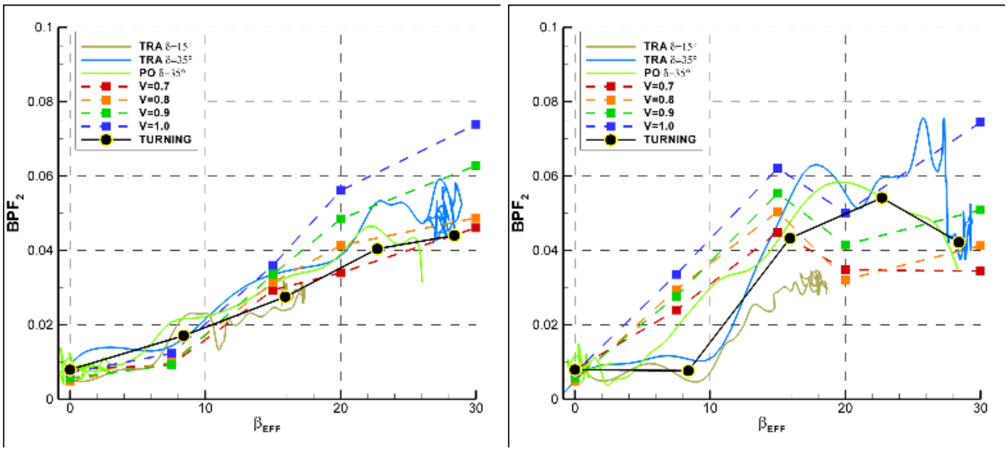

(b) K_{QZ}

Figure 6.31 Comparison between transient and steady maneuvers by oblique towing and turning maneuver. Harmonic analysis - 2^{nd} BPF. Left: external propeller; right: internal propeller

On the external side, the harmonics of K_{Tx} and K_{Qz} increase monotonically with the increase of the β_{EFF}. Conversely, on the internal side the trend is non linear, the magnitude establishing (1^{st} BPF) or decreasing after $\beta_{EFF} \sim 20°$. These trends are confirmed by the oblique towing tests. In general, it is interesting to observe that the discrepancy between the harmonics associated to different propeller loading smoothly increases for 1^{st} BPF on the external propeller, whereas it is markedly stronger for the second component for both external and internal propellers. The deviations with the transient and steady state results are consistent with those observed for the absolute fluctuation. In general it can be evidenced that for the external propeller and the 2^{nd} BPF of the internal one, the free running data fall inside the band spanned by $O.T.$ for both blade thrust and spindle torque, see panels on the right in figures 6.30 and 6.31. Conversely, the 1^{st} BPF of thrust and spindle torque developed by the blade of the internal propeller is under predicted at highest drift angles.

Chapter 7

Conclusions

The present dissertation has concerned the study of propeller performance during off-design condition, with an experimental and phenomenological approach. A novel measurement system has been developed by the author, which provides the complete set of loads (three forces and three moments) acting on the single blade of a naval propulsor.

A detailed description of its development, main features and preliminary capabilities assessment has been reported. The system has been installed on a twin screw ship scaled model and several experimental campaigns, both in free running and in captive model, have been conducted, in order to investigate propeller performance during a wide range of real off-design, in behind hull, operative conditions. The novel measuring system allowed to determine the cause-effect relation between inflow characteristics and blade loads during the cycle.

The study confirmed the markedly different behaviour of the propeller when it works on the windward or leeward side of the maneuver. In fact, the propeller on the external side experiences an inflow which is very close to a pure oblique flow and the increase of the loads is almost linear with the rudder angle. This propeller is subjected to a more critical condition with respect to the internal one at maximum rudder angle: the overloading (for both single blade and whole propeller) of thrust and torque is higher than 100% and 60% compared to the rectilinear motion and it is almost doubled with respect to the propeller on the leeward side. The blade loads measurement showed that this abrupt increase has to be ascribed to the cross–flow induced by the motion, which acts to increase the relative tangential flow with respect to the blade section in the lower half of the disk and, consequently, the incidence angle and the developed loads. The imbalance of the loads between the upper and lower halves of the propeller disk causes also the development of the side force and pitching moment (higher with respect to the leeward side), that correspond respectively to about 30%

and 80% of the axial thrust and torque developed in straight ahead motion. On the other hand, on the internal side, the propeller hydrodynamics is strongly affected by the interaction with complex vortex structures, which originate from hull appendages, and the cross-flow induced by the motion. The vortexes themselves evolve, depending on the severity of the manoeuvre. The dominance of one effect with respect to the other at different conditions is the reason of the non–linear variation of the loads with rudder angle. The complexity of those interactions is confirmed by the side investigation performed by means of the Fourier analysis of loads: it highlighted the higher harmonic content of leeward propeller, which being overall less loaded than windward one, is more subjected to higher amplitude vibrations. Another result is the trend of the spindle torque with propeller loading and drift angle: it showed a non–linear behaviour with drift angle for both propellers and its variation with propeller loading, observed also for the periodic load, was consistent with the movement of the point of action of hydrodynamic forces to inner blade radii with the increase of load. The thesis is also focused on the comparison of the single blade loads obtained with towing test with the free running results of the same reference speed (correspondent to $F_N = 0.26$) and equivalent (or close) drift angle, in order to assess the reliability of towing tank experiments to reproduce, through quasi-steady tests, the different maneuver conditions and to investigate the off–design performance of the propeller, highlighting critical conditions. The blade loads obtained with captive model tests are in good agreement with steady turning regime obtained by free running test, in terms of absolute values and split contribution of the source loads over halves of the disk. Namely, best results have been obtained for the external propeller, given the simpler nature of the (unperturbed) flow; on the leeward propeller, quite evident discrepancies arose, especially in the first half of the cycle characterized by the most severe propeller/wake interactions. These differences are associated to alterations of the inflow caused by removing roll and yaw motion during the oblique towing tests, this last being the cause of an uniform speed distribution along the hull which does not reflect the real operative condition during free running tests. Nevertheless, the non linear evolution of the loads, associated to complex blade/wake interaction and hydrodynamic interference, is captured.

In the face of such peculiar results and the opportunity to apply this experimental technique in other conventional hydrodynamic tests (i.e. seakeeping, cavitation tunnels), one of the most important outcomes of the present research is the development of this new experimental setup, which has made it possible to reach such a great detail in propeller/wake interaction insight and reveal the marked oscillating and rapid time-varing nature of single blade loads, that is not possible to investigate through the use of traditional measuring systems.

In a broader view, if applied to benchmark or unclassified models, the proposed research, beside the investigation of hydrodynamics phenomena related to propeller operation through the development of a novel measurement system and the assessment of blade loads in off-design conditions, could provide a valuable dataset for the validation of CFD simulations, the structural analysis of a propulsive system and noise evaluation across a larger research community. Moreover, it aims to contribute to lay the basis for the enhancement (see Figure 7.1) of comprehensive ship system mathematical models, already used in ship design.

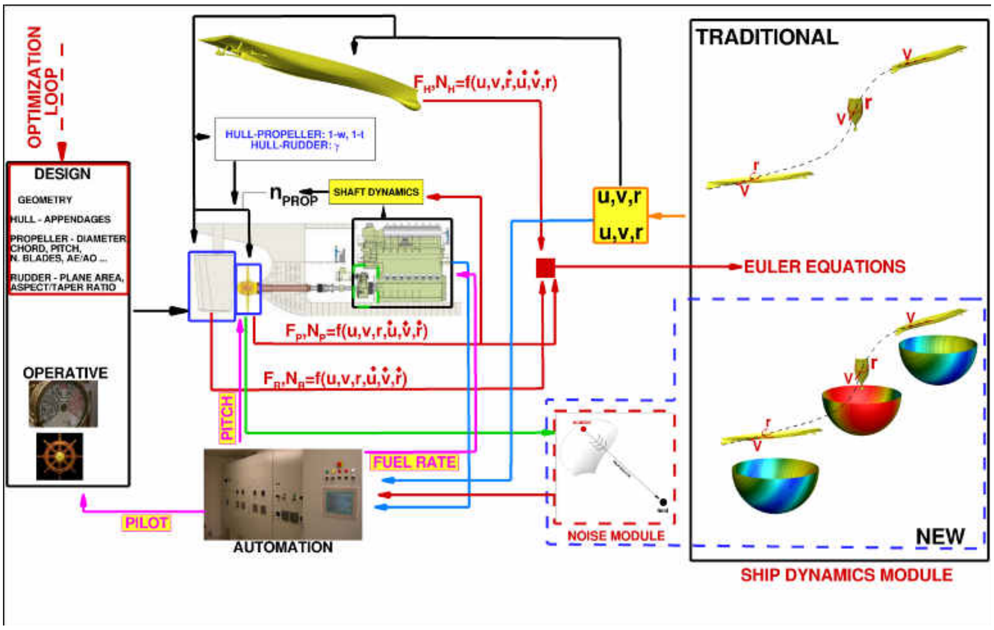

Figure 7.1 Comprehensive model structure

In particular, these tools, being the core of training simulators and mission planning software, can be executed in real–time as a support of operators, thanks to the advance of computational resources. In this framework, the enhancement of these computational methodologies by real–time analysis of loads, vibrations and emitted noise, used both for preliminary forecast of ship performance and during navigation, can support the design of lower mechanical stress and low noise mission profiles. In fact, with the aim of expanding the scope of this investigation, the loading state of the blade obtained by the present measuring technique inherently provides a lumped description of the noise source associated to the propeller dipole, or at least, it characterizes the incident load that contributes to the complete hull–propeller scattering problem.

If the total noise field is measured during the experimental activities, the availability of the loading noise in principle simplifies the identification of other sources, for example those related to turbulence. Moreover, since the computation of the loading noise (and thickness) noise for a single source is computationally cheap, the real time availability of the blade loading can be included in real time control strategies in a straightforward way. This approach is currently under validation by the aid of CFD simulations with rotating propellers and, obviously, should be verified by field measurements. This is a current research activity by the author.

References

Altosole, M. and Martelli, M. (2017). Propulsion control strategies for ship emergency manoeuvres. *Ocean Engineering*, 137:99 – 109.

Amini, H. and Steen, S. (2011). Theoretical and experimental analysis of propeller shaft loads in oblique flow. *Journal of Ship Research*, 55(4):268–288.

Amini, H. and Steen, S. (2012). Theoretical and experimental investigation of propeller shaft loads in transient condition. *International Shipbuilding Progress*, 59:55–82.

Atsavapranee, P., Miller, R., Day, C., Klamo, J., and Fry, D. (2010). Steady-Turning Experiments and RANS simulations on a Surface Combatant Hull form (Model#5617). In *Proc. of* 28^{th} *Symposium on Naval Hydrodynamics*, Pasadena, California.

Berchiche, N., Krasilnikov, V., and Koushan, K. (2018). Numerical analysis of azimuth propulsor performance in seaways: Influence of oblique inflow and free surface. *Journal of Marine Science and Engineering*, 6(2):1–24.

Blaurock, J. (1975). Propeller blade loading in non-uniform flow. In *Propellers Symposium*.

Boswell, R., Jessup, S., and Kim, K. (1981). Periodic blade loads on propellers in tangential and longitudinal wakes. In *Propellers Symposium*.

Boswell, R., Nelka, J., and Denny, S. (1976). Experimental unsteady and mean loads on a cp propeller blade on a model of the ff-1088 for simulated modes of operation. Technical Report No. 76-0125, David Taylor Naval Ship Research and Development Center (DTNSRWDC).

Breslin, J. and Andersen, P. (1994). *Hydrodynamics of ship propellers*. Cambridge University Press, Cambridge, second edition.

Calcagni, D., Dubbioso, G., Capone, A., Ortolani, F., and Broglia, R. (2021). A generalized hybrid ranse/bem approach for the analysis of hull–propeller interaction in off-design conditions. *Journal of Marine Science and Engineering*, 9(5).

Carrica, P. M., Sadat-Hosseini, H., and Stern, F. (2012). Cfd analysis of broaching for a model surface combatant with explicit simulation of moving rudders and rotating propellers. *Computers and Fluids*, 53:117 – 132.

Castro, A. M., Carrica, P. M., and Stern, F. (2011). Full scale self-propulsion computations using discretized propeller for the kriso container ship kcs. *Computers and Fluids*, 51:35 – 47.

Coraddu, A., Dubbioso, G., Mauro, S., and Viviani, M. (2013). Analysis of twin screw ships' asymmetric propeller behaviour by means of free running model tests. *Ocean Engineering*, 68:47–64.

Dubbioso, G., Muscari, R., and Mascio, A. D. (2013). Analysis of the performances of a marine propeller operating in oblique flow. *Computers and Fluids*, 75:86 – 102.

Dubbioso, G., Muscari, R., and Mascio, A. D. (2014). Analysis of a marine propeller operating in oblique flow. part 2: Very high incidence angles. *Computers and Fluids*, 92:56 – 81.

Dubbioso, G., Muscari, R., Ortolani, F., and Di Mascio, A. (2017). Analysis of propeller bearing loads by CFD. Part I: Straight ahead and steady turning maneuvers. *Ocean Engineering*, 130:241–259.

Dubbioso, G., Muscari, R., Ortolani, F., and Di Mascio, A. (2020). Numerical analaysis of marine propellers low frequency noise during maneuvering. *Applied Ocean Research*, 71:399–419.

Dubbioso, G. and Ortolani, F. (2020). Analysis of fretting inception for marine propeller by single blade loads measurement in realistic operating conditions. straight ahead and turning circle maneuver. *Marine Structures*, 71:102720.

Funeno, J., Pouw, C., and Bosman, R. (2013). Measurements and computations for blade spindle torque of controllable pitch propellers in open water. In *Proc. of* 3st *Symposium on Marine Propellers and Propulsion*, Tasmania, Australia.

Gaggero, S., Dubbioso, G., Villa, D., Muscari, R., and Viviani, M. (2019). Propeller modeling approaches for off–design operative conditions. *Ocean Engineering*, 178:283 – 305.

Grigoropoulos, G., Campana, E., Diez, E., Serani, A., Goren, O., Sarioz, K., Danisman, D., Visonneau, M., Queutey, P., Abdel-Maksoud, M., and Stern, F. (2017). Misson–based hull form and propeller optimization of a transom stern destroyer for best performance in the sea environment. In *Proc. of* 7th *MARINE*, Nantes, France.

Hagesteijn, G., Brouwer, J., and Bosman, R. (2012). Development of a six–component blade load measurement test setup for propeller–ice impact. In *Proc. of* 31rd *International Conference on Ocean, Offshore and Arctic Engineering*, Rio de Janeiro, Brazil.

Jessup, S. (1990). Measurements of multiple blade rate unsteady propeller forces. Technical Report No. DTRC-90/015, David Taylor Naval Ship Research and Development Center (DTNSRWDC).

Jessup, S. and Boswell, R. (1982). The effects of hull pitching motions and waves on periodic propeller blade loads. Technical Report No. 82-093, David Taylor Naval Ship Research and Development Center (DTNSRWDC).

Jessup, S., Boswell, R., and Nelka, J. (1977). Experimental unsteady and time averaged loads of the cp propeller on a model of the dd963 class destroyer for simulated modes of operations. Technical Report No. 77-0110, David Taylor Naval Ship Research and Development Center (DTNSRWDC).

Jessup, S., Donnelly, M., McClintock, I., and Carpenter, S. (2009). Measurements of Controllable Pitch Propeller Blade loads Under Cavitating Conditions. In *Proc. of* 1st *Symposium on Marine Propellers and Propulsion*, Throndheim, Norway.

Koushan, K. (2006). Dynamics of ventilated propeller blade loading on thrusters due to forced sinusoidal heave motion. In *Proc. of* 28th *Symposium on Naval Hydrodynamics*, Rome, Italy.

Krasilinov, V., Zhang, Z., and Hong, F. (2009). Analysis of Unsteady Propeller Blade Forces by RANS. In *Proc. of* 1st *Symposium on Marine Propellers and Propulsion*, Throndheim, Norway.

Lewis, J. (1998). *Principles of Naval Architecture - vol. 3*. Society of Naval Architects and Marine Engineers (SNAME), New York, second edition.

Misztal, F. (1933). The problem of the propeller in yaw with special reference to airplane stability. Technical Report No. TN 696, National Advisory Committee for Aeronautics (NACA).

Mofidi, A. and Carrica, P. M. (2014). Simulations of zigzag maneuvers for a container ship with direct moving rudder and propeller. *Computers and Fluids*, 96:191 – 203.

Muscari, R., Dubbioso, G., Ortolani, F., and Di Mascio, A. (2017). Analysis of propeller bearing loads by CFD. Part II: Transient maneuvers. *Ocean Engineering*, 146:217–233.

Muscari, R., Felli, M., and Di Mascio, A. (2011). Analysis of the Flow Past a Fully Appended Hull with Propellers by Computational and Experimental Fluid Dynamics. *Journal of Fluids Engineering*, 133:061104 1–16.

Ortolani, F. and Dubbioso, G. (2020). In-plane and single blade loads measurement setups for propeller performance assessment during free running and captive model tests. *Ocean Engineering*, 217:107928.

Ortolani, F., Mauro, S., and Dubbioso, G. (2015a). Investigation of the radial bearing force developed during actual ship operations. part 1: Straight ahead sailing and turning maneuvers. *Ocean Engineering*, 94:67 – 87.

Ortolani, F., Mauro, S., and Dubbioso, G. (2015b). Investigation of the radial bearing force developed during actual ship operations. part 2: Unsteady maneuvers. *Ocean Engineering*, 106:424 – 445.

Queutey, P., Wackers, J., Leroyer, A., Deng, G., Guilmineau, E., Visonneau, M., Hagesteijin, G., and Brouwer, J. (2014). Dynamic behaviour of the loads of podded propellers in waves: experimental and numerical simulations. In *Proc. of* 33rd *International Conference on Ocean, Offshore and Arctic Engineering*, San Francisco, USA.

Saettone, S., Tavakoli, S., Taskar, B., Jensen, M. V., Pedersen, E., Schramm, J., Steen, S., and Andersen, P. (2020). The importance of the engine-propeller model accuracy on the performance prediction of a marine propulsion system in the presence of waves. *Applied Ocean Research*, 103:102320.

Savio, L., Spence, S., Koushan, K., and Steen, S. (2013). Full Scale and Model Scale Propeller Ventilation Behind Ship. In *Proc. of* 3st *Symposium on Marine Propellers and Propulsion*, Tasmania, Australia.

Sun, S., Li, L., Wang, C., and Zhang, H. (2018). Numerical prediction analysis of propeller exciting force for hull–propeller–rudder system in oblique flow. *International Journal of Naval Architecture and Ocean Engineering*, 10(1):69 – 84.

Taskar, B. and Steen, S. (2016). Effect of waves on cavitation and pressure pulses. *Applied Ocean Research*, 60:61–74.

Taskar, B., Steen, S., and Eriksson, J. (2017). Effect of waves on cavitation and pressure pulses of a tanker with twin podded propulsion. *Applied Ocean Research*, 65:206–218.

Vrijdag, A., Stapersma, D., and van Terwisga, T. (2010). Control of propeller cavitation in operational conditions. *Journal of Marine Engineering and Technology*, 14(3).

Wang, J., Akinturk, A., Jones, S., Bose, N., Kim, M., and Chun, H. (2006). Ice loads acting on a model podded propeller blade (omae2005-67416). *Journal of Offshore Mechanics and Arctic Engineering*, 129(3):236 – 244.

Yao, J. (2015). Investigation on hydrodynamic performance of a marine propeller in oblique flow by ranse computations. *International Journal of Naval Architecture and Ocean Engineering*, 7(1):56–69.

Appendix A

Single blade and propeller loads: plots and tables

A.1 Free running - straight ahead navigation

A.1.1 Blade loads values in blade (rotating) frame

LOAD	$\bar{x}_1$	σ_1	$\bar{x}_2$	σ_2
K_{Tx}^B	3.53E-02	1.64E-03	3.52E-02	1.27E-04
K_{Ty}^B	-2.46E-02	4.70E-03	-2.50E-02	8.13E-05
K_{Tz}^B	2.52E-06	3.88E-03	1.06E-05	6.14E-05
K_{Qx}^B	9.10E-03	1.45E-03	9.28E-03	2.38E-05
K_{Qy}^B	1.16E-02	5.13E-03	1.15E-02	4.15E-05
K_{Qz}^B	1.99E-03	1.30E-04	2.02E-03	1.12E-05

Table A.1 Single blade loads (blade frame), $F_N = 0.26$

LOAD	$\bar{x}_1$	σ_1	$\bar{x}_2$	σ_2
K_{Tx}^B	3.33E-02	5.35E-04	3.33E-02	1.53E-04
K_{Ty}^B	-2.35E-02	3.04E-04	-2.35E-02	9.76E-05
K_{Tz}^B	4.17E-03	1.26E-03	4.58E-03	6.14E-05
K_{Qx}^B	8.74E-03	5.80E-05	8.64E-03	2.91E-05
K_{Qy}^B	1.08E-02	1.55E-04	1.08E-02	5.05E-05
K_{Qz}^B	2.24E-03	3.10E-05	2.24E-03	1.39E-05

Table A.2 Single blade loads (blade frame), $F_N = 0.34$

LOAD	$\bar{x}_1$	σ_1	$\bar{x}_2$	σ_2
K_{Tx}^B	3.59E-02	6.02E-04	3.60E-02	1.43E-04
K_{Ty}^B	-2.51E-02	8.99E-04	-2.51E-02	9.41E-05
K_{Tz}^B	4.30E-03	2.13E-03	4.87E-03	6.54E-05
K_{Qx}^B	9.13E-03	1.83E-04	9.13E-03	2.76E-05
K_{Qy}^B	1.17E-02	2.05E-04	1.17E-02	4.60E-05
K_{Qz}^B	2.11E-03	8.89E-05	2.09E-03	1.34E-05

Table A.3 Single blade loads (blade frame), $F_N = 0.40$

A.2 Free running - steady turning

A.2.1 Blade loads values in blade (rotating) frame

δ	LOAD					
	K_{Tx}^B	K_{Ty}^B	K_{Tz}^B	K_{Qx}^B	K_{Qy}^B	K_{Qz}^B
-35	8.031E-002	-4.586E-002	4.386E-003	1.612E-002	2.684E-002	-1.225E-003
-25	6.526E-002	-4.234E-002	-2.702E-003	1.405E-002	2.142E-002	-1.008E-004
-15	5.335E-002	-3.513E-002	3.258E-003	1.232E-002	1.742E-002	9.185E-004
-7.5	4.533E-002	-2.914E-002	5.076E-004	1.060E-002	1.461E-002	1.420E-003
0	3.517E-002	-2.504E-002	1.058E-005	9.280E-003	1.147E-002	2.022E-003
7.5	3.157E-002	-1.990E-002	3.914E-003	7.848E-003	1.024E-002	2.221E-003
15	4.386E-002	-3.685E-002	-6.109E-003	1.314E-002	1.434E-002	1.197E-003
25	4.478E-002	-2.223E-002	-2.028E-004	8.920E-003	1.520E-002	6.501E-004
35	5.332E-002	-3.279E-002	6.270E-003	1.165E-002	1.777E-002	1.965E-004

Table A.4 Blade loads; $F_N = 0.26$

δ	LOAD					
	K_{Tx}^B	K_{Ty}^B	K_{Tz}^B	K_{Qx}^B	K_{Qy}^B	K_{Qz}^B
-35	7.894E-002	-4.756E-002	5.359E-003	1.646E-002	2.633E-002	-9.524E-004
-25	6.523E-002	-4.168E-002	6.200E-003	1.439E-002	2.142E-002	-5.995E-005
-15	5.033E-002	-3.402E-002	5.148E-003	1.193E-002	1.652E-002	1.125E-003
-7.5	4.465E-002	-2.755E-002	1.011E-002	9.808E-003	1.414E-002	1.377E-003
0	3.335E-002	-2.356E-002	4.167E-003	8.749E-003	1.087E-002	2.233E-003
7.5	3.309E-002	-2.419E-002	1.314E-002	8.243E-003	1.058E-002	1.922E-003
15	3.973E-002	-2.658E-002	4.310E-003	9.683E-003	1.309E-002	1.451E-003
25	4.627E-002	-2.908E-002	6.437E-003	1.053E-002	1.545E-002	8.008E-004
35	5.210E-002	-3.218E-002	1.923E-003	1.141E-002	1.745E-002	3.695E-004

Table A.5 Blade loads; $F_N = 0.34$

δ	LOAD					
	K_{Tx}^B	K_{Ty}^B	K_{Tz}^B	K_{Qx}^B	K_{Qy}^B	K_{Qz}^B
-25	6.226E-002	-3.942E-002	5.712E-003	1.371E-002	2.034E-002	2.915E-004
-15	5.108E-002	-3.441E-002	5.459E-003	1.202E-002	1.669E-002	1.143E-003
-7.5	4.464E-002	-3.191E-002	3.450E-003	1.096E-002	1.455E-002	1.475E-003
0	3.591E-002	-2.510E-002	4.301E-003	9.129E-003	1.173E-002	2.105E-003
7.5	3.323E-002	-2.247E-002	5.360E-003	8.339E-003	1.084E-002	2.233E-003
15	4.041E-002	-2.678E-002	5.674E-003	9.682E-003	1.322E-002	1.461E-003
25	4.663E-002	-2.968E-002	5.670E-003	1.062E-002	1.549E-002	8.165E-004

Table A.6 Blade loads; $F_N = 0.40$

A.2.2 Propeller loads values in hub (fixed) frame

δ	LOAD					
	K_{Tx}^{PROP}	K_{Ty}^{PROP}	K_{Tz}^{PROP}	K_{Qx}^{PROP}	K_{Qy}^{PROP}	K_{Qz}^{PROP}
-35°	4.01E-01	4.40E-02	-2.04E-02	8.06E-02	-3.03E-02	3.12E-02
-25°	3.27E-01	4.16E-02	-1.94E-02	7.02E-02	-2.77E-02	2.51E-02
-15°	2.67E-01	2.93E-02	-7.18E-03	6.16E-02	-2.17E-02	1.39E-02
-7.5°	2.27E-01	1.53E-02	2.03E-03	5.31E-02	-1.62E-02	2.27E-03
0°	1.76E-01	-6.17E-03	3.62E-02	4.66E-02	-8.00E-03	-1.31E-02
7.5°	1.57E-01	-2.71E-02	4.88E-02	3.92E-02	-2.22E-03	-2.13E-02
15°	2.19E-01	-4.35E-02	6.48E-02	6.57E-02	1.04E-03	-3.45E-02
25°	2.23E-01	-4.70E-02	6.53E-02	4.46E-02	3.16E-03	-3.98E-02
35°	2.67E-01	-6.12E-02	4.21E-02	5.82E-02	1.45E-02	-3.59E-02

Table A.7 Propeller loads; $F_N = 0.26$

δ	LOAD					
	K_{Tx}^{PROP}	K_{Ty}^{PROP}	K_{Tz}^{PROP}	K_{Qx}^{PROP}	K_{Qy}^{PROP}	K_{Qz}^{PROP}
-35°	3.95E-01	5.75E-02	-1.87E-02	8.23E-02	-3.29E-02	2.87E-02
-25°	3.27E-01	4.93E-02	-2.04E-02	7.20E-02	-2.80E-02	2.47E-02
-15°	2.52E-01	4.20E-02	-4.78E-03	5.96E-02	-2.31E-02	1.20E-02
-7.5°	2.23E-01	1.63E-02	5.61E-03	4.91E-02	-1.50E-02	6.09E-03
0°	1.66E-01	1.40E-03	3.44E-02	4.37E-02	-7.07E-03	-1.28E-02
7.5°	1.65E-01	-1.48E-02	5.10E-02	4.12E-02	-8.41E-03	-1.90E-02
15°	1.99E-01	-3.92E-02	6.17E-02	4.84E-02	5.21E-03	-3.46E-02
25°	2.31E-01	-4.19E-02	6.09E-02	5.26E-02	6.13E-03	-3.96E-02
35°	2.62E-01	-5.53E-02	4.15E-02	5.72E-02	1.43E-02	-3.58E-02

Table A.8 Propeller loads; $F_N = 0.34$

δ	LOAD					
	K_{Tx}^{PROP}	K_{Ty}^{PROP}	K_{Tz}^{PROP}	K_{Qx}^{PROP}	K_{Qy}^{PROP}	K_{Qz}^{PROP}
-25°	2.93E-01	3.13E-02	-3.18E-02	6.36E-02	-1.70E-02	2.71E-02
-15°	2.41E-01	3.34E-02	-9.85E-03	5.57E-02	-1.87E-02	1.36E-02
-7.5°	2.10E-01	2.13E-02	1.13E-02	5.07E-02	-1.42E-02	5.23E-04
-0°	1.69E-01	5.01E-03	2.95E-02	4.23E-02	-9.80E-03	-1.00E-02
7.5°	1.56E-01	-1.04E-02	4.40E-02	3.85E-02	-6.38E-03	-1.90E-02
15°	1.90E-01	-2.62E-02	5.95E-02	4.49E-02	-2.63E-03	-3.14E-02
25°	2.19E-01	-3.12E-02	6.33E-02	4.91E-02	-1.54E-03	-3.61E-02

Table A.9 Propeller loads; $F_N = 0.40$

A.2.3 Blade loads time histories in blade (rotating) frame

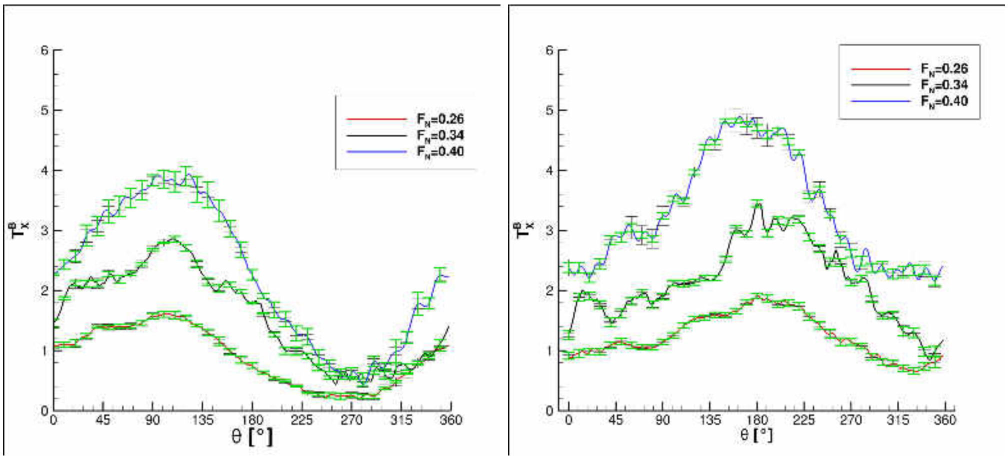

(a) T_X^B

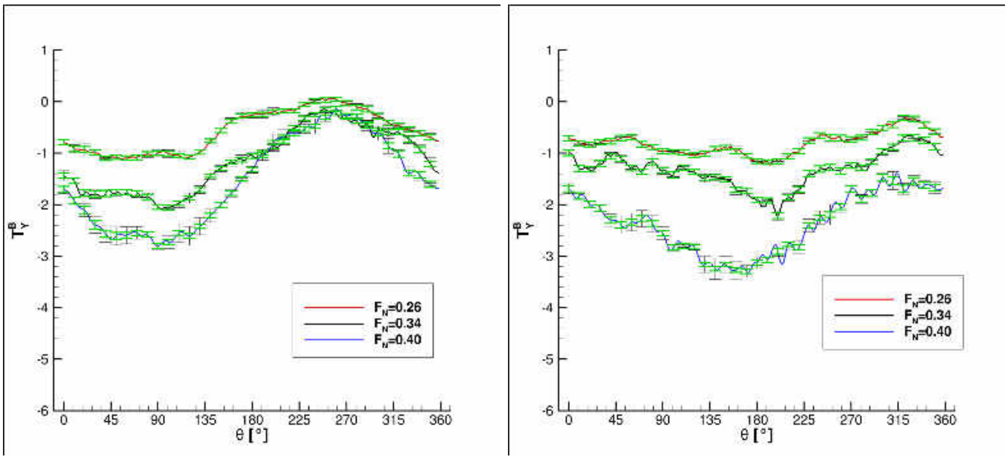

(b) T_Y^B

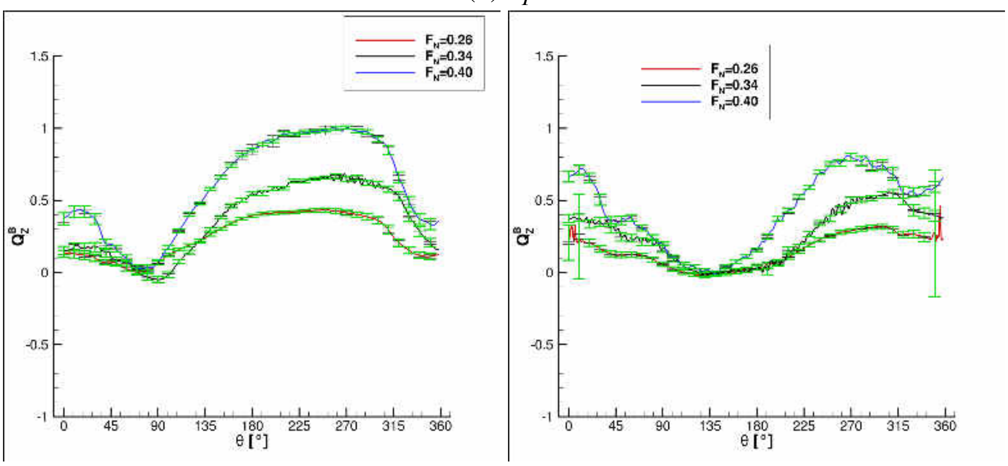

(c) Q_Z^B

Figure A.1 Single blade loads (rotating frame) and errors represented in terms of σ_1 (black) and σ_2 (green); $\delta = 7.5°$

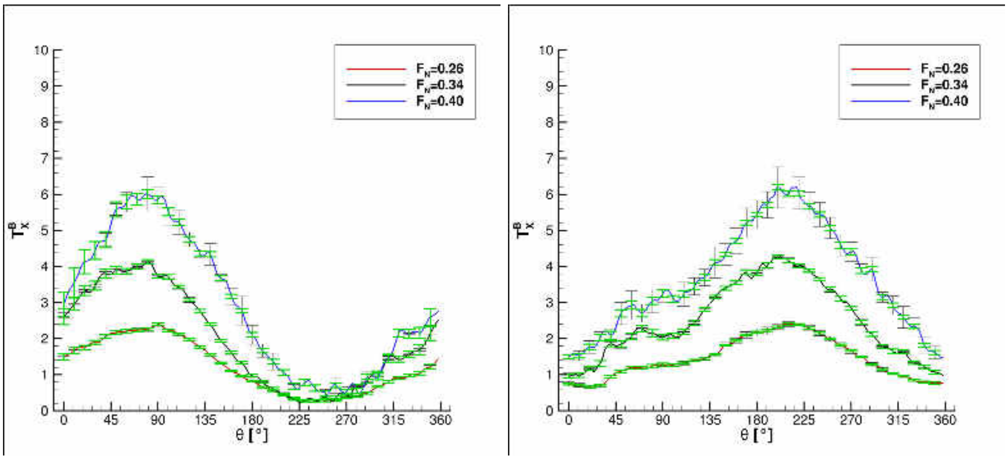

(a) T_X^B

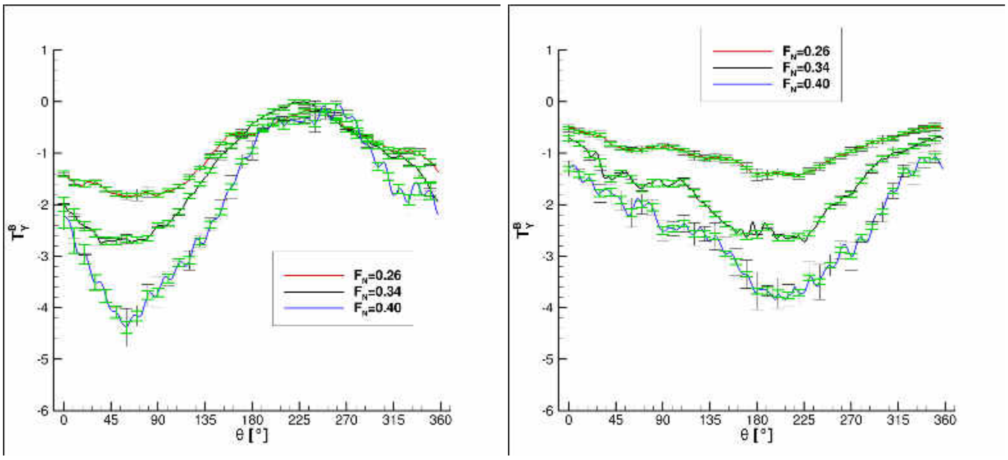

(b) T_Y^B

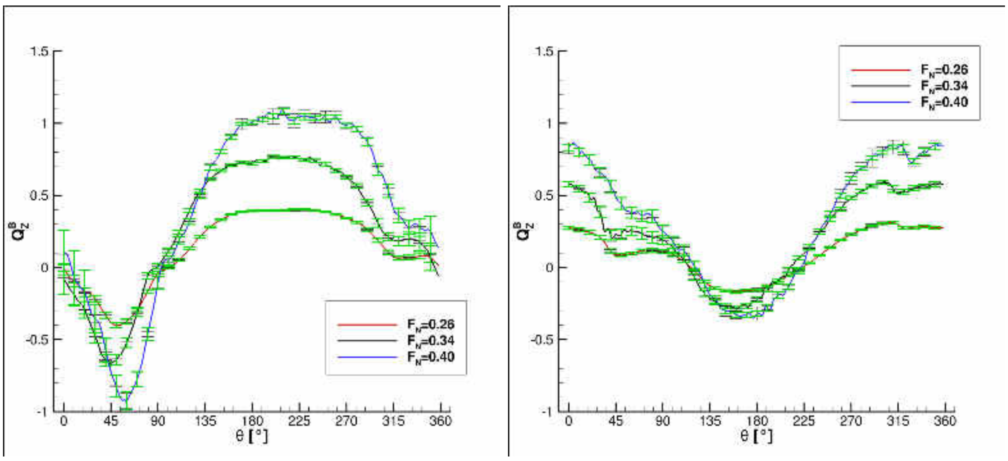

(c) Q_Z^B

Figure A.2 Single blade loads (rotating frame) and errors represented in terms of σ_1 (black) and σ_2 (green); $\delta = 15°$. Leeward side (left); windward side (right)

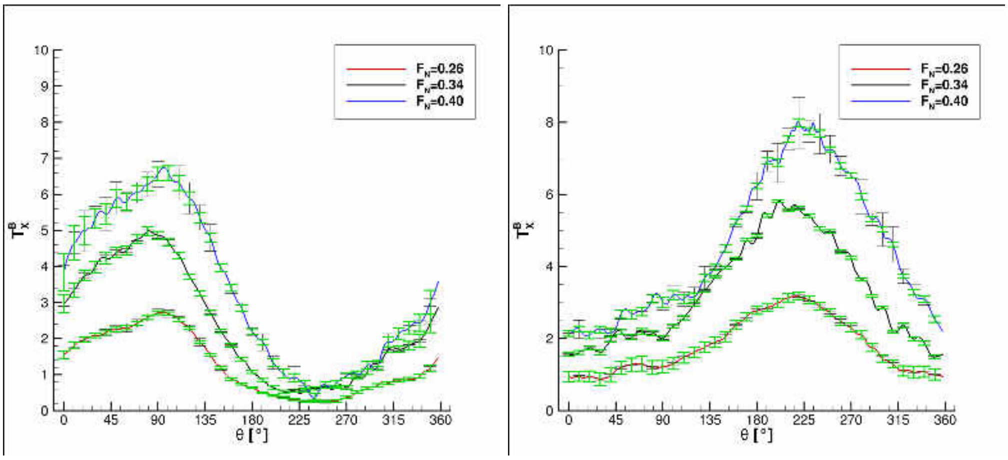

(a) T_X^B

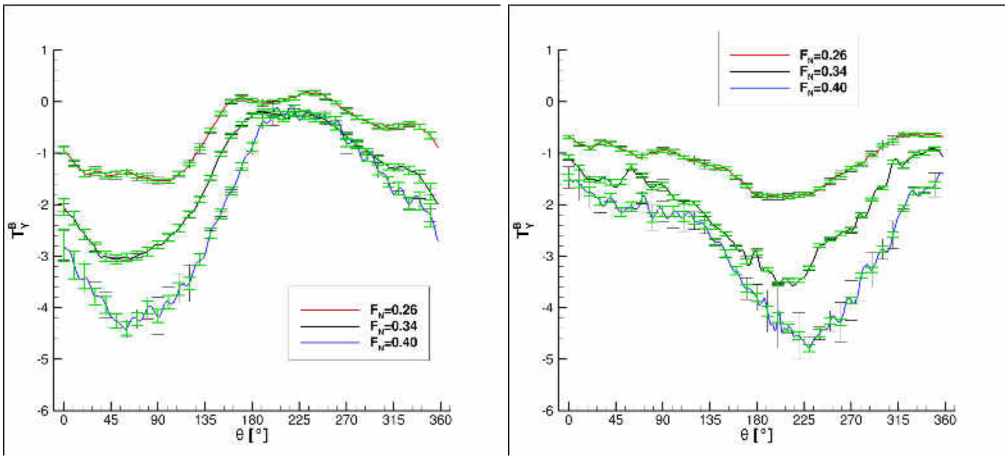

(b) T_Y^B

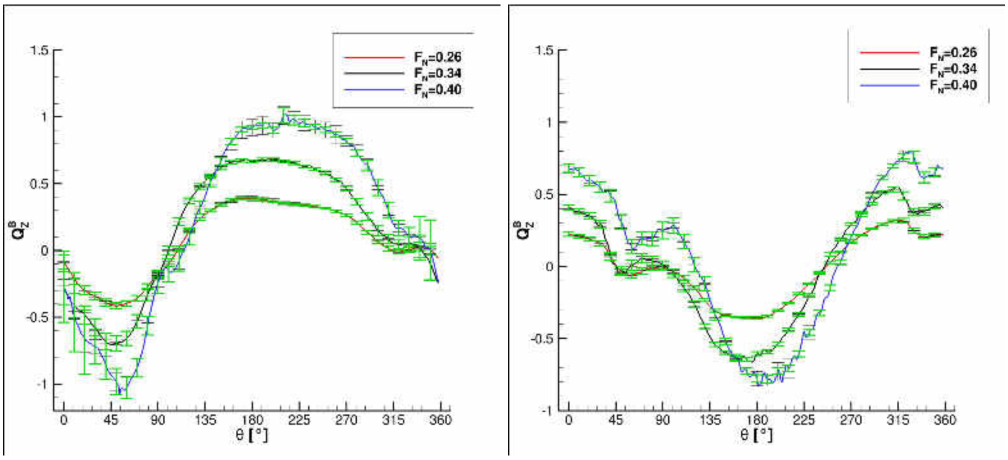

(c) Q_Z^B

Figure A.3 Single blade loads (rotating frame) and errors represented in terms of σ_1 (black) and σ_2 (green); $\delta = 25°$. Leeward side (left); windward side (right)

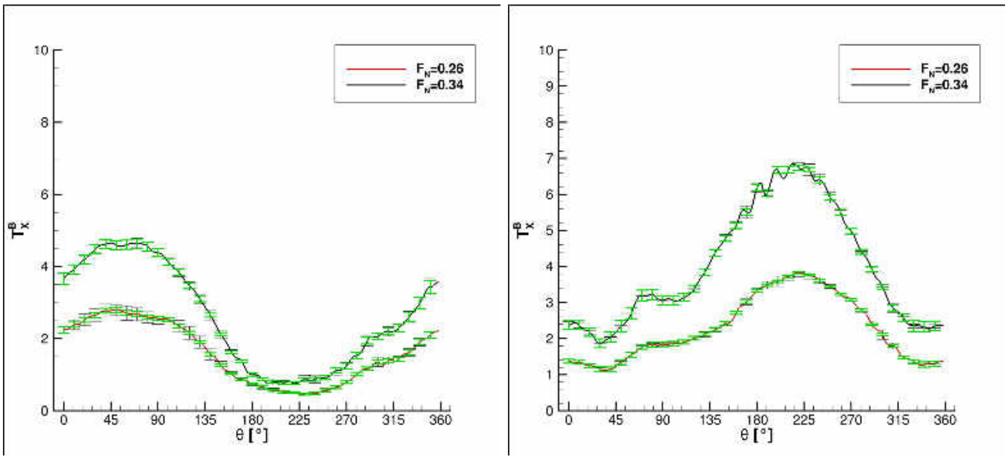

(a) T_X^B

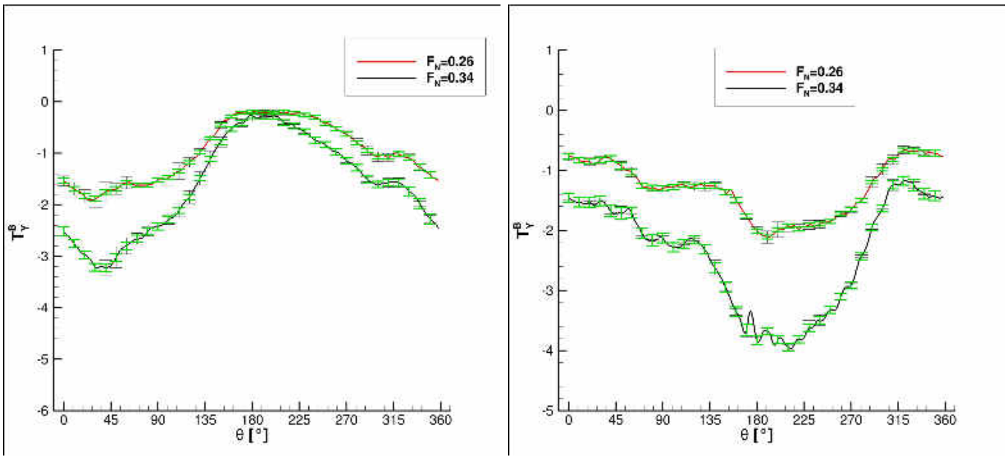

(b) T_Y^B

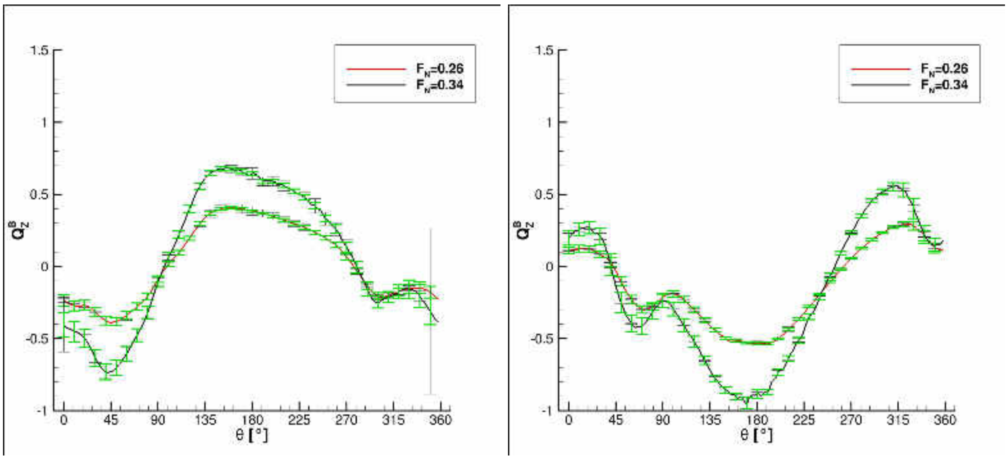

(c) Q_Z^B

Figure A.4 Single blade loads (rotating frame) and errors represented in terms of σ_1 (black) and σ_2 (green); $\delta = 35°$. Leeward side (left); windward side (right)

A.2.4 Thrust Eccentricity

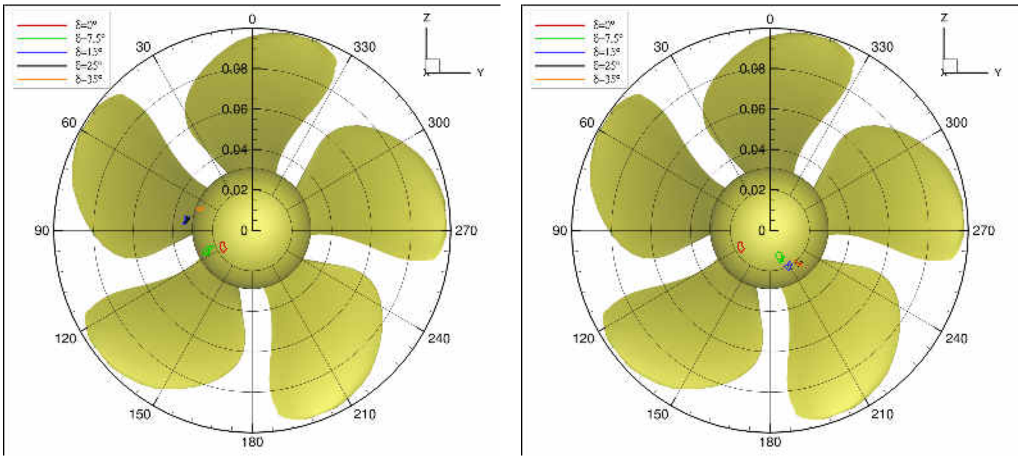

(a) internal propeller (b) external propeller

Figure A.5 Eccentricity of propeller thrust; $F_N = 0.34$

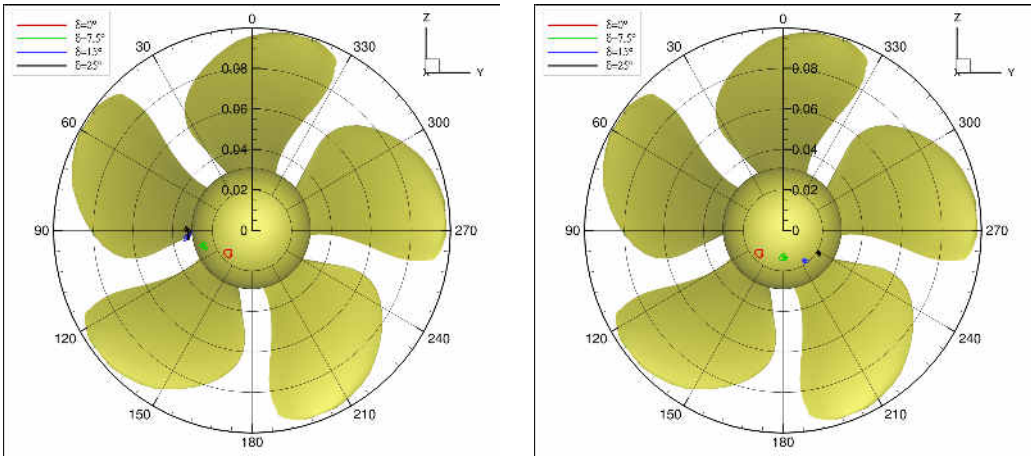

(a) internal propeller (b) external propeller

Figure A.6 Eccentricity of propeller thrust; $F_N = 0.40$

A.3 Captive tests

A.3.1 Blade loads values in blade (rotating) frame

	V=0.70		V=0.80		V=0.90		V=1.00		V=0.70		V=0.80		V=0.90		V=1.00	
β	$\overline{K_{Tx}}$	err%	$\overline{K_{Tx}}$	err%	$\overline{K_{Tx}}$	err%	$\overline{K_{Tx}}$	err%	$\overline{K_{Ty}}$	err%	$\overline{K_{Ty}}$	err%	$\overline{K_{Ty}}$	err%	$\overline{K_{Ty}}$	err%
-30	0.824	4.490	0.736	5.512	0.640	7.304	0.552	10.107	-0.481	-4.360	-0.442	-5.401	-0.395	-7.568	-0.349	-9.968
-20	0.842	2.657	0.730	3.741	0.607	4.663	0.491	7.455	-0.501	-2.538	-0.448	-3.406	-0.387	-4.445	-0.325	-7.230
-15	0.935	2.534	0.809	3.045	0.688	3.840	0.545	6.139	-0.547	-2.473	-0.488	-3.104	-0.429	-3.933	-0.356	-6.413
-7.5	0.955	1.435	0.831	1.633	0.694	2.307	0.558	3.111	-0.566	-1.309	-0.509	-1.532	-0.441	-2.278	-0.367	-2.906
0	1.000	1.014	0.862	1.322	0.699	1.599	0.563	2.092	-0.600	-0.933	-0.538	-1.176	-0.460	-1.586	-0.389	-2.002
7.5	1.111	1.430	0.987	1.393	0.865	1.717	0.737	2.022	-0.660	-1.142	-0.607	-1.243	-0.552	-1.562	-0.492	-1.904
15	1.147	1.293	1.019	1.712	0.894	2.076	0.759	2.829	-0.679	-1.112	-0.622	-1.413	-0.565	-2.057	-0.501	-2.951
20	1.202	0.933	1.079	1.146	0.942	1.425	0.805	2.213	-0.710	-1.008	-0.661	-1.270	-0.601	-1.570	-0.533	-2.425
30	1.311	1.860	1.233	1.668	1.138	2.188	1.037	2.971	-0.746	-1.843	-0.717	-1.738	-0.675	-2.476	-0.628	-3.121

Table A.10 Mean value of blade thrust and side force ratio and error

	V=0.70		V=0.80		V=0.90		V=1.00		V=0.70		V=0.80		V=0.90		V=1.00	
β	$\overline{K_{Qx}}$	err%	$\overline{K_{Qx}}$	err%	$\overline{K_{Qx}}$	err%	$\overline{K_{Qx}}$	err%	$\overline{K_{Qy}}$	err%	$\overline{K_{Qy}}$	err%	$\overline{K_{Qy}}$	err%	$\overline{K_{Qy}}$	err%
-30	0.829	3.695	0.758	4.480	0.675	6.060	0.598	8.181	1.318	4.442	1.157	5.430	0.985	7.201	0.824	10.523
-20	0.848	2.190	0.756	3.004	0.653	3.690	0.552	5.866	1.341	2.639	1.143	3.820	0.930	4.643	0.728	7.591
-15	0.926	2.102	0.824	2.529	0.723	3.168	0.605	4.927	1.480	2.477	1.258	3.068	1.050	3.704	0.815	5.870
-7.5	0.956	1.145	0.857	1.317	0.752	1.862	0.639	2.407	1.511	1.465	1.290	1.671	1.067	2.347	0.843	3.219
0	1.000	0.819	0.894	1.021	0.768	1.314	0.660	1.532	1.588	1.038	1.351	1.306	1.084	1.680	0.864	1.989
7.5	1.089	1.130	0.995	1.095	0.901	1.391	0.806	1.541	1.741	1.538	1.518	1.381	1.312	1.840	1.101	2.082
15	1.122	1.073	1.024	1.382	0.930	1.720	0.826	2.317	1.808	1.427	1.573	1.768	1.364	2.063	1.143	2.765
20	1.165	0.803	1.075	0.979	0.972	1.237	0.868	1.846	1.890	0.890	1.668	1.027	1.431	1.331	1.209	2.109
30	1.239	1.620	1.179	1.509	1.108	2.097	1.028	2.653	2.076	1.828	1.915	1.654	1.748	2.150	1.573	2.901

Table A.11 Mean value of blade torque and bending moment ratio and error

	V=0.70		V=0.80		V=0.90		V=1.00	
β	$\overline{K_{Qz}}$	err%	$\overline{K_{Qz}}$	err%	$\overline{K_{Qz}}$	err%	$\overline{K_{Qz}}$	err%
-30	0.019	86.258	0.008	244.988	0.022	96.084	0.044	56.441
-20	0.001	1374.006	0.016	66.245	0.058	23.480	0.074	20.846
-15	-0.048	-21.956	-0.025	-41.501	-0.006	-192.277	0.041	37.093
-7.5	-0.045	-15.224	-0.044	-14.690	0.017	50.079	0.066	11.777
0	-0.016	-30.343	0.005	89.853	0.056	8.985	0.097	6.025
7.5	-0.095	-4.830	-0.094	-7.062	-0.060	-11.392	-0.009	-77.334
15	-0.052	-13.325	-0.052	-13.660	-0.024	-30.380	0.011	78.639
20	-0.091	-5.996	-0.080	-7.963	-0.048	-12.397	-0.009	-87.685
30	-0.139	-6.711	-0.143	-5.332	-0.124	-7.090	-0.101	-11.811

Table A.12 Mean value of blade spindle torque ratio and error

Appendix B

FFT analysis results

B.1 Free running - straight ahead navigation

B.1.1 Amplitude values in blade (rotating) frame

	1^{st} BPF			
LOAD	$\bar{x}_1$	σ_1	$\bar{x}_2$	σ_2
K^B_{Tx}	1.70E-02	4.95E-04	1.70E-02	1.09E-04
K^B_{Ty}	1.35E-02	4.98E-04	1.35E-02	8.99E-05
K^B_{Tz}	2.35E-03	6.94E-04	2.30E-03	6.23E-05
K^B_{Qx}	3.39E-03	1.46E-04	3.39E-03	2.50E-05
K^B_{Qy}	5.31E-03	1.77E-04	5.32E-03	3.48E-05
K^B_{Qz}	1.34E-03	3.72E-05	1.34E-03	1.15E-05

Table B.1 Amplitudes of harmonic content of single blade loads (blade frame); $F_N = 0.26$ (continued)

	2^{nd} BPF				3^{rd} BPF			
LOAD	$\bar{x}_1$	σ_1	$\bar{x}_2$	σ_2	$\bar{x}_1$	σ_1	$\bar{x}_2$	σ_2
K^B_{Tx}	3.67E-03	3.63E-04	3.67E-03	9.54E-05	2.86E-03	2.11E-04	2.86E-03	9.08E-05
K^B_{Ty}	2.16E-03	4.49E-04	2.16E-03	8.51E-05	1.68E-03	1.97E-04	1.66E-03	8.13E-05
K^B_{Tz}	9.19E-04	3.92E-04	7.87E-04	5.93E-05	7.41E-04	4.10E-04	6.14E-04	4.51E-05
K^B_{Qx}	7.62E-04	1.36E-04	7.68E-04	2.23E-05	5.76E-04	5.73E-05	5.71E-04	2.14E-05
K^B_{Qy}	1.38E-03	1.23E-04	1.38E-03	3.27E-05	1.04E-03	6.89E-05	1.04E-03	3.07E-05
K^B_{Qz}	1.44E-04	2.27E-05	1.40E-04	8.90E-06	9.90E-05	8.82E-06	9.76E-05	7.61E-06

Table B.2 Amplitudes of harmonic content of single blade loads (blade frame); $F_N = 0.26$ (continued)

	4^{th} BPF				5^{th} BPF			
LOAD	$\bar{x}_1$	σ_1	$\bar{x}_2$	σ_2	$\bar{x}_1$	σ_1	$\bar{x}_2$	σ_2
K_{Tx}^B	2.66E-03	1.02E-03	2.56E-03	8.37E-05	1.16E-03	1.74E-04	1.14E-03	7.13E-05
K_{Ty}^B	4.33E-03	1.86E-03	4.15E-03	8.32E-05	1.01E-03	1.56E-04	1.00E-03	5.81E-05
K_{Tz}^B	3.12E-03	1.24E-03	2.98E-03	7.82E-05	7.29E-04	3.40E-04	6.14E-04	4.67E-05
K_{Qx}^B	1.23E-03	5.36E-04	1.20E-03	2.02E-05	2.31E-04	3.70E-05	2.29E-04	1.44E-05
K_{Qy}^B	8.75E-04	3.12E-04	8.59E-04	2.70E-05	3.57E-04	4.98E-05	3.53E-04	2.12E-05
K_{Qz}^B	1.45E-04	4.27E-05	1.36E-04	8.12E-06	1.20E-04	1.23E-05	1.18E-04	7.73E-06

Table B.3 Amplitudes of harmonic content of single blade loads (blade frame); $F_N = 0.26$

	1^{st} BPF			
LOAD	$\bar{x}_1$	σ_1	$\bar{x}_2$	σ_2
K_{Tx}^B	1.64E-02	1.99E-04	1.64E-02	1.36E-04
K_{Ty}^B	1.24E-02	2.98E-04	1.23E-02	1.11E-04
K_{Tz}^B	1.71E-03	8.43E-04	1.45E-03	8.05E-05
K_{Qx}^B	3.33E-03	7.94E-05	3.32E-03	3.04E-05
K_{Qy}^B	5.07E-03	6.49E-05	5.06E-03	4.30E-05
K_{Qz}^B	1.24E-03	2.32E-05	1.24E-03	1.49E-05

Table B.4 Amplitudes of harmonic content of single blade loads (blade frame); $F_N = 0.34$ (continued)

	2^{nd} BPF				3^{rd} BPF			
LOAD	$\bar{x}_1$	σ_1	$\bar{x}_2$	σ_2	$\bar{x}_1$	σ_1	$\bar{x}_2$	σ_2
K_{Tx}^B	3.70E-03	2.09E-04	3.70E-03	1.18E-04	2.46E-03	3.63E-04	2.46E-03	1.16E-04
K_{Ty}^B	2.53E-03	2.33E-04	2.53E-03	7.65E-05	1.45E-03	2.52E-04	1.44E-03	8.95E-05
K_{Tz}^B	1.49E-03	7.87E-04	1.27E-03	7.28E-05	8.28E-04	7.34E-04	6.04E-04	6.43E-05
K_{Qx}^B	8.46E-04	5.86E-05	8.44E-04	2.32E-05	4.92E-04	7.19E-05	4.90E-04	2.49E-05
K_{Qy}^B	1.39E-03	7.27E-05	1.39E-03	3.99E-05	9.22E-04	1.11E-04	9.21E-04	3.97E-05
K_{Qz}^B	1.22E-04	1.98E-05	1.20E-04	1.12E-05	1.11E-04	1.12E-05	1.10E-04	1.01E-05

Table B.5 Amplitudes of harmonic content of single blade loads (blade frame); $F_N = 0.34$ (continued)

	4^{th} BPF				5^{th} BPF			
LOAD	$\bar{x}_1$	σ_1	$\bar{x}_2$	σ_2	$\bar{x}_1$	σ_1	$\bar{x}_2$	σ_2
K_{Tx}^B	2.69E-03	8.87E-04	2.65E-03	9.93E-05	1.16E-03	3.26E-04	1.14E-03	8.04E-05
K_{Ty}^B	3.18E-03	1.47E-03	2.96E-03	7.39E-05	5.11E-04	6.49E-05	5.04E-04	4.98E-05
K_{Tz}^B	2.59E-03	1.09E-03	2.39E-03	7.13E-05	7.31E-04	6.16E-04	5.44E-04	5.49E-05
K_{Qx}^B	9.01E-04	4.16E-04	8.21E-04	2.02E-05	1.05E-04	1.16E-05	1.03E-04	1.19E-05
K_{Qy}^B	8.41E-04	2.59E-04	8.29E-04	3.22E-05	3.06E-04	6.88E-05	2.99E-04	2.39E-05
K_{Qz}^B	1.03E-04	2.76E-05	9.54E-05	9.26E-06	1.05E-04	1.82E-05	1.01E-04	9.48E-06

Table B.6 Amplitudes of harmonic content of single blade loads (blade frame); $F_N = 0.34$

	1^{st} BPF			
LOAD	$\bar{x}_1$	σ_1	$\bar{x}_2$	σ_2
K^B_{Tx}	1.68E-02	1.81E-04	1.68E-02	1.42E-04
K^B_{Ty}	1.21E-02	3.31E-04	1.21E-02	1.16E-04
K^B_{Tz}	2.33E-03	4.19E-03	1.14E-03	9.13E-05
K^B_{Qx}	3.34E-03	7.26E-05	3.33E-03	3.12E-05
K^B_{Qy}	5.25E-03	6.03E-05	5.24E-03	4.35E-05
K^B_{Qz}	1.26E-03	6.58E-05	1.24E-03	1.57E-05

Table B.7 Amplitudes of harmonic content of single blade loads (blade frame); $F_N = 0.40$ (continued)

	2^{nd} BPF				3^{rd} BPF			
LOAD	$\bar{x}_1$	σ_1	$\bar{x}_2$	σ_2	$\bar{x}_1$	σ_1	$\bar{x}_2$	σ_2
K^B_{Tx}	3.71E-03	2.02E-04	3.69E-03	1.33E-04	2.30E-03	2.53E-04	2.30E-03	1.13E-04
K^B_{Ty}	2.26E-03	2.85E-04	2.24E-03	8.52E-05	1.53E-03	2.05E-04	1.53E-03	8.53E-05
K^B_{Tz}	2.46E-03	4.21E-03	1.20E-03	8.38E-05	2.30E-03	4.20E-03	9.88E-04	8.06E-05
K^B_{Qx}	7.53E-04	7.69E-05	7.49E-04	2.53E-05	4.75E-04	4.45E-05	4.75E-04	2.34E-05
K^B_{Qy}	1.32E-03	6.18E-05	1.32E-03	4.44E-05	8.18E-04	6.34E-05	8.21E-04	3.64E-05
K^B_{Qz}	1.33E-04	8.37E-05	1.10E-04	1.28E-05	1.42E-04	7.61E-05	1.21E-04	1.26E-05

Table B.8 Amplitudes of harmonic content of single blade loads (blade frame); $F_N = 0.40$ (continued)

	4^{th} BPF				5^{th} BPF			
LOAD	$\bar{x}_1$	σ_1	$\bar{x}_2$	σ_2	$\bar{x}_1$	σ_1	$\bar{x}_2$	σ_2
K^B_{Tx}	2.62E-03	9.74E-04	2.66E-03	1.09E-04	4.53E-04	6.69E-05	4.34E-04	5.89E-05
K^B_{Ty}	2.63E-03	1.09E-03	2.62E-03	7.15E-05	4.80E-04	8.91E-05	4.66E-04	4.98E-05
K^B_{Tz}	3.79E-03	3.70E-03	2.51E-03	8.57E-05	1.65E-03	3.92E-03	5.12E-04	6.89E-05
K^B_{Qx}	7.55E-04	2.99E-04	7.63E-04	2.00E-05	9.93E-05	1.55E-05	9.74E-05	1.20E-05
K^B_{Qy}	7.91E-04	2.51E-04	7.79E-04	3.30E-05	1.49E-04	1.67E-05	1.46E-04	1.90E-05
K^B_{Qz}	1.11E-04	8.23E-05	8.91E-05	1.05E-05	1.34E-04	8.84E-05	1.10E-04	1.10E-05

Table B.9 Amplitudes of harmonic content of single blade loads (blade frame); $F_N = 0.40$

B.1.2 Amplitude values in hub (fixed) frame

	$F_N = 0.26$									
LOAD	1^{st} BPF		2^{nd} BPF		3^{rd} BPF		4^{th} BPF		5^{th} BPF	
	$\bar{x}_1$	$\bar{x}_2$	$\bar{x}_1$	$\bar{x}_2$	$\bar{x}_1$	$\bar{x}_2$	$\bar{x}_1$	$\bar{x}_2$	$\bar{x}_1$	$\bar{x}_2$
K^H_{Ty}	2.55E-02	2.60E-02	7.04E-03	7.04E-03	1.80E-03	1.68E-03	8.66E-04	7.83E-04	3.63E-03	3.53E-03
K^H_{Tz}	2.43E-02	2.47E-02	5.78E-03	5.78E-03	1.39E-03	1.29E-03	1.40E-03	1.35E-03	3.80E-03	3.72E-03
K^H_{Qy}	1.21E-02	1.21E-02	2.92E-03	2.92E-03	7.96E-04	7.93E-04	4.74E-04	4.69E-04	4.02E-04	3.87E-04
K^H_{Qz}	1.12E-02	1.12E-02	1.85E-03	1.84E-03	8.54E-04	8.50E-04	5.85E-04	5.84E-04	4.70E-04	4.55E-04

Table B.10 Amplitudes of harmonic content of single blade loads (hub frame); $F_N = 0.26$

LOAD	$F_N = 0.34$									
	1^{st} BPF		2^{nd} BPF		3^{rd} BPF		4^{th} BPF		5^{th} BPF	
	$\bar{x}_1$	$\bar{x}_2$	$\bar{x}_1$	$\bar{x}_2$	$\bar{x}_1$	$\bar{x}_2$	$\bar{x}_1$	$\bar{x}_2$	$\bar{x}_1$	$\bar{x}_2$
K^H_{Ty}	2.49E-02	2.49E-02	6.12E-03	6.10E-03	2.01E-03	2.01E-03	1.06E-03	1.03E-03	2.72E-03	2.55E-03
K^H_{Tz}	2.31E-02	2.30E-02	5.20E-03	5.08E-03	1.88E-03	1.72E-03	6.81E-04	4.92E-04	2.99E-03	2.83E-03
K^H_{Qy}	1.18E-02	1.18E-02	2.72E-03	2.72E-03	7.74E-04	7.66E-04	4.04E-04	3.96E-04	4.62E-04	4.58E-04
K^H_{Qz}	1.05E-02	1.04E-02	1.82E-03	1.82E-03	8.26E-04	8.13E-04	5.12E-04	5.04E-04	3.57E-04	3.41E-04

Table B.11 Amplitudes of harmonic content of single blade loads (hub frame); $F_N = 0.34$

LOAD	$F_N = 0.40$									
	1^{st} BPF		2^{nd} BPF		3^{rd} BPF		4^{th} BPF		5^{th} BPF	
	$\bar{x}_1$	$\bar{x}_2$	$\bar{x}_1$	$\bar{x}_2$	$\bar{x}_1$	$\bar{x}_2$	$\bar{x}_1$	$\bar{x}_2$	$\bar{x}_1$	$\bar{x}_2$
K^H_{Ty}	2.67E-02	2.67E-02	6.53E-03	6.28E-03	1.27E-03	1.01E-03	1.76E-03	1.45E-03	2.83E-03	2.71E-03
K^H_{Tz}	2.53E-02	2.47E-02	6.61E-03	5.49E-03	2.98E-03	1.72E-03	2.02E-03	8.16E-04	3.61E-03	2.52E-03
K^H_{Qy}	1.25E-02	1.25E-02	2.73E-03	2.72E-03	4.37E-04	4.28E-04	3.77E-04	3.79E-04	3.88E-04	3.88E-04
K^H_{Qz}	1.13E-02	1.13E-02	1.90E-03	1.89E-03	9.98E-04	9.80E-04	4.13E-04	3.83E-04	3.79E-04	3.67E-04

Table B.12 Amplitudes of harmonic content of single blade loads (hub frame); $F_N = 0.40$

B.2 Free running - steady turning

B.2.1 Amplitude values in blade (rotating) frame

δ	LOAD					
	K^B_{Tx}		K^B_{Ty}		K^B_{Qz}	
	1^{st} BPF	2^{st} BPF	1^{st} BPF	2^{st} BPF	1^{st} BPF	2^{st} BPF
-35°	4.209E-002	1.177E-002	2.037E-002	8.068E-003	3.307E-003	7.937E-004
-25°	3.742E-002	1.011E-002	1.891E-002	7.319E-003	2.754E-003	7.487E-004
-15°	2.729E-002	6.940E-003	1.382E-002	4.607E-003	2.030E-003	5.201E-004
-7.5°	1.769E-002	5.119E-003	9.672E-003	3.048E-003	1.491E-003	3.181E-004
0°	1.704E-002	3.671E-003	1.355E-002	2.155E-003	1.344E-003	1.439E-004
7.5°	2.316E-002	2.316E-003	1.953E-002	1.253E-003	1.830E-003	1.375E-004
15°	3.611E-002	3.787E-003	2.763E-002	3.350E-003	3.110E-003	7.986E-004
25°	4.061E-002	8.749E-003	2.858E-002	7.477E-003	3.245E-003	9.782E-004
35°	3.849E-002	4.133E-003	2.633E-002	4.083E-003	3.119E-003	7.205E-004

Table B.13 Harmonics of blade loads; $F_N = 0.26$

δ	LOAD					
	K_{Tx}^{B}		K_{Ty}^{B}		K_{Qz}^{B}	
	1^{st} BPF	2^{st} BPF	1^{st} BPF	2^{st} BPF	1^{st} BPF	2^{st} BPF
-35°	4.281E-002	1.115E-002	2.326E-002	8.086E-003	3.160E-003	8.398E-004
-25°	3.818E-002	9.033E-003	2.110E-002	6.445E-003	2.656E-003	7.356E-004
-15°	2.792E-002	6.504E-003	1.685E-002	4.562E-003	2.059E-003	4.216E-004
-7.5°	1.721E-002	5.719E-003	8.626E-003	3.645E-003	1.352E-003	3.180E-004
0°	1.639E-002	3.704E-003	1.241E-002	2.537E-003	1.247E-003	1.225E-004
7.5°	2.231E-002	7.948E-004	1.768E-002	1.114E-003	1.801E-003	1.471E-004
15°	3.702E-002	4.399E-003	2.590E-002	3.255E-003	3.052E-003	8.093E-004
25°	4.129E-002	8.272E-003	2.708E-002	6.082E-003	3.143E-003	8.736E-004
35°	3.914E-002	5.557E-003	2.548E-002	5.340E-003	3.044E-003	1.007E-003

Table B.14 Harmonics of blade loads; $F_N = 0.34$

δ	LOAD					
	K_{Tx}^{B}		K_{Ty}^{B}		K_{Qz}^{B}	
	1^{st} BPF	2^{st} BPF	1^{st} BPF	2^{st} BPF	1^{st} BPF	2^{st} BPF
-25°	3.612E-002	8.325E-003	1.897E-002	6.244E-003	2.438E-003	7.538E-004
-15°	2.698E-002	6.026E-003	1.558E-002	4.425E-003	2.027E-003	3.524E-004
-7.5°	1.689E-002	4.132E-003	1.068E-002	1.763E-003	1.217E-003	3.479E-004
0°	1.684E-002	3.709E-003	1.217E-002	2.256E-003	1.269E-003	1.334E-004
7.5°	2.342E-002	2.047E-003	1.790E-002	1.039E-003	1.702E-003	1.498E-004
15°	3.616E-002	4.077E-003	2.557E-002	3.339E-003	2.915E-003	7.620E-004
25°	4.096E-002	4.807E-003	2.797E-002	4.338E-003	3.223E-003	7.070E-004

Table B.15 Harmonics of blade loads; $F_N = 0.40$

B.2.2 Amplitude plots

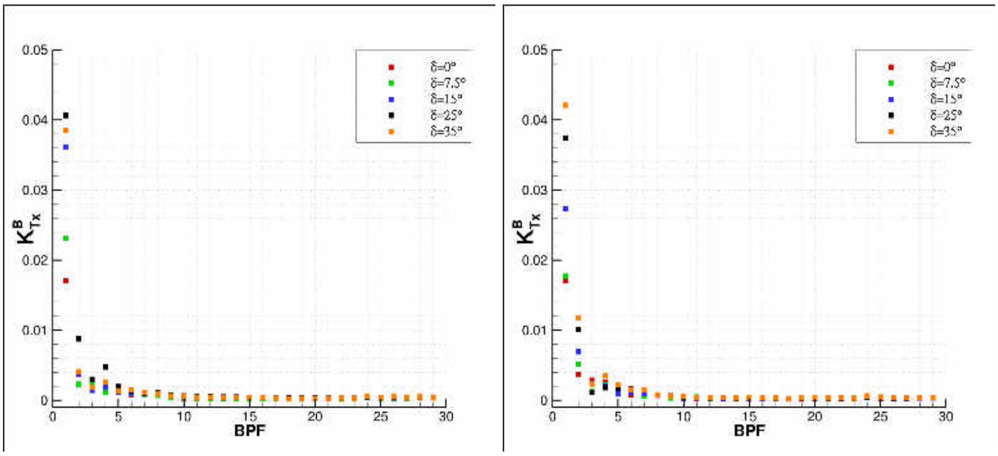

(a) K^B_{Tx}

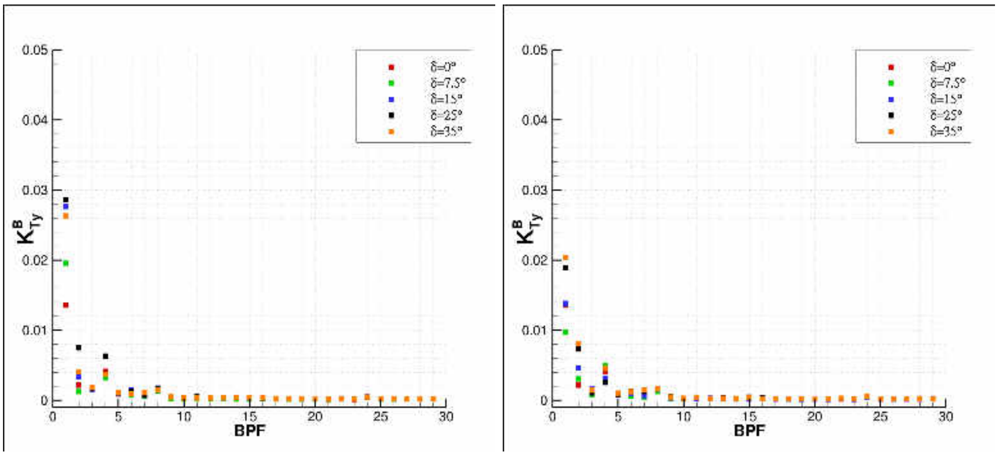

(b) K^B_{Ty}

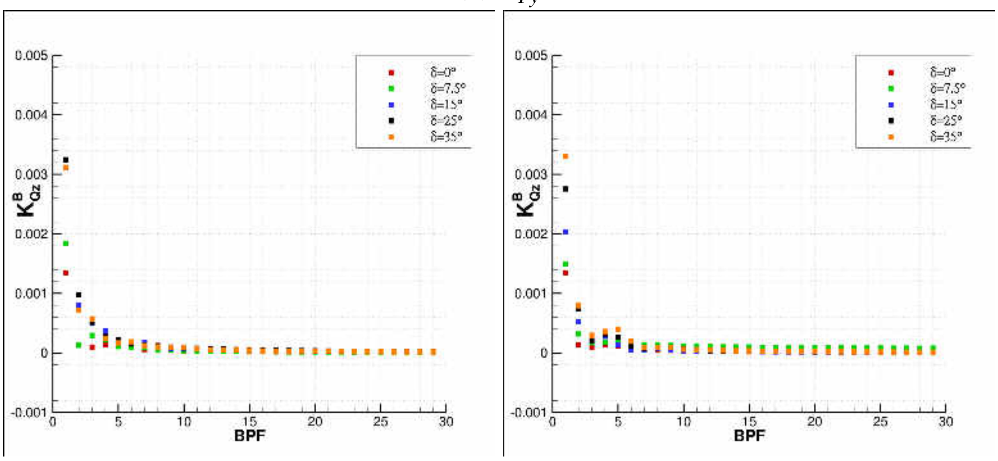

(c) K^B_{Qz}

Figure B.1 $F_N = 0.26$. Leeward side (left); windward side (right)

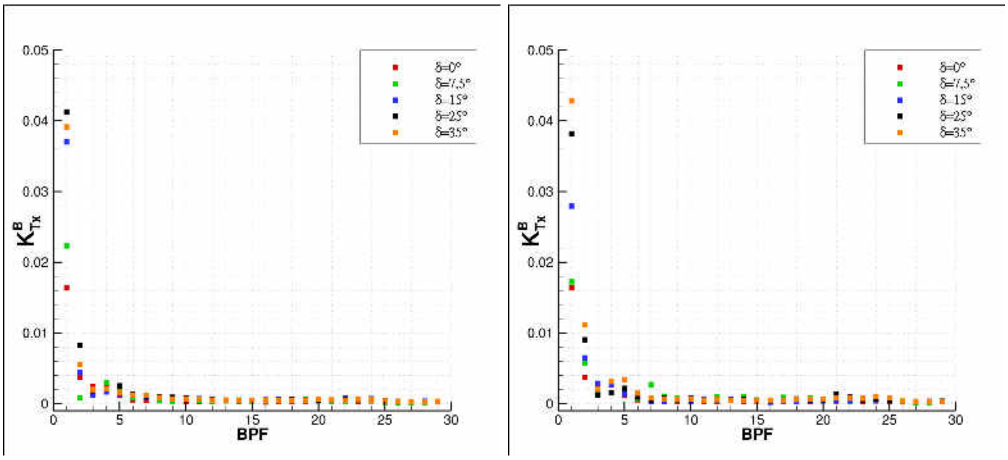

(a) K^B_{Tx}

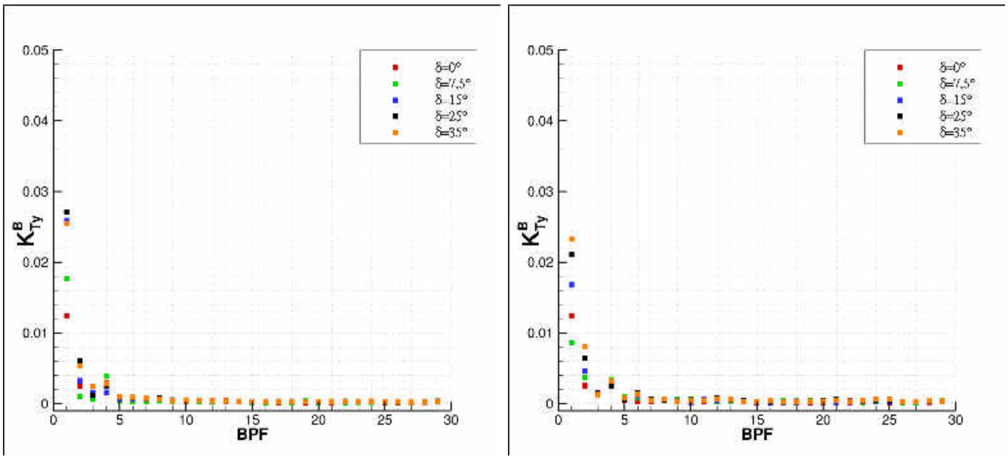

(b) K^B_{Ty}

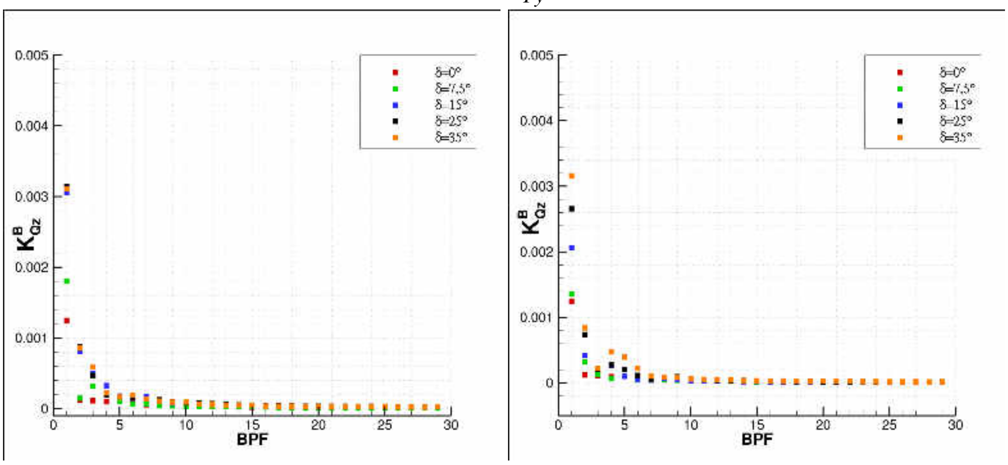

(c) K^B_{Qz}

Figure B.2 $F_N = 0.34$. Leeward side (left); windward side (right)

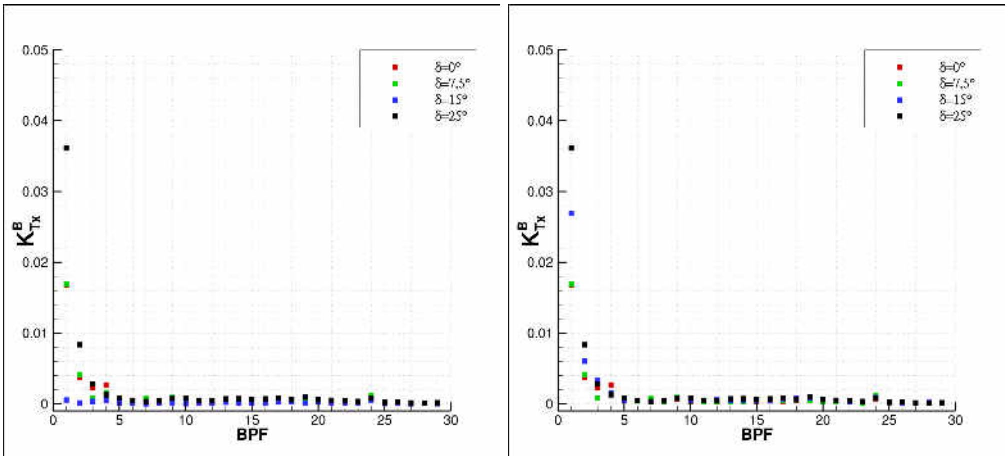

(a) K^B_{Tx}

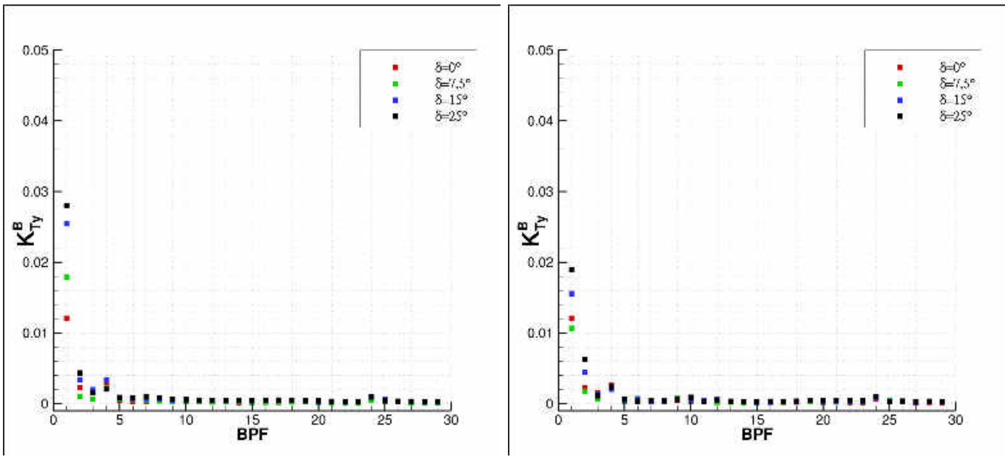

(b) K^B_{Ty}

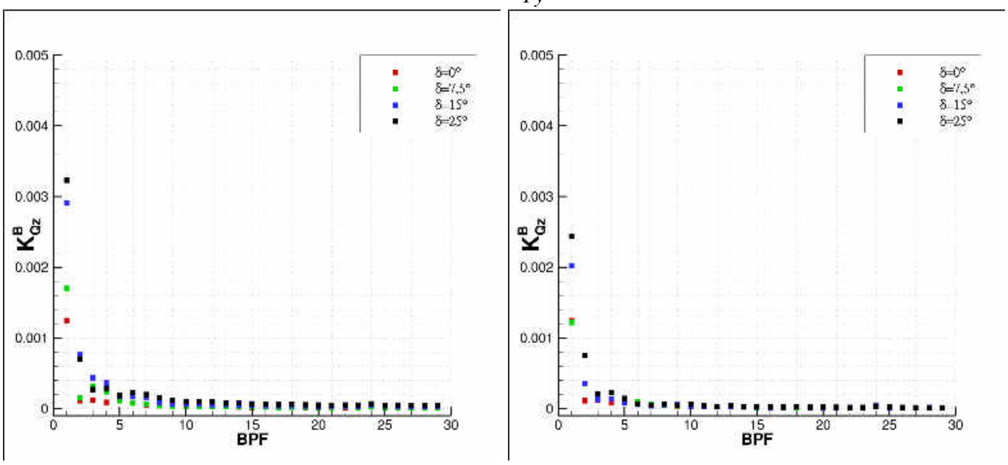

(c) K^B_{Qz}

Figure B.3 $F_N = 0.40$. Leeward side (left); windward side (right)